ODESSA ASTRONOMICAL PUBLICATIONS

Volume 25 Issue 2
(2012)

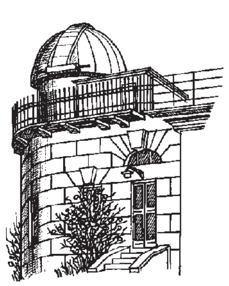

Odessa
«AstroPrint»

FOREWORD

This issue of the “Odessa Astronomical Publications” (vol. 25 issue 2) gathered articles that were presented at the XII Odessa International Astronomical Gamow’s Conference-School “ASTRONOMY AND BEYOND: ASTROPHYSICS, COSMOLOGY AND GRAVITATION, COSMO-MICROPHYSICS, RADIO-ASTRONOMY AND ASTROBIOLOGY”.

Conference-School has been devoted to:

– the 100th anniversary of the beginning of the directorship period in Odessa Astronomical Observatory of the outstanding astronomer Alexsander Yakovlevich Orlov;
– the 80th anniversary of the first radio-astronomical observations made by K.Jansky;
– 25th anniversary of the operation of the radio-interferometry system "URAN" of the National Academy of Sciences of Ukraine.

A.Ya.Orlov was working in Odessa since 1912 to 1934. During this time he became the doctor of astronomy (1915), the professor (1916), the academician of the Ukrainian Academy of Sciences (1918), and the corresponding member of the Soviet Union Academy of Sciences (1927). A.Ya.Orlov was the outstanding organizer of the scientific work and he was one of the founders of a new science at that time – geodynamics. The progenies of the "Orlov’s School" successfully worked in Russia, Poland, France, Bulgaria and other countries.

The Conference was organized by I.I.Mechnikov Odessa National University on August 20-26, 2012. Together with University, the following organizations took part in the Conference organization: Radio-astronomical Institute of the National Academy of Science of Ukraine and its Odessa Observatory branch “URAN-4”, the Department of Astronomy and Astronomical Observatory of I.I.Mechnikov Odessa National University, the Ukrainian Astronomical Association (Kiev), the Euro-Asian Astronomical Society (Moscow), the Odessa Astronomical Society, the Southern Scientific Center of the National Academy of Science of Ukraine. Co-chairs of the SOC were G.S.Bisnovatyi-Kogan (Russia) and V.M.Shulga (Ukraine), vice-chairs – A.I.Zhuk (Ukraine) and M.I.Ryabov (Ukraine).

The scientific program included the following sections: Memorial and Jubilee Meetings; Cosmology, Cosmomicrophysics and Gravitation; Astrophysics; Radioastronomy; Sun, Solar System and Astrobiology; Planetariums and Popularization of Astronomy.

About 100 scientists from Ukraine, Russia, Belorussia, Moldova, Kazakhstan and Armenia participated in the Conference-School. During the Memorial section 7 talks were presented. 44 reports and 34 posters were presented during the regular sections. In addition, the several discussions were organized. Among them:

Dark Matter and dark energy, and their alternatives (chair A.D.Chernin);

The theory, models and observations of active galaxies and quasars (chair G.S.Bisnovatyi-Kogan);

The special section “URAN“– 25 years of investigations (chair O.A.Litvinenko).

Editor-in-Chief
S.M. Andrievsky

CONTENTS

Plenary session

Cosmology, Cosmomicrophysics and Gravitation

Astrophysics

Radio-astronomy

Sun, solar system and astrobiology

ALEXANDER Ya. ORLOV – WELL-KNOWN SCIENTIST AND RECOGNIZED ORGANIZER OF ASTRONOMICAL RESEARCH. LITTLE-KNOWN FACTS OF HIS LIFE

Ya.S. Yatskiv [1], I.B. Vavilova [2], A.A. Korsun' [3]
Main Astronomical Observatory of the NAS of Ukraine, Kyiv, Ukraine

[1]*yatskiv@mao.kiev.ua,* [2]*irivav@mao.kiev.ua,* [3]*akorsun@mao.kiev.ua*

ABSTRACT. Alexander Ya. Orlov is a well-known astronomer and geophysicist as well as a world-recognized organizer of scientific research in Russia, the USSR, and Ukraine. Orlov has formulated his main scientific ideas during the Odesa's period of life. He studied a tidal deformation of the Earth and its polar motion using the gravity and latitude observations. He has proposed new defenitions of a mean pole and a mean latitude, as wel as a new method for determing the Earth pole coordinates. To the end of 1940-ties, the Orlov's scientific ideas were implemented and stimulated a development of a research field, which is now called as Astrogeodynamics or Space Geodynamics. Among the representatives of the Orlov's scientific school are about 20 Doctors of Sciences and more than 40 Candidates of Sciences, including the members of Academy of Sciences of Ukraine and other countries. Among them are N.Stoyko-Radilenko (France), J.Witkowski (Poland), V.Zhardetsky (Yugoslavia-Austria-USA), D.Pyaskovsky, Z.Aksent'eva, E.Lavrentieva, N.Popov, E.Fedorov and A.Korol in Ukraine. The deserved followers of the Orlov's scientific ideas were also I.Androsov, I.Dyukov, K.Mansurova, B.Novopashennyj, N.V.Zimmerman in Russia and M.Bursa (Chesh Republic), who worked with him, as well as his sons, A.A.Orlov and B.A. Orlov.

The Orlov's life and scientific activity were fully described in many articles. For that reason in this paper we will focus on the little-known facts of the Orlov's scientific-organizational activity, for example, the Orlov's appointments as a director of observatories in Odesa, Poltava, m.Pip-Ivan, Pulkovo, and Kyiv; interesesting facts related to his membership in the Academies of Sciences of the USSR and Ukrainian SSR; organization of a large-scale program on the latitude observations and gravimetric survey. We describe briefly his life and his astrogeodynamic scientific school.

Key words: History of astronomy; Personalities: A.Ya. Orlov (A. Orloff): biography.

Figure 1: A.Ya. Orlov (1880, Smolensk – 1954, Kyiv).

1. Introduction

Alexander (Olexandr) Ya.Orlov is a well-known astronomer and geophysicist as well as a recognized organizer of scientific research in Russia, the USSR, and Ukraine. The Orlov's life and scientific activity were fully described in many articles (see, for example, Aksent'eva, 1961; Fedorov, 1980; Korsun', 2003) as well as were written himself (published in (Orlov, 1997)). His "Selected papers" were issued in 1961. Since 1980, the Special Orlov's conferences "Study of the Earth as a planet by methods of astronomy, geodesy and geophysics" were organized in Kyiv (1980), Poltava (1986), Odesa (1992), and Kyiv (2009) as well as the Special Orlov's sessions at the International conferences JOURNEES in Paris (1998) and St. Petersburg (2003). In our paper "A.Ya. Orlov and his astrogeodynamical scientific school" (Yatskiv, Korsun', Vavilova, 2005), we provided also the Orlov's biography and analyzed attentively his principal scientific ideas, which were developed later by representatives of his scientific school. For that reason in this article we will focus on the little-known facts of the Orlov's scientific-organizational activity describing briefly his life.

Table 1: The key stones of a biography by A.Ya.Orlov (Archive of the NAS of Ukraine. A.Ya.Orlov, Personal Dossier)

Years	Position	Place of work
1901	Assistant-astronomer at the Pulkovo Observatory (summer period)	Pulkovo
1902-1905	Post-graduated student at the St. Peterbourg University	St. Peterbourg
1903-1905	Foreign feloowship	
1905-1907	Assistant-astronomer at the Observatory of the Tartu University	Tartu
1907-1908	Assistant-astronomer at the Pulkovo Observatory	Pulkovo
1908-1912	Astronomer-observer at the Observatory of the Tartu University	Tartu
1912-1934	Professor and Director of Observatory, Odesa University	Odesa
1926-1934	Director of the Poltava Gravimetrical Observatory AS UkrSSR (part-time)	Poltava
1919-1922	Member of the Ukrainian Academy of Sciences	Kyiv
1927	Corresponding-member of the AS USSR	Moscow
1934-1938	Professor of the P.K. Shternberg State Astronomical Institute	Moscow
1934-1938	Professor of the Institute for Geodesy and Cartography	Moscow
1938-1941	Director of the Poltava Gravimetrical Observatory AS UkrSSR	Poltava
1939	Member of the AS UkrSSR (secondly elected)	Kyiv
1939-1941	Director (part-time) of the Carpatian Observatory	m. Pip-Ivan
1941-1943	Director of the Poltava Gravimetrical Observatory AS UkrSSR	Irkutsk
1943-1944	Director (part-time) of the Pulkovo Observatory	Pulkovo
1943-1951	Director of the Poltava Gravimetrical Observatory AS UkrSSR	Poltava
1945-1948	Director of the Main Astronomical Observatory AS UkrSSR	Kyiv
1951-1952	Director of the Main Astronomical Observatory AS UkrSSR	Kyiv

The key data of the Orlov‘s biography are given in Table 1 as it follows from his Personal file of life (Archive of the NAS of Ukraine. A.Ya. Orlov, F. 251, op. 293, Personal Dossier No. 4). Hereafter we will use the present-day names of organizations and cities indicating sometimes their previous names.

2. Orlov‘s activity in 1902-1912

In 1902, A.Ya.Orlov graduated from the St. Petersbourg University with a diploma of the first degree and was left to prepare for teaching. In a short time after this, in 1903, he went abroad for three year period being financially supported by his aunt, Mrs. E.Witte (who put Orlov in ward since 1891). Orlov has attended the lectures of the well-known scientists (Poincare, Angel, Picard and others) in Paris. Afterwards he worked at the Geophysical Observatory in Gottingen and studied celestial mechanics in Lund.

After returning from foreign trips to Russia, Orlov has occupied the assistant position at the Astronomical Observatory of the Tartu University and was soon appointed as an assistant editor of the “Seismic Bulletin” of the Russian Academy of Sciences (RAS). In 1907, he returned to Pulkovo for observations of latitude variations with zenith telescope. In 1908, Orlov published (on the proposal by Prof. A.F.Bredikhin) his first paper on the Perseid‘s observations in the Proceedings of the RAS.

In 1908, Orlov was elected as an astronomer of the Tartu University and moved to Tartu again. Here he conducted observations of plumb line variations using a horizontal pendulum. In 1910, he obtained a Master Degree in astronomy and geodesy for his work “The first series of observations of the deformations of the Earth under the influence of the lunar-solar tides with a horizontal pendulum in Yur‘yev (Tartu)”. In the same year he was elected as an assistant professor at the Tartu University and a member of the Standing Seismic Commission of the RAS.

In 1911, Orlov took part in the International Seismic Congress in Manchester, where he submitted the proposal for organizing a wide world net of gravimetric stations to observe the lunar-solar tides, including the Siberia region (Tomsk city), the USSR. This proposal was accepted, and Orlov was elected as a member of the International Commission for Study of elastic deformation of the Earth. Meanwhile, in 1911, Orlov traveled to the USA to visit the Yerkes Observatory for studying the comet’s plates taken by Bernard. The result of this work was published in several papers on the theory of cometary forms. Returning to Russia in 1912, Orlov (together with A.M.Chizhitsky and P.K.Sobolevsky) undertook the complicated expedition to Siberia for gravimetric measuring on the Tobol‘sk-Tomsk-Biisk route. At the same time a new gravimetric station was built in Tomsk according to the Orlov‘s plan (this station worked with some interruptions in 1912-1920).

3. Odesa‘s period of the Orlov‘s life (1912-1934)

The Orlov‘s scientific and organizational skills were recognized, and, on December 1912, he was elected as a professor of the astronomy department and director of the Astronomical Observatory of the Odesa University. Orlov pointed out in his biography: *“After what I saw abroad in Europe and America, the Odesa Observatory has made me a very bad impression. I wanted to create an observatory which will meet the contemporary level of science and wanted to bring it out of sleepy state”*.

Besides of the observatory governing Orlov found time for teaching astronomy at the University and for scientific work. He lectured spherical and theoretical astronomy, celestial mechanics and higher geodesy. In 1915, he made reduction of the Tartu, Tomsk, and Potsdam observations of the lunar-solar tides for deriving the elastic properties of the Earth, and obtained for this work a doctorate in astronomy and geodesy in St.Peterbourg. In 1916 and 1917, Orlov undertook two expeditions to determine the force of gravity in the Altai region. This hard expedition was conducted at the mountainous Altai at high altitudes, in rainy weather, and with poor communication conditions. Nevertheless, this work was completed in 1917, even during the Civil War. Remarks by Orlov: *“On the way back from the Altai to Odesa, I fell ill with typhus in a very severe form and after prolonged unconsciousness I woke up in a struggle for a new order of life”*. And in this “a new order of life” there have been significant events in a life of the country, and the Orlov‘s personal life.

The Orlov‘s activity in Odesa Observatory was recognized too. In 1919, he was elected as a member of the newly organized (in 1918) the All-Ukrainian Academy of Sciences (AS UkrSSR, at present, the National Academy of Sciences of Ukraine (NAS of Ukraine)). According to the plan proposed by its founding president, Vladimir Vernadsky, the Central Astronomical Observatory of Ukraine should be established in an academic structure. And Orlov has begun to fulfill this task. At the same time, he was appointed as a rector of the Kyiv University and professor of the Astronomical Observatory of this university (unfortunately, no documents have been found, which explain why Orlov had not served for these duties).

For implementation of a plan on the establishing an academic observatory Orlov has created the Astronomical Computing Bureau headed by the Kyiv astronomer M.Dichenko (Tchernega, 1969). The Bureau had a duty to choose the site for an observatory and to develop a plan of its construction. In 1921, Orlov asked in a letter to the General Meeting of the AS UkrSSR *“to provide a land of one square mile near the grave of Taras Shevchenko and to appoint a special academic commission for a final selection of the observatory site near Kaniv city”* (Fig. 2). At that time he was not able to come often to Kyiv because of great difficulties of transportation between Kyiv and Odesa as well as of a family situation (six children) and a lack of appropriate apartment in Kyiv.

When Orlov was out of Kyiv, the decision about closing the Astronomical Computing Bureau was accepted, that was in fact a cessation of observatory‘s construction. Orlov took it as a personal outrage and distrust. He refused the status of a member of the Academy and other honorary positions in Kyiv in protest on such a decision. Orlov wrote in his official letter (Fig. 3): *“... Because the institutions entrusted to me can be destroyed by the Ukrainian Academy itself and because the reasons, for which it have been already happened as to the Astronomical Computing Bureau, did not tally with my high view on an authority of the Ukrainian Academy of Sciences, I has to decline the honor to be Ukrainian academician and ask to exclude me from the list of members”*. But the idea of establishing the Central Astronomical Observatory with the academic status did not leave him and was realized in 1944.

So, in the 1920-ties Orlov concentrated his activity in Odesa. These years have been very heavy both for the Odesa Observatory and the Orlov‘s family. Nevertheless, in a short period of time, there were realized scientific programs and projects aimed to support an economic development in Ukraine. Among them were a restoration of the triangulation network from the Dniester river to the Dniper river; preparation of the Marine astronomical calendar; leveling the Odesa coast for determining the movement of soil; development of an Ukrainian gravimetric network for mineral‘s search (see, in details, Tsesevich, 1980; Karetnikov, 1996, 2012; Volyanska et al., 2005).

To provide the Odesa Observatory with gravimetric instrumentations Orlov decided to undertake in 1923-1924 a perilous trip from Odesa to Tomsk. As Orlov noted: *“These trips were faced with difficulties. It was exceptional. Now I wondered how I could cope with all these things. And I managed not only all that was planning, but has done something more”*. Everybody who was acquanted with the Orlov‘s life and work has been also surprised by this undertaking. So, after overcoming all difficulties, Orlov delivered gravimetric devices to Odesa. Moreover, being in Irkutsk he persuaded V.K.Abolt, professor of the Irkutsk University, to organize the latitude observations in Irkutsk.

In 1924-1926, Orlov headed a large-scale program on the gravimetric survey of the areas of Ukraine. In 1926, with this aim and on the Orlov‘s proposal, the Poltava Gravimetric Observatory was established in the AS UkrSSR structure. At the same year Orlov was charged by the Academy of Sciences of the USSR (AS USSR) to travel to Nizhny Novgorod for choosing the site for a new gravity station (later the Gorky Latitude Station was organized).

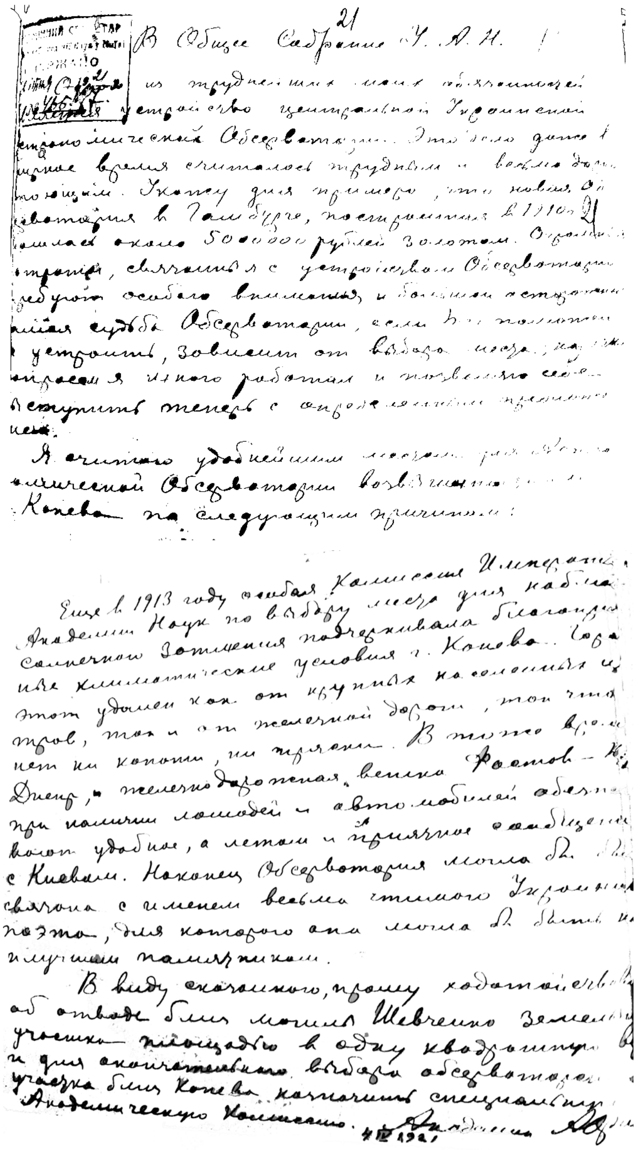

21

В Общее Собрание У.А.Н.

[illegible] из труднейших моих обязанностей [illegible] устройство центральной Украинской [illegible]номической Обсерватории. Это дело даже в [illegible]ное время считалось трудным и весьма дорогостоящим. Укажу для примера, что новая Обсерватория в Гамбурге, построенная в 1910 г., [illegible]шлась около 500000 рублей золотом. Огромные [illegible]траты, связанные с устройством Обсерватории, требуют особого внимания, и [illegible] судьба Обсерватории, если ее и получится устроить, зависит от выбора места; над этим вопросом я много работал и позволяю себе выступить теперь с определенным предложением.

Я считаю удобнейшим местом для Астрономической Обсерватории возвышенность [illegible] Канева по следующим причинам:

Еще в 1913 году особая Комиссия Императорской Академии Наук по выбору места для наблюдения Солнечного Затмения подчеркивала благоприятные климатические условия г. Канева. Город этот удален как от крупных населенных центров, так и от железной дороги, так что нет ни копоти, ни тряски. В то же вре[illegible] Фастов–К[illegible] Днепр, и железнодорожная ветка при наличии лошадей и автомобилей обеспечивает зимою удобное, а летом и приятное сообщение с Киевом. Наконец Обсерватория могла бы быть связана с именем весьма чтимого Украинского поэта, для которого она могла бы быть и лучшим памятником.

В виду сказанного, прошу ходатайствовать об отводе близ могилы Шевченко земельного участка площадью в одну квадратную версту и для окончательного выбора обсерваторского участка близ Канева назначить специальную Академическую Комиссию.

4 IV 1921 Академик А. Ор[illegible]

Figure 2: Letter by A.Ya. Orlov on April 4, 1921 with argumentation on a selection of the Kaniv site for an academic Central Astronomical Observatory in Ukraine (Archive of the NAS of Ukraine. A.Ya. Orlov, F. 251, op. 293, Personal Dossier No. 4, p. 21-22).

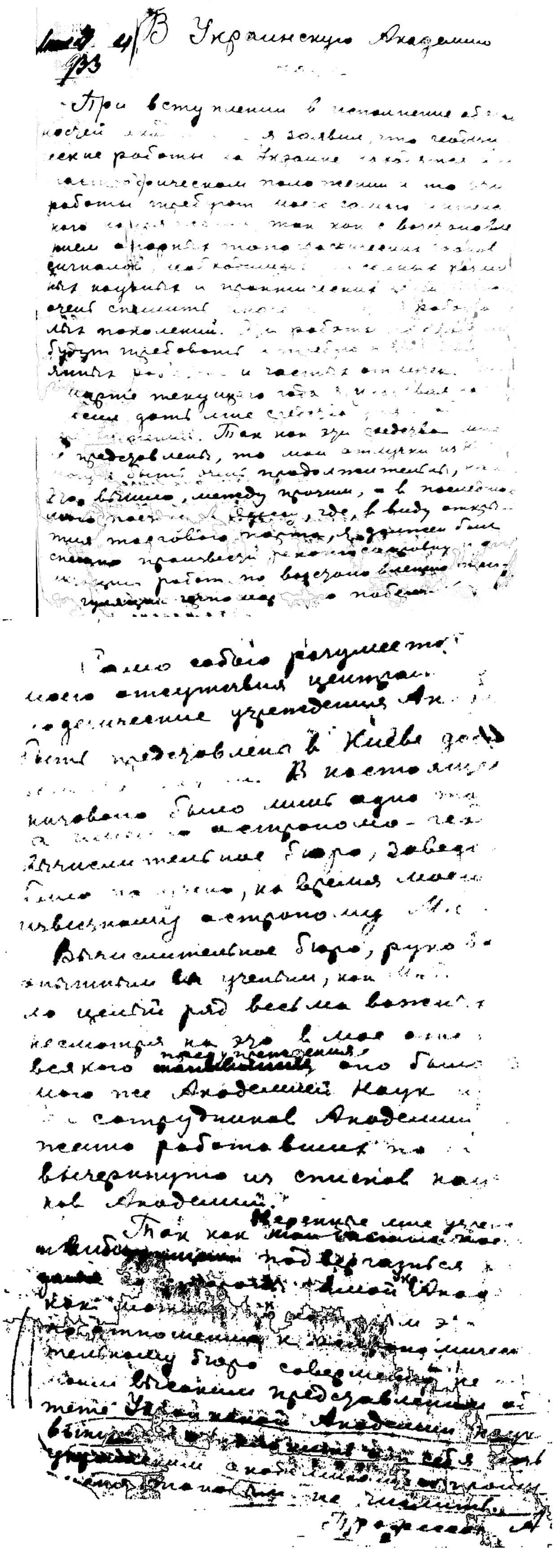

4 / 93 В Украинскую Академию [illegible]

При вступлении в исполнение обязанностей [illegible] я заявил, что [illegible]ческие работы на Украине находятся [illegible] [illegible]графическом положении и что эти работы требуют моего самого [illegible] так как с возобновлением опорных точек [illegible] сигналов [illegible] научных и промышленных [illegible] очень спешить [illegible] будущих поколений. Эти работы [illegible] будут требовать [illegible] личных [illegible] и частых отлучек. [illegible] марте текущего года [illegible] сессии дать мне [illegible]. Так как эта командировка мне предоставлена, то мои отлучки из [illegible] могут быть очень продолжительны, [illegible] это вызвано, между прочим, и в последнюю [illegible] поездку в Одессу, где, в виду отсутствия морского порта, я должен был спешно произвести рекогносцировку [illegible] работ по водяному [illegible] побе[illegible]

Само собою разумеется, что отсутствие центрального [illegible] учреждения Ак[illegible] должно быть предоставлено в Киеве [illegible] В настоящ[illegible] начато было лишь одно [illegible] астрономо-геодезическое [illegible] Вычислительное бюро, заведывание [illegible] было поручено, на время моего [illegible] известному астроному М. [illegible] Вычислительное бюро, руко[illegible] [illegible] учеными, как [illegible] ло целый ряд весьма важных [illegible] несмотря на это в мое отсутствие ~~[illegible]~~ представления всякого оно было [illegible] члены Академии Наук [illegible] сотрудников Академии [illegible] работавших [illegible] вычеркнуто из списков [illegible] Академии.

Так как ~~[illegible]~~ Недоверие мне [illegible] подвергнулся [illegible] [illegible] отношение к Вычислительному бюро совершенно [illegible] предоставлении [illegible] Украинской Академии [illegible]

Профессор А[illegible]

Figure 3: Letter by A.Ya. Orlov on July 29, 1921, in which he refused his status of a member of the AS UkrSSR in protest on the decision not to build an academic Central Astronomical Observatory in Ukraine (Archive of the NAS of Ukraine. A.Ya. Orlov, F. 251, op. 293, Personal Dossier No. 4, p. 40-41).

In 1927 A.Ya.Orlov was elected a corresponding member of the AS USSR, and in 1928 an honorary member of the Society of Natural History in Moscow.

4. Orlov‘s actvivity in 1934-1954

In 1934, Orlov started his activity as a professor of the Sternberg State Astronomical Institute (the reasons, why he moved to Moscow, are not still cleared up). In 1937, he was appointed as an astronomer at the Institute of Geodesy and Cartography. Working in Moscow, he proposed a plan to organize the Soviet Latitude Service based on observations in Poltava, Ust‘-Kamnogorsk, and Khabarovsk as well as took part in some projects concerned with the Moscow metro construction.

In 1938, he returned to the duties of a director of the Poltava Gravimetric Observatory. That year Orlov applied unsuccessfully to a membership in the AS USSR. But in 1939 Orlov was elected once again (the first time in 1919-1922) as a full member of the AS UkrSSR. At the end of 1939, being appointed as a part-time director of the Carpathian Highaltitude Observatory, Orlov undertook a trip to the Pip Ivan mount for decission making whether the operation of this observatory could be possible (Korsun‘ et al., 1998). This observatory was constructed by the Polish government, but in 1939 its status was changed due to the Second World War realities. In 1940, the Carpatian Observatory began to work, but soon its activity was stopped by the war (today this observatory is under reconstruction in frame of a joint Ukrainian-Polish project). That year Orlov made also a trip to the Far East of the USSR for the choosing the site for constructing new latitude station.

On September 1941, Orlov organized the evaquation of the Poltava Observatory to Irkutsk. Here he erranged astronomical and geophysical observations under rigorous Siberian conditions. On October 1943, the staff of observatory removed to Poltava.

At the end of 1943, Orlov was appointed unexpectively for him as a part-time director of the Pulkovo Observatory, but very soon he left the director‘s position. There are several explanations for this decision. First of all, this is a private motivation, which is evidenced from the Orlov‘s letter appeal to the Presidium of the AS USSR: *“On January 20, 1944, I received an extract from the minutes of the administrative meeting of the Presidium on December 23, 1943 as concerns with my appointment as a director of the Main Astronomical Observatory in Pulkovo with subsequent approval by the General Meeting of the Academy of Sciences of the USSR. Of course, no one of astronomers should abandon the reconstruction of the Pulkovo Observatory. However, each of us must take in this affair a proper job. In view of the exceptional importance and difficulty of reneval of the Pulkovo Observatory, for which former glory and importance have to be returned, the chairperson of this observatory has to have the full confidence and high powers. Such a person can only be a member of the Academy of Sciences of the USSR, what I am not. Therefore I can not be a director of the Pulkovo Observatory. I have written repeatedly about this situation to the Presudium, to the Department of Physics and Mathematics, and to the Astronomical Council of the Academy of Sciences of the USSR. I ask kindly again to put the question about the election of a director of the Main Astronomical Observatory among the members of the Academy at the forthcoming General Meeting. I ask kindly not to consider my candidature for this appointment... Member of the AS UkrSSR, A.Ya.Orlov, January 28, 1944”* (Archive of the RAS. A.Ya.Orlov, Personal Dossier, F. 411, op. 4-A, No. 97). By the way, the Orlov‘s candidature was proposed for the full membership in the AS USSR, but he was not elected again. It might be related to his own principal position mentioned in this letter.

The second reason is concerned with that, in the same year, Orlov raised once again an issue on the construction of the Central Astronomical Observatory in Ukraine. The decision was accepted by the AS UkrSSR and supported by the Government of the Ukrainian SSR. In 1944, Orlov was appointed as a director of the Main Astronomical Observatory of the AS UkrSSR and was obligated to start to a very crucial work on its establishment in the after war economic realities. In other words, Orlov had to realize his own idea proposed yet in 1921.

Alexander Ya.Orlov served as a director of the Main Astronomical Observatory of the AS UkrSSR in years of 1944-1948 and 1951-1952. He conducted a lot of work for its construction and spent the most of his energy. At the same time, in the last years of life, Orlov did not stop his scientific activity and put forward many ideas, first of all, altogether with collaborators from the Poltava Gravimetric Observatory in the work of the Soviet Latitude Service in frame of the International Latitude Service (see, Aksent‘eva, 1961; Dychko et al., 1980; Matveev, 1980; Fedorov, 1980; for overview of the Orlov‘s activity in this observatory) as well as for standing the perspective research fields at the Main Astronomical Observatory of the AS UkrSSR altogether with its new staff. On January 14, 1951 Orlov wrote to the Presidium of the AS UkrSSR: *“I bring to the attention of that thanks to the hard work of the staff of the Main Astronomical Observatory of the AS UkSSR in 1951, its two main instruments, vertical circle and a large astrograph-400mm, long after their inaction are finally in a state that they can now start a regularly scheduled work. In addition, last year the instrument of great importance is purchased, and microphotometer is established, as well as a plan to build the Observatory is approved. Writing this, I'm with a sense of duty once again ask the Bureau to relieve me of the administrative work for the post of director of the Main Observatory, as it is to me no more in force, nor on health. After retiring on a pension, I'm done I started some work, bring more benefit, and will not be*

Figure 4: Astronomical Observatories headed by A.Ya.Orlov. From left to right: Astronomical Observatory, I.I.Mechnikov Odesa National University (1912-34); Poltava Gravimetrical Observatory, Institute of Geophysics, NAS of Ukraine (1926-34, 1938-51). Carpatian Observatory (1939-41); Pulkovo Observatory, RAS (1943-44). Main Astronomical Observatory, NAS of Ukraine (1945-48, 1951-52) (photo is taken by P.Korsun).

dependent. There are no shortage of candidates in my place. The Department of Physics-Mathematics and Chem. Sciences appoints of them worthed. That would facilitate and improve the selection, it is necessary to eliminate discrimination of a director of the Main Observatory, when for large and responsible work is assigned him to pay 25 % less than the directors of other academic institutes". (Archiv of the NAS of Ukraine. A.Ya.Orlov, F. 251, op. 293, Personal Dossier No. 4, p.152). In 1948-1950, Prof. V.P.Tsesevich headed (part-time) the Main Astronomical Observatory of the AS UkrSSR being at the same time the director of the Astronomical Observatory of the Odesa University. In 1952, A.Ya.Orlov handed over the directorship of this observatory to Prof. A.A.Yakovkin.

5. The Orlov‘s Scientific School

A.Ya.Orlov has formulated his principal scientific ideas during the Odesa‘s period of his life. He studied a tidal deformation of the Earth and its polar motion using the gravity and latitude observations. He has proposed new defenitions of a mean pole and a mean latitude, as wel as a new method for determing the pole coordinates. To the end of 1940-ties, A.Ya.Orlov was recognised as a world wide expert in this field of research, which is now called as Astrogeodynamics or Space Geodynamics (Yatskiv, 1998). Among the representatives of the Orlov‘s scientific school are about 20 Doctors of Sciences and more than 40 Candidates of Sciences, including the members of Academy of Sciences of Ukraine and other countries. Some of them conducted their thesises in Odesa, Poltava, and Kyiv under the Orlov‘s supervision: J.Witkowski (Poland), N.Stoyko-Radilenko (France), V.Zhardetsky (Yugoslavia-Austria-USA), D.Pyaskovsky, Z.Aksent’eva, E.Lavrentieva, N.Popov, E.Fedorov and A.Korol in Ukraine (Yatskiv et al., 2005; Rikun, 2005; Yatskiv & Vavilova, 2011). The deserved followers of the Orlov‘s scientific ideas were also his sons, A.A.Orlov and B.A.Orlov (Neizvestnyj, 2001). N.Stoyko wrote: *The last time I met Orlov at the International Astronomical Congress in Zurich in 1948. Despite heavy administrative duties, his studies of the motion of the pole of the Earth were in full swing. However, his ideas about a Latitude Service and a mean pole of epoch did not attract enough attention to be too innovative. Only in 1958, after the Orlov‘s death, his ideas have been universally recognized the International Astronomical Congress in Moscow... Orlov could not even dream that his methods, ten years after his death, will be used to determine the coordinates of the instantaneous pole of the Earth using the results of 31 astronomical stations. He himself could calculate the coordinates of the instantaneous pole of the Earth, using a maximum of 9 astronomical stations"* (Stoyko-Radilenko, 1969).

A wider continuation of the Orlov‘s research in field of geodynamics and nutation, i.e. the motion of Earth pole in space, is related to the works by E.Fedorov with colleagues from Poltava and Kyiv (the second generation of the Orlov‘s scientific school) (see, Korsun‘, 1989). Since the 1970-ties, astronomical and space observation techniques (laser ranging of the Moon and satellites, GNSS observations, VLBI, etc.) was put for studying the Earth rotation as related to the polar rotation motion, precession-nutation motion, and other geodynamical phenomea (Yatskiv, 1998, 2003; Paton et al., 2001; Pavlenko et al., 2006).

This transformation from classical to new techniques for studying the Earth rotation was initiated in Ukraine by Ya.Yatskiv with colleagues from the Main Astronomical Observatory in a tight international cooperation (the third generation of the Orlov’s scientific school).

6. Instead of conclusion

A.Ya.Orlov was the outstanding scientist and organizer of astronomical research being principal in persistance of own opinions. He has played a decisive role in the development of astronomy in Ukraine in the XX century. The best evidences are both his astrogeodynamics scientific school and directorship at the five observatories, for two of those (in Poltava and Kyiv) he was a founder (Fig. 4).

Evgen P.Fedorov (1909-1986), member of the AS UkrSSR, has successfully followed the Orlov‘s study of the Earth rotation and put it in a theory and practice at the new higher level (Korsun‘ et al., 1989; Korsun‘, 2000, 2005). He became a well-known expert in the nutation theory, positional astronomy, and astronomical data analysis (President of the IAU Commission 19 in 1955-1061, Head of the Commission on the Earth rotation of the Astronomical Council of the AS USSR in 1962-1966). In 1980, E.P.Fedorov noted in his paper "Alexander Yakovlevich Orlov: Life, Activity, and Scientific Heritage" about foresight that Alexander Ya.Orlov has written just before the death in 1954: “'Through 15 or 20 years the study of the latitude variations and polar motion will be improved and will cover another research fields than it is now". It was happened.

References

Aksent‘eva Z.N.: 1961, *In "A.Ya. Orlov. Selected papers. – K.: AS UkrSSR*, **1**, p.7.

Dychko I.A., Bulatsen V.G., Balenko V.G.: 1980, *Geodynamics and Astrometry.–K.: Naukova dumka*, p.52.

Fedorov E.P.: 1980, *Geodynamics and Astrometry. – K.: Naukova dumka*, p.7.

Karetnikov V.G.: 1996, *AAT*, **10**, p.21.

Karetnikov V.G.: 2012, *Odessa Astron. Publ.*, **25/2**, 81.

Korsun‘ A.A.: 2005, *Kinemat. Fiz. Nebesn. Tel, Suppl.*, **5**, p.359.

Korsun‘ A.A.: 2003, *In "The Names of Ukraine in Space. ISBN 966-95745-5-2*, p.293.

Korsun‘ A.A.: 2000, *ASP Conf. Ser.*, **208**, p. 185.

Korsun‘ A.A.: 1989, *Istor.-Astron. Issled.*, **21**, p.327.

Korsun‘ A.A., Botvinova V.V., Iatskiv Ia.S.: 1989, *Evgenij Pavlovich Fedorov. – K.: Naukova dumka*

Korsun‘ A.A., Zablotskyj F.I., Sledzinski J.: 1998, *IBUAA*, **12**, p.61.

Matveev P.S.: 1980, *Geodynamics and Astrometry. – K.: Naukova dumka*, p.27.

Neizvestnyj I.G.: 2001, *Selected problems of astronomy. – Irkutsk*, p.53.

Paton B.E., Vavilova I.B., Negoda O.O., Yatskiv Ya.S.: 2001, *Kosm. Nauk. Technol.*, **7**, p.1.

Orlov A.Ya: 1997, *SAI Proceedings*, **67**, P. 1, p.94.

Pavlenko Y.V., Vavilova I.B., Kostiuk T.: 2006, *OSA*, **6**, p.71 (*arXiv:astro-ph/0512442).*

Rikun I.: 2005, *http://odessitclub.org/publications/almanac*, **22**, p.31.

Stoyko-Radilenko N.M.: 1969, *Istor.-Astron. Issled.*, **10**, p.245.

Tsesevich V.P.: 1980, *Geodynamics and Astrometry. – K.: Naukova dumka*, p.24.

Volyanska M.Yu., Karetnikov V.G., Mandel O.E.: 2005, *Odessa Astron. Publ.*, **18**, p.138.

Yatskiv Ya.S.: 1998, *Proc. Journees*, p.189.

Yatskiv Ya.S., Korsun‘ A.A., Vavilova I.B.: 2005, *Kinemat. Fiz. Nebesn. Tel*, **21**, p.403.

Yatskiv Ya.S., Vavilova I.B.: 2003, *Kinemat. Fiz. Nebesn. Tel*, **19**, p.569.

Yatskiv Ya.S., Vavilova I.B.: 2011, *Proc. IAU Symp.*, **260**, p.696.

ALEXANDER YAKOVLEVICH ORLOV
(Odessa period – 1912-1934)

V.G. Karetnikov
Astronomical observatory, Odessa National University, Odessa, Ukraine
vgkar@alpha-serv.net

A.Ya. Orlov came to Odessa in the fall of 1912. Just before it he defended his master thesis (1912) and visited several countries. In Odessa he occupied position of the chair of Astronomy Department and head of Astronomical Observatory of the Emperor Novorossia University. Being young and active man he brought to Astronomical Observatory and Astronomy Department new topics of the scientific studies. At the same time he did not destroy traditional directions that were developed by his predecessors. Here, in Odessa he headed Odessa branch of the Russian Society of "world knowledge" amateurs. It should be noted that G.A. Gamow and V.P Glushko starter their way in technics and science in this society.


Александр Яковлевич ОРЛОВ
(6 апреля 1880 – 28 января 1954)

Orlov A.Ya. (06.04.1880–28.01.1954) is a famous specialist in astronomy and geophysics, ScD, professor, honored worker of science and technics of Ukraine, academician of the Ukrainian Academy of Sciences (1918–1922), corresponding member of Soviet Union Academy of Sciences (since 1927), academician of Academy of Sciences of Ukraine (since 1938). He graduated St.–Petersburg University in 1902, then worked in Novorossia University in 1912–1920, the director of Odessa Astronomical Observatory in 1920–1934, the director of Poltava Gravimetry Observatory in 1926–1951, the director of the Main Astronomical Observatory of Academy of Sciences of Ukraine in 1944–1948 and in 1950–1952.

To the time of arrival of A.Ya. Orlov in Odessa, the Astronomy Department and Astronomical Observatory were already well known in the world due to his predecessors – L.F.Berkevich and A.K.Kononovich.

Leopold Fomich Berkevich (1828–1897) was a specialist in the field of celestial mechanics of the Solar system small bodies, he had the level of ScD and professor, graduated from St.–Petersburg University in 1849. He founded education and scientific researches in Odessa. In 1865–1880 he headed the Department of Astronomy and Geodesy and Astronomical Observatory.

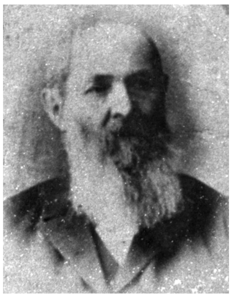

Alexander Konstantinovich Kononovich (1850–1910) in fact was the first astrophysicist at the southern part of the Russia Empire. He graduated from the Novorossia University in 1871, then he headed Department of Astronomy and Geodesy, and also Astronomical Observatory in Odessa (1881–1890). He was ScD and professor (and honored professor of Novorossia University).

During the first years of the work of A.Ya. Orlov in Odessa he performed studies that were of the highest priority in science. He organized preparations of astronomers and geodesists, equipped laboratories with modern instruments. Then he started investigation of the sea inflows in Odessa region, made geodetic shooting of the sea cost line in the north–west part of the Black Sea and in the region of the Odessa estuaries, created the network of stations and gravimetric maps of the European part of the Soviet Union, as well as part of Siberia and Altai regions. With this he connected gravimetric network with fundamental reference point in Potsdam.

During his Odessa period A.Ya. Orlov defended his ScD thesis (1915), became a professor (1916), was elected as academician of the Ukrainian Academy of Sciences (1918), the corresponding member of Soviet Union Academy of Sciences (1927). After the liquidation of Novorossia University in 1920 he became the director of

Odessa State Astronomical Observatory (1920–1933). During the part of this period observatory worked as the Main Astronomical Observatory of Ukraine. At the same time in Kiev A.Ya. Orlov made an attempt to create new structure – the Central Astronomical Observatory, but several members of Ukrainian Academy of Sciences acted with counteraction. After this Orlov decided to leave the ranks of this academy (1922).

In his Odessa period A.Ya. Orlov also realized himself as author and publisher. In 1914–1915 he published "Transactions of the Astronomical Observatory", in 1915 "News of the Astronomical Observatory", and also brochure "Lectures on spherical astronomy". In 1919–1923 "Odessa Astronomical Calendar" was published. In 1921 Orlov published the textbook "Course of the theoretical astronomy", and after request of the Sea Department of Ukraine he started to publish "Marine Annual Book" (1921–1924), as well as "Circular of the Astronomical Observatory" (1921–1927). One should note that Orlov created the necessary conditions for his co–workers to publish their articles.

Working in Odessa A.Ya.Orlov began (1924) and completed construction of the Poltava Gravimetric Observatory. He was the director of that observatory in 1926–1934. He equipped observatory with instruments and with a staff prepared in Odessa. In 1934 A.Ya.Orlov left Odessa for the Geophysical Department of the Moscow Astronomical Observatory (in Kuchino), and after this he never came back to Odessa for a work. Later he went to Poltava Gravimetric Observatory where he occupied the position of director, then he was the director of Carpathian observatory, and finally he realized his main aim – the Main Astronomical Observatory to Kiev where he worked a s a director in 1944–1948 and 1950–1952.

During his period of life in Odessa A.Ya. Orlov was working with some known astronomers that either were prepared in Odessa, or were invited for a work. Among many of his pupils and colleagues we would like to mention the following: Z.N.Aksentyeva, V.A.Albitsky, I.N.Androsov, Y.Y.Vitkovsky, I.A.Dyukov, V.S.Zhardetsky, N.M.Lyapin, N.M.Mihalsky, B.V.Novopashenny, D.V.Pyaskovsky, N.M.Stoiko, N.V.Zimmerman. Short presentation of these astronomers is given below.

Zinaida Nikolaevna Aksentyeva (1900–1969) was the outstanding and well–known specialist in the gravimetry area. She graduated from Novorossia University in 1924, then she was working in Odessa Astronomical Observatory (1919–1926). She was ScD, corresponding member of Academy of Sciences of Ukraine, honored worker of science and technics, the director of Poltava Gravimetric Observatory (1951–1969).

Vladimir Alexandrovich Albitsky (1891–1952) was the well–known specialist in the astrophysics area. He graduated from Moscow University in 1913, then he was working in Odessa Astronomical Observatory (1915–1922), and after that in Simeiz Observatory (the head of this observatory since 1934).

Innokenty Dmitrievich Androsov (1888–1948) was the outstanding and well–known specialist in the field of geodesy and astrometry. He graduated from the Moscow Institute in 1910, and then he was working in Odessa Astronomical Observatory in 1926–1939. He founded the Department of Geodesy and Cartography in Odessa University. Since 1944 he was fulfilling the duties of the director of the Construction Institute (at present it is Academy of Construction and Architecture).

Yosif Yosifovich Vitkovsky (1892–1976) was the well–known and outstanding Polish astronomer, ScD, professor, academician of the Polish Academy of Sciences. He graduated from Novorossia University in 1914, then he was working in Odessa Astronomical Observatory (1914–1919). After 1919 he went back to Poland.

Ivan Alexandrovich Dyukov (1888–1961). Dyukov was outstanding and well–known specialist in astrometry area. He graduated Derpt University. In 1919 he came to Odessa where he started first observations using the Odessa meridional circle (125 near–to–pole stars). Since 1921 he was working in Engelgard Observatory and in Kazan University. He was chair of the Department Geodesy and Gravimetry. In 1971–1951 he headed Astronomy Department, and at the same time he was the deputy rector (1937–1938 and 1941–1952). In 1941–1958 he was the director of Kazan City Astronomical Observatory.

Vyacheslav Sigizmundovich Zhardetsky (1896–1962), the well–known and outstanding specialist in astronomy, geophysics and mechanics, ScD, professor. He graduated from Novorossia University in 1917, then he was working in Astronomical Observatory in Odessa (1917–1920). After this period he emigrated to Serbia (professor of the Belgrad University), from 1945 he was professor of Columbia University (USA).

Nikolai Mihailovich Lyapin (1884–1963), the outstanding and well–known specialist in the astrometry field and celestial mechanics, professor. He first attended Moscow University, then, in 1910 passed exams in Yuriev (Derpt) University (without attending lectures). In 1913–1922 he was working as a staff member of the Astronomy Department and Astronomical Observatory of the Novorossia University (1913–1920). At this time he was deputy director of Odessa State Astronomical Pbservatory. In 1922–1924 he was professor of the Astronomy Department of the Crimean University, and in 1924–1953 – chair of the Astronomy Department of the Rostov University.

Nikolai Marianovich Mihalsky (1982–1942), the outstanding and well–known specialist in the area of celestial mechanics of the comets and meteor swarms, professor. He graduated from Kiev University in 1911. Since 1923 he was working in Astronomy Department and Astronomical Observatory in Odessa. In 1941–1942 he was the chair of Astronomy Department in evacuation.

Boris Vladimirovich Novopashenny (1891–1975), the outstanding and well–known specialist in astrometry. He graduated from Petrograd University in 1915, then he was working in Astronomical Observatory in Odessa (1929–1975), PhD, associated professor. He was fulfilling the duties of the observatory director in 1934 and 1944.

Dmitri Vladimirovich Pyaskovsky (1891–1971), well–known and outstanding specialist in the gravimetry, professor. He graduated from Novorossia University in 1916. During three years he was passing the foreign training. In period from 1919 to 1931 he was working in Odessa Astronomical Observatory as senior astronomer and deputy director.

Nikolai Mihailovich Stoiko (1884–1976), the well–known and outstanding specialist in geophysics and theory of the time. He graduated from the Novorossia University in 1916. In period from 1916 to 1920 he was working in Odessa observatory. He was corresponding member of the Polish Academy of Sciences and the director of International bureau of time, latitude and longitude in Paris.

Nikolai Vladimirovich Zimmerman (1890–1942). He was the well–known and outstanding specialist in astrometry, ScD, professor. He graduated from the Novorossia University in 1912. First time he was working in Astronomical Observatory in Odessa (1912–1915), then in Pulkovo observatory. He was the head of Astrometrical Commission of Soviet Union Academy of Sciences.

This photo was made on portal in Odessa Astronomical Observatory approximately in 1915. From the left to right: Albitsky, Rybakov, Pyaskovsky, Lyapin, Orlov, Vitkovsky, Zhardetsky, Donich, Stoiko.

N.N.Donich and A.M.Rybakov was pupils of A.K. Kononovich.

ARTEMIJ ROBERTOVICH ORBINSKY – ASTRONOMER, EDUCATOR, PUBLISHER

I.E.Rikun

Odessa National Scientific Library named after M.Gor'ky
Ukraine, Odessa, Pastera, 13
rikun_inna@mail.ru

A.R.Orbinsky was born August 3(15) 1869 in Odessa. His father, R.V.Orbinsky, was a well-known educator, financier, public figure.

In 1887 Orbinsky finished Rishelevskaya gymnasium and entered Novorossiysky University. He grew interested in astronomy and became the pupil of outstanding astrophysicist A.K.Kononovich.

In 1892 A.R.Orbinsky finished the University with the gold medal for the student writing and Kononovich offered him a post-graduate studentship. During his post-graduate study he worked hard, read a lot of scientific books and articles, worked at the Observatory of Novorossiysky University and at the Pulkovo Observatory. Working there he offered the new original method of mass definition of radial speeds of the stars using the prism camera. This method is still one of the best.

In 1896 Orbinsky was invited by the prominent Russian astronomer A.A.Belopolsky to take part at the observation of the total solar eclipse in the village Orlovskoe on the Amur river. Because of that his post-graduate study lasted for one more year.

Director of Pulkovo Observatory O.A.Baklund decided to organize in Odessa the Southern branch of the Observatory. Orbinsky took an active part in the creation of the branch and in the organizing of it work. At first he became the supernumerary astronomer and beginning from 1902 – the senior astronomer of the Odessa branch. During his work Orbinsky carried the vast series of the observations, in particular he observed by absolute method the right ascensions of four hundreds stars of the wide terrestrial equator zone. These stars were added to the list of the stars of the Southern sky and then included into into the interim star catalog (1915). Among those who helped Orbinsky in his observations was V.V.Lebedintsew, the cousin of the world known physicist George Gamow.

In 1908, after the tragic death of the prominent astronomer A.P.Gansky, Orbinsky was send on an official trip to Simeiz branch of Pulkivo Observatory. He did a lot for the organizing of the scientific work at the branch.

Orbisky held his position of the senior astronomer of the Southern branch of Pulkovo in Odessa till 1912 when it was moved to Nikolaev.

The scientist did not want to leave his native city and his native University. From 1899 till 1920 he was lecturer in various astronomical courses: theoretical, applied and spherical astronomy, celestial mechanics, geodesy, special course of the theory of perturbation.

In 1911-1920 he also lectured at the Higher Women Courses, for two years (1909-1911) he was the secretary of the physical and mathematical faculty.

Orbinsky was also a public figure, in 1918 he was the deputy mayor of Odessa, took an active part in the organizing of the Odessa Polytechnic Institute.

In 1920 the reform of the Ukrainian Higher School began, the universities were liquidated, and the new educational institutions organized. In 1920 Orbinsky became a professor, at first he lectured astronomy at the Odessa Institute of Physics and Mathematics and then in 1921-1924 at the Odessa Institute of People's Education. He continued to work as a senior astronomer at the Odessa Astronomical Observatory.

Besides his educational and scientific activity Orbinsky was one of the organizers and member of the publishing house «Mathesis». «Mathesis» was the best publishing house of Russian Empire specialized in scientific and popular scientific literature. Orbinsky translated and edited twenty two books in astronomy and physics. His translations were recognized as masterpieces.

February 21, 1928 A.R.Orbinsky died of a heart attack. He was only 59.

His grandson Arthur Anthony Page (1922-2011) was a well-known Australian amateur astronomer. He worked in the field of astrophysical phenomena relating to Flare Stars. He was the first Australian amateur astronomer who become a member of the prestigious International Astronomical Union (1985). The Berenice and Arthur Page Medal awarded in his and his wife honor is given by the Astronomical Society of Australia to distinguished amateur astronomers who contribute to scientific astronomy.

A.R.Orbinsky and A.A.Page has the Asteroids named after them – 11361 Orbinsky and 11516 Arthurpage, discovered by the Japanese astronomer Eiji Kato.

PLENARY SESSION

HOLOGRAPHIC DYNAMICS

Yu.L. Bolotin[1], V.V. Yanovsky[2]

[1] A.I.Akhiezer Institute for Theoretical Physics, National Science Center «Kharkov Institute of Physics and Technology», Kharkov, Ukraine, *ybolotin@gmail.com*
[2] Institute for Single Cristals, Nat. Academy of Science Kharkov,Ukraine, *yanovsky@isc.kharkov.ua*

ABSTRACT. This paper is a brief introduction to the new physical conception – holographic dynamics. Formulated in the early 90's of the last century, the holographic principle helped to overcome some fundamental challenges facing the traditional cosmology.

Key words: holographic principle, entropy force, cosmological constant, dark energy, Friedmann equation, black hole, ageographic model.

1. Introduction

The mankind has created two Great axiomatic theories. It is Geometry and Thermodynamics. The first of them provides description of the space and time and forms the basis of the General theory of relativity created by Einstein, Hilbert and many other scientists. The second describes giant number of various processes in the World surrounding us. Actually, only this physical theory contains the postulate specifing the direction of time flow. As Nobel winner I.Prigozhin figuratively noted - «arrow of time». Apparently, time is the only thing that connects these two Great theories. Attempts to get into the darkness surrounding origin of our World demands understanding of how Space-time emerge. Most of theories start much later, postulating existence of space-time and discussing processes proceeding in it. Extremely attractive is the approach presenting attempt to develop the concept in which the space-time itself is somehow emerging structure. At the heart of the new approach lays the holographic principle, dynamics which is based on this principle has received the name of holographic dynamics. This work represents short introduction to this subject.

2. Holographic principle

Let's begin with the formulation of a holographic principle. The traditional point of view assumed that dominating part of degrees of freedom in our World are composed by fields that fill the space. However it became then clear that such estimate complicates construction of quantum gravity: it is necessary to introduce small distance cutoffs for all integrals in the theory in order to make it sensible. As a consequence, our world should be described on a three-dimensional discrete lattice with period of order of Planck length. In the latest time some physicists share even more radical point of view: instead of the three-dimensional lattice, complete description of Nature requires only two-dimensional one, situated on the space boundary of our World. Such approach bases on the so-called «holographic principle» ['t Hooft : 1993, Susskind : 1995, Bousso : 2002]. Therefore, central place in the holographic principle is occupied by the assumption that all the information about the Universe can be coded on some two-dimensional surface - the holographic screen.

All that is in it, we will write on it. Presence of such record means occurrence of space in it. The most important in this postulate - the space is understood not as primary object, but as consequence of the inventory of everything that is "inside"sphere. In other words, the space is macroscopical object. Certainly, possibility and record precision are limited by the size of a surface. For taking this restriction into concideration, the axiom postulating quantity of information which can be written down on this surface is introduced. So the quantity of the bits which have been written on a surface, having area A, cannot exceed one bit per plank square L_{Pl}^2

$$N = \frac{A}{L_{Pl}^2} = \frac{Ac^3}{G\hbar} \tag{1}$$

The data record on the two-dimensional screen is closely connected with fundamental physical quantity - entropy. Actually, information $I = -\Delta S$ is understood as change of entropy ΔS. The screen on which the record is carried out, is called the holographic screen. Thus, certain entropy can be assigned to the holographic screen. Naturally, penetration of objects in the screen would lead to renewal of record on the holographic screen. So, if the particle of mass m comes closer to the holographic screen record, entropy of the holographic screen changes on:

$$\Delta S = 2\pi k_B \frac{mc}{\hbar} \Delta x \tag{2}$$

Presence of mass in the coefficient can be justified by additivity of entropy, and proportionality to Δx is natural even as result of small-parameter expansion. In other words, this postulate looks quite naturally. Now we use the first law of thermodynamics. Equating work of force to entropy change on the screen, we will receive

$$F\Delta x = T\Delta S$$

In other words, entropy change leads to some force occurrence

$$F = T\frac{\Delta S}{\Delta x} \tag{3}$$

It is possible to call it entropy force. This force has purely statistical nature. The value of this force is defined by screen temperature. Thus it is necessary to introduce a postulate defining temperature of the holographic screen. As such postulate, a principle of equal distribution of energy on freedom degrees is used.

$$E = \frac{1}{2} k_B T N \tag{4}$$

Thus, the temperature of the holographic screen is defined by energy E contained in the screen and number of bits N on the screen or number of degrees of freedom of the screen. The formulated postulates lead to the holographic dynamics pretendind on the description of occurrence of everything. This theory operates the forces having the statistical nature or entropy forces. Within the scope of such holographic theory becomes clear even the nature of the fundamental Newton's second law [Verlinde : 2010].

3. Entropic force. The law of Gravity

Let's show within the limits of the holographic theory occurrence of the gravitational force, acting on a particle of mass m located near some holographic screen. Let the mass M be placed behind the spherical screen, then full energy according to Einstein's formula is defined as:

$$E = Mc^2 \tag{5}$$

Using parities (1), (2) and (4), we will receive for the temperature:

$$k_B T = \frac{2MG}{cA}$$

Having substituted this temperature in the parity (3) for entropy force and considering that screen area is $A = 4\pi r^2$, we will receive

$$F = G\frac{mM}{r^2} \quad , \tag{6}$$

It is well-known famous law of universal gravitation. Now, it is possible to state that the factor of proportionality G coincides with a gravitational constant. Certainly, the most important in such way of deducion of this law is the change of interpretation of gravitational force. From this point of view gravitational force gains sense of entropic statistical force. It is caused by aspiration to the most chaotic state. Such point of view at gravitational force is well compatible with the basic observable facts. We will concern only one of them. The main property of gravitation is its universality. Gravitation equally acts on everything, that possesses energy, irrespective of presence of huge distinctions between different structures of matter. Within the scope of statistical or entropy nature of gravitational force this property looks obvious.

Certainly, the deduction provided here concerns only the elementary nonrelativistic and stationary case. The holographic theory is extended on much more general situation. By means of holographic principles equations of Einsteins General Theory of Relativity are deduced (see for example [Барьяхтар, Болотин, Тур, Яновский : 2010]). It should be noted that one of the first attempts to explain gravitation from thermodynamic considerations can be found in [Jacobson: 1995]. In this work, Einstein's equations were derived from the fundamental relation $dQ = TdS$ and proportional to the entropy area horizon.

4. Holographic Universe

In this section we use holographic principle to describe the dynamics of the Universe. We will demonstrate that this approach not only allows to reproduce the achievements of traditional description, but also to resolve a number of problems which were encountered in it. Using Hubble sphere of radius $R = H^{-1}$ as a holographic screen, we will reproduce the Friedmann equations without resorting to either Einstein equations, or Newtonian dynamics. Holographic screen has an area of $A = 4\pi R^2$ and carries information (maximum) of $N = 4\pi R^2/L_{Pl}^2$ bits. The change in information dN during the period of time dt due to the expansion of the Universe $R \to R + dR$ is

$$dN = \frac{dA}{L_{Pl}^2} = \frac{8\pi R}{L_{Pl}^2} dR \tag{7}$$

Here we use $c = k_B = 1$. The change in Hubble radius leads to the change of Hawking temperature $\left(T = \frac{\hbar}{2\pi R}\right)$, which is

$$dT = -\frac{\hbar}{2\pi R^2} dR \tag{8}$$

Using the equidistribution of energy we can write

$$dE = \frac{1}{2} N dT + \frac{1}{2} T dN = \frac{\hbar}{L_{Pl}^2} dR = \frac{dR}{G} \tag{9}$$

$\left(L_{Pl}^2 = \frac{\hbar G}{c^3}\right)$ and dR can be expressed in the form

$$dR = -H\dot{H}R^3 dt \tag{10}$$

On the other hand, we can calculate the energy flux through the Hubble sphere given the energy-momentum tensor for the substance which fills the Universe. Treating this substance as an ideal fluid and using $T_{\mu\nu} = (\rho + p) u_\mu u_\nu + p g_{\mu\nu}$, we obtain

$$dE = A\,(\rho + p)\,dt \tag{11}$$

Equating (9) and (11) using (10), we obtain

$$\dot{H} = -4\pi G\,(\rho + p) \tag{12}$$

As is well known, the system

$$\begin{aligned} &\dot{H} = -4\pi G\,(\rho + p)\,; \\ &\dot{\rho} + 3H\,(\rho + p) = 0 \end{aligned} \tag{13}$$

is equivalent to the standard Friedmann equations

$$\begin{aligned} &H^2 = \tfrac{8\pi G}{3}\rho; \\ &\tfrac{\ddot{a}}{a} = -\tfrac{4\pi G}{3}(\rho + 3p) \end{aligned} \tag{14}$$

Thus, we can say that the goal is achieved.

5. Holographic Dark energy

The derivation of the Friedmann equations from the holographic principle is an important result, but by itself it is merely a recreation of what is known. Can we somehow use this principle to construct a new approach to the description of the dynamics of the universe? If so, can we use this approach to overcome the fundamental problems of the traditional approach? Holographic dynamics gives a positive answer to this question. As an example, let's present a solution of the cosmological constant problem.

In the Standard cosmological model, the density of dark energy is about 70% of the critical density

$$\rho_\Lambda \approx 0.7 \frac{3H_0^2}{8\pi G} \approx 10^{-47} GeV \tag{15}$$

If dark energy in the form of the cosmological constant is really zero-point energy oscillations of vacuum, then

$$\rho_{vac} \approx \frac{k_{\max}^4}{16\pi^2}$$

where $k_{\max}$- is a certain cutoff scale. The natural choice for this role is the Planck mass $k_{\max} = M_{Pl} \simeq 1.22 \times 10^{19} GeV$, since this value is typically synonymous with the limits of use of GR. The result of this choice is

$$\rho_{vac} \approx 10^{74} GeV$$

This value is larger than the observed value by 120 orders of magnitude. This contradiction is the so-called cosmological constant problem. Physicists have never before faced such a gigantic numerical contradiction.

The holographic principle allows us to replace rough dimensional estimate with a more strict evaluation. In any effective quantum field theory, defined in the spatial region with the characteristic size L and that uses the ultraviolet cutoff (UV-cutoff) Λ, entropy $S \propto \Lambda^3 L^3$. According to the holographic principle, this value must be in agreement with the inequality

$$L^3\Lambda^3 \le S_{BH} = \frac{A}{4L_{Pl}^2} = \pi L^2 M_{Pl}^2 \tag{16}$$

Here, S_{BH} is the entropy of a black hole with the gravitational radius$L$. We have therefore obtained an important result[Cohen : 1998]: in the bounds of holographic dynamics, the value of the IR-cutoff (L) is strictly linked to the value of the UV-cutoff (Λ) . In other words, physics on small UV-scales depends on the parameters of physics on small IR-scales. Specifically, in the case of the saturation of the inequality (16)

$$L \sim \Lambda^{-3} M_{Pl}^2$$

In the cosmological aspect that interests us, the correlation between small and large scales can be obtained from a natural demand: the total energy bound in an area of the size L must not be larger than the mass of a black hole of the same size:

$$L^3 \rho_{de} \le M_{BH} \sim L M_{Pl}^2 \tag{17}$$

Here, ρ_{de} is the density of so-called «holographic dark energy» [Li : 2004]. If this inequality was not fulfilled, the universe would be composed entirely of black holes. If we in the context of cosmology take L as the size of the current universe, for instance the Hubble scale H^{-1} , then the dark energy density will be close to the observed data (15)

$$\rho_{de} \approx 10^{-46} GeV$$

Thus, the problem of the cosmological constant in the holographic dynamics absent.

Even though the value of the density of dark energy is correct, problems arise with the equation of state due to our choice of the Hubble radius as the IR-scale [Hsu : 2004] This is easily seen from the following. Let's analyze a Universe composed of holographic dark energy, defined by the relation (17) and matter. In this case, $\rho = \rho_{de} + \rho_M$. From the first Friedmann equation it follows that$\rho \propto H^2$. If $\rho_{de} \propto H^2$, then the dynamic behavior of holographic dark energy and dark matter is identical. In this case equation of state for holographic dark energy$p_{de} = w\rho_{de} = 0$, meaning$w = 0$. Obviously such value of the parameter w violates the condition of the cosmic accelerated expansion $w < -1/3$.

To make holographic dark energy cause accelerated expansion of the Universe, the IR-cutoff must be a scale different from the Hubble radius. Specifically, the problem can be solved if we use the event horizon as the IR-cutoff. However, for this model problems arise with the causality principle, since according to the definition of the event horizon, the current dynamics of dark energy will depend on the future evolution of the scale factor. One of the possible ways of resolving this issue is to equalize the scale of the IR-cutoff with a length scaled defined by the age of the universe T . In this case

$$\rho_\Lambda \propto M_{Pl}^2 T^{-2} \tag{18}$$

The holographic model of dark energy, in which the scale of the IR-cutoff is the age of the universe (Ageogaphic model [Cai : 2007]) allows us to 1) obtain the observed value of density of dark energy; 2) provide accelerated expansion at the latter phases of the Universe's evolution; 3) resolve contradictions related to the causality principle.

6. Emergence of Space

To understand why cosmic space emerges Padmanabhan [Padmanabhan 1,2 :2012] proposed a specific version of holographic principle. At first consider a pure de Sitter universe with a Hubble constant H. Let us assume that such a universe obeys the holographic principle in the form

$$N_{sur} = N_{bulk} \tag{19}$$

Here the N_{sur} is the number of degrees of freedom on the spherical surface of Hubble radius H^{-1} given by

$$N_{sur} = \frac{4\pi}{L_{Pl}^2 H^2} \tag{20}$$

The $N_{bulk} = |E| \,/\, (1/2)\, k_B T$ is the effective number of degrees of freedom which are in equipartition at the horizon temperature $T = H/2\pi k_B$. If we take |E|to be the energy $|\rho + 3p|\, V$ contained inside the Hubble volume $V = \frac{4\pi}{3H^3}$ we obtain

$$N_{bulk} = \frac{16\pi^2\, |\rho + 3p|}{H^4} \tag{21}$$

For de Sitter universe $p = -\rho$, then Eq. (1) reduces to the standard Friedmann equation

$$H^2 = \frac{8\pi L_{Pl}^2}{3}\rho \tag{22}$$

Our universe is only asymptotically de Sitter. This would suggest that the expansion of the universe, which conceptually equivalent to the emergence of space, is being driven towards holographic equipartition. Then the basic law governing the emergence of space must relate the emergence of space to the difference $N_{sur} - N_{bulk}$. The most natural and simplest form of such a law will be

$$\frac{dV}{dt} = L_{pl}^2 \left(N_{sur} - N_{bulk}\right) \tag{23}$$

where V is the Hubble volume in Planck units and t is the cosmic time in Planck units. Using (13) and (14) we obtain the standard dynamical Friedmann equation. By this means Friedmann equations can be reinterpreted as an evolution to holographic equipartition. In other words, "if the holographic principle is not correct, it is very difficult to understand why Friedmann equations hold in our universe"[Padmanabhan 1 :2012].

6. Summary

First successful applications of holographic principle brought forth hopes to build on its base adequate description of Universe dynamics, lacking number of problems, innate in traditional approach. Conversely, that success from our point of view became the source of unreasonable optimism. One has to remember the words of Churchill «Success is the ability to go from one failure to another with no loss of enthusiasm». Holographic dynamics is one of the most perspective branches of theoretical physics. There were too few failures to expect ultimate success.

Acknowledgements. The authors are thankful to anybody who has read this contribution to the end.

References

Bousso R.: 2002, *Reviews of Modern Physics*, **74**, 825.

Cai R.: 2007, *Phys. Lett. B*, **657**, 228.

Cohen A., Kaplan D., Nelson A.: 1998, *arXiv:hep-th/9803132.*

't Hooft G.: 1993, *arXiv:gr-qc/9310026.*

Jacobson T.: 1995, *Phys.Rev.Lett.*, 75, 1260.

Hsu S.: 2004, *arXiv: hep-th/0403052.*

Li M.: 2004, *Phys. Lett. B* **603**, 1.

Padmanabhan T.: 2012, *arXiv: astr0-ph/1207.0505.*

Padmanabhan T.: 2012, *arXiv: hep-th/1206.4916.*

Susskind L.: 1995, *Journal of Mathematical Physics*, **36**, 6377.

Verlinde E.: 2010, *arXiv:hep-th/1001.0785.*

Барьяхтар В., Болотин Ю., Тур А., Яновский В.: 2010, *Физическая ткань Вселенной*, Харьков, ИСМА, 512с.

ON THE THEORETICAL BASING THE DIRECTION DEPENDENCE COSMOLOGICAL DECELERATION PARAMETER

L.M.Chechin
Astrophysical institute named after Fessenkov V.G., Almaty, Kazakhstan
chechin-lm@mail.ru

ABSTRACT. For theoretical describing the asymmetry of Hubble's diagrams and calculating the anisotropy of deceleration parameter phenomenon the concepts of Universe rotation and its two-component model were involved. Our result $\left(\frac{\Delta q}{q_0}\right)_{\max} \leq 0.48$ is in good correlation with the value $\left(\frac{\Delta q}{q_0}\right)_{\max} = 0.76^{-0.46}_{+0.41}$ in (Cai & Tuo, 2011).

Key words: anisotropy of the deceleration parameter, Universe principal axis

1. Introduction

One of the novel cosmological effects that are intensively searched at last time is the space asymmetry of Hubble's diagram (Hudson et al., 2004). In this context it's necessary to mark the original article (Schwarz & Weinhorst, 2007) where the asymmetry of Hubble's diagrams for the North and the South sky hemispheres was examined accurately. This asymmetry, according to authors, cannot be explains by peculiar motion of the observer, but most apparently due to the any bulk flow along the direction ((l, b) = $(300^0,\ 10^0)$) in the Universe existence that earlier was argued in article (Hudson et al., 2004). Recently R.-G.Cai and Z.-L.Tuo (2011) determined more precisely this direction ((l, b) $=314^{0-13^0}_{+20^0},\ 28^{0-33^0}_{+11^0}$) and found the maximum anisotropy of the deceleration parameter $\frac{\Delta q}{q} = 0.76^{-0.46}_{+0.41}$.

Their results are possible to summaries as follows – our Universe is anisotropic in realty and possesses by any principal space axis. That is why the cosmological deceleration parameter will be anisotropic, also and must be depend on the principal space direction in definite way. These statements require theoretical basing the direction dependence of the cosmological deceleration parameter phenomenon.

2. Basic cosmological equations

Our searching we start from the well-known results. The uniform isotropic metric of the space-flat Universe ($k = 0$) have the standard form

$$ds^2 = dt^2 - a^2(t)\left[dr^2 + r^2\left(d\theta^2 + \sin^2\theta d\varphi^2\right)\right]. \quad (1)$$

Einstein's equations for the scale factor $a(t)$ are

$$\ddot{a} = -\frac{4\pi G}{3}(\rho + 3p)a, \quad (2)$$

$$\left(\frac{\dot{a}}{a}\right)^2 = -\frac{8\pi G}{3}\rho, \quad (3)$$

$$\dot{\rho}a + 3(\rho + p)\dot{a} = 0. \quad (4)$$

These equations is possible to deduce and from the Newtonian mechanics in the following way. Let's consider the spherical volume of radius r where concentrates any substance with the density ρ and with the Hubble velocity distribution

$$\vec{v} = H\vec{r}. \quad (5)$$

In the motionless frame of reference the equation of motion of a probe particle that locates on the surface of this sphere, have the usual form

$$\frac{d\vec{v}}{dt} = -\frac{GM}{r^3}\vec{r} = -\frac{4\pi G}{3}\rho\vec{r}. \quad (6)$$

Making the well-known Tolman transformation $\rho \to \rho + 3p$, that allows taking into account the pressure influence on equation of motion, and putting it into (6) we get equation (2). Next, multiplying left and right sides of (6) by $\vec{v} = \frac{d\vec{r}}{dt}$ we get equation (3), that is connected with (6) by the law of energy conservation (4) (Zel'dovich & Novikov, 1983).

In article (Chechin, 2010) it was shown that cosmic vacuum produces not only the Universe expansion but its rotation, also. Here the main results of this article are reproducing briefly.

Let's start from searching the rotational movement of galaxies caused by the antigravitational vacuum force, only. As the model of examining type of galaxy the elliptical galaxy was chosen. For this shape of galaxy its equations of rotational motion are

$$\begin{aligned}\frac{d\theta}{dt} &= \frac{1}{C\omega\sin\theta}\cdot\frac{\partial U}{\partial\psi},\\ \frac{d\psi}{dt} &= -\frac{1}{C\omega\sin\theta}\cdot\frac{\partial U}{\partial\theta}\end{aligned}\quad . \tag{7}$$

In (7) ω is the first integral of the rotational motion, i.e. $\omega = const$. It describes the component of angular velocity with respect to the specific momentum - C. Next, at deducing (7) it was put forward condition that galaxy angular velocity is very small. This allowed neglect the squared angular velocity components and the corresponding angular accelerations. And at last, it was assumed that arbitrary potential in (7) equals to the vacuum potential $U = U_V$, where

$$U_V = -4G\times I_j S_j \times \left(\begin{aligned}&\cos\psi\int\frac{e_1^{\,2}}{R_0^{\,3}}dR_0 + \sin\psi\cos\theta\int\frac{e_1e_2}{R_0^{\,3}}dR_0 - \sin\psi\cos\theta\int\frac{e_1e_2}{R_0^{\,3}}dR_0 + \\ &+\cos\psi\cos\theta\int\frac{e_2^{\,2}}{R_0^{\,3}}dR_0 + \sin\psi\sin\theta\int\frac{e_1e_3}{R_0^{\,3}}dR_0 - \cos\psi\sin\theta\int\frac{e_2e_3}{R_0^{\,3}}dR_0 + \\ &+\sin\theta\int\frac{e_2e_3}{R_0^{\,3}}dR_0 + \cos\theta\int\frac{e_3^{\,2}}{R_0^{\,3}}dR_0\end{aligned}\right) \tag{8}$$

Analysis of equation (7) shown that solution for the precession angle evolving is $\psi(t) = 8\dfrac{GI_jS_J}{C\omega R_0^{\,2}}\cdot t$. Basing on this result it is easy to calculate the angular velocity of the elliptical galaxy around OZ axis. As for this case the following condition $\omega = -\dot{\psi}$ takes place, than its module equals

$$\omega = \omega_V = \sqrt{8\frac{GI_jS_j}{CR_0^{\,2}}} = const\cdot \tag{9}$$

This expression describes the angular velocity that galaxy acquires due to the vacuum antigravitational force.

Admitting $I_jS_j \sim 3IS \sim \rho_V l^4$ and putting that $C \sim l^2$, we find $\omega_V \propto \sqrt{8G\rho_V}\cdot\dfrac{l}{R_0} \propto \omega_0\cdot\dfrac{l}{R_0}$. So, its maximal magnitude will be under the condition $l \propto R_0$. Then expression for the vacuum angular velocity simplifies and takes on the form

3. Universe rotation axis

$$\omega_V = \omega_0 \propto \sqrt{G\rho_V}\ . \tag{10}$$

This expression interprets as the minimal angular velocity in the Universe that possesses an arbitrary object due to the vacuum presence. Its present numerical value is $10^{-19}\sec^{-1}$. Hence, the vacuum creates the identical initial angular velocity for all of cosmic objects, including the Universe itself.

At the earliest stages of the Universe evolution, for instance at the baryonic asymmetry epoch when vacuum density was $10^{-15} g/cm^3$ of order, the angular velocity occurs equal $\omega_V \propto 10^{-11}\sec^{-1}$. For the very early Universe when vacuum density was - $10^{90}\ g/cm^3$, the Universe angular velocity is $\omega_V \propto 10^{42}\sec^{-1}$. This magnitude practically equals to the result of article [13], which was done in the framework of general relativity theory ($\omega \propto 10^{43}\sec^{-1}$).

Henceforth, from these investigations we get the following conclusion - the Universe rotation leads to picking out the principal direction in the space, it may be named as the Universe rotation axis. (Mark, that measurement along this axis only gives the Hubble parameter for the uniform Universe, because in the perpendicular directions the Carioles and centrifugal forces act, also.)

4. Basing the direction dependence of the cosmological deceleration parameter

For enriching our target, which was formulated in section 1, put that distance

$$r = r_0 + \delta r\,, \tag{11}$$

where r_0 is the distance in uniform space, while δr - small addition (perturb term) for describing the possible space anisotropy. Putting (11) into the Newtonian equation (6) we get the equation

$$\frac{d^2(r_0+\delta r)}{dt^2} = -\frac{4\pi G}{3}\rho(r_0+\delta r), \tag{12}$$

that may be decomposed on two parts, easily: main part

$$\frac{d^2r_0}{dt^2} = \frac{dv_0}{dt} = -\frac{4\pi G}{3}\rho r_0 \tag{13}$$

and perturb one

$$\frac{d^2\delta r}{dt^2} = -\frac{4\pi G}{3}\rho\delta r\,. \tag{14}$$

Later on these equations will be considered as are independent each other.

Performing the above mentioned Tolman transformation $\rho \to \rho + 3p$ and substituting it into (13) we find equation

$$\frac{d^2 r_0}{dt} = -\frac{4\pi G}{3}\left(\rho + 3p\right) r_0 . \qquad (15)$$

For the case of vacuum ($\rho = \rho_v$, $p = -\rho_v$) the inflationary regime of the Universe expanding follows from (15) immediately –

$$r_0 = \mathrm{R} \cdot \exp\left(\sqrt{\frac{8\pi G}{3}\rho_v} \cdot t\right) = R \cdot \exp\left(H_0 \cdot t\right). \qquad (16)$$

It leads to the Hubble expansion law

$$v_0 = \frac{dr_0}{dt} = \dot{r}_0 = \sqrt{\frac{8\pi G}{3}\rho_v} \cdot r_0 = H_0 r_0 \qquad (17)$$

and to the corresponding acceleration

$$\ddot{r}_0 = H_0{}^2 r_0 . \qquad (18)$$

Now consider the equation (14). Suppose that in this equation $\rho = \rho_b$, where ρ_b is the baryonic substance density. The baryonic substance pressure p_b let equals zero, for simplicity. Last requirement means considering the presence of two-component substance – cosmic vacuum and baryonic dust – in the Universe, that are not interact each other in the main approximation.

By introducing the designation $\Omega^2 = \frac{4\pi G}{3}\rho_b$, from (14) it follows

$$\frac{d^2 \delta r}{dt^2} + \Omega^2 \delta r = 0 . \qquad (19)$$

This oscillatory-type equation possesses by two roots

$$\delta r_{\pm} = \pm \delta R \cdot \exp\left(i\Omega \cdot t\right) = \pm \delta R \cdot \cos\left(\Omega \cdot t\right). \qquad (20)$$

They lead to the presence of two perturb (with respect to (17)) velocities

$$\begin{aligned} \delta v_{+} &= \frac{d\delta r_{+}}{dt} = +\delta R \cdot i\Omega \exp\left(i\Omega \cdot t\right) = -\delta R \cdot \Omega \cdot \sin \Omega t \\ \delta v_{-} &= \frac{d\delta r_{-}}{dt} = -\delta R \cdot i\Omega \exp\left(i\Omega \cdot t\right) = +\delta R \cdot \Omega \cdot \sin \Omega t \end{aligned} \qquad (21)$$

and two corresponding accelerations

$$\begin{aligned} \frac{d^2 \delta r_{+}}{dt^2} &= \frac{d\delta v_{+}}{dt} = -\Omega^2 \cdot \delta r_{+} \\ \frac{d^2 \delta r_{-}}{dt^2} &= \frac{d\delta v_{-}}{dt} = -\Omega^2 \cdot \delta r_{-} \end{aligned} . \qquad (22)$$

From physical viewpoint expressions (20) – (22) mean that presence of baryonic dust matter creates two space-opposite fluxes that are propagate on the background of expanding and accelerating “Hubble vacuum flux” along the Universe rotation axis (see division 3). That is why it possible writes down the expressions for total distance, velocity and acceleration of any probe particle (galaxy)

$$\begin{aligned} r &= r_0\left(1 \pm \frac{\delta r}{r_0}\right), \\ \dot{r} &= \dot{r}_0\left(1 + \frac{\delta \dot{r}}{\dot{r}_0}\right), \\ \ddot{r} &= \ddot{r}_0\left(1 + \frac{\delta \ddot{r}}{\ddot{r}_0}\right). \end{aligned} \qquad (23)$$

Thus the cosmological deceleration parameter q with the accuracy no higher than $\frac{\delta r}{r_0} \sim \frac{\delta \dot{r}}{\dot{r}_0} \sim \frac{\delta \ddot{r}}{\ddot{r}_0} < 1$ is

$$q_{\pm} \approx -1 \pm 3\frac{\delta R \cdot \cos \Omega t}{r_0} \mp 2\frac{\delta R \cdot \Omega \cdot \sin \Omega t}{H_0 r_0} \pm \frac{\delta R \cdot \Omega^2 \cdot \cos \Omega t}{H_0^2 r_0} . \qquad (24)$$

Basing on the definitions of H_0 and Ω we introduce the new coefficient $\kappa = \frac{\Omega}{H_0} = \sqrt{\frac{\rho_b}{2\rho_v}}$. As in unit of the critical density $\rho_b \sim 0.04$ and vacuum density $\rho_v \sim 0.7$, coefficient $\kappa \approx 0.17$, henceforth.

From (24) it is possible find the relative acceleration difference between two baryonic fluxes with respect to the “Hubble vacuum flux” –

$$\frac{\Delta q}{q_0} = 2\frac{\delta R}{R}\left[\left(3 + \kappa\right)\frac{\cos \kappa H_0 t}{\exp H_0 t} - 2\kappa \frac{\sin \kappa H_0 t}{\exp H_0 t}\right]. \qquad (25)$$

Assuming that for modern epoch $H_0 t \sim 1$ we approximately get $\frac{3+\kappa}{e^1} \sim 1.2$. Hence, the first term in right side of (25) tends to 1.2, while the second term tends to zero. So,

$$\frac{\Delta q}{q_0} \approx 2.4\frac{\delta R}{R} . \qquad (26)$$

Basing on our assumption $\frac{\delta r}{r_0} < 1$, that was argued earlier, we may put that it will satisfy if the ratio

$\left(\frac{\delta R}{R}\right)_{\max} \leq 0.2$. This leads to the estimation $\left(\frac{\Delta q}{q_0}\right)_{\max} \leq 0.48$ that is in good correlation (case of the upper magnitude index) with the value $\left(\frac{\Delta q}{q_0}\right)_{\max} = 0.76^{-0.46}_{+0.41}$ in (Cai & Tuo, 2011).

5. Conclusions

From observational data it was established the asymmetry of Hubble's diagrams for the North and the South sky hemispheres (Hudson et al., 2004). Moreover it was estimated the space anisotropy of the deceleration parameter phenomenon, that was done by R.-G.Cai and Z.-L.Tuo (2011). These facts require the adequate theoretical basing, hence.

For doing this the concepts of Universe vacuum rotation and its two independent component model (cosmic vacuum and baryonic dust) were attracted. Our result on the phenomenon of anisotropy the deceleration parameter calculation - $\left(\frac{\Delta q}{q_0}\right)_{\max} \leq 0.48$ - is in good correlation (case of the upper magnitude index) with the value $\left(\frac{\Delta q}{q_0}\right)_{\max} = 0.76^{-0.46}_{+0.41}$, which was evaluated in (Cai & Tuo, 2011).

References

Cai R.-G., Tuo Zh.-L.: 2011, *arXiv:1109.0941v4 [astro-ph.CO]*.

Schwarz D., Weinhorst B.: 2007, *astro-ph 0706.0165v2.*

Hudson M.J, Smith R.J., Lucey J.R., Branchini E.: 2004, *arXiv:astro-ph/0404386v1*

Zel'dovich Ya.B., Novikov I.D.: 1983, *Relativistic Astrophysics, 2. The structure and evolution of the Universe*. University of Chicago Press, 751 p.

Chechin L.M.: 2010, *Astronomy Reports,* **54,** 719.

DARK ENERGY AND KEY PHYSICAL PARAMETERS OF CLUSTERS OF GALAXIES

A.D. Chernin[1], G.S. Bisnovatyi-Kogan[2]

[1] Sternberg Astronomical Institute, Moscow University,
Moscow, Russia, *chernin@sai.msu.ru*
[2] Space Research Institute, Russian Academy of Sciences,
Moscow, Russia

ABSTRACT. We discuss the physics of clusters of galaxies embedded in the cosmic dark energy background and show that 1) the halo cut-off radius of a cluster like the Virgo cluster is practically, if not exactly, equal to the zero-gravity radius at which the dark matter gravity is balanced by the dark energy antigravity; 2) the halo averaged density is equal to two densities of dark energy; 3) the halo edge (cut-off) density is the dark energy density with a numerical factor of the unity order slightly depending on the halo profile.

1. Introduction

Dark energy treated as Λ-vacuum produces antigravity, and at the present cosmic epoch, the antigravity is stronger than the gravity of matter for the global universe considered as a whole. May the dynamical effects of dark energy be strong on smaller scales as well? Local dynamical effects of dark energy were first recognized by Chernin et al. (2000); the studies of the Local Group of galaxies and the expansion outflow of dwarf galaxies around it revealed that the antigravity may dominate over the gravity at distance of $\simeq 1-3$ Mpc from the barycenter of the group (Chernin, 2001, 2008; Baryshev et al., 2001; Karachentsev et al., 2003; Byrd et al., 2007; Teerikorpi, 2008, 2010).

Further studies (Chernin et al., 2010) show that the nearest rich cluster of galaxies, the Virgo cluster and the Virgocentric expansion outflow around form a system which is a scale-up version of the Local Group with its expanding environment. It proves that the matter gravity dominates in the volume of the cluster, while the dark energy antigravity is stronger than the matter gravity in the Virgocentric outflow at the distances of $\simeq 10-30$ Mpc from the cluster center. On both scales of 1 and 10 Mpc, the key physical parameter of the system is its "zero-gravity radius" which is the distance (from the system center) where the matter gravity and the dark energy antigravity balance each other exactly. The gravitationally bound system can exist only within the sphere of this radius; outside the sphere the flow dynamics is controlled mostly by the dark energy antigravity.

The static solutions for polytropic configurations, and their dynamic stability, in presence of the cosmological constant, have been investigated numerically by Bisnovatyi-Kogan et al. (2011).

2. Dark energy on the cluster scale

Dark energy is a relativistic fluid and its description is based on General Relativity. Nevertheless it may be treated in terms of the Newtonian mechanics, if the force field it produces is weak in the ordinary accepted sense. The Newtonian treatment borrows from General Relativity the major result: the effective gravitating density of a uniform medium is given by the sum

$$\rho_{eff} = \rho + 3p. \tag{1}$$

With its equation of state $p_\Lambda = -\rho_\Lambda$, dark energy has the negative effective gravitating density:

$$\rho_{\Lambda eff} = \rho_\Lambda + 3p_\Lambda = -2\rho_\Lambda < 0. \tag{2}$$

It is because of this negative value that dark energy produces antigravity.

With this result, one may introduce "Einstein's law of universal antigravity" which says that two bodies imbedded in the dark energy background undergo repulsion from each other with the force which is proportional to the distance r between them:

$$F_E(r) = -\frac{4\pi G}{3}\rho_{\Lambda eff} r^3/r^2 = +\frac{8\pi G}{3}\rho_\Lambda r. \tag{3}$$

(This is the force for the unit mass of the body.) Let us consider a spherical mass M of non-relativistic matter embedded in the dark energy background. A test particle at the distance r from the mass center (and out of the mass) has the radial acceleration in the reference frame related to the mass center:

$$F(r) = F_N(r) + F_E(r) = -G\frac{M}{r^2} + \frac{8\pi G}{3}\rho_\Lambda r. \quad (4)$$

(Note that (4) comes directly from the Schwazcshild-de Sitter spacetime in the weak field approximation (see, for instance, Chernin et al., 2006); (4) may also be used for the mass interior; in this case $M = M(r)$ in (4), see Bisnovatyi-Kogan et al., 2011).

It is seen from (4) that the total force F and the acceleration are both zero at the distance

$$r = R_\Lambda = [\frac{M}{\frac{8\pi}{3}\rho_\Lambda}]^{1/3}. \quad (5)$$

Here R_Λ is the zero-gravity radius (Chernin et al., 2000; Chernin, 2001, 2008). The gravity dominates at distances $r < R_\Lambda$, the antigravity is stronger than the gravity at $r > R_\Lambda$. It implies that the gravitationally bound system with the mass M can exist only within the zero-gravity sphere of the radius R_Λ. Clusters of galaxies are known as the largest gravitationally bound systems. Thus, the zero-gravity radius is an absolute upper limit for the radial size R of a static cluster:

$$R < R_\Lambda = [\frac{M}{\frac{8\pi}{3}\rho_\Lambda}]^{1/3}. \quad (6)$$

The total mass of the Virgo cluster estimated by Karachentsev & Nasonova (2010) with the "zero-velocity" method is $M = (6.3 \pm 2.0) \times 10^{14} M_\odot$. This result agrees well with the earlier virial mass of the cluster $M_{vir} = 6 \times 10^{14} M_\odot$ estimated by Hoffman and Salpeter (1980). Teerikorpi et al. (1992), Ekholm et al. (1999, 2000) found that the real cluster mass M might be from 1 to 2 the virial mass: $M = (0.6 - 1.2) \times 10^{15} M_\odot$. Tully and Mohayaee (2004) obtained the Virgo cluster mass $M = 1.2 \times 10^{15} M_\odot$. Taking for an estimate the total mass of the Virgo cluster (dark matter and baryons) $M = (0.6 - 1.2) \times 10^{15} M_\odot$ and the cosmological dark energy density ρ_Λ (see Sec.1), one finds the zero-gravity radius of the Virgo cluster:

$$R_\Lambda = (9 - 11) Mpc \simeq 10 \quad Mpc. \quad (7)$$

3. Cluster overall parameters

The data of the Hubble diagram for the Virgo system (Nasonova & Karachentsev, 2010) enable us to obtain another approximate empirical equality:

$$[\frac{RV^2}{GM}]_{Virgo} \simeq 1. \quad (8)$$

This dimensionless combination of the overall physical parameters of the cluster resembles the traditional virial relation. However its physical sense is different from that of the virial theorem, which has a form for the polytropic star with the polytropic index n

$$\varepsilon_g = -\frac{n}{3}\varepsilon_g + \frac{2n}{3}\varepsilon_\Lambda,$$

see Bisnovatyi-Kogan et al. (2011).

The equation (8) does not assume any kind of equilibrium state of the system; it does not assume either any special relation between the kinetic and potential energies of the system. It assumes only that the system is embedded in the dark energy background and it is gravitationally bound.

The data on the Local Group (Karachentsev et al., 2009; Chernin et al., 2009) show in combination with (8) that

$$[\frac{RV^2}{GM}]_{Virgo} \simeq [\frac{RV^2}{GM}]_{LG} \simeq 1. \quad (9)$$

Here we use for the Local Group the following empirical data: $R \simeq 1$ Mpc, $M \simeq 10^{12} M_\odot, V \simeq 70$ km/s which give the radius, the total mass and the velocity dispersion in the Local Group, correspondingly (Karachentsev et al., 2009).

Assuming that the bound inner component (the cluster) of the Virgo system has a zero-gravity radius R_Λ (6), we obtain from the empirical relation (9) that

$$V^2 \simeq \left(\frac{8\pi}{3}\right)^{1/3} G M^{2/3} \rho_\Lambda^{1/3}. \quad (10)$$

As we see, the velocity dispersion in the gravitationally bound system depends only on its mass and the universal dark energy density. The relation (10) enables one to estimate the matter mass of a cluster, if its velocity dispersion is measured in observations:

$$M \simeq G^{-3/2}[\frac{8\pi}{3}\rho_\Lambda]^{-1/2} V^3 \simeq 10^{15}[\frac{V}{700 km/s}]^3 M_\odot. \quad (11)$$

On the other hand, the approximate empirical relation (9) may serve as an estimator of the local dark energy density, ρ_{loc}. Indeed, if the mass of a cluster and its velocity dispersion are independently measured, one has:

$$\rho_{loc} \simeq \frac{3}{8\pi G^3} M^{-2} V^6 \simeq \rho_\Lambda [\frac{M}{10^{15} M_\odot}]^{-2} [\frac{V}{700 km/s}]^6, \quad (12)$$

what indicates that the observational data on the Local System and the Virgo System provide strong evidence in favor of the universal value of the dark energy density which is the same on both global and local scales.

4. Dark matter halos

Observations and computer simulations indicate – in acceptable agreement with each other – that the spherically-averaged density profiles of the halos in various clusters are rather regular and reveal a simple dependence on the radial distance. In the simplest case, the halo density profile may be approximated by the isothermal power law:

$$\rho = \rho_1 (\frac{r_1}{r})^2, \tag{13}$$

where ρ_1, r_1 are two constants; $\rho_1 = \rho(r_1)$. It was demonstrated (for $\Lambda = 0$) that the density profile of (13) may exist in a system of particles moving along circular orbits (Bisnovatyi-Kogan & Zeldovich, 1969) and in systems with almost radial orbits as well (Antonov & Chernin, 1975).

According to the considerations of the section above, the zero-gravity radius of a cluster like the Virgo cluster is roughly (or maybe exactly) equal to the total radius of the halo. If this is the case, we may identify r_1 with $R = R_\Lambda$, and ρ_1 is then the dark matter density at the halo's outer edge ρ_{edge}. With this, we find the total mass of the halo:

$$M = 4\pi \int_0^R \rho r^2 dr = 4\pi \rho_{edge} R_\Lambda^3. \tag{14}$$

On the other hand, $M = \frac{8\pi}{3}\rho_\Lambda R_\Lambda^3$; then (14) gives:

$$\rho_{edge} = \frac{2}{3}\rho_\Lambda. \tag{15}$$

The cut-off density $\rho_1 = \rho(R_\Lambda)$ proves to be a constant value which does not depend on the total mass or velocity dispersion of the isothermal halo; the density is just the universal dark energy density with the order-of-unity numerical factor.

It follows from (14) that the mean halo density, $< \rho >$, is given again by the dark energy density, but with another numerical factor:

$$< \rho >= 3\rho_{edge} = 2\rho_\Lambda. \tag{16}$$

The last relation is obviously valid for any halo's profile, not only for the isothermal one.

5. Conclusions

The antigravity produced by dark energy puts a clear limit to the extension of dark matter halos in clusters: the halo may exist only in the area $r \leq R_\Lambda$ where the antigravity is weaker than the gravity produced by non-vacuum matter of the cluster. The dark energy density determines the mean matter density of the halo and its edge (cut-off) density. These are the three key physical parameters of clusters. More details see in Bisnovatyi-Kogan & Chernin (2012).

Acknowledgements. A.C. appreciates a partial support from the RFBR grant 02-10-00178. The work of G.S.B.-K. was partially supported by RFBR grant 08-02-00491, the RAN Program Formation and evolution of stars and galaxies and Russian Federation President Grant for Support of Leading Scientific Schools NSh-3458.2010.2.

References

Antonov V.A., Chernin A.D.: 1975, *Sov. Astron. Lett.*, **1**, No 3, 121.

Baryshev Yu.V., Chernin A.D., Teerikorpi P.: 2001, *A&A*, **378**, 729.

Bisnovatyi G.S., Chernin A.D.: 2012, *Ap&SS*, **338**, 337.

Bisnovatyi-Kogan G.S., Zeldovich Ya.B.: 1969, *Astrohysics*, **5**, 105.

Bisnovatyi-Kogan G.S., Merafiva M., Tarasov S.O.: 2011, *In preparation.*

Byrd G.G., Chernin A.D. and Valtonen M.J.: 2007, *Cosmology: Foundations and Frontiers*, Moscow, URSS.

Chernin A.D.: 2001, *Physics-Uspekhi*, **44**, 1099.

Chernin A.D.: 2008, *Physics-Uspekhi*, **51**, 267.

Chernin A.D., Teerikorpi P., Baryshev Yu.V.: 2000, [astro-ph/0012021] *Adv. Space Res.*, **31**, 459, 2003.

Chernin A.D., Teerikorpi P., Baryshev Yu.V.: 2006, *A&A*, **456**, 13.

Chernin A.D., Karachentsev I.D., Valtonen M.J. et al.: 2009, *A&A*, **507**, 1271.

Chernin A.D., Karachentsev I.D., Nasonova O.G. et al.: 2010, *A&A*, **520**, A104.

Ekholm T. et al.: 1999, *A&A*, **351**, 827.

Ekholm T. et al.: 2000, *A&A*, **355**, 835.

Karachentsev I.D., Kashibadze O.G., Makarov D.I. et al.: 2009, *MNRAS*, **393**, 1265.

Karachentsev I.D., Nasonova O.G.: 2009, *MNRAS*, **405**, 1975.

Kofman L.A., Starobinskii A.A.: 1985, *Sov. Astron. Lett.*, **11**, 271.

Teerikorpi P. et al.: 1992, *A&A*, **260**, 17.

Teerikorpi P., Chernin A.D., Karachentsev I.D. et al.: 2008, *A&A*, **483**, 383.

Teerikorpi P., Chernin A.D.: 2010, *A&A*, **516**, 93.

SUPERNOVAE EXPLOSIONS THEORY AND COMPACT REMNANT OF SN 1987A

V.M. Chechetkin[1], A.A. Baranov[2], M.V. Popov[1,2], A.Yu. Lugovsky[1]

[1] Keldysh Institute of Applied Mathematics,
Russian Academy of Science, Miusskay sq. 4, 125047, Moscow, Russia.
[2] Laboratoire d'Annecy-le-Vieux de Physique Theorique (LAPTH), Université de Savoie,
9, Chemin de Bellevue BP 110, 74941 Annecy-le-Vieux Cedex, France.
mikhail.v.popov@gmail.com

ABSTRACT. Hydrodynamics of massive star explosion within a non-spherical supernova model is presented. The explosive burning is computed in the He-core of a progenitor. It is assumed that the iron core and the other layers of the intermediate-mass nuclei formed a compact central object beyond the mass cut and its formation did not disturb the stellar envelope. A Piecewise Parabolic Method on a Local stencil (PPML) is applied to simulate the hydrodynamics of the explosion. The problem of compact remnant creation after the explosion is discussed in relation with SN 1987A observations. The computations show that at the neighbourhood of compact remnant a significant quantity of the matter should remain. The accretion of this matter to the compact remnant should produce strong radiation which is not observed in the case of SN 1987A.

Key words: hydrodynamics, PPML; supernovae, compact remnant, accretion, SN 1987A.

1. Introduction

As is well known there are two classes of supernovae (SNe) with different mechanisms of explosion – thermonuclear SNe (type Ia), with the white dwarfs progenitors, and core-collapse SNe (type II, Ib/c) with the massive stars progenitors. The theory of SNe involves a large number of fundamental problems of modern physics and astrophysics which are not solved yet. Although the explosion mechanisms are completely different, the large-scale convective processes and hydrodynamic instabilities play a very important role in both cases (Ustyugov et al. 1999, Popov et al. 2004, Bychkov et al. 2006). In this paper we discuss the hydrodynamic of massive star explosion by an example of non-spherical model and the problem of compact remnant after the explosion in relation with SN 1987A observations.

For our hydrodynamic model of core-collapse SN we have chosen the parameters of a Population I metal rich 25 $M_\odot$ star. We have assumed that by the explosion moment the inner part of the star collapsed and produced $\sim 10^{52}$ ergs. Assuming that the size of this collapsed part is small in comparison with the size of He-envelope, we start the hydrodynamic computations of propagation of the shock through the He-envelope. The explosion is initiated by inserting the energy into the central part of the star and distributing it in an asymmetric way. So we assume a jet-like structure of the explosion when the ejected matter preferentially moves along the rotational axis. This kind of asymmetry could be explained by acting of Archimedes' force on the hot and light products of explosive burning. In the case of rotation the levels of constant density have a form, similar to ellipsoids of rotation, making the steepest pressure gradient along the axis. It means that the Archimedes' force is acting along this direction. This mechanism requires time to deform the shape of the burnt matter, extending it along the axis. Here we must assume the deflagration regime of burning when at the initial stage the burning front propagates with subsonic velocity. In this case a hot core disintegrates forming two large-scale convective bubbles which are floating up and down. As a result this should produce a jet-like structure of the explosion. The dynamics of such bubbles was studied, for example, in (Bychkov et al. 2006). Also the acting of magnetic fields favours a jet-like structure, see for example the magnetorotational mechanism of SN (Moiseenko et al. 2010).

A theoretical reason for the axisymmetric explosion could be an assumption of the deflagration regime of nuclear burning in the stellar core under the conditions of hydrostatic equilibrium for SNe type Ia and nonequilibrium neutronization of the matter in the central part of the protoneutron star for SNe type II, Ib/c. For SNe type Ia formation of large-scaled bubbles is the first stage of explosion, after which the deflagration flame could transform to a detonation regime. This is a delayed detonation scenario (deflagration-detonation transition) (Ivanova et al. 1974, Khokhlov 1991).

One of the main problems in the theory of SNe II is to show how a neutron star is born in the explosion. During the gravitational collapse of the iron core of a massive star, huge energy is released in the form of neutrinos. However, these neutrinos remain trapped in the central layers of a star under the conditions of the extremely high density. In order to stop the collapse and to support the explosion, the neutrinos have to be transported fast to the bounce shock. Our theoretical results confirm the idea that a large-scale convection should be the main transport mechanism for the neutrinos in SNe II. Large convective bubbles drift the high-energy neutrinos to the outer layers of the star, where they finally escape and reach the bounce shock.

The explosion of SN 1987A is of considerable interest for modern fundamental physics, both the physics of elementary particles and modern theoretical astrophysics. This supernova exploded in the Large Magellanic Cloud in 1987, when astronomical instruments allowed observations over the entire electromagnetic spectrum, as well as instruments for neutrino detection were operating. Neutrino events were recorded by the IMB, Kamiokande II, LSD instruments and the Baksan telescope (Bionta et al. 1987, Hirata et al. 1987, Aglietta et al. 1987). The LSD signal was detected five hours earlier than the other signals. Though models explaining this delay were subsequently suggested, a completely consistent model is still lacking.

The presence of a neutrino burst was interpreted as an indication of the gravitational collapse of the massive stellar core, forming a compact remnant – neutron star or black hole. Several papers in the early 1990s claimed that we would see the neutron star in the next three to five years, after the expansion of the envelope. However, no evidence of the presence of a compact remnant has been found more than 25 years after the outburst.

Another remarkable feature of this supernova is early detection of lines of ^{56}Co, which is created in the central region of the outburst (Syunyaev et al. 1987, Shigeyama et al. 1987). A proposed model describing the transport of cobalt from the interior by convection was not confirmed in numerical computations. This early appearance of ^{56}Co lines could be explained by either an asymmetric explosion or by the complete disruption of the star (Chechetkin et al. 1980, 1988).

One of the main methods used to study newborn neutron stars is the detection of X-rays emitted during the accretion of matter from the envelope left behind. The upper limit for the X-ray flux from a point source in the SN 1987A remnant established by the Chandra space observatory is $5.5 \cdot 10^{34}$ erg/s (Park et al. 2004). The intensity of the optical radiation measured with the Hubble Space Telescope doesn't exceed $8 \cdot 10^{33}$ erg/s [Graves et al. 2005]. Several explanations of very low radiation in presence of compact remnant were suggested in paper by (Graves et al. 2005). The possible absence of a compact remnant is of great interest for the scientific community.

In this study we have computed the mass of matter remains in the neighborhood of a possible compact remnant in case of spherically symmetrical supernova explosion. We also have estimated accretion rate and X-ray luminosity for comparison with the observations of SN 1987A.

2. Hydrodynamics of SN explosion

We have used a polytropic model of a star with index $\gamma = 4/3$ which corresponds to Eddington standard model with purely radiative heat transport. The pressure in this case is determined by radiation. This assumption is valid only in the central hot core of a star. Initial configuration was calculated from the condition of hydrostatic equilibrium of non-rotating ideal gas sphere with a simple equation of state $P = \rho RT/\mu$, where the mean molecular weight was assumed as $\mu = 0.7$. We did not recompute gravity field assuming the explosion does not violate its initial spherically symmetric distribution. To construct the equilibrium initial profiles of density and temperature we take the central values $\rho_c \sim 762$ g/cm^3 and $T_c \sim 1.96 \times 10^8$ K what corresponds to the realistic pre-supernova star model at the beginning of helium burning stage (Woosley et al. 2002).

Hydrodynamic simulations were performed with our own numerical code based on the Piecewise Parabolic Method on a Local stencil (PPML) (Popov et al. 2007, Popov 2012). The key PPML-procedure written on FORTRAN could be found in (Ustyugov et al. 2009). PPML is an improvement over the popular Piecewise Parabolic Method (PPM) suggested in (Colella et al. 1984) for compressible flows with strong shocks. PPM was implemented in many modern hydrodynamic codes and is widely used in computational practice now. The principal difference between PPM and PPML is the way how the interface values of the variables are computed between the adjacent cells. Instead of 4-point interpolation procedure in the standard PPM we have suggested to evolve them with time using the conservation property of Riemann invariants. Only local information within the left and the right cells is utilized to construct the interface values in this approach. The price for this is a double application of the Riemann solver procedure and a greater memory requirement for the storage of the boundary values from the previous time step, i.e. more computational capacity is required. However the method has demonstrated a high accuracy on both smooth and discontinued solutions. It could be more suitable for problems where the requirement of low dissipation is crucial.

There are two possibilities to simulate the SN explo-

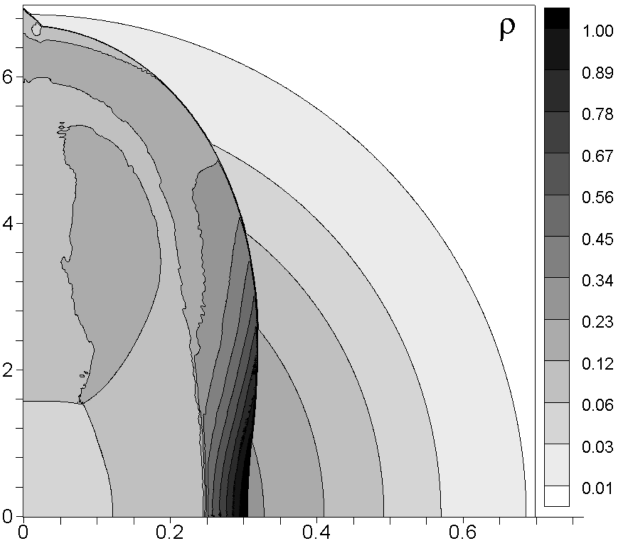

Figure 1: Density distribution for the moment $t = 19.5$ s after the inducing of the explosion. The coordinates are shown in the units of solar radius. Color represents the density in the units of $\rho_c = 762$ g/cm^3.

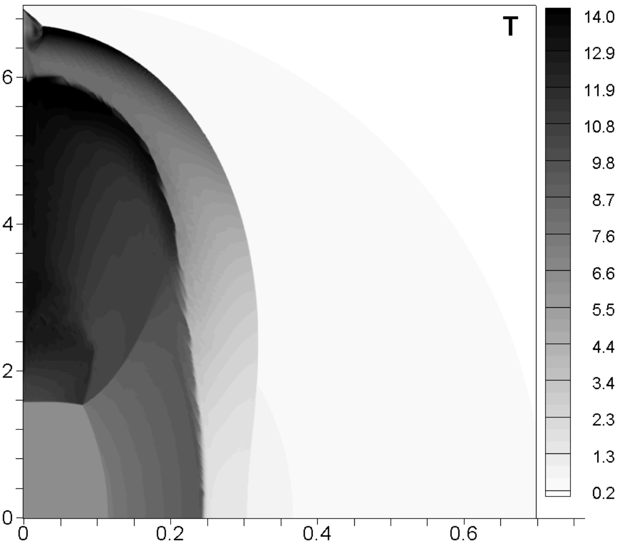

Figure 2: Temperature distribution for the same moment and in the same coordinate units as on fig. 1. Color represents the temperature in the units of 10^8 K.

sion: either by moving a piston as an inner boundary or depositing of the energy. Both of them involve free parameters. Piston is a time-dependent momentum deposition which requires the specification of the way how to move it (Woosley et al. 1995). It is easier to implement in Lagrangian hydrodynamics (mainly 1D) but the falling down matter could accumulate on the boundary reducing the accretion. The result yield is also sensitive to the mixing, fallback and explosion energy. In our SN model we use an alternative approach of the energy depositing to the central region of a star what is more natural for Eulerian hydrodynamics. As a parameter we need to define the size of the region where to insert the energy. The disadvantage of this approach is the possibility of the artificially entropy increase.

For numerical treatment we used a cylindrical coordinate system where all the variables depend on the vertical coordinate z and the distance r to z-axis, i.e. we assume rotational symmetry. Reflecting boundary conditions were imposed along the cylindrical axis and the equatorial plane, free outflow was allowed across the outer boundaries. We performed simulation in one quadrant with 800 × 800 grid resolution. We chose asymmetric explosion model "C" from (Maeda et al. 2002). The explosion energy $E \sim 1 \times 10^{52}$ ergs was divided between thermal and kinetic parts into two equal halves. The kinetic energy was distributed in an axisymmetric way by imposing different initial velocities in different directions: $v_z = \alpha z$ in the vertical direction and $v_r = \beta r$ on the equatorial plane. According to model "C" the ratio of the coefficients $\alpha : \beta = 8 : 1$. The energy E was deposit below 0.17 $R_\odot$ radius which contained 2 $M_\odot$.

The simulation of supernova hydrodynamics with the initial parameters described above is presented on fig. 1-2 where the density and the temperature are shown respectively for the moment $t = 19.5$ s. The coordinates are in the units of solar radius. Color represents the density in the units of ρ_c and the temperature in 10^8 K. We detected a forward and a reverse shocks. The forward shock is moving up along the cylindrical axis, splitting into two shocks which are accelerating, entering into the lower density. This structure is tending to Sedov-Taylor self-similar solution when the energy of gravitational field becomes small comparatively to the kinetic energy of the expansion. The formation of the reverse shock in SNe models is a well known phenomenon, see for example (Couch et al. 2011, Gawryszczak et al. 2010). It forms on the distance $z \sim 0.2$ due to the resistance of the matter in front of propagating forward shock. The thrilling of the fronts near the cylindrical axis is a grid effect. Since in our model the most of the kinetic energy was introduced along the cylindrical axis, the motion in the equatorial plane is much less intensive (fig. 1). On fig. 2 you can see a bubble of hot matter which is formed between the reverse shock and the 'second' forward shock which is similar to the result obtained in (Couch et al. 2011). In this region the rates of the nuclear reactions must be most rapid.

3. Computations of compact remnant in SN explosion

To estimate the amount of ejected matter and matter that left in the vicinity of a compact remnant in

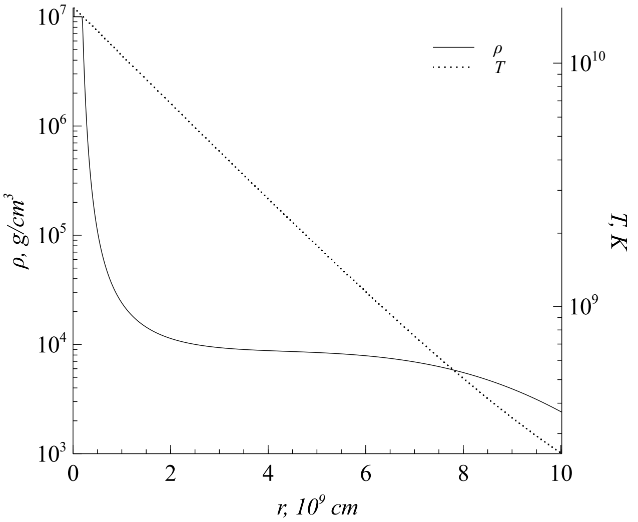

Figure 3: Initial distribution of density ρ and temperature T.

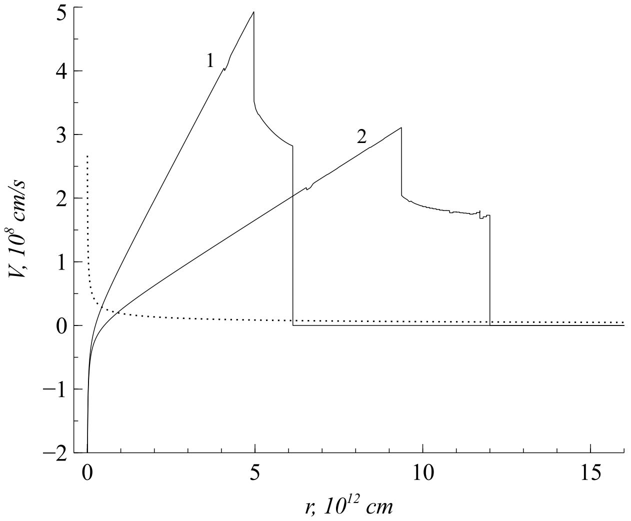

Figure 4: Velocity profiles for time of 1000 s (1) and 5000 s (2) after the outburst. The escape velocity is shown by dotted line.

the process of the supernova outburst, we have computed the propagation of a shockwave through the pre-supernova shell. A gravitating object with mass $M_C = 1.35M_\odot$ and radius 10^7 cm was placed at the coordinate origin. This object corresponded to a proto-neutron star that was born as a result of the core collapse of the pre-supernova. It was surrounded by the envelope of helium with total mass around $15M_\odot$. The matter of the star shell was assumed as compressible non-viscous fluid. The generalized explicit Belotserkovskii–Gushchin–Kon'shin scheme (Belotserkovskii et al. 2005) was used to solve the set of hydrodynamical equations. For simplicity, explosion was assumed spherically symmetric, star was assumed non-rotating (only the radial velocity component is nonzero). Equation of state was one of the ideal gas with adiabatic index γ equals to 5/3. Initial distribution of density and temperature were computed using hydrostatic equilibrium condition (see Fig. 3).

The shockwave was initiated by energy deposition in the $2 \cdot 10^7$ cm $< r < 2 \cdot 10^8$ cm spherical layer. Two kinds of energy deposition were used: positive radial velocity of $3 \cdot 10^7$ cm/s; and temperature jump by a factor of 10. The value of initial excitation was taken to provide kinetic energy of the shell of the order of 10^{51} ergs.

Calculations were performed on variable-scale grids. First the problem was solved in the range $2 \cdot 10^7$ cm $< r < 10^{10}$ cm . After the grid was changed by more rough one and external radius was increased up to 10^{13} cm. It was assumed that matter with velocity less than escape velocity will remain near the compact remnant and take part in subsequent accretion onto it.

Velocity profiles for different moments of time are presented on Fig. 4, together with escape velocity. It is seen from the figure that close to the center some part of matter has negative velocity. It shows that accretion has started.

One of the important results is the fact that after some time since the beginning of explosion ($2 \cdot 10^4$ s) matter of the envelope divides on two parts. The first part has velocity smaller than escape velocity. And total mass of this part is about $0.8M_\odot$ and remains constant (see Fig. 5). The outer boundary of this region expands with a decreasing velocity.

4. Estimation of accretion

The results of computations presented in the previous section show that more than $0.8M_\odot$ of matter in the envelope does not achieve the escape velocity, and forms the shell around the compact gravitating object. The next task was to evaluate the rate of accretion of remaining matter onto this object.

In the beginning we have performed rough estimates. To compute the rate of matter accretion, $\dot{M}$, onto the surface of the compact remnant of mass M, we used the formula for gas accretion from (Zeldovich and Novikov 1971):

$$\dot{M} = 10^{-14}\frac{\rho}{10^{-24}\frac{g}{cm^3}}\frac{M}{M_\odot}\left(\frac{V_\infty}{10\frac{km}{s}}\right)^{-3}, \ \frac{M_\odot}{year}. \quad (1)$$

The accretion rate depends on the distribution of the matter density ρ in the envelope. However, for simplicity density was assumed to be uniform. It was derived from the size and mass of the remaining shell around the compact central object:

$$\rho = \frac{M_r}{4/3\ \pi R_r^3}, \quad (2)$$

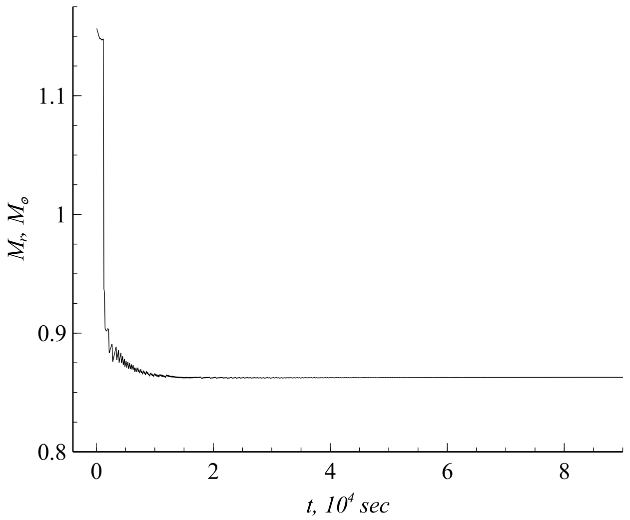

Figure 5: Mass of the compact shell M_r depending on time.

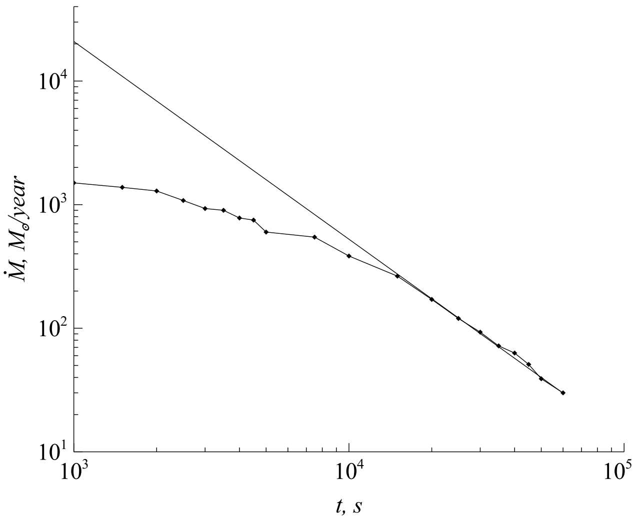

Figure 6: Accretion rate versus time since the outburst. The straight line is an extrapolation.

where M_r and R_r are the mass of the remaining shell and the maximum radius of its expansion; we treated R_r as parameter. For various values of R_r we have made estimation of accretion rate, lifetime of the shell and luminosity. The luminosity, L, was estimated by the formula:

$$L = \eta \dot{M} c^2, \tag{3}$$

where c is the speed of light and η is the efficiency of the transformation of the rest-mass energy into radiation, taken to be 0.1 (Graves et al. 2005). The results for various radii are presented in the Table 1.

Table 1: Luminosity L estimated for a uniform density distribution in the remaining shell.

R_r, cm	$\dot{M}, M_\odot/year$	Lifetime	L, erg/s
10^{14}	10^3	less than a day	10^{49}
10^{15}	1	~ 1 year	10^{46}
10^{16}	10^{-3}	10^3 years	10^{43}
10^{17}	10^{-6}	10^6 years	10^{40}
10^{18}	10^{-9}	10^9 years	10^{37}

The estimated luminosity is higher than is observed one by three orders of magnitude even for a radius of 10^{18} cm.

However, the physical problem is more complicated because of the non-uniform density profile along the radius. It is very difficult to perform a direct computation of the accretion for a time span of several years, starting from the beginning of explosion, because the velocity is very different in the neighborhood of the central object and at large radii.

The accretion rate was computed for a period about 20 hours starting from the outburst. The results are presented in Fig 6.

The accretion rate is fairly high at small times, but the computations show that it decreases with time. To estimate the accretion at later stages, we have extrapolated the accretion rate derived in our computations. The computations show that the decrease in the accretion rate is close to a power law:

$$\dot{M} = 1,37 \cdot 10^9 \left(\frac{t}{1s}\right)^{-1,6} M_\odot/year. \tag{4}$$

In this case, after ten years, when the envelope has certainly become transparent, the accretion rate drops to 10^{-5} $M_\odot$/year. Following (Graves et al. 2005), the X-ray luminosity for this accretion rate is about 10^{40} erg/s. It is higher by six orders of magnitude than the observational upper limit of X-ray luminosity in the remnant of SN 1987A.

5. Conclusions

We have presented a simple approach for SNe modelization which allows to obtain a reliable picture of the explosion. The model is not overloaded with complicated physics and gives a clear understanding what is important and what could be neglected. More sophisticated models could be constructed against the background of this one. We did not compute self-gravity and used a simple equation of state. This is also not a full 3D simulation since we have assumed a rotational symmetry.

Our computations show that in case of supernova explosion with compact remnant (neutron star or black hole) significant amount of matter from the envelope remains in its vicinity. Computations were performed with parameters close to SN 1987A (mass of the progenitor and energy of explosion). The estimations of spherical accretion presented in this paper indicate that X-ray luminosity after 10 years from explosion far exceeds the upper limits of luminosity from observations of the remnant of SN 1987A.

Acknowledgements. The computations were performed on LAPTH Cluster, Université de Savoie, France and on MVS-100K of Joint Supercomputer Center of the Russian Academy of Sciences. The work was supported by the Russian Foundation for Basic Research (project nos. 12-01-00606a, 12-02-00687a, 12-02-31737mol_a), Basic Research Programs no. 15 and no. 21 of the Presidium of the Russian Academy of Science and by the scientific school NSh-1434.2012.2.

References

Aglietta M., Badino G., Bologna G., et al.: 1987, IAU Cir., **4323**.

Belotserkovskii O.M., Oparin A.M., Chechetkin V.M.: 2005, *Turbulence: New Approaches* (Cambridge International Science Publishing, Cambridge).

Bionta R.M., Blewwit G., Bratton C.B., et al.: 1987, *Phys. Rev. Lett.*, **58**, 1494.

Bychkov V., Popov M.V., Oparin A.M., Stenflo L., Chechetkin V.M.: 2006, *Astron. Rep.*, **50**, 298.

Chechetkin V.M., Gershtein S.S., Imshennik V.S., et al.: 1980, *Astrophys. Space Sci.*, **67**, 61.

Chechetkin V.M., Denisov A.A., Koldoba A.V., et al.: 1988, in *Supernova Remnants and the Interstellar Medium*, Ed. by R.S.Roger and T.L.Landecker (Cambridge, Cambridge University).

Colella P., Woodward P.R.: 1984, *J. Comput. Phys.*, **54**, 174.

Couch S.M., Pooley D., Wheeler J.C., Milosavljević M.: 2011, *Astropys. J.*, **727**, 104.

Gawryszczak A., Guzman J., Plewa T., Kifonidis K.: 2010, *A&A*, **521**, A38.

Graves G.J.M.; Challis P.M., Chevalier R.A., et al.: 2005, *Astrophys. J.*, **629**, 944.

Hirata K., Kajita T., Koshiba M., et al.: 1987, *Phys. Rev. Lett.*, **58**, 1490.

Ivanova L.N., Imshennik V.S., Chechetkin V.M.: 1974, *Ap&SS*, **31**, 497.

Khokhlov A.: 1991, *A&A*, **245**, 114.

Maeda K., Nakamura T., Nomoto K., Mazzali P.A., Patat F., Hachisu I.: 2002, *Astropys. J.*, **5**65, 405.

Moiseenko S.G., Bisnovatyi-Kogan G.S., Ardeljan N.V.: 2010, *AIP Conf. Proc.*, **1**206, 282.

Park S., Zhekov S.A., Burrows D.N., et al.: 2004, *Adv. Space Res.*, **33**, 386.

Popov M.V., Ustyugov S.D., Chechetkin V.M.: 2004, *Astron. Rep.*, **48**, 921.

Popov M.V., Ustyugov S.D.: 2007, *Comput. Mathem. & Mathem. Phys.*, **47**, 1970.

Popov M.V.: 2012, *Comput. Mathem. & Mathem. Phys.*, **52**, 1186.

Shigeyama T., Nomoto K., Hashimoto M., Sugimoto D.: 1987, *Nature*, **328**, 320.

Syunyaev R.A., Kaniovskii A.S., Efremov V.V., et al.: 1987, *Sov. Astron. Lett.*, **13**, 431.

Ustyugov S.D., Chechetkin V.M.: 1999, *Astron. Rep.*, **43**, 718.

Woosley S.E., Weaver T.A.: 1995, *ApJS*, **101**, 181.

Ustyugov S.D., Popov M.V., Kritsuk A.G., Norman M.L.: 2009, *J. Comput. Phys.*, **228**, 7614.

Woosley S.E., Heger A., Weaver, T.A.: 2002, *Rev. Mod. Phys.*, **74**, 1015.

Zeldovich Ya.B. and Novikov I.D.: 1971, *Gravitation Theory and Stellar Evolution*, (Moscow, Nauka) [in Russian].

LOW MISSING MASS, SINGLE- AND DOUBLE DIFFRACTION DISSOCIATION AT THE LHC

L. Jenkovszky [1,2,a], A. Salii [1,b], J. Turóci [3,c] and D. Himics [3,d]

[1] Bogolyubov Institute for Theoretical Physics, National Academy of Sciences of Ukraine
UA-03680 Kiev, Ukraine
[2] Wigner Research Centre for Physics, Hungarian Academy of Sciences 1525 Budapest,
POB 49, Hungary
[3] Uzhorod State University
[a] jenk@bitp.kiev.ua, [b] saliy.andriy@gmail.com, [c] turoczi.jolika@citromail.hu, [d] himicsdia@hotmail.com

ABSTRACT. Low missing mass, single- and double diffraction dissociation is calculated for the LHC energies from a dual-Regge model. The model reproduces the rich resonance structure at low mass region, and approximate behavior for high mass-region.

1. Introduction

Measurements of single (SD) double (DD) and central (CD) diffraction dissociation (Dif.) are among the priorities of the Large Hadron Collider (LHC)) at CERN.

In the past, intensive studies of high-energy diffraction dissociation were performed at the Fermilab, on fixed deuteron target, and at the ISR, see [1] for an overview and relevant references. One can see the rich resonance structure there, typical of low missing masses, often ignored by extrapolating this region by a simple $1/M^2$ dependence. When extrapolating (in energy), one should however bear in mind that, in the ISR region, secondary Reggeon contributions are still important (their relative contribution depends on momentum transfer considered), amounting to nearly 50% in the forward direction. At the LHC, however, their contribution in the nearly forward direction in negligible, i.e. less than the relevant error bars in the measured total cross section [3].

This new situation makes diffraction at the LHC unique in the sense that for the first time Regge-factorization is directly applicable.

2. Pre-LHC measurements: ISR, Fermilab and Tevatron (CDF)

Previous to the LHC, single diffraction dissociation was intensively studied at the ISR the Fermilab (fixed deuteron target) and at the Tevatron in the range of $14 < \sqrt{s} < 1800\,GeV$, $|t| < 2GeV^2$, and missing masses ranging from the threshold up to $\xi < 0.15$. The main results of these measurements and of their theoretical interpretation can be summarized as follows, for details see, e.g. [1, 2]:

1. Energy dependence. At the ISR and Fermilab energies the integrated SD cross section rises with s according to the standard prescription of the Regge-pole theory, however in slows down beyond. This effect was expected due to the familiar problem related to the violation of unitarity, namely that at high energies, implying the triple Pomeron limit, the D cross section overshoot the total cross section, $\sigma_{SD} > \sigma_t(s)$. Various means were suggested [5] to remedy this deficiency, including decoupling (vanishing) of the triple Pomeron vertex. Goulianos renormalizes the standard Pomeron flux to meet the data, see [2]. Such a “renormalization" produces a break near $\sqrt{s} \approx 20GeV$ slowing down the rise of $\sigma_{SD}(s)$ in accord with the CDF data from the Tevatron.

We instead will cure this problem by using rudiments of a dipole Pomeron (DP), compatible with unitarity without any renormalization factor, that produces a sharp (non-analytic) change in the behavior of $\sigma_{SD}(s)$: a dipole Pomeron (double Pomeron pole) is compatible with unitarity, in particular in the sense that both the SD cross section rises proportionally with the total cross section. The DP produces logarithmically growing cross sections at unit Pomeron intercept, however to meet the observed rise of the ratio σ_{el}/σ_{tot}, the Pomeron intercept is allowed to be slightly beyond unity, namely, $\alpha_{IP}(t)=1.04$. In other words, the rise of the cross sections is driven both by the dipole (by a logarithmic factor) and a tiny (half of Donnachie-Landshoff's [8] supercritical intercept).

2. t-dependence of σ_{SD} and the slope *B*(*s; t;M*^{2}) was calculated in the range $0.01<t<2GeV^2$. Although nothing dramatic was found (the diffraction cone essentially is exponential in *t*, the shape of the diffraction cone is DD may contain important detail to be unveiled by future measurements: a dip similar to that in elastic scattering is likely to appear (near $t\sim 1GeV^2$). Another important issue in the behavior of the cone of Dif. is a possible turn-down towards small-t due to the kinematical factor, denoted below by $F(t,M^2)$, connecting the *pP* structure function with the total cross section (see Sec. IV). This tiny effect is located in the kinematical region where Coulomb interaction is sizable. However, as noticed in Ref. [4], in DD processes, the Coulomb interaction, at small squared momentum transfers, is suppressed compared to that in elastic diffractive *pp* scattering, allowing for a better determination of the strongly interacting part of the amplitude (in *pp;* at small t this is possible only indirectly, by means of the Bethe-Heitler interference formula).

3. M^2*-dependence***.** The data compilation for SD processes form different experiments (ISR, Fermilab, Tevatron e.g. see Ref. [1]) shows that the small-M^2 region, is full of resonances. In most of the papers on the subject this resonance structure is ignored and it is replaced by a smooth function $\sim M^{-2}$ allegedly approximating the resonances. Moreover, this simple power-like behavior is extended to the largest available missing masses. In sec. IV we question this point on the following reasons: a) the low-M^2 resonances introduce strong irregularities in the behavior of the resulting cross sections; b) the large-M^2 behavior of the amplitude (cross sections) is another delicate point. Essentially, it is determined by the proton-Pomeron (*pP*) total cross section, proportional to the *pP* structure function, discussed in details in Sec. IV. By duality, the averaged contribution from resonances sums up to produce high missing-mass Regge behavior $(M^{-2})^n$, where *n* is related to the intercept of the exchanged Reggeon (essentially, that of the *f* trajectory). Furthermore, according to the ideas of two-component duality, see e.g. [7], the cross sections of any process, including that of $pP\rightarrow X$,is a sum of a non-diffractive component, in which resonances sum up in high-energy (here: mass) Regge exchanges and the smooth background (below the resonances) is dual to a Pomeron exchange. The dual properties of Diff. can be quantified also by finite mass sum rules, see [1]. In short: the high-mass behavior of the $pP\rightarrow X$ cross section is a sum of a decreasing term going like $\sim M^{-2}$ and a "Pomeron exchange" increasing slowly with mass. All this has little affect on the low-mass behavior at the LHC, however normalization implies calculation of cross sections integrated over all diffraction region up to $\xi<0.05$.

3. Factorization relation

So, with the advent of the LHC, diffraction, elastic and inelastic, entered a new area, where it can be seen uncontaminated by non-diffractive events. In terms of the Regge-pole theory this means, that the scattering amplitude is completely determined by a Pomeron exchange, and in a simple-pole approximation, Regge factorization holds and it is of practical use! Note that the Pomeron is not necessarily a simple pole: pQCD suggests that the Pomeron is made of an infinite number of poles (useless in practice), and the unitarity condition requires corrections to the simple pole, whose calculation is far from unique. Instead a simple Pomeron pole approximation [8] proved to be efficient in describing a variety of diffractive phenomena.

The DL elastic scattering amplitude is simply:

$$A(s,t)=\xi(t)\beta(t)(s/s_0)^{\alpha_{IP}(t)-1}+A_R(s,t), \qquad (1)$$

where $\xi(t)=e^{i\pi/2}$ is the signature factor, and $\alpha_{IP}(t)=1.04+0.25t$ is the Pomeron trajectory. The residue is chosen to be a simple exponential, $\beta(t)=e^{b_P t}$ with $b_P=8.4GeV^{-1}$ [3]. "Minus one" in the power of (1) anticipates of norm $\sigma_{tot}(s)=\operatorname{Im}A(s,t=0)$ the scale parameter s_0 isn't fixed by the Regge-pole theory: it can be fitted do the data or fixed to a "plausible" value of a hadronic mass, or to the inverse "string tension" (inverse of the Pomeron slope), $s_0=1/\alpha'$ according to DL. The second term in Eq. (1), correspond to sub-leading Reggeons, has the same functional form as the first one (Pomeron), just the values of the parameters differ. We ignore this term for reason mentioned above.

Factorization of the Regge residue $\beta(t)$ and the "propagator" $(s/s_0)^{\alpha_{IP}(t)-1}$ is a basic property of the theory. As mentioned, at the LHC for the first time, we have the opportunity to test directly Regge-factorization, since the scattering amplitude is dominated by a simple Pomeron-pole exchange, identical in elastic and inelastic scattering. Simple factorization relations between elastic, single and double are known from the literature [1].

$$\frac{d^3\sigma_{DD}}{dtdM_1^2dM_2^2}=\frac{d^2\sigma_{SD}}{dtdM_1^2}\frac{d^2\sigma_{SD}}{dtdM_2^2}\Bigg/\frac{d\sigma_{el}}{dt} \qquad (2)$$

4. Model for single and double diffraction dissociation

The construction of our model relies on the following premises:

1. *Regge factorization*. This is feasible since, as stressed repeatedly, at the LHC energies and for $t<1GeV^2$, typical of diffraction, the contribution from secondary Reggeons is negligible, and, for a single Pomeron term, factorization is exact;

2. Due to factorization, the relevant expressions for the cross sections (elastic, SD, DD) are simple, as written

below, (3-5). Such relations are known from the literature, see e.g. [1] and references therein;

3. The inelastic pPX vertex receives special care. Following Refs. [9,10] we consider this vertex as a deeply inelastic process, similar to the $\gamma p \to X$ vertex in lepton-hadrons DIS e.g et HERA or JLab. The virtual photon of DIS here is replaced by the (virtual) Pomeron with an obvious change of Q^2 typical of DIS to $-t$ in the present $pP \to X$ sub-processes the total c.m. energy here being M. There is one important difference between the two, namely the quantum numbers of the Pomeron and the photon (positive and negative C parities, respectively). However, this is not essentially since the dynamics is the same and the produced states in the pP system will be those of the relevant nucleon trajectory with the right quantum numbers (see below). Contrary to Jaroszewicz and Landshoff [10], who use the Regge asymptotic (in the missing mass) form of the Pp structure function and, consequently the triple Pomeron limit, leaving outside the low-M resonance structure, we concentrate on the low-M resonance region with and use a "Reggeized Breit-Wigner" formula for the structure function elaborated in ref.[9] (see also earlier citations therein). By duality, the relevant sum of the two parts (low- and high missing mass) should be equivalent. This interesting feature of Dif. was studied in the 70-ies (see [1] and references therein), and it merits to be revived.

4. *The background* is always a delicate issue. In the reactions (SD, DD) under consideration there are two sources for the background. The first is that related to the t channel exchange and can be accounted for by rescaling the parameter $s0$ in the denominator of the Pomeron propagator. In any case, at high energies, i.e. those of the LHC, this background is included automatically in t-channel Pomeron exchange. The second type of background comes from the sub processes $pP \to X$. The Pp total cross section at high energies (here: missing masses) has two components: a decreasing one dual to direct-channel resonances and going as $M^{2\alpha(0)}$, where $\alpha(0)$ is the intercept of the effective (non-leading) Regge trajectory exchanged in the cross-channel of the sub process, and a background below the resonances, whose dual is a slowly rising term. There is some freedom in choosing the background and they are important in fixing the normalization, compatible with earlier measurements.

In this section we consider only single (SD) and double (DD) diffraction dissociation of the proton at LHC energies. Central diffractive production will be treated elsewhere. We follow the dual-Regge approach of Ref. [9], but simplify the expressions for Pp inelastic form factors (transition amplitudes) by replacing them with high-energy Pomeron-proton total cross sections, dominated by Pomeron exchange. The resulting cross sections are:

$$\frac{d^2\sigma_{el}}{dt} = A_{el}F_P^4(t)(s/s_0)^{2(\alpha(t)-1)}, \tag{3}$$

$$\frac{d^2\sigma_{SD}}{dtdM_x^2} = F_P^2(t)F(x_B,t)\frac{\sigma_T^{Pp}(t,M_x^2)}{2m_p}(s/M_x^2)^{2(\alpha(t)-1)}\ln(s,M_x^2), \tag{4}$$

$$\frac{d^3\sigma_{DD}}{dtdM_1^2dM_2^2} = C_nF^2(x_B,t)\frac{\sigma_T^{Pp}(t,M_1^2)}{2m_p}\frac{\sigma_T^{Pp}(t,M_2^2)}{2m_p} \tag{5}$$

$$\times(s/(M_1+M_2)^2)^{2(\alpha(t)-1)}\ln(s/(M_1+M_2)^2),$$

$$\sigma_T^{Pp}(M_X^2,t) = \mathrm{Im}A(M_X^2,t) = \frac{A_{N^*}}{\sum_n n-\alpha_{N^*}(M_X^2)} + Bg(t,M^2) = \tag{6}$$

$$= A_{norm}\sum_{n=0,1\ldots}\frac{[f(t)]^{2(n+1)}\,\mathrm{Im}\alpha(M_X^2)}{(2n+0.5-\mathrm{Re}\alpha(M_X^2))^2} + Bg(t,M^2),$$

where:

$$\alpha(t) = \alpha(0) + \alpha' t, \quad f(t) = e^{b_{in}t},$$

$$F_P(t) = \frac{1}{1-\frac{t}{0.71}},$$

$$F(x_B,t) = \frac{-t(1-x_B)}{4\pi\alpha_s(1+4m^2x_B^2/(-t))}, \tag{7}$$

$$Bg(t,M^2) = B_{norm}e^{b_{in}^{bg}t}(M^2-M_{p+\pi}^2)^{\epsilon}. \tag{8}$$

5. Results

Table 1: Parameters set

σ_{SD} (mb)	10.2	16.4
$\sigma_{SD}(M < 3.5GeV)$ (mb)	4.8	5.4
$\sigma_{SD}(M > 3.5GeV)$ (mb)	5.4	11.0
$\sigma_R^{SD}es$ (mb)	3.6	3.3
$\sigma_B^{SD}g$ (mb)	6.6	13.1
b_{in} (GeV^{-2})	0.2	0.2
b_{in}^{bg} (GeV^{-2})	3	3
α' (GeV^{-2})	0.25	0.25
$\alpha(0)$	1.04	1.04
ϵ	1.03	1.06
A_{norm}	27.0	25.0
B_{norm}	5.0	8.0

As the input, elastic cross section and the slope of the cone for elastioc cross section for pp scattering from TOTEM were also used:

$\sigma_{el}(7TeV) = 24.8 \pm 0.2 \pm 1.2mb$,

$B_{el}(7\mathrm{TeV}) = 20.1 \pm 0.2 \pm 0.3\ \mathrm{GeV}^{-2}$.

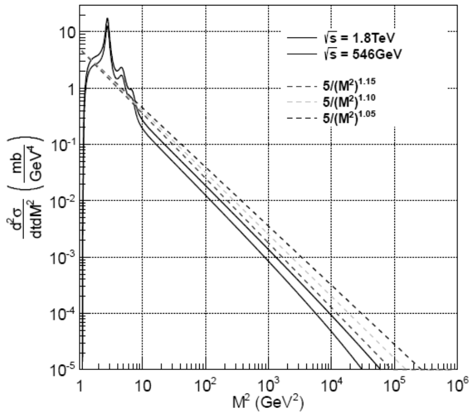

Figure 1: Double differential cross sections, $t = -0.05$. Comparison to of calculated cross section reference line (see. Fig.3,a). $\sigma_{SD} \approx 10mb$.

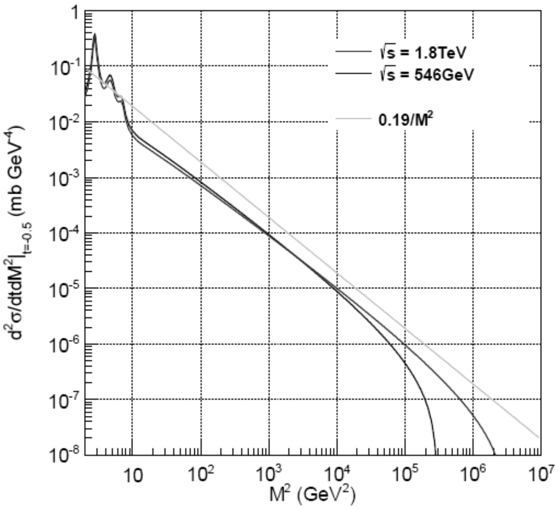

Figure 2: Double differential cross sections, $t = -0.05$. Comparison of calculated cross section to the reference line (see. Fig.3, b). Normalization: $\sigma_{SD} \approx 10mb$.

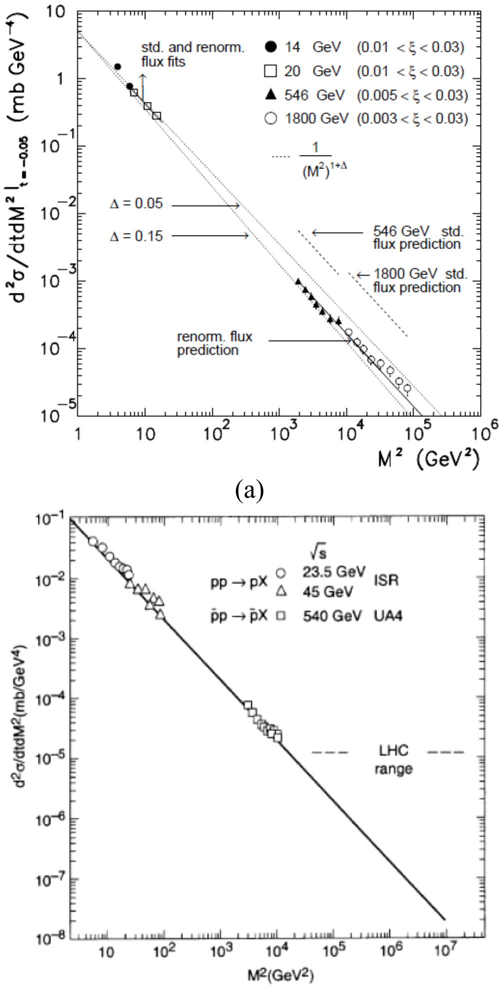

(a)

(b)

Figure 3: Reference points for $\frac{d^2\sigma_{SD}}{dtdM^2}$.

(a) For $t = -0.05$, from [7];

(b) For $t = -0.5$, form [8].

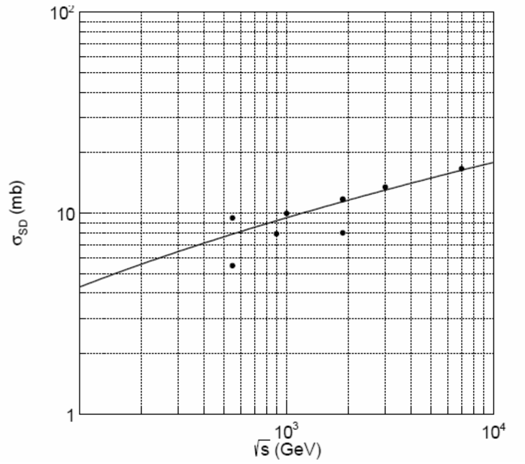

Figure 4: Single diffraction cross section vs. $\sqrt{s}$. Normalization: $\sigma_{SD} \approx 10mb$.

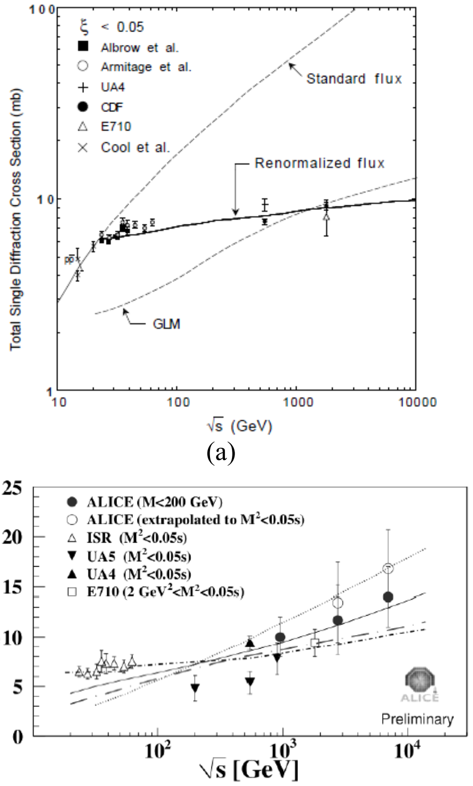

(a)

(b)

Figure 5: Single defraction cross section vs. $\sqrt{s}$.

(a) Goulianos [7];

(b) With the new preliminary points form ALICE [9].

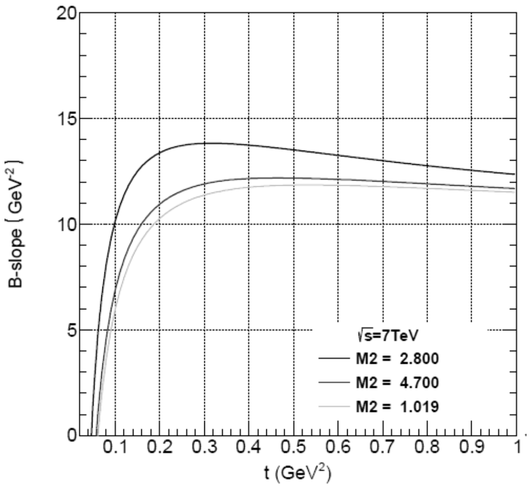

Figure 6: B-Slopes for differential SD cross section as a function of t for appropriate M^2 values. with normalization $\sigma_{SD} \approx 10mb$.

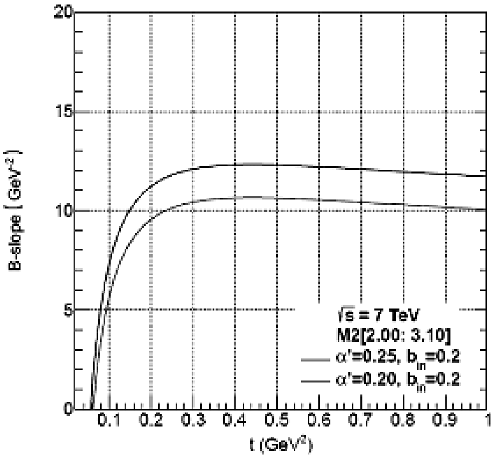

Figure 7: B-Slopes for differential SD cross cross section integrated in the region of the first resonance $M \in [2.0:3.1GeV^2]$. Normalization $\sigma_{SD} \approx 16$.

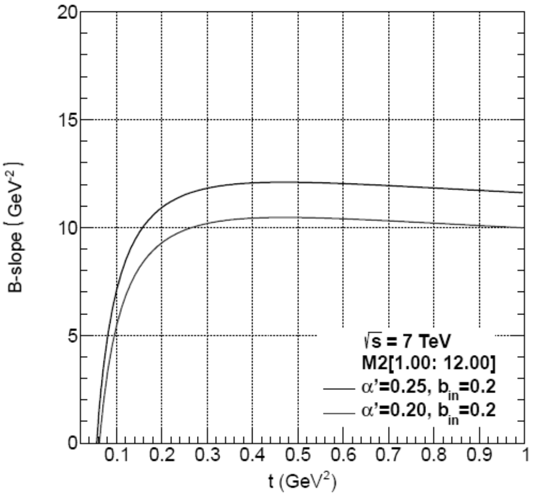

Figure 8: B-Slopes for differential SD cross section integrated in the region of the resonances $\sigma_{SD} \approx 10mb$, normalization $\sigma_{SD} \approx 10mb$.

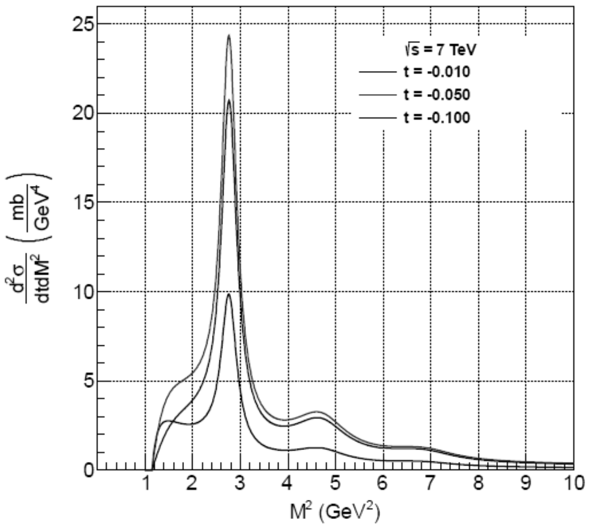

Figure 9: Double differential SD cross sections as a function of M^2 for different t values. normalization $\sigma_{SD} \approx 10mb$.

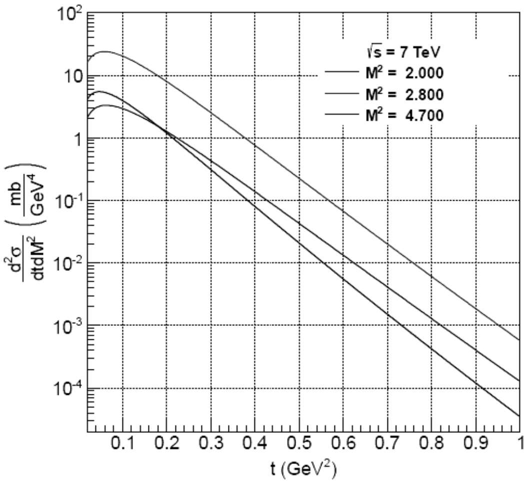

Figure 10: Double differential SD cross sections as a function of t for different M^2 values. Normalization $\sigma_{SD} \approx 10mb$.

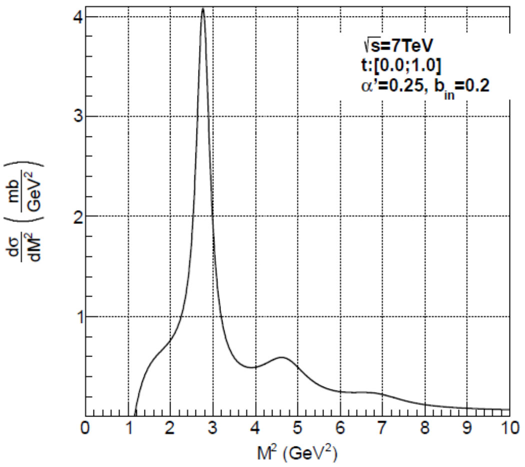

Figure 11: Single differential SD cross sections as a function of M^2 integrated over the region $t \in [0.0:1.0]$, normalization $\sigma_{SD} \approx 10mb$.

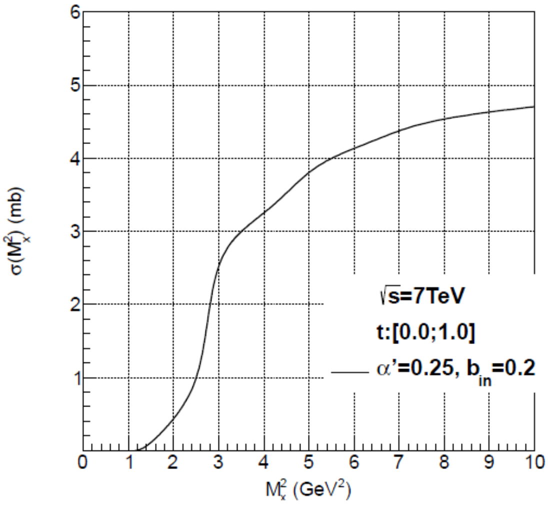

Figure 12: SD cross section as a function of upper M_x^2 bound. $\sigma_{SD}(M_x^2)=\int_1^{M_x^2}\frac{d\sigma_{SD}}{dM^2}dM^2$, $\frac{d\sigma_{SD}}{dM^2}=\int_{-1}^{0}\frac{d\sigma_{SD}}{dt}dt$ Normalization $\sigma_{SD}\approx 16$.

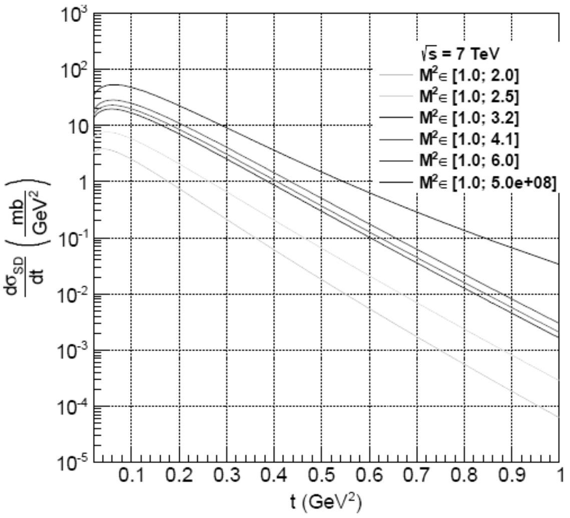

Figure 13: Single differential SD cross sections integrated in different M^2 regions as a function of t, normalization $\sigma_{SD}\approx 10mb$.

Acknowledgements. L. J. is grateful to the organizers of this Gamov conference, especially to Professors M.Ryabov and A.Zhuk for their invitation and for the pleasant and creative atmosphere during the conference.

References

1. Goulianos K.: 1983, Phys. Rep., **101**, 169.
2. Goulianos K.: *In Proc.* 13th International Conf. on Elastic and Diffractive Scattering (Blois Workshop) Moving Forward into the LHC Era, hep-ph/1002.3527, p. 6; 121.
3. Jenkovszky L., Lengyel A., Lontkovskiy D.: 2011, *Int. J. Mod. Phys. A,* **26**, **27,** 4755-4771.
4. Goulianos K., Jenkovszky L.L., Struminsky B.V.: 1991, *Yad. Fizika,* **54**, 573.
5. Roy D.P., Roberts R.G.: 1974, *Nucl. Phys. B*, **77**, 246.
6. Jenkovszky L., Martynov E., Paccanoni F.: 1996, in *Proc. of the Crimean Conference on Diffraction*.
7. Fiore R., Jenkovszky L., Magas V., Melis S., Prokudin A.: 2009, *Phys.Rev., D* **80**, 116001, arXiv:0911.2094.
8. Donnachie S., Dosch G., Landshoff P., Nachtmann O.: 2002, *Pomeron physics and QCD*, *Cambridge University Press*.
9. Jenkovszky L., Kuprash O., Lamsä J., Magas V., Orava R.: 2011, *Phys.Rev.,* **D83**, 056014, arXiv:hep/ph/1011.0664.
10. Jaroszewicz G.A., Landshoff P.V.: 1974, *Phys. Rev.*, **10**, 170.
11. Antchev G. et.al.: 2011, CERN-PH-EP-2011-158, hep-exp/1110.1395.
12. Fiore R., Jenkovszky L., Magas V., Paccanoni F., Papa A.: EPJ A10 (2001); 217-221, hep-ph/0011035 (2000).
13. Poghosyan M.G.: 2011, arXiv:1109.4510 [hep-ex].
14. Goulianos K.: 2001, *Nucl.Phys.Proc.Suppl.*, **99A**, 9, arXiv:hep-ex/0011060v1.
15. Bozzo A. et.al.: 1984, *Phys. Letters,* **B136**, 217.
16. Matthiae G.: 2000, *Brazilian Journal of Physics 30*, **30**, scielo, 244.

GEOMAGNETIC FIELD OF UKRAINE: ESTIMATION OF INTERNAL AND EXTERNAL SOURCES CONTRIBUTION

M.I.Orliuk, A.A.Romenets, T.P.Sumaruk, Yu.P.Sumaruk
Bnstitute of Geophysics S.I.SubbotBn of the UkraBnian NAS, Kiev
orlyuk@igph.kiev.ua

ABSTRACT. This article is considering some aspects of differentiation between internal and external sources of the Earth's magnetic field; it estimates also the contribution of different sources into total field as well as its variations. The surveys results of ukrainian magnetic observatories were used to fulfil the task.

1. Introduction

Geomagnetic field of the Ukraine is the unique one compairing with the fields of Central and Western Europe countries. It is concerned the presence of high-intensive regional and local anomalies and important temporal variations of the field too.

As it is known the Earth's magnetic field is a fields total of numerous internal and external sources. It is important to estimate the contribution of one or another sources into total Earth's magnetic field to single out its component per se as a means of studying its nature, origination mechanism and so on. Specifically, to study the processes that are having place into the Earth's liquid core it is necessary to separate only the part of the field that is connected exactly with this object; to study lithspheric magnetization it is required to exclude the effects of the core field, of ionospheric and magnetospheric sources that is to subtract it from the measured field values. But the problem is that different sources anomalies are frequently overlapping by waves and intensity wide-ranging. Thus the magnetic field anomalies having thousands kilometres wavelengths may be connected with the Earth's core as well as with its lithosphere (even partially). Naturally it is more difficult to make out the nature of sources of the Earth's magnetic field variations: long-period as well as short-period ones. The variations of internal and external nature are often interdependent and mutually causal. Those are for instance geomagnetic variations induced into Earth's crust. It occurs due to the core field variation as well as due to ionospheric and magnetospheric field sources (Verbanac et al., 2007; Thebault et al., 2009; Orliuk et al., 2011). That is why in this article some aspects of differentiation between internal and external sources of the Earth's magnetic field are analysed; estimation of the contribution of different sources into total field as well as its variations are presented. The surveys results of ukrainian magnetic observatories were used uppermost to fulfill the task.

2. Magnetic field of the Earth

Space-temporal structure of the Earth's magnetic field B is defined by total of different sources fields:

$$B = Bn + Ba + B\text{в}$$

where Bn is normal (main) Earth's; Ba is anomal magnetic field (lithospheric field); $B\text{в}$ is external field. In whole for the planet magnetic field B is considerably changing above ground and in its near space (Orliuk & Romenets, 2011).

Data about magnetic field on the territory of the Ukraine are obtained as a result of different-scale mapping of magnetic field induction module or its vertical component. In conformity with created map, magnetic field induction module B on the territory of the Ukraine is varying from 48000 nTs to 57000 nTs (Fig. 1).

Measurements of magnetic induction B full vector, its northern component Bx, eastern one By and vertical one Bz are carrying out by geomagnetic observatories (GO). On the territory of the Ukraine there are three Gos: "Kyiv", "Lviv" and "Odesa" that are equipped by up-to-date instrumentation for precise measurement (see Fig. 1).

Total values of magnetic field components of internal and external sources are registered during observations surveys. According to surveys and calculations results the increment of full vector of magnetic field induction over the period of 1958-2008 is 1223 nT for GO "Kyiv", 1144 nT for GO "Odesa", 1323 nT for GO "Lviv". Average annual increment makes correspondingly 24.5 nT, 23.3 nT и 26.5 nT (Orliuk et al., 2011). On this background the anomalies of geomagnetic field increment are observed. They are represented in the figure 2.

Internal Earth's magnetic field is composed of main and anomal magnetic fields. Main geomagnetic field (core field) consists from dipole and non-dipole parts and is taking as a normal geomagnetic field of the Earth pertinence B_{IGRF}. As a rule it is seen as spheric harmonic series having certain quantity harmonics, usually 10-13 (Purucker, 2011). At this field an anomaly magnetic field is imposed that is conditioned by magnetic sources into Earth's crust as well as induced magnetic field that is due to the conductivity and permanent of lithospheres rocks. Normal field value B_{IGRF} was calculated by the model *IGRF 1945-2015 Model Coefficients 2015* (http://omniweb.gsfc.nasa).

After the observations results and its interpretation is defined that the most important changes take place into main (normal) magnetic field, the increment of it for the territory of the Ukraine makes about 1200 nT during last 50 years.

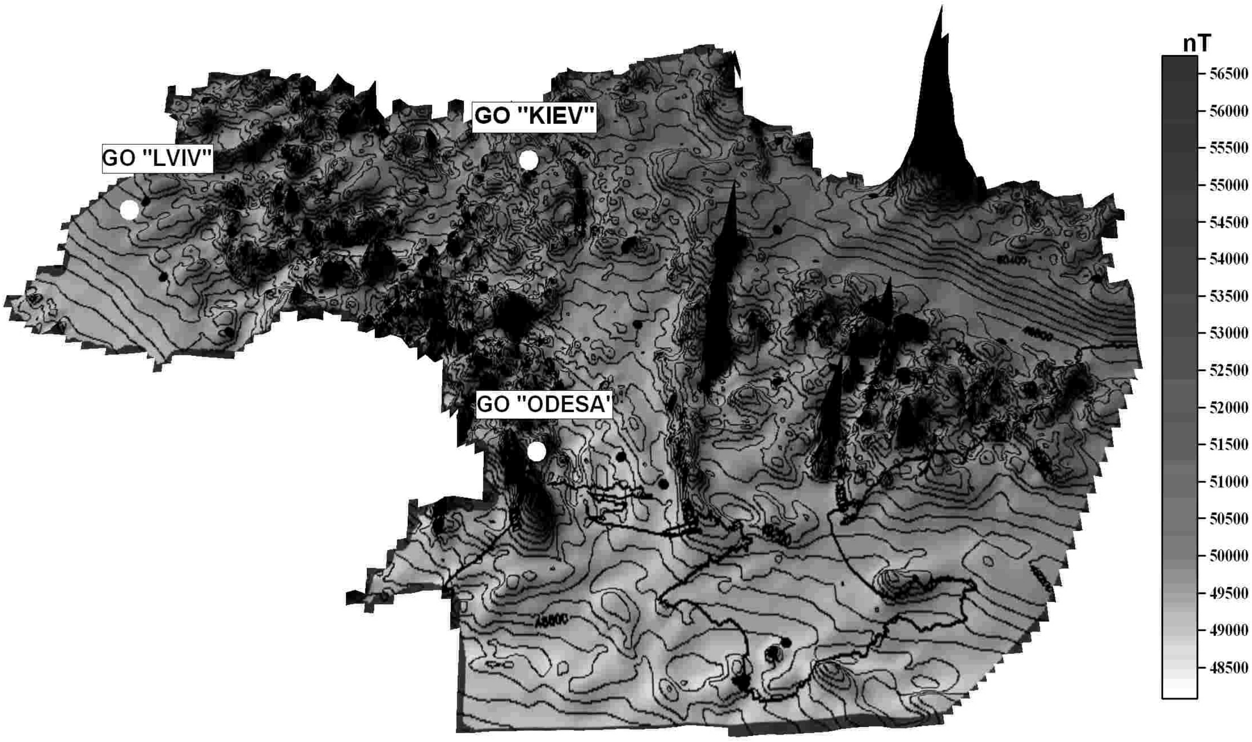

Figure 1: 3D surface of the geomagnetic field *B* on the territory of Ukraine (Orliuk, Romenets, 2002) and location of magnetic observatories

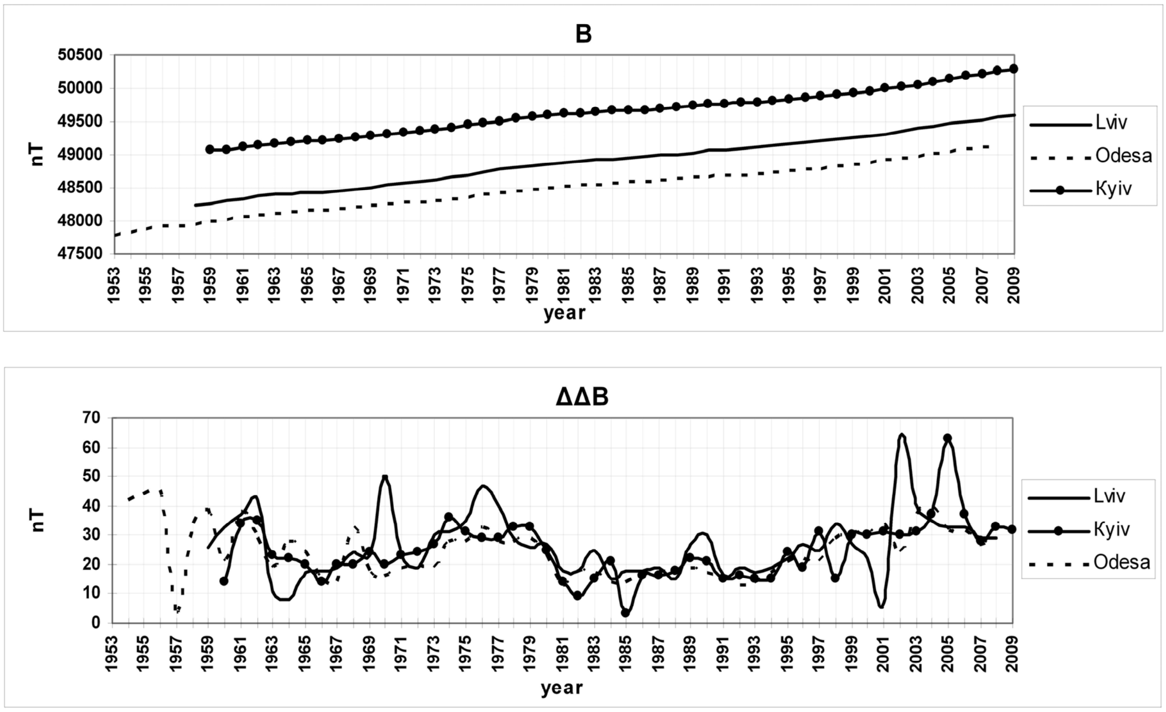

Figure 2: Variation of full vector of magnetic field *B* intensity and its average annual increment by the data of Ukrainian geomagnetic observatories

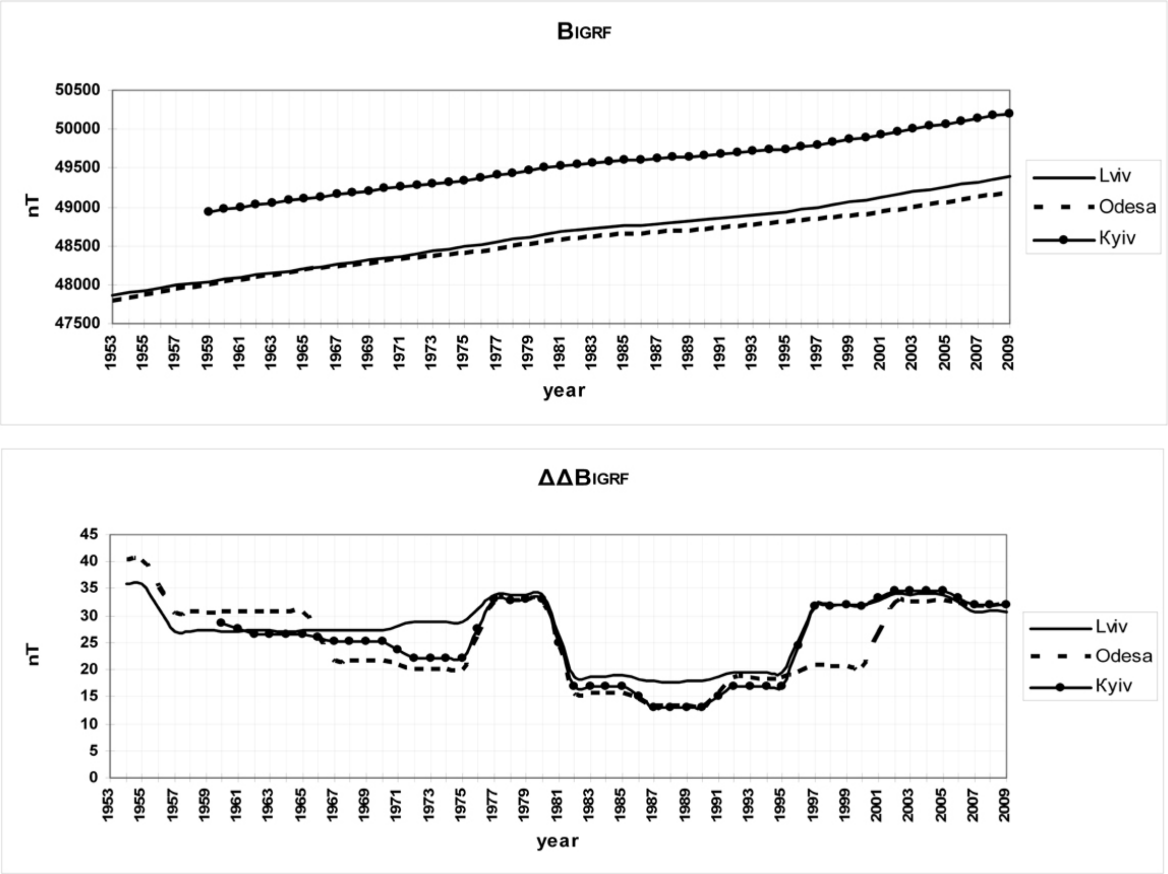

Figure 3: Variation of normal component B_{IGRF} and its average annual increment by the data of Ukrainian geomagnetic observatories

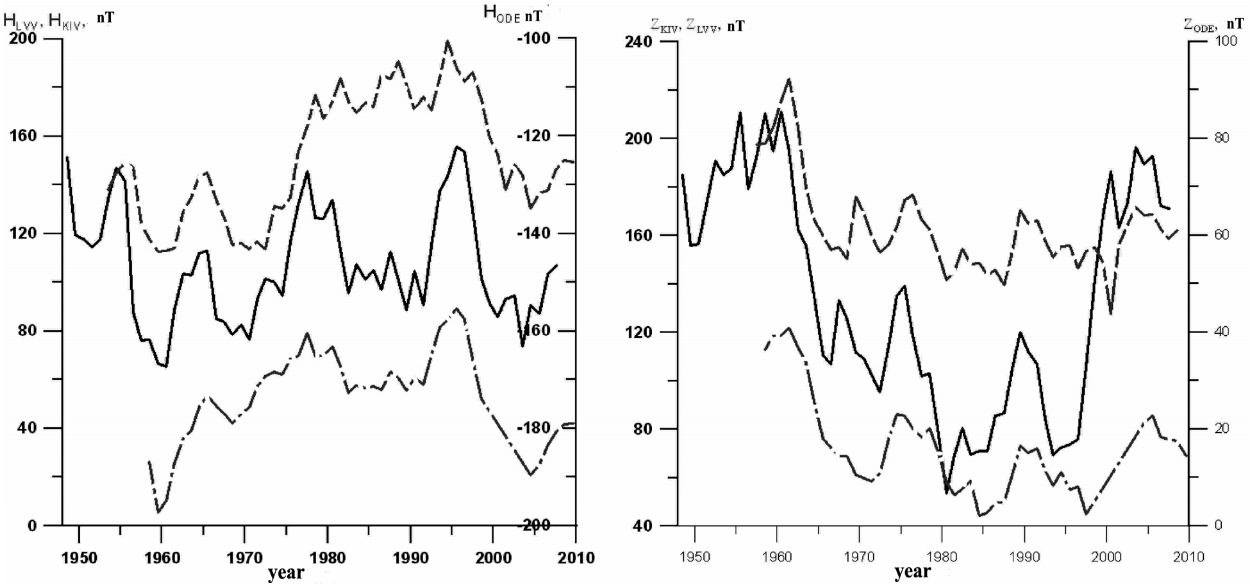

Figure 4: Average annual values B-B_{IGRF} of horizontal (a) and vertical (b) components of alternating field vector for geomagnetic observatories "Kyiv" (point – dotted curve), "Lviv" (dotted curve) and "Odesa" (black curve)

Specifically comparing the module *Bn* value for different parts of the Ukraine we can see that at 1950 south-western and southern parts are characterized by 47000 nT module *Bn* value, north-eastern and northern parts – by 49800 nT module *Bn* value, whereas at 2000, correspondingly, by 48200 nT and 50500 nT module *Bn* values (Orliuk, Romenets, 2002). According to the data of GO "Kyiv" the increment of normal *Bn* component during 1958-2008 is 1256 nT, for GO "Odesa" it makes 1186 nT, for GO "Lviv" – 1343 nT. So average annual increment *Bn* is characterized correspondingly by the following values: GO "Kyiv" – 25.1 nT/year, GO "Odesa" – 23.8 nT/year, GO "Lviv" – 26.8 nT/year (Fig. 3).

Let us examine long-term changing's of secular variations (*SV*) field. *SV*-value is defined as difference between consecutive average annual values of three orthogonal components and absolute intensity of geomagnetic field that are fixed continuously by magnetic observatories. Calculations admit to exclude automatically those field variations that have less than one year periods, that are generated by external sources and that are alternating-sign ones. However the variations of geomagnetic field generated by ring magnetospheric current that are reflecting at horizontal *Bn* field component and vertical *Bz* one are always of the same sign. Therefore in magnetically active years *Bn* component is always smaller and *Bz*-component is always greater, than in quiet years. Solar-diurnal *Bs*-variation (*Sq*) has the same effect. Under the influence of external sources the secular variations *SV* obtained by average annual values will include the components related to solar and, correspondingly, magnetic activity (Verbanac et al., 2007). It is extremely actual task to define each source components of the field. To distinguish the variations depending on external and internal sources we have to subtract main part of a field that is formed by the currents at core-mantle discontinuity from average annual field value measured in the observatory. External sources contribution for all observatories have been evaluated by difference of average annual value for all days and by quiet days ($B - B_{Sq}$).

3. External geomagnetic field

At present vast data array (ground as well as aerocosmic ones) about space and temporal alterations of geomagnetic field are accumulated however the identification procedure of geomagnetic variations at midlatitudes from different sources is not worked out. In connection with large-scale researches of terrestrial space it become evident that main external sources of geomagnetic variations are located in high-latitude ionosphere and distant magnetosphere. Irregular variations are caused by magnetospheric currents and currents of high-latitude ionospheric currents that are appearing in the Earth's field in the form of magnetic storms (Akasofi, Chapman, 1975). Regular variations are originating by solar and cosmic radiation and are revealing as a quiet solar-diurnal variation (Yanovsky, 1978).

External sources contribution for all the observatories is evaluated by means of difference between average annual induction value *B* during all the days and in quiet ones ($B - B_{Sq}$). Fig. 4 (a, b) shows average annual B-B_{IGRF} value of horizontal (B_H) and vertical (B_Z) component of geomagnetic field full vector. As it is seen by Fig 4 (a) average annual value of *Bn* component at GO "Lviv", "Kyiv" and "Odesa" is changing in in-phase way. Ranges of variations at GO "Lviv" are from 112.6 nTs to 199.3 nTs, at "Kyiv" – from 5.7 nTs to 89.3 nTs, at "Odesa" from -122.2 to 167.4 nTs. Average annual values of B_Z – component (Fig. 4 (b) at GO "Lviv" (dotted curve), "Kyiv" (point-dotted curve), "Odesa" (black curve) are changing in in-phase way. Ranges of variations at GO "Lviv" are from 140.6 nTs to 224.6 nTs, at "Kyiv" – from 44.9 nTs to 121.6 nTs, at "Odesa" from 6.8 nTs to 85.5 nTs.

Numerous researches were devoted to the problem of external sources of geomagnetic disturbances. Specifically geomagnetic field variation induced by magnetospheric and ionospheric sources in the midlatitudes may be represented as

$$\Delta = DR + DT + DCF + DP + Sq \qquad (1)$$

where *DR* is the variation of ring magnetospheric current (includes and partial ring current);

DT is the variation of currents at magnetosphere tail;

DCF is the variation of currents at magnetopause;

DP is the variation of ionospheric currents in auroral zone and reverse currents spreading in midlatitudes;

Sq is quiet solar-diurnal variation.

To identify the variation sources during magnetic storms it is necessary to choose a reference (zero) level of geomagnetic variations values and its alterations depending on season and solar activity. As usually solar-diurnal variation (*Sq*) serves a reference level for irregular variations. However it is known well (Sumaruk & Sumaruk, 2004), that this variation amplitude is changing under season change and alteration of solar activity cycle phase as well as of latitude one.

Ionospheric current systems are the source of *Sq*-variations (Space Geophysics, 1976). Its intensity is depending generally on electromagnetic radiation of the sun in visible light, ultraviolet and X-ray ranges. Ionosphere lighting is changing after seasons and is negligible depending on alteration of solar activity cycle phase. Intensity of ultraviolet and X-ray radiation of the sun is depending on alteration of solar activity and is not depending on season. *Sq*-variation is intimately connected with equatorial electrojet (Yaremenko, 1970).

As it is shown in the work (Sumaruk, Sumaruk, 2005), solar-diurnal variation in midlaltitudes has two components: constant one for given month, that is not depending on solar activity and variable one, its value is depending on solar activity. Constant for given month component Sq^{i} is not changing during solar activity cycle but its amplitude is varying for each month. The most probable is that Sq^{i} is generated by ionospheric dynamo currents whose intensity is proportional to ionospheric conductivity linked up with electromagnet sun radiation.

Value of alternating component Sq^{m} is depending in straight lines on the sun activity expressed by Wolf numbers (*W*). Sq^{m} is generated by magnetospheric currents whose intensity is changing with changing of solar wind parameters and "trapped" in it interplanet magnetic field.

Amplitudes of *Sq*-variations of ukrainian observatories are given in the Table 1.

Table 1: Changes of *Sq*-variations diurnal amplitudes.

Solar activity	Winter		
	Sq(H), nT	*Sq*(D), min	*Sq*(Z), nT
Low	7-13	1,7-3,1	4-15
High	27-50	6,5-13,6	5-18
	Summer		
Low	20-32	6,4-11,5	5-14
High	37-62	12,7-18,5	12-36

Magnetospheric sources *DR, DT, DCF* variations reflect well *Dst*-index of magnetic activity. It is obtained from the data of four low-latitude geomagnetic observatories. Index is regularly calculated and published in *IAGA* bulletins as well as is exposed at the sites of international data centers specifically in Kioto (Japan, *http://swdccdb.kugi.kyoto-u.ac.jp*).

In midlatitudes the value of Δ_m magnetospheric sources can be in a first approximation calculated by formula

$$\Delta_m = D_{st}\cdot\cos\Phi$$

where Φ is geomagnetic latitude of the observatory. As the geomagnetic latitudes difference of ukrainian observatories is changing in the range of 4^0 so Δ_m will change in the range of 0.003 that not exceed the calculation error.

Value of *DCF* variation from currents during magnetopause is determined by model calculations. Paraboloid A2000 magnetospheric model (Alexeev et al., 1996), T02 magnetospheric model of Tsyganenko (Tsyganenko, 2002; Maksimenko et al., 2006), magnetospheric model of Mead (Mead & Beard, 1964) are used frequently with it. *DCF*-variation value calculated by different models is balanced/ proportional in size. For instance, variation corrections caused by magnetopause currents that were calculated by Mead model (Sumaruk & Sumaruk, 2006), in quiet days (*DCF*) have +14 nTs value of horizontal component and -13 nTs of vertical component for midlatitude observatory. Error for *DCF*-variation of magnetic declination in quiet periods is reaching ±0.05^0 and is changing after phase with *Sq*-variation change. As it is shown (Feldstein, 1973), during magnetically quiet days *DCF*- variations are compensated by *DT*-variations.

Variation from ionospheric currents in auroral zone and its reverse currents in midlatitudes are described by means of auroral activity indexes *AE, AU, AL.* As it is known (Space Geophysics, 1976), when large-scale magnetic storms (*Dst* > –150 nTs) take place the focuses of auroral ionospheric currents are shifting towards midlatitudes. During initial phase of magnetic storm midlatitude observatories are influenced directly by reverse ionospheric currents. *Dst* increase is conditioning direct influence of eastern (*AU*) or western (*AL*) electrojets on the observatories (Sumaruk & Sumaruk, 1994) depending on local time. *AE*-indexes are calcilated by the data of magnetic observatories train of auroral belt. When magnetic activity is high *AE*-indexes are underestimated and to calculate it we need to use suauroral observatories data (Sumaruk & Sumaruk, 2006).

Value of irregular variations of geomagnetic field can be defined as

$$H - Sq$$

where *H* is the value of geomagnetic field horizontal component (Sumaruk & Sumaruk, 2006). *Sq*-variation is calculated by five internationaly quiet days. Horizontal component is reflecting best the variations caused by external sources. Proposed difference minimizes the influence of internal sources of geomagnetic field.

Based on above-stated the identification of geomagnetic variations external sources after ukrainian observatories data is proposed. As it is shown in the research (Sumaruk & Sumaruk, 2006), about eighty percents of irregular variations of magnetic field on the territory of the Ukraine during magnetic storms are generated by magnetospheric sources and only one fifth of them has ionospheric nature. Results obtained for 11 maximal storms of 21-22 solar activity cycles agree well with the results of other researchers (Maksimenko et al., 2006; Yaremenko, Melnyk, 2005) and are represented in the Table 2.

Table 2: Ratio of variation value from magnetospheric and ionospheric currents.

№	*Dst*, nT	*DR+DT*,%	*DCF*,%	*DP*,%
1	249	62	17	21
2	220	71	17	12
3	291	74	14	12
4	219	72	11	17
5	338	65	19	16
6	303	66	20	14
7	169	55	18	27
8	559	66	18	16
9	298	62	20	18
10	198	55	23	22
11	297	62	22	16
average		65	18	17

Results discussion and summary

Fulfilled investigations of space-temporal structure of geomagnetic field of the Ukrainian territory are significant to work out some problems of magnetology and ecology. Magnetic field of the Ukraine is in a manner unique as compared with the fields of another countries of the Europe in terms of regional and local anomalies occurrence of high intensity as well as of its important changes with time.

The dynamics of magnetic field are calculated as well as internal and external sources contribution in field variations is evaluated with use of data obtained by ukrainian observatories during last fifty years.

First of all let us to underline important changes of magnetic field for the Ukraine in whole. Specifically the increment of full vector value of magnetic field induction during 1958 – 2008 years is 1223 nTs for GO “Kyiv”, 1144 nTs for GO “Odesa”, 1323 nTs for GO “Lviv”. Dominant part of this increment (B_n=1200 nTs during 50 years) is caused by increasing of main Earth’s magnetic field.

High-frequency geomagnetic variations of external field with periods of day or less caused by magnetospheric or ionospheric currents are not changing so signaficantly compairing with long-period variations of internal nature. External field variations are changing in the range of nTs first tens and only under very important magnetic storms its intensity can reach some hundreds nTs.

The variations from magnetospheric and ionospheric sources have been calculated by models. They were compared with observed field changes on the Earth surface subject to variable reference level. It shown that during magnetic distorbances about 80% of field variations in midlatitudes are generated by magnetospheric sources and 20% – by ionospheric ones.

On the whole summarizing the above it is possible to state a fact that the Earth’s magnetic field on the territory of the Ukraine is changing considerably in space as well as in time. The contribution of internal sources is important for long-period variations and of external ones – for short-period variations.

References

Akasofi S.-I., Chapman S. *Solar-Earth’s physics*, *p. II*: 1975, M.: Mir, 512 p.

Alexeev I.I., Belenkaya E.S., Kalegaev V.V., Feldstein Ya.I., Grafe A.: 1996, *J. Geophys. Res*., **101**, 7737.

Feldstein Ya.I.: 1973, Herald of the AS of the USSR, **8**, 532.

http://omniweb.gsfc.nasa.gov/vitmo/igrf_vitmo.html

Hulot G., Balogh A., Christensen U., Constable G., Mandea M., Olsen N.: 2010, *Space. Sci. rev.*, **155**, 1.

Maksimenko O.I., Yaremenko L.N., Shenderovskaya O.Ya., Melnik G.V., Mozgovaya T.A.: 2006, *Space science and technology*, **12**, №1, 64.

Mead G.D., Beard D.B.: 1964, *J.Geophys. Res.,* **69**, 1169.

Orliuk M.I., Romenets A.O., Sumaruk T.P.: 2011, *X^{th} International Conference on Geoinphormatics – Theoretical and Applied Aspects*, 10-13 May 2011, Kiev, Ukraine. Paper 086. Conference CD-ROM Proceedings, p4.

Orliuk M.I., Romenets A.O., Sumaruk Yu.P., Sumaruk T.P.: 2011, *5th MagNetE Workshop on European geomagnetic repeat station survey 2009-2010,* Rome 9-11 May 2011, p16.

Orliuk M.I., Romenets A.A.: 2005, *Geophys. J.*, **27**, №6, 1012.

Orliuk M.I., Romenets A.A.: 2011, Odessa Astron. Publications, 24, 124.

Orliuk M.I., Romenets A.O.: 2002, *Herald of Kyiv National University. Geology*, **23-24**, 88.

Purucker M.:2011, *Planetary magnetic fields of the solar system// http://planetary-mag.net/index.html/*

Space Geophysics: 1976, M.: Mir, 544p.

Sumaruk P.V., Sumaruk T.P.: 2006, *Space science and technology*, **12**, №1, 76.

Sumaruk P.V., Sumaruk Yu.P.: 1994, *Geophys. J.*, **16**, №4, 51.

Sumaruk T.P., Sumaruk Yu.P.: 2004, *Geophys. J.*, **26**, №6, 139.

Sumaruk T.P., Sumaruk Yu.P.: 2005, *Geophys. J.*, **27**, №2, 299.

Thébault E., Hemant K., Hulot G., Olsen N.: 2009, *Geophys. Res. Lett.*, **36**, L01307, doi:10.1029/2008GL036416.

Tsyganenko N.A.: 2002, *J. Geophys. Res*., **107**, 10.1029/ 2001 JA000219.

Verbanac G., Luhr H., Rother M., Korte M., Mandea M.: 2007, *Earth Planets Space*, **59**, 251.

Yanovsky B.M. *Earth’s magnetism.* L.: Publ. LSU. – 1978. – 591p.

Yaremenko L.N. *Equatorial electrojet current*. – Kiev: Naukova Dumka, 1970. – 116 p.

Yaremenko L.N. Melnyk G.V.: 2005, *Geophys. J.* , **27**, №5, 874.

SPIN IDENTIFICATION OF RANDALL-SUNDRUM GRAVITON IN PROTON-PROTON COLLISIONS AT LHC WITH 8 TEV AND 14 TEV

A.Pankov [1,a], V.Bednyakov [2,b], A.Tsytrinov [1,c]

[1] Abdus Salam ICTP Affiliated Centre & Gomel State Technical University,
Gomel, Belarus
[2] Laboratory of Nuclear Problems, Joint Institute for Nuclear Research,
Dubna, Moscow oblast, Russia
[a] pankov@ictp.it, [b] vadim.bednyakov@cern.ch, [c] tsytrin@rambler.ru

ABSTRACT. New physics models, widely discussed in the literature, predict the existence of new heavy resonances with mass above 1 TeV that can possibly be observed at the Large Hadron Collider (LHC). These resonances, predicted by different nonstandard models can generate peaks with the same mass and same number of events under the peak. In this case, spin determination of a peak becomes crucial in order to identify the relevant new physics scenario. Here we discuss a possibility for spin identification of spin-2 Randall-Sundrum graviton excitations against spin-1 heavy neutral gauge bosons Z' and scalar heavy bosons in Drell-Yan dilepton and diphoton events at the LHC at $\sqrt{s} = 8$ TeV and 14 TeV by using a center-edge asymmetry.

Key words: Randall-Sundrum graviton, center-edge asymmetry, LHC.

1. Introduction

The existence of new heavy bosons predicted by many models beyond the standard model, with mass scales $M \gg M_{W,Z}$. They can be signalled by the observation of (narrow) peaks in the cross sections for reactions among standard model particles at the LHC. However, the observation of a peak/resonance at some large mass $M = M_R$ may not be sufficient to identify its underlying nonstandard model, in the multitude of potential sources of such a signal. Indeed, in 'confusion regions' of the parameters, different models can give the same M_R and same number of events under the peak. In that case, the test of the peak/resonance quantum numbers, the spin first, is needed to discriminate the models against each other in the confusion regions. Specifically, one defines for the individual nonstandard scenarios a *discovery reach* as the maximum value of M_R for peak observation over the standard model (SM) background, and an *identification reach* as the maximum value of M_R for which the model can be unambiguously discriminated from the other competing ones as the source of the peak. Particularly clean signals of heavy neutral resonances are expected in the inclusive reactions at the LHC:

$$p + p \to l^+ l^- + X \quad (l = e, \mu), \quad p + p \to \gamma\gamma + X, \quad (1)$$

where they can show up as peaks in the dilepton and diphoton invariant mass M. While the total resonant cross section determines the number of events, hence the discovery reaches on the considered models, the angular analysis of the events allows to discriminate the spin-hypotheses from each other, due to the (very) different characteristic angular distributions. In the next sections we discuss the identification of the spin-2 against spin-1 and spin-0 hypotheses (and spin-0 only for diphoton case), modeled by the Randall-Sundrum model with one warped extra dimension [1], a set of Z' models [2], and the R-parity violating sneutrino exchange [3] (spin-0 scalar [4] for diphoton final states), respectively.

2. Cross sections and center-edge asymmetry

The total cross section for a heavy resonance discovery in the events (1) at an invariant dilepton (or diphoton) mass $M = M_R$ (with $R = G, Z', \tilde{\nu}$ denoting graviton, Z' and sneutrino, respectively) is:

$$\sigma(pp \to R) \cdot \mathrm{BR}(R \to l^+ l^-) = \\ = \int_{-z_{\mathrm{cut}}}^{z_{\mathrm{cut}}} \mathrm{d}z \int_{M_R - \Delta M/2}^{M_R + \Delta M/2} \mathrm{d}M \int_{y_{\mathrm{min}}}^{y_{\mathrm{max}}} \mathrm{d}y \frac{\mathrm{d}\sigma}{\mathrm{d}M\,\mathrm{d}y\,\mathrm{d}z}. \quad (2)$$

Resonance spin-diagnosis makes use of the comparison between the different differential angular distributions:

$$\frac{\mathrm{d}\sigma}{\mathrm{d}z}=\int_{M_R-\Delta M/2}^{M_R+\Delta M/2}\mathrm{d}M\int_{y_{\min}}^{y_{\max}}\frac{\mathrm{d}\sigma}{\mathrm{d}M\,\mathrm{d}y\,\mathrm{d}z}\mathrm{d}y. \qquad (3)$$

In Eqs. (2) and (3), $z=\cos\theta_{\mathrm{cm}}$ and y are the lepton-quark (or photon-quark) angle in the dilepton (or diphoton) center-of-mass and the dilepton rapidity, respectively, and cuts on phase space due to detector acceptance are indicated. For integration over the full phase space, the limits would be $z_{\mathrm{cut}}=1$ and $y_{\max}=-y_{\min}=\log(\sqrt{s}/M)$ with $\sqrt{s}$ the LHC collider center-of-mass energy. Furthermore, ΔM is an invariant mass bin around M_R, reflecting the detector energy resolution [5]. To evaluate the number N_S of resonant signal events time-integrated luminosities of 100 fb^{-1} for 14 TeV LHC (the ultimate expectations) and 20 fb^{-1} for 8 TeV LHC (expected to be archived before long shutdown) will be assumed, and reconstruction efficiencies of 90% for both electrons and muons and 80% for photons). Typical experimental cuts are: $p_\perp>20$ GeV and pseudorapidity $|\eta|<2.5$ for both leptons; $p_\perp>40$ GeV and $|\eta|<2.4$ for photons. Finally, with N_B the number of 'background' events in the ΔM bin, determined by the SM predictions, the criterion $N_S=5\sqrt{N_B}$ or 10 events, whichever is larger, will be adopted as the minimum signal for the peak discovery. To evaluate Eqs. (2) and (3) the parton subprocesses cross sections will be convoluted with the CTEQ6.6 parton distributions of Ref. [6]. Next-to-leading QCD effects for dilepton case can be accounted for by K-factors, and for simplicity of the presentation we here adopt a flat value $K=1.3$. For diphoton case the full NLO calculations were done [7]. In practice, due to the completely symmetric pp initial state, the event-by-event determination of the sign of z may at the LHC be not fully unambiguous. This difficulty may be avoided by using as the basic observable for angular analysis the z-evenly integrated center-edge angular asymmetry, defined as [8,9]:

$$A_{\mathrm{CE}}=\frac{\sigma_{\mathrm{CE}}}{\sigma};\ \sigma_{\mathrm{CE}}\equiv\left[\int_{-z^*}^{z^*}-\left(\int_{-z_{\mathrm{cut}}}^{-z^*}+\int_{z^*}^{z_{\mathrm{cut}}}\right)\right]\frac{\mathrm{d}\sigma}{\mathrm{d}z}\mathrm{d}z. \qquad (4)$$

In Eq. (4), $0<z^*<z_{\mathrm{cut}}$ defines the separation between the 'center' and the 'edge' angular regions and is *a priori* arbitrary, but the numerical analysis shows that it can be 'optimized' to $z^*\simeq 0.5$. The additional advantage of using A_{CE} is that, being a ratio of integrated cross sections, it should be much less sensitive to systematic uncertainties than 'absolute' distributions (examples are the K-factor uncertainties from different possible sets of parton distributions and from the choice of factorization vs renormalization mass scales).

3. New physics models

RS model with one compactified extra dimension. Originally, this model was proposed to solve the so-called gauge hierarchy problem, $M_{\mathrm{EW}}\ll M_{\mathrm{Pl}}\simeq 10^{16}$ TeV. The simplest set-up, called RS, consists of one warped extra spatial dimension, y, two three-dimensional branes placed at a compactification relative distance $y_c=\pi R_c$, and the specific 5-D metric [1]

$$ds^2=\exp(-2k|y|)\eta_{\mu\nu}dx^\mu dx^\nu-dy^2. \qquad (5)$$

In (5), $\eta_{\mu\nu}$ is the usual Minkowski tensor and $k>0$ is the 5-D curvature. SM fields are localized to the so-called TeV brane, and gravity can propagate in the full 5-D 'bulk', included the other, so-called Planck, brane. On this brane, the effective 4-D mass scale is related to the Newton constant by the relation $\overline{M}_{\mathrm{Pl}}=1/\sqrt{8\pi G_{\mathrm{N}}}=2.44\times 10^{15}$ TeV. Denoting by M_* the 5-D effective mass scale, analogously related to the cubic root of the 5-D Newton constant, the relation can be derived: $\overline{M}_{\mathrm{Pl}}^2=(M_*^3/k)(1-\exp(-2k\pi R_c))$. Under the basic 'naturalness' assumption $\overline{M}_{\mathrm{Pl}}\sim M_*\sim k$, needed to avoid further fine tunings, for $kR_c\sim 11$ the geometry of Eq. (5) implies that the mass spectrum on the Planck brane, of the 10^{15} TeV order, can on the TeV brane where SM particles live and interact, be exponentially 'warped' down to the effective scale $\Lambda_\pi=\overline{M}_{\mathrm{Pl}}\exp(-k\pi R_c)$ of the one (or few) TeV order. Interestingly, this brings gravitational effects into the reach of LHC. Junction conditions on the graviton field at the branes y-positions imply the existence of a tower of spin-2 graviton excitations, $h_{\mu\nu}^{(n)}$, with a specifically spaced mass spectrum $M_n=x_nk\exp(-k\pi R_c)$ in the TeV range (x_n are the roots of $J_1(x_n)=0$). Denoting by $T^{\mu\nu}$ the SM energy-momentum tensor, and by $h_{\mu\nu}^{(0)}$ the zero-mode, ordinary, graviton, the couplings of graviton excitations to the SM particles are only $(1/\Lambda_\pi)$ suppressed (not $1/\overline{M}_{\mathrm{Pl}}$):

$$L_{\mathrm{TeV}}=-\left[\frac{1}{\overline{M}_{\mathrm{Pl}}}h_{\mu\nu}^{(0)}(x)+\frac{1}{\Lambda_\pi}\sum_{n=1}^{\infty}h_{\mu\nu}^{(n)}(x)\right]T^{\mu\nu}(x). \qquad (6)$$

The RS model can be conveniently parameterized by the mass of the lowest graviton excitation $M_G\equiv M_1$, the only one presumably in the reach of LHC, and the 'universal', dimensionless, coupling constant $c=k/\overline{M}_{\mathrm{Pl}}$. The scale Λ_π and the (narrow) widths $\Gamma_n=\rho M_n x_n^2 c^2$ (with $\rho\simeq 0.1$), are then derived quantities. Theoretically 'natural' ranges expected for these parameters are $0.01\le c\le 0.1$ and $\Lambda_\pi<10$ TeV. Current 95% limits from ATLAS and CMS experiments are, at the 7 TeV, 5 fb^{-1} LHC [10,11]: $M_G>910$ GeV ($c=0.01$) up to $M_G>2160$ GeV ($c=0.1$).

Heavy neutral gauge bosons. The spin-1 hypothesis is in process (1) realised by $q\bar{q}$ annihilation into lepton pairs through Z' intermediate states [2]. Such bosons are generally predicted by electroweak models beyond the SM, based on extended gauge symmetries. Generally, Z' models depend on $M_{Z'}$ and on the left- and right-handed couplings to SM fermions. Further results will be given for a popular class of models for which the values of these couplings are fixed theoretically, thus only $M_{Z'}$ is a free parameter. These are the Z'_χ, Z'_ψ, Z'_η, Z'_{LR}, Z'_{ALR} models, and the 'sequential' Z'_{SSM} model with Z' couplings identical to the Z ones. Current experimental lower limits (95% CL) on $M_{Z'}$ depend on models, and range from 2260 GeV for Z'_ψ up to 2590 TeV for Z'_{SSM} [12]. The leading *z*-even angular distributions for the LO partonic subprocess $\bar{q}q \to Z' \to l^+l^-$ has the same form as the SM and, therefore, the resulting A_{CE} is *the same for all* Z' models.

R-parity violating sneutrino exchange. R-parity is defined as $R_p = (-1)^{(2S+3B+L)}$, and distinguishes particles from their superpartners. In scenarios where this symmetry can be violated, supersymmetric particles can be singly produced from ordinary matter. In the dilepton process (1) of interest here, a spin-0 sneutrino can be exchanged through the subprocess $\bar{d}d \to \tilde{\nu} \to l^+l^-$ and manifest itself as a peak at $M = M_{\tilde{\nu}}$ with a flat angular distribution [3]. Results on next-to-leading QCD orders available in the literature indicate the possibility of somewhat large K-factors, in particular due to supersymmetric QCD corrections. Besides $M_{\tilde{\nu}}$, the cross section is proportional to the R-parity violating product $X = (\lambda')^2 B_l$ where B_l is the sneutrino leptonic branching ratio and λ' the relevant sneutrino coupling to the $\bar{d}d$ quarks. Current limits on the relevant λ' s are of the order of 10^{-2}, and the experimental 95% CL lower limits on $M_{\tilde{\nu}}$ range from 397 GeV (for $X = 10^{-4}$) to 866 GeV (for $X = 10^{-2}$) [13]. We take for X, presently not really constrained for sneutrino masses of order 1 TeV or higher, the (rather generous) interval $10^{-5} < X < 10^{-1}$.

Model for scalar particle exchange. For the process with diphoton final states we consider the simple model of a scalar particle S, singlet under the SM gauge group and with mass $M \equiv M_S$ of the TeV order, proposed in Ref. [4]. The trilinear couplings of S with gluons, electroweak gauge bosons and fermions, are in this model:

$$\begin{aligned} L_{\mathrm{Scalar}} &= c_3 \frac{g_s^2}{\Lambda} G^a_{\mu\nu} G^{a\mu\nu} S + c_2 \frac{g^2}{\Lambda} W^i_{\mu\nu} W^{i\mu\nu} S \\ &+ c_1 \frac{g'^2}{\Lambda} B_{\mu\nu} B^{\mu\nu} S + \sum_f c_f \frac{m_f}{\Lambda} \bar{f} f S. \end{aligned} \qquad (7)$$

In Eq. (15), Λ is a high mass scale, of the TeV order of magnitude, and c's are dimensionless coefficients that are assumed to be of order unity, reminiscent of a strong novel interaction. Following Ref. [4], we assume $\Lambda = 3$ TeV and allow the coefficients c_i to take values equal to, or less than, unity. The leading order diphoton production process is in this model dominated by the s-channel exchange $gg \to S \to \gamma\gamma$. Numerically, it turns out from the cross section that there exist a 'confusion region' of the c's where scalar diphoton states can be produced with same mass M_S and number of events as the RS gravitons, and the width Γ_S comparable to (or smaller than) the mass window ΔM. The difference lies in the differential cross section, which in this case has the flat z-behavior.

4. Spin identification with center-edge asymmetry

The nonstandard models briefly described in the previous section can mimic each other as sources of an observed peak in M, for values of the parameters included in so-called 'confusion regions' (of course included in their respective experimental and/or theoretical discovery domains), where they can give same numbers of signal events N_S. The M_R - N_S plots in Fig. 1 show as an example 'confusion regions' between spin-2 graviton and spin-0 sneutrino, spin-1 Z' for dilepton process and spin-0 scalar for diphotons. The number of events needed for 5-σ discovery at the 8 TeV LHC with luminosity $L_{\mathrm{int}} = 20\,\mathrm{fb}^{-1}$ and current limits on RS resonance obtained from 7 TeV LHC data are also shown. In such confusion regions, one can try to discriminate models from one another by means of the angular distributions of the events, directly reflecting the different spins of the exchanged particles. We continue with the examples of confusion regions in Fig. 1 and start from the assumption that an observed peak at $M = M_R$ is the lightest spin-2 graviton (thus, $M_R = M_G$). We define a 'distance' among models accordingly:

$$\Delta A^{Z'}_{\mathrm{CE}} = A^{G}_{\mathrm{CE}} - A^{Z'}_{\mathrm{CE}}; \qquad \Delta A^{\tilde{\nu}}_{\mathrm{CE}} = A^{G}_{\mathrm{CE}} - A^{\tilde{\nu}}_{\mathrm{CE}}. \qquad (8)$$

To assess the domain in the (M_G, c) plane where the competitor spin-1 and spin-0 models giving the same N_S under the peak can be *excluded* by the starting RS graviton hypothesis, a simple-minded χ^2-like criterion can be applied, which compares the deviations (8) with the uncertainty (statistical and systematic combined) δA^G_{CE} pertinent to the RS model. We impose the two conditions

$$\chi^2 \equiv \left(\Delta A^{Z',\tilde{\nu}}_{\mathrm{CE}} / \delta A^{G}_{\mathrm{CE}}\right)^2 > \chi^2_{\mathrm{CL}}. \qquad (9)$$

Eq. (9) contains the definition of χ^2, and the χ^2_{CL} specifies a desired confidence level (3.84 for 95% CL). This condition determines the minimum number of events, $N_S^{\min}$, needed to exclude the spin-1 and spin-0 hypotheses (hence to establish the graviton spin-2), and this in turn will determine the RS graviton *identification* domain in the (M_G, c) plane. Of course, an analogous procedure can be applied to the identification of Z' and $\tilde{\nu}$ exchanges against the two competing ones as sources of a peak in process. In process for RS graviton identification exploiting the same procedure one needs to exclude spin-0 only, since spin-1 resonance is forbidden by Landau-Yang theorem. Figure 2 show the identification domain for the RS graviton excitation, foreseeable from both the diphoton and the dilepton events, at the 8 TeV LHC with luminosity 20 fb^{-1}. Specifically: the regions to the left of the 'Discovery' lines are discovery domains at 5σ; the identification domains at 95 % CL are to the left of the 'ID' lines; the line 'LHC (7 TeV)' represents the current experimental lower limits from the 7 TeV LHC, it delimits the 'allowed' region from below; the line 'oblique corrections' represents constraints (from below) from a fit to the oblique EW parameters.

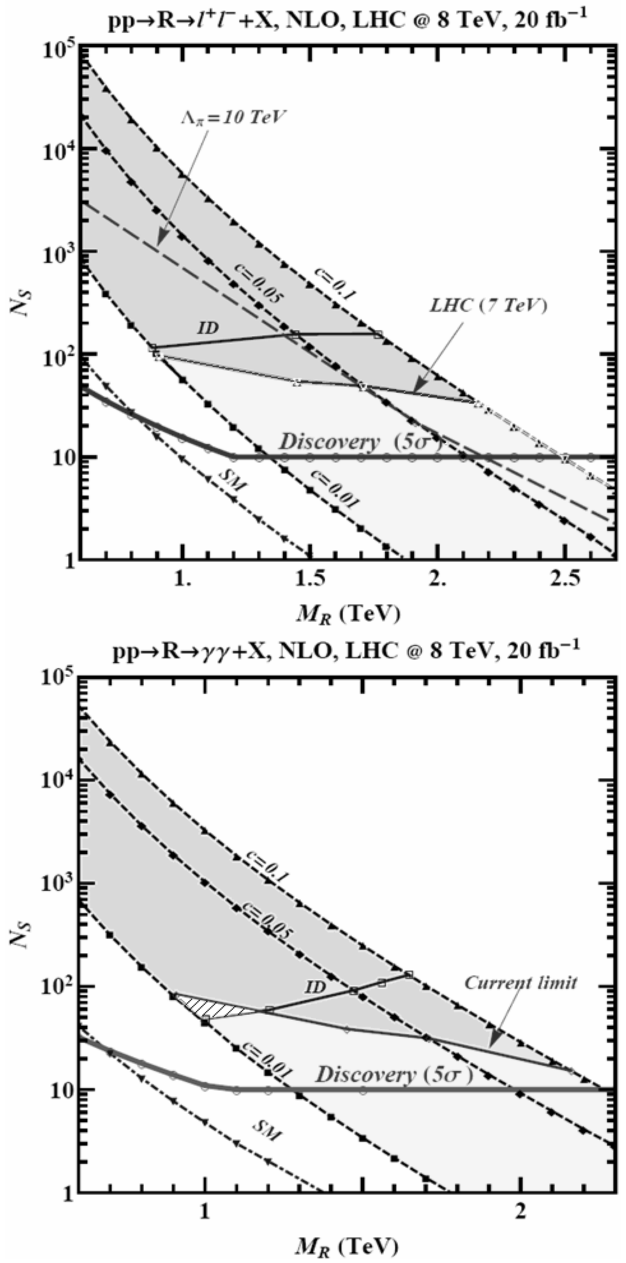
$pp \to R \to l^+l^- + X$, NLO, LHC @ 8 TeV, 20 fb^{-1}

$pp \to R \to \gamma\gamma + X$, NLO, LHC @ 8 TeV, 20 fb^{-1}

Figure 1. Number of resonance (signal) events N_S *vs* M_R ($R = G$) at the LHC with $\sqrt{s} = 8$ TeV and $L_{int} = 20$ fb^{-1} for the process $pp \to G \to l^+l^- + X$ (top panel) and $pp \to G \to \gamma\gamma + X$ (bottom panel). The shaded area corresponds to the KK graviton signature space for $0.01 \le c \le 0.1$. Current experimental limits, 5σ discovery level and minimal number of events for RS graviton identification are also shown.

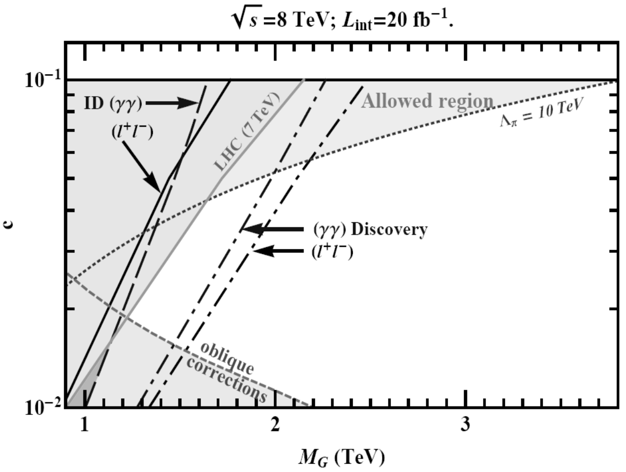
$\sqrt{s}$ =8 TeV; $L_{\rm int}$=20 fb^{-1}.

Figure 2. Discovery and identification on RS graviton at the 8 TeV LHC with luminosity 20 fb^{-1}.

Table 1: Discovery and identification reaches (in TeV) on RS graviton mass for 14 TeV LHC with L_{int} = 100 fb^{-1}.

c	Discovery	Identification
	$pp \to l^+l^- + X$	
0.01	2.5	1.6
0.1	4.6	3.2
	$pp \to \gamma\gamma + X$	
0.01	2.5	2.0
0.1	4.3	3.3

Fig.1 and Fig.2 show that accounting the current LHC (7 TeV) limits on RS graviton parameters and masses as well as those obtained from low energy data (oblique corrections) the discovery of heavy graviton excitations is still possible at LHC with $\sqrt{s} = 8$ TeV, while identification of their spin will be impossible.

Table 1 represents the discovery (5σ) and identification (95%CL) reaches on RS graviton at the 14 TeV LHC with luminosity 100 fb^{-1}. Table 1 shows that the χ^2-based angular analysis of dilepton and diphoton events described here can at the 14 TeV LHC provide identification limits on the RS graviton resonance ranging from M_G = 2.0 TeV ($c = 0.01$) up to M_G = 3.3 TeV ($c = 0.1$).

Acknowledgments. This work was supported in part by the Abdus Salam ICTP (TRIL and Associates Scheme) and by the Belarussian Republican Foundation for Fundamental Research.

References

1. Randall L., Sundrum R.: 1999, *Phys. Rev. Lett*, **83**, 3370.
2. Langacker P.: 2008, *Rev. Mod. Phys*, **81**, 1199.
3. Kalinowski J., et al.: 1997, *Phys. Lett. B*, **406**, 314.
4. Barbieri R., Torre R.: 2011, *Phys. Lett. B*, 259.
5. ATLAS Collaboration.: 1999, *CERN-LHCC-99-14*, *CERN-LHCC-99-15*.
6. Nadolsky P. M., et al.: 2008, *Phys. Rev. D*, 013004.
7. Kumar M. C., Mathews P., Pankov A. A., Paver N., Ravindran V., Tsytrinov A. V.: 2011, *Phys. Rev. D*, 115008.
8. Osland P., Pankov A. A., Paver N., Tsytrinov A. V.: 2008, *Phys. Rev. D*, 035008; 2009, *Phys. Rev. D*, 115021; 2010, *Phys. Rev. D*, 115017.
9. Serenkova I. A., Pankov A. A., Tsytrinov A. V., Bednyakov V. A.: 2010, *Phys. Atom. Nucl.*, **73**, 1266.
10. ATLAS Collaboration.: 2012, *ATLAS-Conf-2012-087*.
11. CMS Collaboration.: 2012, *Phys. Lett. B*, **714**, 158.
12. CMS Collaboration.: 2012, *CMS-Pas-Exo-12-015*; ATLAS Collaboration.: 2012, *ATLAS-Conf-2012-007*.
13. CDF Collaboration.: 2009, *Phys. Rev. Lett.*, **102**, 091805.

COSMOLOGY, COSMOMICROPHYSICS AND GRAVITATION

THE DISTRIBUTION OF BARYON MATTER IN THE NEARBY X-RAY GALAXY CLUSTERS

Iu.V. Babyk[1,2,3], I.B. Vavilova[1]

[1] Main Astronomical Observatory of NAS of Ukraine, Kyiv, Ukraine
[2] Dublin Institute for Advanced Studies, Dublin, Ireland
[3] Dublin City University, Dublin, Ireland,
babikyura@gmail.com, irivav@mao.kiev.ua

ABSTRACT. We present the results on the distribution of baryon matter in the galaxy clusters ($z < 0.2$), based on the *Chandra* X-ray Observatory data. The observed surface brightness profiles were approximated by $\beta-$ model, which provides a good fit for all clusters. We found a correlation between cluster's radius R_{200} and temperature T, taking into account that their measurements are statistically independent because of the mass of gas is almost independent on cluster's temperature: $R_{200} = 850$ kpc $\times T^{0.61 \pm 0.04}$ keV. We obtained an empirical relation for a total mass of baryon matter (intercluster medium and galaxies), and the upper limit (25-30%) on its changes in a total mass of nearby X-ray galaxy clusters.

Key words: Galaxy clusters: X-ray galaxy clusters.

1. Sample and data processing

To analyze the evolution of the baryon mass function of galaxy clusters we should provide relevant measurements for galaxy clusters at all redshifts, including the small ones. With this aim and to reveal the distribution of visible/dark matter we compiled a sample of 34 X-ray nearby galaxy clusters ($z < 0.2$). These clusters were selected from a larger sample of *Chandra* X-ray galaxy clusters ($0.01 < z < 1.5$), which is described fully in our previous work (Babyk, Vavilova, Del Popolo, 2012 (hereafter BVP sample). The main criteria were that clusters should be sufficiently symmetrical and each X-ray cluster image should trace the surface brightness profile at larger as possible radii. To satisfy the second statement we selected clusters with a wide exposure interval (not less 5000 s) and, moreover, under the condition that a virial radius fits on the line of sight. The value of a virial radius was taken as R_{200} (a providing accuracy is sufficient for the purposes of our study). Following these criteria, we excluded A754, A1750, A2151, etc clusters from our BVP sample, nevertheless that are at $z < 0.2$, because of their irregular morphology or double structure. Our sample of 34 nearby X-ray galaxy clusters is given in Tab. 1.

In fact, there is a question, how to remove all sources where a width response function strongly increases at large deviations from the optical axis, resulting in the center and on the end of the images of pointed source's focuses of a different future intensity of a cosmic X-ray background.

Nevertheless, we decided to eliminate all such sources, but after checking we found that it does not affect significantly the results contributing only to reduction of a non-static background in the obtained brightness profiles (see Babyk et al., 2012; Babyk, 2012a; Babyk, 2012; Babyk, Vavilova, 2012).

We have measured the brightness profiles in concentric rings of equal logarithmic width, which were centered on the cluster's maximum brightness; the radii's ratio of inner and outer rings is equal to 1.1. We have used two types of profiles: the average azimuthal brightness profiles and profiles in six angle sectors $0-60, ..., 300-360$. It allowed us to verify the choice of other "reasonable" centroid profiles: the measured surface brightness distribution at large radii were practically identical.

As for a cosmic X-ray background, we have measured it individually for each cluster because of a significant contribution to the overall brightness of X-ray galaxy cluster may occure even at large distances from the center. Usually, the X-ray cluster's surface brightness is about 5-20% of the background near the radius R_{200}. Since, in many cases, this radius is a quite close to the size of the telescope's field of view, it is practically impossible to isolate the studied image for a direct determination of the background level.

Thus, we have considered that the surface brightness cluster radius at large radii should follow the exponential law, and therefore the observation surface brightness could be approximated as $Ar^{-\gamma}+const$. Thus, this approximation in the range of radii $r > R_{200}/3$ allows us to find the intensity level of the background. According to the observations of distant clusters, in which the level of background can be measured directly, we verified that this method gives the correct result.

Finally, using observations of blank fields, we checked the images alignment quality: the difference between the background level in the center and on the end of the image does not exceed $\sim 5\%$ after eliminating all the sources. We notice that this 5% variation in the background levels gives an additional uncertainty of $\beta-$ parameter of the $\beta-$ model at $\delta\beta \sim 0.3 - 0.4$ and 2.1% uncertainty in the value of R_δ. We used the cosmological parameters $H_0 = 73$ km/s/Mpc, $\Omega_M = 0.27$, and $\Omega_\Lambda = 0.73$ in our study.

2. X-ray galaxy clusters surface brightness profiles: methods

2.1. Modeling the surface brightness profiles

We used the *Sherpa* software package and $\beta-$ model (Cavaliere, Fusco-Femiano, 1976) to determine the galaxy cluster brightness profiles:

$$S(r) = S_0(1 + r^2/r_c^2)^{-3\beta+0.5}, \qquad (1)$$

S_0, r_c and β are the free parameters. Such a model was used firstly by (Jones, Forman, 1999,) when analyzing the images of galaxy clusters based on the data from "Einstein" X-ray space observatory. The value of β for those clusters was in the range from 0.5 to 0.8 (the better value is 0.67). The authors noticed also a non-significant correlation between β - parameter and temperature of clusters: X-ray clusters with a higher temperature have a higher value of β - parameter.

The numerical simulations of that times provided more steeper profiles of density matter distribution, and $\beta \approx 0.8 - 1$ (see, for example, Navarro, Frenk, White, 1998), which was contrary to the observations. Bartelmann and Steinmetz (1996) argued that the surface brightness profiles may curl at the larger radii but we can not observe such a process because the brightness of cluster is decreasing due to the influence of background. They proposed to check an accuracy of modeling of brightness profiles using $\beta-$ model, because it allows to determine the mass of cluster under the condition of the hydrostatic equilibrium of intracluster gas (Hoekstra, 2007). We decided to apply a simple $\beta-$model for analyzing the observational surface brightness profiles in the studied nearby X-ray clusters as well as to clear up how such a procedure likely the azimuthal corrections of surface brightness profiles in galaxy clusters is fair one.

2.2. Excluding the cold galaxy cluster's centers

The most number of X-ray clusters with a normal morphology consists of a strong central peak of surface brightness, which is usually explained as a consequence of radiative cooling of the gas. Using the central parts of such clusters the approximation by $\beta-$ model leads to the small values of the core radius r_c and $\beta-$ parameter as well as to the weak data approximation in general. Obviously, a central part of the X-ray galaxy cluster images must be excluded during their processing, if the aim of a study concerns with a correct analyzis of the gas distribution at large cluster's radii.

There are several approaches to this problem. For example, Jones, Forman (1999) increased gradually a value of the minimal radius until the approximation of the surface brightness profile not leds to the acceptable values of χ^2. A new method to resolve such a problem is concerns with the search of the required radius parameter while a gas radiative cooling does not affect the distribution of a gas in the galaxy cluster till a typical value of a gas cooling time not exceeds the age of the Universe. Such a method, where a gas radiative cooling parameter described in a value of the radius R_{col}, and a gas radiative cooling time is 1.3×10^{10} years, was introduced and analysed by White, Fabian (1995), Peres et al. (1998). Taking into account these results and the aforementioned analytical approximation we calculated R_{col} parameter and excluded range of radii $r < R_{col}$ for each cluster from our sample.

2.3. The slope of surface brightness profile at the large radii

Our results on the approximation of surface brightness profiles are given in Tab. 1. The values obtained for the nuclei radii r_c are often comparable with the R_{col} parameter in the case of clusters with the central peaks of a surface brightness, indicating thus that r_c can not be reliably measured. Meanwhile, the value of $\beta-$ parameter is measured accurately and reliably as well as such an approximation responds well to the observations.

The obtained values of $\beta-$ parameter are shown in Fig. 2. If we compare these values with those from the work by Jones, Forman (1999), where $\beta-$ parameter had a fairly narrow range 0.7 ± 0.1, we may conclude as follows from Fig. 2: only a few nearby *Chandra* X-ray clusters from our sample have $\beta < 0.6$.

As concerns with the question on the correlation between $\beta-$ parameter and cluster's temperature T (left panel in Fig. 2). Our analysis allows to conclude that the previous statement about the absense of $\beta - T_X$ correlation was based on the small values of $\beta \sim 0.5$ for the cold X-ray clusters ($T \sim 3$ keV), which are characterized by the steeper surface brightness profiles. The most likely explanation for this discrepancy is related to the incomplete removal of the cooling central parts during processing the data on X-ray clusters in earlier works. We considered the same radial range (by the coordinate's position): $0.3R_{200}(T) < R < 1.5R_{200}(T)$. The nuclei r_c parameter can not be determined in this range from the *Chandra* data, so we fixed it at $0.1R_{200}$ or at the value that was obtained in the entire range of radii during approximation. Since r_c is usually much less than $0.3R_{200}(T)$, so the data approximation is equivalent to the application of a power law model,

$S \sim r^{-6\beta+1}$.

The obtained values of β_{out} are given in Tab. 1 and are presented dependently on the cluster's temperature T in Fig. 2 (right panel). The measured slope of a surface brightness profile in the outer part of this Figure was slightly steeper than it follows from approximating $\beta-$ model across the range of radii. An extreme case is related to the A2163 cluster, where β is changed to 0.17. The swirled surface brightness profile of the A2163 at $r > 0.3R_{200}(T)$ is obvious (Fig. 2). We notice that the changes of β in the outer parts of the clusters are much smaller, $\Delta\beta \approx 0.05$, as well as are not statistically significant for the most of galaxy clusters of our sample.

Thus, we concluded on the correlation between β_{out} parameter and cluster's temperature T. It is caused mainly by a group of five hot ($T =$ 6-10 keV) clusters (A85, A401, A478, A644, A1413, etc.) with $\beta > 0.7$, as well as by a strong twist profile of the hottest A2163 cluster. However, one can see from Fig. 2 that there are systematic changes in the slope of surface brightness profile at the large radii of clusters, which are within the scatter at the high temperatures. We notice that the observed trend is a weak for $\beta \approx 0.67$ for clusters with $T = 3$ keV to $\beta \approx$ 0.7-0.75 with $T =$ 10-13 keV.

2.4. Azimuthal variations of the surface brightness profile

Here we consider the question how the procedure of an azimuthal averaging of the surface brightness profile has been applied to the study of the intergalactic gas distribution at the large radii. With this aim we have compared the values of β_{out}, measured in the angle sectors $0-60, ..., 300-360$. The presence of azimuthal variations of β_{out} means a cluster's irregularity.

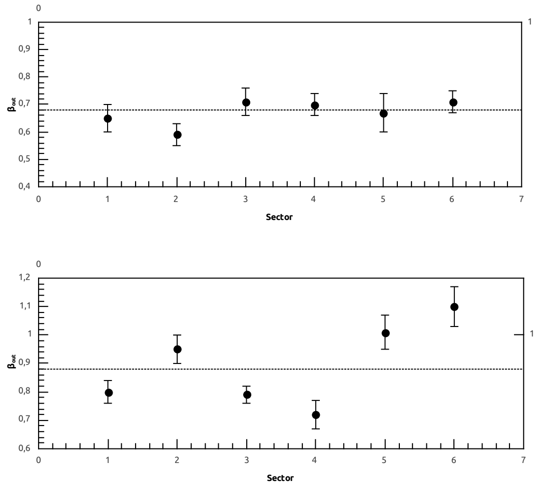

Figure 1: The azimuthal variations of β_{out} in the galaxy clusters 2029 (top) and 1795 (down).

We found that our sample contains both the symmetrical clusters (likely A2029) and the clusters with significant variations in the slope in the outer part (likely A1795) (see, Fig. 1), but these variations in the slope are small in general. The values of all azimuthal variations β_{out} in the studied clusters are given in Tab. 1. In the most cases they are less than 0.1 and demonstrate often a strong deviation in a single sector. Thus, we may conclude about the absense of the major errors through the azimuthal averaging brightness profiles in the outer parts of the studied clusters.

3. The intracluster gas density distribution

Under the condition of spherical symmetry of the cluster and the observed surface brightness profile we can find the volume of emitting ability, which is then easily transferred to the gas density profile, using the fact that the plasma radiating capacity in the soft X-ray range is proportional to the square of the density and dependent very weakly on the temperature (Einasto, 2001).

3.1. The correlation between radius of contrast of density baryons and temperature of cluster galaxy

The theory of the formation of clusters provides correlation between mass and temperature of clusters, $M \sim T^{3/2}$. Since the mass and radius corresponding to this density contrast associated as $M_{200} \sim R^3_{200}$, we can expect the following correlation R_{200} and temperature: $R_{200} \sim T^{1/2}$. Since most of the baryons are concentrated in the X-ray intergalactic gas, this ratio $(R_{200} - T_X)$ for baryons can be easily verified.

The contrast of baryon density is defined as the ratio of the mass of gas within a certain radius and the value of $(4\pi/3)\rho_0 R^3(1+z)^3$, where ρ_0 is the current density of baryons in the Universe. This compares reliably the relative content of light elements from the theory of primary nucleosynthes, $\rho_0 = (5.55 \pm 0.28) \times 10^9 M_\odot$ Mpc^{-3}. Radius R_{200} is sufficiently close to the virial radius $r_{vir}(T)$. Correlation between the cluster's radius R_{200} and temperature T is shown in Fig. 3. We notice that since the measurement of the mass of gas is almost independent of temperature clusters, measuring R and T are also statistically independent.

The observed correlation has a small scatter and close to the theoretically expected correlation of $R \sim T^{0.5}$. Note, that even A3391 with abnormally flat surface brightness profile is well accumulated within the average dependence. The measured correlation $R_{200} - T_X$ was modeled (Akritas, Bershady, 1996) using a power law model that allowed us also to consider both statistical and internal variations in the data on both axes.

Table 1: The sample and results of approximation of the surface brightness profiles of galaxy clusters on $z < 0.2$ using $\beta-$ model.

Name	T, (keV)	z,	R_{200}, (Mpc)	β,	β_{out},	r_c, (kpc)
A13	$5.76^{+0.15}_{-0.15}$	0.094	$1.51^{+0.47}_{-0.33}$	0.65±0.08	0.68±0.03	84±8
A85	$6.20^{+0.40}_{-0.15}$	0.055	$2.71^{+0.65}_{-0.73}$	0.75±0.03	0.76±0.03	374±54
A119	$5.71^{+0.16}_{-0.15}$	0.044	$2.66^{+0.13}_{-0.15}$	0.64±0.06	0.61±0.04	342±49
A400	$2.33^{+0.21}_{-0.17}$	0.024	$1.55^{+0.24}_{-0.13}$	0.55±0.07	0.58±0.03	185±20
A401	$8.16^{+0.87}_{-0.78}$	0.074	$3.07^{+1.21}_{-0.99}$	0.63±0.07	0.69±0.02	267±51
A478	$6.90^{+0.35}_{-0.35}$	0.088	$2.60^{+0.41}_{-0.55}$	0.75±0.04	0.80±0.06	311±30
A496	$4.89^{+0.12}_{-0.14}$	0.033	$1.93^{+0.48}_{-0.35}$	0.70±0.06	0.75±0.03	237±22
A539	$3.33^{+0.29}_{-0.31}$	0.028	$1.88^{+0.33}_{-0.18}$	0.69±0.03	0.73±0.04	244±33
A644	$6.59^{+0.17}_{-0.17}$	0.070	$2.92^{+0.77}_{-0.81}$	0.71±0.03	0.71±0.04	244±41
A780	$4.33^{+0.15}_{-0.18}$	0.054	$1.69^{+0.48}_{-0.37}$	0.65±0.08	0.61±0.04	119±25
A1413	$6.77^{+0.36}_{-0.26}$	0.14	$1.83^{+0.66}_{-0.57}$	0.68±0.01	0.70±0.02	219±17
A1651	$6.11^{+0.20}_{-0.21}$	0.085	$2.45^{+0.46}_{-0.37}$	0.70±0.02	0.77±0.04	256±43
A1689	$9.02^{+0.40}_{-0.30}$	0.183	$2.23^{+0.03}_{-0.07}$	0.75±0.05	0.81±0.06	265±64
A1795	$6.88^{+0.14}_{-0.14}$	0.063	$2.46^{+0.36}_{-0.54}$	0.77±0.06	0.88±0.07	377±48
A2029	$8.45^{+0.47}_{-0.45}$	0.077	$2.94^{+0.96}_{-0.82}$	0.68±0.03	0.66±0.04	277±74
A2052	$3.22^{+0.22}_{-0.22}$	0.035	$1.93^{+0.55}_{-0.61}$	0.64±0.03	0.66±0.03	133±35
A2063	$4.21^{+0.55}_{-0.36}$	0.035	$2.01^{+0.45}_{-0.37}$	0.68±0.02	0.69±0.04	210±45
A2124	$10.88^{+1.78}_{-2.01}$	0.065	$2.16^{+0.63}_{-0.61}$	0.67±0.03	0.59±0.04	254±73
A2142	$9.57^{+0.92}_{-1.11}$	0.091	$2.82^{+0.59}_{-0.61}$	0.75±0.05	0.73±0.04	387±47
A2163	$14.01^{+1.89}_{-1.45}$	0.203	$4.22^{+0.68}_{-0.66}$	0.73±0.04	0.87±0.04	417±36
A2199	$4.15^{+0.23}_{-0.21}$	0.030	$2.14^{+0.28}_{-0.19}$	0.64±0.03	0.67±0.05	155±25
A2218	$7.39^{+1.03}_{-0.89}$	0.175	$1.65^{+0.16}_{-0.12}$	0.66±0.03	0.71±0.03	234±46
A2255	$7.30^{+1.20}_{-1.20}$	0.081	$3.21^{+0.46}_{-0.27}$	0.74±0.04	0.73±0.06	552±37
A2256	$7.53^{+0.91}_{-0.75}$	0.058	$3.33^{+0.62}_{-0.58}$	0.72±0.03	0.75±0.04	436±57
A2462	$2.55^{+0.71}_{-0.66}$	0.073	$2.51^{+0.27}_{-0.22}$	0.65±0.03	0.66±0.04	221±36
A2597	$4.39^{+0.45}_{-0.51}$	0.085	$2.01^{+0.57}_{-0.73}$	0.66±0.03	0.66±0.04	166±45
A2657	$3.77^{+0.81}_{-0.77}$	0.040	$1.98^{+0.15}_{-0.11}$	0.75±0.05	0.73±0.02	372±40
A2717	$2.31^{+0.34}_{-0.15}$	0.049	$2.16^{+0.79}_{-0.81}$	0.68±0.03	0.66±0.02	71±3
A3112	$4.86^{+0.56}_{-0.67}$	0.075	$2.43^{+0.31}_{-0.26}$	0.61±0.04	0.65±0.03	119±12
A3391	$7.01^{+0.63}_{-0.73}$	0.051	$2.45^{+0.84}_{-0.35}$	0.55±0.01	0.56±0.03	210±17
A3571	$8.21^{+0.86}_{-0.73}$	0.039	$2.88^{+0.46}_{-0.37}$	0.69±0.03	0.61±0.05	271±32
A4038	$3.32^{+0.53}_{-0.42}$	0.030	$1.87^{+0.25}_{-0.17}$	0.60±0.04	0.61±0.03	162±43
A4059	$4.11^{+0.35}_{-0.32}$	0.047	$2.03^{+0.28}_{-0.34}$	0.65±0.04	0.66±0.03	222±48
AWM4	$2.44^{+0.19}_{-0.25}$	0.032	$1.73^{+0.27}_{-0.22}$	0.62±0.04	0.67±0.07	125±42

The variation has value only 5.5% for R_{200} at this temperature. Although the obtained slopes differ formally from the theoretical value of 0.5 for $2-3\sigma$, the discrepancy between the best approximation and the power law $R \sim T^{0.5}$ lies completely within the scatter of data. The resulting ratio is as follows:

$$R_{200} = 850kpc \times T^{0.61\pm0.04}keV \qquad (2)$$

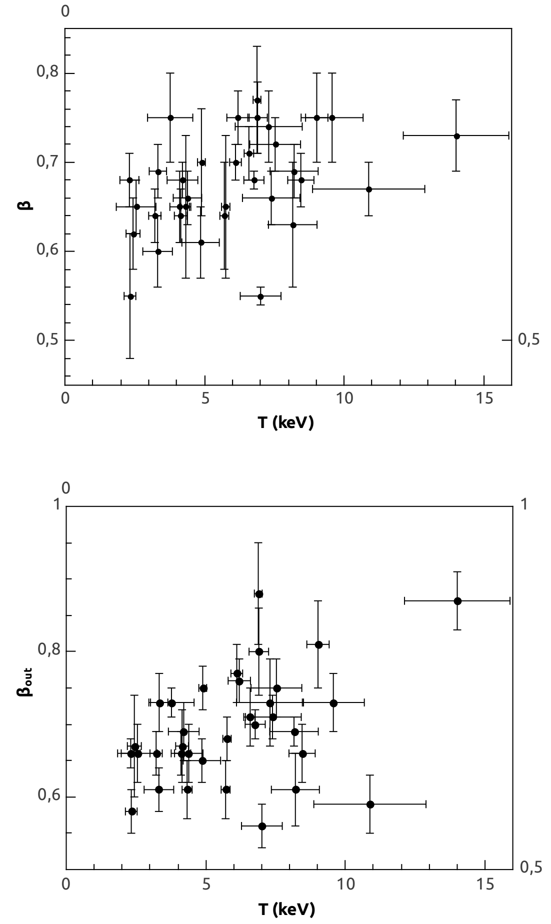

Figure 2: The correlation between β and temperature of galaxy clusters. Top: β is taken from approximation at all range of radii. Down: β is taken from approximation at $0.3R_{200} < R < 1.5R_{200}$.

Main difference with other relations, such as luminosity-temperature or size-temperature, are related to the fact that the data, which are depending on the parameters of concentrated gas distribution, were obtained from the inner parts of cluster, but the correlation between R_{200} and T was obtained based on the data from the outer parts. So, the properties of the central parts of clusters can strongly affect various non-gravitational processes, which are not important at large radii, where the main part of the cluster's mass is concentrated.

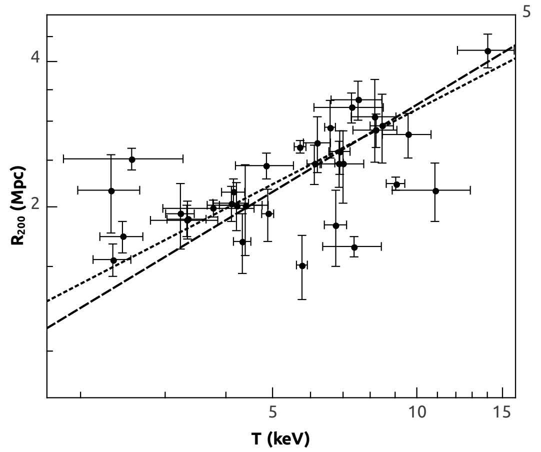

Figure 3: The correlation of R_{200} and temperature clusters. Doted line shows approximations with power law model, and dashed line shows theoretical model from correlation $R \sim T^{0.5}$.

3.2. The upper limit on the changes of baryons in total mass of galaxy clusters

Small scatter observed in the correlation $R_{200}-T$ can help us to find upper limit on variation in the proportion of baryons in total mass between different clusters and its systematic dependence on temperature. We used the theoretically expected fact that the total mass of the cluster within a radius of density contrast correlated with temperature as $M_{tot} \sim T^{3/2}$. Observed ratio for baryons, $R \approx const \times T^{1/2}$ is equivalent $M_{gas} \sim T^{3/2}$. It means that $f_{gas} = M_{gas}/M_{tot} \approx const$. Since the hot gas is the dominant baryon component in clusters, we can conclude that the proportion of baryons in total mass is constant too. The best approximation is $R_{200} \sim T^{0.57}$ and corresponds to a small change in gas content in total mass: $f_{gas} \sim T^{0.2}$. However, if we consider the fraction of stars in the mass of baryons, which is higher in cold clusters, then this trend is significantly reduced and we can count that for wide range of temperatures the fraction of baryon mass in total mass of clusters is constant.

We now consider possible the variations of f_{gas} between different clusters with a given temperature. In the outer parts of the clusters radial correlation of the contrast density of gas is $\delta \sim r^{-3\beta}$. Accordingly, the observed 6.5%-variations within the fixed δ_{gas} corresponds to approximately $3\beta \times 6.5\%$ variation of contrast at a given radius. Hence, we can predict that the total mass of clusters clearly related to temperature.

In fact, the ratio $M_{tot}-T$ has scatter of f_{gas} for clusters with a given mass of somewhat reduced. Thus, the findings suggest that the contribution of baryons in the total mass is constant, the same for different clusters of galaxies, and is independent from their temperature.

4. The total mass of baryons and the upper limit on its changes in the nearby X-ray clusters

We now consider possible the variations of f_{gas} between different clusters with a given temperature. The radial correlation of the contrast density of gas is $\delta \sim r^{-3\beta}$ in the outer parts of clusters. Accordingly, the observed 6.5%-variations within the fixed δ_{gas} correspond to approximately $3\beta \times 6.5\%$ variation of contrast at a given radius. Hence, we can predict that the total mass of clusters clearly related to the temperature. In fact, the ratio $M_{tot} - T$ has the scatter of f_{gas} for clusters with a given mass of somewhat reduced. Thus, we may suggest that the contribution of baryons in the total mass is constant being the same for different clusters of galaxies, and it's independent on their temperature.

Voevodkin, Vikhlinin & Pavlinskii (2002a) calculated the correlation ratio between the baryon's mass and the total X-ray luminosity of clusters. This ratio provides an opportunity to make a rough estimate of the mass in those situations when the quality of the X-ray data are not available. More importantly that an availability of $M - L$ ratio helps to determine the volume, which is covered by the survey, with any restriction on the flow, depending on the mass of the cluster, and thus, finally, the mass function. These authors obtained also (Voevodkin, Vikhlinin & Pavlinskii, 2002b) an integral function of the baryon mass which takes into account a statistical measurement error of the mass function of close clusters as well as distortions caused by the measurement errors for the masses of individual clusters.

We measured the mass profiles of intracluster gas in all the studied galaxy clusters using *Chandra* data and aforementioned analysis. Afetr a very accuracy applying the correlation ratio between the mass of hot gas and total optical luminosity taken from the paper by Voevodkin, Vikhlinin, Pavlinskii (2002a), we found not only the mass of gas, but also the total mass of baryons (intracluster gas + stars) for the X-ray clusters from our sample:

$$M_b = M_g \times \left[1.33 + 0.05 \left(\frac{M_g}{10^{15} M_\odot}\right)^{-0.52}\right] \qquad (3)$$

Here, M_b is the mass of baryons at the contrast $\delta = 200$, M_g is the mass of gas at the same contrast without a fraction of stars. The fraction of stars in the total mass of baryons is significant and equal $\sim$ 10-15 % for massive clusters. Considering that the mass ratio of the gas and stars do not evolve at large z (i.e., galaxies do not associate themselves hot intergalactic gas), this ratio can be used for a measurement of the total baryonic mass of distant clusters, for which the sufficient quality optical observations are not available yet.

Thus, the baryon mass function for X-ray galaxy clusters at the small redshifts can be estiimated with the use of Eq. 3. Observations of *Chandra* distant clusters can give us an opportunity to measure the baryon mass function also at the large redshifts (see, for example, the related paper by Schmidt & Allen (2007), and on the distinguished use of this approach by Babyk, Vavilova, Del Popolo (2012)).

*Acknowledgements.*We notice on the usage of the *Chandra* Data Archive and the Chandra Source Catalog, and software provided by the *Chandra* X-ray Center (CXC) in the application packages *CIAO*, *ChIPS*, and *Sherpa*. This work was partially supported in frame of the "CosmoMicroPhysics" Program and the Target Project of the Physics and Astronomy Division of the NAS of Ukraine.

References

Akritas M.G., Bershady M.A.: 1996, *ApJ*, **470**, 706.
Babyk Iu.: 2012, *Journ. Phys. Studies*, **16**, 7.
Babyk Iu.: 2012, *Izv. CrAO*, **108**, 127.
Babyk Iu., Melnyk O., Elyiv A., Krivodubskij V.: 2012, *Kinemat. Physics Celest. Bodies*, **28**, 69.
Babyk Iu., Vavilova I., Del Popolo A.: 2012, *submitted to MNRAS*, **arXiv:1208.2424**.
Babyk Iu., Vavilova I.: 2012, *Proc. Confer. Young Scientists of CIS Countries, Armenia, 2011*, 162.
Bartelmann M., Steinmetz M.: 1996, *MNRAS*, **283**, 431.
Cavaliere A., Fusco-Femiano R.: 1976, *A&A*, **49**, 137.
Einasto J.: 2001, *New Astronomy Reviews*, **45**, 355.
Jones C., Forman W.: 1999, *ApJ*, **511**, 65.
Hoekstra H.: 2007, *MNRAS*, **379**, 317.
Mohr J.J., Evrard A.E.: 1997, *ApJ*, **491**, 38.
Navarro J.F., Frenk C.S. & White S.D.: 1998, *MNRAS*, **275**, 720.
Peres C. et al.:1998, *MNRAS*, **298**, 416.
Schmidt R.W., Allen S.W.: 2007, *MNRAS*, **379**, 209.
Voevodkin A.A., Vikhlinin A.A., Pavlinskii M.N.: 2002, *Letters in AJ*, **28**, 366.
Voevodkin A.A., Vikhlinin A.A., Pavlinskii M.N.: 2002, *Letters in AJ*, **28**, 793.
White D.A. & Fabian A.C.: 1995, *MNRAS*, **273**, 72.

QUINTESSENCE AND PHANTOM ENERGY INHOMOGENEITIES AT LATE STAGES OF UNIVERSE EVOLUTION

A.Burgazli [1*], M.Eingorn [2**], A.Zhuk [2***]

[1]Department of Theoretical Physics, [2]Astronomical Observatory
Odessa National University named after I.I.Mechnikov, Ukraine
[*] *aburgazli@gmail.com,* [**] *maxim.eingorn@gmail.com,* [***] *ai_zhuk2@rambler.ru*

ABSTRACT. As it directly follows from the scalar perturbations, applied to the late stages of evolution of the Universe, filled with dark energy, nonrelativistic matter and, possibly, quintessence or phantom energy, the last two components can not be homogeneous.

We demonstrate that ω=-1/3 is only admissible negative parameter in the non-vacuum equation of state, determine the corresponding gravitational potentials and discuss their main properties.

Key words: quintessence, phantom field, scalar perturbation, cosmology

At the present time the most popular cosmological model, describing evolution of the homogeneous and isotropic Universe, is well known ΛCDM-model. The dark energy can be presented in the form of a perfect fluid with the linear equation of state $p=\varepsilon\omega$ (ε is the energy density and p is the pressure), where the parameter ω is constant and equal to -1.

In the case when parameter ω is arbitrary, these perfect fluids are usually called quintessence ($-1<\omega<0$) or the phantom field ($\omega<-1$). The acceleration is achieved for $\omega<-1/3$.

Our work is devoted to the test of quintessence and phantom field with the constant negative parameter ω for compatibility with the theory of scalar cosmological perturbations at late stages of the Universe evolution. Inside the cell of uniformity (the spatial region with the scale ~150 Mpc) hydrodynamics in inapplicable, so we use the mechanical approach. We showed that the investigated fluids can not be homogeneous. Therefore, we perturb the background values of their energy density and pressure. Then we try to derive formulas for gravitational potentials of usual point-like masses in closed, flat and open Universes. This procedure leads to severe constraints imposed on the parameter ω. As a result, we single out unforbidden cases deserving further investigation.

We used the background metrics

$$ds^2 = a^2\left(d\eta^2 - \gamma_{\alpha\beta}dx^\alpha dx^\beta\right),\quad \gamma_{\alpha\beta} = \frac{\delta_{\alpha\beta}}{\left[1+\frac{1}{4}\mathcal{K}(x^2+y^2+z^2)\right]^2},\quad \alpha,\beta=1,2,3,$$

and the corresponding Friedmann equations

$$\frac{3\left(\mathcal{H}^2+\mathcal{K}\right)}{a^2} = \kappa\overline{T}{}_0^0 + \Lambda + \kappa\varepsilon\,,\quad \frac{2\mathcal{H}'+\mathcal{H}^2+\mathcal{K}}{a^2} = \Lambda - \kappa p = \Lambda - \kappa\omega\varepsilon,$$

where $\overline{T}{}_0^0$ is the average energy density of the usual nonrelativistic dust-like, $\mathcal{K}$ is the spatial curvature, $\mathcal{H}\equiv a'/a$ and $\kappa\equiv 8\pi G_N/c^4$ (c is the speed of light and G_N is Newton's gravitational constant), Λ is the cosmological constant and a is the time-dependent scale factor.

Finally, in ω=-1/3 we get respectively

$$\delta\varepsilon = \frac{2\varepsilon_0 a_0^2}{c^2 a^3}\varphi,\quad \Delta\varphi + \left(3\mathcal{K} - \frac{8\pi G_N}{c^4}\varepsilon_0 a_0^2\right)\varphi = 4\pi G_N(\rho - \overline{\rho}).$$

The produced investigation of inhomogeneous quintessence and phantom field with a constant parameter ω in the linear equation of state allows to draw the following three main conclusions:

the phantom field is completely forbidden;

the models containing quintessence may be viable only if $-1/3\le\omega<0$;

in the boundary case ω=-1/3 the gravitational potential are defined for all generally accepted types of spatial topology, and some of them demonstrate satisfactory asymptotical behaviour and allow the averaging procedure, i.e. these gravitational potentials have clear physical meaning.

References

Mukhanov V., Feldman H., Brandenberger R.: 1992, *Phys. Rep.*, **215**, 203.

Eingorn M., Zhuk A.: 2012, *JCAP*, **09**, 026.

Gorbunov D., Rubakov V.: 2011, *World Scientific*.

Gonzalez-Diaz P.: 2000, *Phys. Rev. D*, **62**, 023513.

Chernin A., Santiago D., Silbergleit A.: 2002, *Phys. Lett. A*, **294**, 79-83.

MULTIDIMENSIONAL SOLITONS WITH SPHERICAL COMPACTIFICATION

A.V. Chopovsky[1], M.V. Eingorn[2], A.I. Zhuk[3]

[1] Department of Theoretical Physics and [2,3] Astronomical Observatory,
Odessa I.I.Mechnikov National University,
Odessa, Ukraine

[1]*alexey.chopovsky@gmail.com*, [2]*maxim.eingorn@gmail.com*, [3]*ai_zhuk2@rambler.ru.*

ABSTRACT. Multidimensional static spherically symmetric (with respect to the external 3-dimensional space) vacuum solutions of the Einstein equation were well-known and prevalent in literature for a long time. These solutions are called solitons. Among them, there is a class of particular solutions, called latent solitons, which are indistinguishable from General Relativity concerning the gravitational tests. Black strings and black branes belong to this class. We construct an exact soliton solution, when the internal space represents a sphere of some finite radius.

Key words: Kaluza–Klein models: black branes.

The Kaluza–Klein (KK) model with spherical topology of two additional spatial dimensions is investigated. We consider the metrics of the form:

$$ds^2 = \tilde{A}(\tilde{r}_3)c^2dt^2 + \tilde{B}(\tilde{r}_3)d\tilde{r}_3^2 + \tilde{C}(\tilde{r}_3^2)\left(d\theta^2 + \sin^2\theta\right) + \tilde{E}(\tilde{r}_3^2)\left(d\xi^2 + \sin^2\eta\right),$$

where tilde denotes Schwarzschild-like parametrization for the metrics and the radial coordinate into the external (non-compact) space. The energy-momentum tensor (EMT) of the corresponding background matter may be presented in the form of a perfect fluid with the vacuumlike equation of state in the external space and an arbitrary (parameterized with ω_1) equation of state in the internal (compact) space:

$$T_{ik} = \begin{cases} \varepsilon(\tilde{r}_3)g_{ik}, & \text{for} \quad i,k = 0,\dots,3; \\ -\omega_1\varepsilon(\tilde{r}_3)g_{ik}, & \text{for} \quad i,k = 4,5. \end{cases}$$

We require that the internal space is exactly the 2-sphere: $\tilde{E} \equiv -a^2$, where a is the radius of the internal space. Then, from multidimensional Einstein equations

$$R_{ik} = \kappa_6\left(T_{ik} - \frac{1}{4}Tg_{ik} - \frac{1}{2}\Lambda_6 g_{ik}\right).$$

we get the following equality between the background value of the energy density and the internal space radius: $\varepsilon = \Lambda_6/\omega_1 = \left[(1+\omega_1)\kappa_6 a^2\right]^{-1}$. Choosing different values of the parameter ω_1 we can simulate different types of the background matter.

To get the external spacetime in the form of the Schwarzschild metrics, we have to introduce a compact gravitating object which is spherically symmetric in the external space and uniformly smeared over the internal space. Let the EMT of this source have the following nonzero covariant components:

$$T_{00} = \hat{\varepsilon}g_{00}, \quad T_{ii} = -\hat{p}_1 g_{ii},$$

for $i = 4,5$. In case of a pointlike gravitating mass in the weak-field limit we have $\hat{\varepsilon} \approx m\delta(\mathbf{\tilde{r}}_3)/(4\pi a^2)$. Noting that we want to get the Schwarzschild solution in the external space, it can be easily realized that Einstein equations are compatible only if the equation of state $\hat{p}_1 = -\hat{\varepsilon}/2$ holds. The corresponding exact solution (black brane with spherical compactification) is:

$$ds^2 = \left(1 - \tfrac{r_g}{\tilde{r}_3}\right)c^2dt^2 - \left(1 - \tfrac{r_g}{\tilde{r}_3}\right)^{-1}d\tilde{r}_3^2 - \tilde{r}_3^2 d\Omega_2^2 - a^2(d\xi^2 + \sin^2\xi d\eta^2).$$

Here $r_g = 2G_N m/c^2$. Using the relation between the Schwarzschild-like radial coordinate $\tilde{r}_3$ and the isotropic radial coordinate $r_3 = \sqrt{x^2+y^2+z^2}$, in the weak-field limit (up to the terms $1/c^2$) we can find :

$$ds^2 \approx \left(1 - \tfrac{r_g}{r_3}\right)c^2dt^2 - \left(1 + \tfrac{r_g}{r_3}\right)(dx^2 + dy^2 + dx^2) - a^2(d\xi^2 + \sin^2\xi d\eta^2).$$

This metrics shows that the PPN parameters $\beta = \gamma = 1$, similar to general relativity. Hence, our black brane satisfies the gravitational experiments at the same level of accuracy as general relativity.

References

Eingorn M., de Medeiros O.R., Crispino L.C.B. et. al.: 2011, *Phys. Rev. D*, **84**, 024031.

Chopovsky A., Eingorn M. and Zhuk A.: 2012, *Phys. Rev. D*, **86**, 024025.

SIGNIFICANCE OF TENSION FOR KALUZA-KLEIN MODELS: CRITICAL REMARKS

M. Eingorn

Astronomical Observatory, Odessa National University and
Department of Theoretical and Experimental Nuclear Physics,
Odessa National Polytechnic University
Odessa, Ukraine
maxim.eingorn@gmail.com

ABSTRACT. In this very brief review the crucial problematic aspects of gravitational interaction in the weak field limit of Kaluza-Klein models are clarified. We explain why some models meet the classical gravitational tests, while the others do not. In the case of toroidal compactification of extra spatial dimensions we show how the presence of tension (both with and without effects of nonlinearity with respect to the scalar curvature R) of a single gravitating source results in agreement with the observations. It takes place for so-called latent solitons, in particular, black strings and black branes.

In the case of spherical compactification there is the additional (with respect to the Newtonian one) Yukawa interaction for models with the stabilized internal space. For large Yukawa masses the effect of this interaction is negligibly small, and such models satisfy the gravitational tests at the same level of accuracy as general relativity. However, gravitating masses acquire effective relativistic pressure in the external space. Obviously, such pressure contradicts the observations. We demonstrate that tension is the only possibility to preserve the dust-like equation of state in the external space. Therefore, tension plays a crucial role for multidimensional models.

Key words: Kaluza-Klein models, extra dimensions, black strings, black branes, tension, gravitational tests.

The idea of space-time multidimensionality is one of the most intriguing and breath-taking hypotheses of the past and present centuries. Now there is a large variety of multidimensional models supposing existence of extra spatial dimensions. It is absolutely obvious that the search for them is most effective if we know which of these models are viable. In other words, we need to know which of these models do not contradict the experimental data. For example, the well known gravitational experiments (the perihelion shift, the deflection of light and the time delay of radar echoes) in the Solar system turn out to be very good filters for screening out non-physical theories. It is well known that the weak field approximation is enough for deriving the corresponding formulas for these experiments (Landau & Lifshitz, 2000). For example, in the framework of general relativity these formulas demonstrate excellent agreement with the experimental data of astronomical observations.

In our recent papers we investigated in detail popular Kaluza-Klein models with toroidal compactification of the internal spaces. As we have explicitly shown, in order to be at the same level of agreement with the gravitational tests as general relativity, the gravitating masses should have tension (or, in other words, negative relativistic pressure) in the internal spaces. This statement is true for both linear (Eingorn & Zhuk, 2011; Eingorn et al., 2011) and nonlinear $f(R)$ (Eingorn & Zhuk, 2011a; Eingorn & Zhuk, 2012) models. Unfortunately, the physically reasonable sources of the gravitational field with the dust-like equation of state $p=0$ in all spaces contradict the observations (Eingorn & Zhuk, 2010). For the proper value of tension (which takes place for the latent solitons as well as black strings and black branes as their particular cases) the contradiction is eliminated (see also Eingorn & Zhuk, 2012a).

However, at the given moment we are not aware of the physical meaning of tension for the ordinary astrophysical objects similar to our Sun, which is not relativistic. Consequently, in order to describe motion of a test body in the vicinity of the Sun, there is no need to take into account the relativistic properties of black holes (for example, the presence of the horizon). On the contrary, it is quite sufficient to use the corresponding black strings or black branes metrics in the weak field approximation (see Eingorn & Zhuk, 2011; Eingorn et al., 2011).

Therefore, we continued to search for multidimensional models that satisfy the gravitational tests, being free from such physically unclear property of gravitating masses as tension. For this purpose, we have considered Kaluza-Klein models with spherical compactification of the internal space, being a 2-sphere (Chopovsky et al., 2011; Chopovsky et al., 2012) and a d-sphere (Eingorn et al., 2012), where $d \geq 2$ is absolutely arbitrary. Here we have shown that the Yukawa-type admixture to the standard metric coefficients is generated. The characteristic range of the Yukawa interaction for these models is proportional to the scale factor of the internal spherical space (or, in other words, to the radius of the internal sphere): $\lambda \sim a$.

It should be noted that the sizes of the extra dimensions in Kaluza-Klein models are bounded by the recent collider experiments, and at the same time there are quite strong restrictions imposed on the Yukawa parameter λ from the inverse square law tests (see, for example, Kapner et al., 2007; Adelberger et al., 2003). According to both these limitations, λ is in many orders of magnitude smaller than the radius of the Sun.

Consequently, with very high accuracy we can drop the admixture of the Yukawa terms to the metric coefficients at distances greater than the radius of the Sun, and as a result we achieve good agreement with the gravitational tests for the models with spherical compactification. In these models the gravitating mass may have the dust-like equation of state in all spatial dimensions, and its tension may be absent, at least, at first glance.

Nevertheless, the considered Kaluza-Klein models with spherical compactification of an arbitrary number of extra dimensions and dust-like sources of the gravitational field turn out to be also inconsistent with the observations, but now from the thermodynamic point of view.

Indeed, we have shown that any gravitating body acquires the effective relativistic pressure in the external space. It means that any system of nonrelativistic particles may have the relativistic momentum crossing any spatial area (see Klimontovich, 1986). Of course, it contradicts the laboratory observations. Such predicted, but unobserved relativistic pressure disappears only in the case of the bare tension in the internal space. Therefore, in order to be in agreement with the experimental data, we again should include tension of bare gravitating masses in the internal space, as it takes place in the case of toroidal compactification.

As a conclusion, we want to stress that Kaluza-Klein models with different types of compactification (toroidal, spherical) face severe problems for physically reasonable dust-like sources of the gravitational field, while non-dust-like sources with tension can not be considered as an adequate way out. This critical situation indicates that one should either focus on alternative multidimensional models such as brane world models, or repudiate the idea of space-time multidimensionality at all. If the latter choice is made, the given investigation can be considered as a part of a direct experimental proof that our world is really spatially three-dimensional, as it was accepted for ages.

References

Landau L.D., Lifshitz E.M. *The Classical Theory of Fields*, Fourth Edition: Volume 2 (Course of Theoretical Physics Series), (Pergamon Press, Oxford, 2000).

Eingorn M., Zhuk A.: 2011, *Phys. Rev. D*, **83**, 044005.

Eingorn M., de Medeiros O., Crispino L., Zhuk A.: 2011, *Phys. Rev. D*, **84**, 024031.

Eingorn M., Zhuk A.: 2011a, *Phys. Rev. D*, **84**, 024023.

Eingorn M., Zhuk A.: 2012, *Phys. Rev. D*, **85**, 064030.

Eingorn M., Zhuk A.: 2010, *Class. Quant. Grav.*, **27**, 205014.

Eingorn M., Zhuk A.: 2012a, *Phys. Lett. B*, **713**, 154.

Chopovsky A., Eingorn M., Zhuk A.: 2011, *Weak field limit of Kaluza-Klein models with spherical compactification: problematic aspects*.

Chopovsky A., Eingorn M., Zhuk A.: 2012, *Phys. Rev. D*, **85**, 064028.

Eingorn M., Fakhr S.H., Zhuk A.: 2012, *Observational constraints on Kaluza-Klein models with d-dimensional spherical compactification*.

Kapner D.J., Cook T.S., Adelberger E.G., Gundlach J.H., Heckel B.R., Hoyle C.D., Swanson H.E.: 2007, *Phys. Rev. Lett.,* **98**, 021101.

Adelberger E.G., Heckel B.R., Nelson A.E.: 2003, *Ann. Rev. Nucl. Part. Sci.*, **53**, 77.

Klimontovich Yu.L.: 1986, *Statistical physics*, Harwood Academic Publishers, Chur.

FINE TUNING PROBLEM IN FIVE-DIMENSIONAL BRANE WORLD MODELS

S.H.Fakhr[1], M.Eingorn[2], A.Zhuk[3]

[1,2,3]Astronomical Observatory, Odessa National University
[2]Department of Theoretical and Experimental Nuclear Physics,
Odessa National Polytechnic University
Odessa, Ukraine
[1]seyed.hossein.fakhr@gmail.com, [2]maxim.eingorn@gmail.com, [3]ai.zhuk2@gmail.com

ABSTRACT. Fine tuning can be called a main disadvantage of the Randall-Sundrum model, representing the most popular brane world model, constructed quite artificially in the five-dimensional space-time. It needs a bare multidimensional cosmological constant, which is related strictly to four-dimensional tension (the brane physical property).

Here we try to avoid this problem of naturalness, introducing a perfect fluid with arbitrary equations of state in both three-dimensional external and one-dimensional internal spaces parallel with the cosmological constant. It enables to preserve randomness of parameters of the considered model, which represents the direct generalization of the Randall-Sundrum one. We derive equations for background metric coefficients, determining a wide class of new exact solutions, and discuss uselessness of subsequent development of brane world models in view of their unjustified plurality.

Key words: brane world models, extra dimensions.

Extra spatial dimensions represent one of the approaches to solving such challenges of modern cosmology, astrophysics and elementary-particle physics as dark energy, dark matter and the hierarchy problem. In particular, they are introduced in extremely popular supersymmetric theories [1], pretending to being “theories of everything”. Obviously, they should be examined experimentally for compatibility with the observations. In the recent paper [2] it was explicitly shown that Kaluza-Klein models with toroidal compactification of extra dimensions contradict such famous relativistic gravitational tests as the perihelion shift, the deflection of light and the time delay of radar echoes (see [3-6]). Therefore, these models seem very doubtful, and one should look for their viable multidimensional alternatives. They are the brane world models (see the reviews [7, 8]), in which it is assumed that the Standard Model fields are localized on a three-dimensional subspace (a brane), embedded into the multidimensional space (the bulk), while gravity may propagate everywhere. In this very interesting scenario extra dimensions may be either compact or infinite, and a single brane or even several branes are admissible.

The most popular brane world model is the five-dimensional Randall-Sundrum model with one or two branes [7-10]. In this model the bulk is assumed to be empty (not counting dark energy, represented by the five-dimensional cosmological term), while the branes possess tensions (looking like the four-dimensional cosmological terms). Clearly, this scenario is very simple and unlikely well-grounded. Therefore, a natural question arises whether it can be generalized to the case of perfect fluids with arbitrary linear equations of state, filling the bulk as well as the branes.

We produced this important natural generalization and came to the following two main conclusions.

In the case of the empty bulk we found six different static background solutions, generalizing the Randall-Sundrum metrics, and established fine-tuning conditions, imposed on the cosmological constant as well as energy densities and pressures of the three-dimensional perfect fluids, situated on the branes. Consequently, the fine-tuning problem, consisting in dubious reality of such conditions, remains here unsolved.

At the same time in the case of the nonempty bulk we arrived at the situation, when there are a lot of static solutions, and the unlikely solvable problem of the physically sensible choice of the background metrics arises immediately. This unsatisfactory situation is a serious drawback of brane world models.

References

1. J.Polchinski, String Theory, Volume 2: Superstring Theory and Beyond, Cambridge University Press, Cambridge, 1998.
2. M.Eingorn and A.Zhuk: 2010, *Class. Quant. Grav.* 27, 205014.
3. C.M.Will, Was Einstein Right? Testing Relativity at the Century, in 100 Years of Relativity: Spacetime Structure – Einstein and Beyond, ed. Abhay Ashtekar, World Scientific, Singapore, 2005.
4. N.Straumann, General Relativity and Relativistic Astrophysics, Springer-Verlag, Berlin, Heidelberg, 1984.
5. L.D.Landau and E.M.Lifshitz, The Classical Theory of Fields, Fourth Edition, Volume 2 (Course of Theoretical Physics Series), Pergamon Press, Oxford, 2000.
6. C.M.Will, Theory and Experiment in Gravitational Physics, Cambridge University Press, Cambridge, 2000.
7. V.A.Rubakov: 2001, *Phys. Usp.*, **44**, 871.
8. A.O.Barvinsky: 2005, *Phys. Usp.*, **48**, 545.
9. L.Randall and R.Sundrum: 1999, *Phys. Rev. Lett.*, **83**, 4690.
10. J. Garriga and T. Tanaka: 2000, *Phys. Rev. Lett.*, **84**, 2778.

DYNAMICS OF COSMIC BODIES IN THE OPEN UNIVERSE

A.V. Kudinova[1], M.V. Eingorn[2], A.I. Zhuk[3]

[1] Department of Theoretical Physics, Odessa National University, st. Dvoryanskaya 2, 65082
Odessa, Ukraine, *autumnforever1@gmail.com*
[2] Department of Theoretical and Experimental Nuclear Physics, Odessa National Polytechnic
University, Shevchenko av. 1, 65044
Odessa, Ukraine, *maxim.eingorn@gmail.com*
[3] Astronomical Observatory, Odessa National University, st. Dvoryanskaya 2, 65082
Odessa, Ukraine, *ai.zhuk2@gmail.com*

ABSTRACT. As it has been recently demonstrated, the mathematical model with the hyperbolic space (or, in other words, with the negative spatial curvature) is the most appropriate one for describing the inhomogeneous Universe at late stages of its evolution in the framework of the theory of scalar perturbations. In this model we develop a dynamic approach and investigate nonrelativistic motion of two, three and even more cosmic bodies against the cosmological background, perturbed locally by density inhomogeneities (namely, galaxies). For arbitrary initial conditions, we get solutions of equations of motion (trajectories), demonstrating the most important features of cosmological expansion, only slightly restrained by gravitational attraction. We use our methods for indirect observations of dark energy in the Local Group, analyzing the relative motion of the Milky Way and Andromeda galaxies. The numerical estimation of the time before their collision is obtained. Besides that we consider the Hubble flows anisotropy caused by the non-point mass distribution.

Key words: inhomogeneous Universe, Local Group, Hubble flows.

1. Introduction

In this paper we consider the Universe at the late stages of its evolution deep inside of the cell of uniformity. On these scales (less than $300Mpc$) the hydrodynamic approach of the cosmic bodies motion description is inappropriate, because the space is filled with discrete structures, such as galaxies, clusters of galaxies. The background metrics is Friedmann-Robertson-Walker (FRW) metrics:

$$ds^2 = a^2 \left(d\eta^2 - \gamma_{\alpha\beta} dx^\alpha dx^\beta\right) =$$

$$= a^2 \left(d\eta^2 - \frac{\delta_{\alpha\beta} dx^\alpha dx^\beta}{\left[1 + \frac{1}{4}K\left(x^2 + y^2 + z^2\right)\right]^2}\right),$$

where $K = -1, 0, +1$ for open, flat and closed Universes, respectively. This isotropic and homogeneous background is perturbed by the discrete mass sources.

When analyzing the motion of non-relativistic objects we can write the expression for the perturbed metrics this way:

$$ds^2 \approx \left(1 + \frac{2\varphi}{ac^2}\right) c^2 dt^2 - a^2 \gamma_{\alpha\beta} dx^\alpha dx^\beta .$$

For every $i-$th mass of the system the Lagrange function can be written:

$$L_i = -\frac{m_i \varphi_i}{a} + \frac{m_i a^2 v_i^2}{2},$$

where φ_i is the gravitational potential, and v_i is the comoving peculiar velocity. The gravitational potential is taken in the Newtonian approximation:

$$\varphi_i = -G_N \sum_{j \neq i} \frac{m_j}{|\mathbf{r}_i - \mathbf{r}_j|} .$$

Based on these expressions, we can analyze the motion of objects of arbitrary mass systems.

2. Cosmological "molecular" dynamics

In this section we will apply our mechanical approach to mass systems of different number of particles. We can build the system of Langrange equations. Adding the known initial conditions we can solve such systems numerically and analyze the trajectories of the cosmic bodies' motion in the case of the background cosmological receiding.

To start with, we consider the system of three test particles. The solution of the corresponding Lagrange equations can be visualized on the scheme.

Let us suppose the following initial conditions: $m_A = m_B = m_C = \overline{m}$ and $\tilde{X}_A|_{\tilde{t}=0} = 0$, $\tilde{Y}_A|_{\tilde{t}=0} = -1.5$,

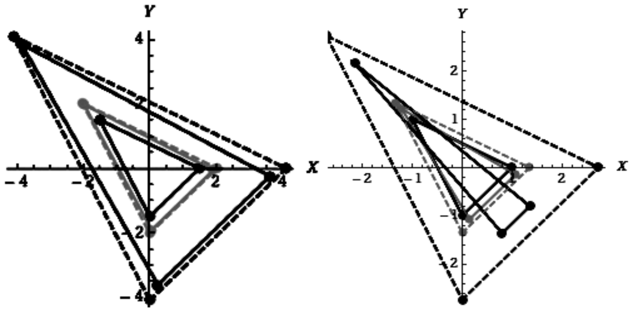

Figure 1: Dynamics of three points motion.

$\tilde{X}_B|_{\tilde{t}=0} = 1.5$, $\tilde{Y}_B|_{\tilde{t}=0} = 0$, $\tilde{X}_C|_{\tilde{t}=0} = -1.5$ $\tilde{Y}_C|_{\tilde{t}=0} = 1.5$, $d\tilde{X}_i/d\tilde{t}|_{\tilde{t}=0} = 0$, $d\tilde{Y}_i/d\tilde{t}|_{\tilde{t}=0} = 0$.

The red triangle with vertices $(0, -1.5)$, $(1.5, 0)$ and $(-1.5, 1.5)$ (see Figure 1, left part) showes the initial position of particles (at $\tilde{t} = 0$). Smooth (where both cosmological expansion and gravitational attraction are taken into account) and dashed (only cosmological expansion) green triangles illustrate the position of particles at $\tilde{t} = 1$, blue ones – at $\tilde{t} = 2$. Two different peculiarities of the motion can be seen on the above mentioned diagrams: smooth triangles are enclosed in the corresponding dashed triangles, meaning that gravitational interaction inhibits expansion. The second feature is that in the case of attraction absence the points A and B, located on the axes of coordinates, recede along the axes (point C recedes along the direction of its initial radius vector). This fact is confirmed by the constructed dashed triangles; in the presence of attraction the points do not recede along the coordinate axes (or along the initial radius vectors), which is confirmed by the smooth triangles.

If we change the initial conditions for the following $\tilde{Y}_A|_{\tilde{t}=0} = -1$, $\tilde{X}_B|_{\tilde{t}=0} = 1$, $\tilde{X}_C|_{\tilde{t}=0} = -1$ and $\tilde{Y}_C|_{\tilde{t}=0} = 1$, the test points will get closer to each other at $\tilde{t} = 0$, and the diagrams will take the form of the right part of Figure 1.:

There is a distinction in kind between these two situations. Gravitational attraction of points A and B predominate cosmological expansion between them, so they start to close in and will collide in the future. At the same time point C becomes gravitationally unbound, so it starts to move off.

The same procedure can be applied to the case of four test masses.

We make an assumption that $m_A = m_B = m_C = m_D = \overline{m}$ and $d\tilde{X}_i/d\tilde{t}|_{\tilde{t}=0} = 0$, $d\tilde{Y}_i/d\tilde{t}|_{\tilde{t}=0} = 0$. On the left side of the diagram (see Figure 2) at $\tilde{t} = 0$ the points form the square with verteces $(1, 1)$, $(1, -1)$, $(-1, -1)$ and $(-1, 1)$, on the right side of the diagram – with verteces $(0.75, 0.75)$, $(0.75, -0.75)$, $(-0.75, -0.75)$ and $(-0.75, 0.75)$.

The squares can be rebuilt with the different initial conditions.

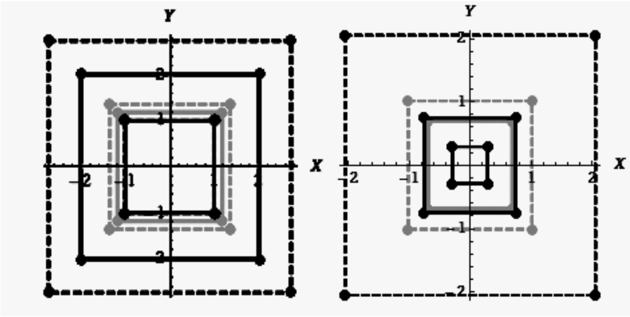

Figure 2: Dynamics of four points motion.

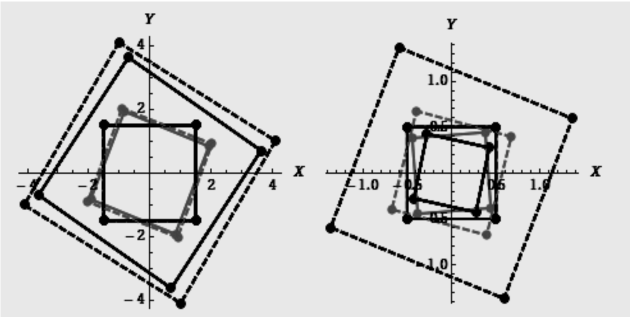

Figure 3: Dynamics of four points with initial non-zero velocities.

In this case the test points have the initial non-zero velocities. On the left side of the diagram (srr Figure 3) the points form the square with verteces $(1.5, 1.5)$, $(1.5, -1.5)$, $(-1.5, -1.5)$ and $(-1.5, 1.5)$ at $\tilde{t} = 0$, their velocities are $(0, -1)$, $(-1, 0)$, $(0, 1)$ and $(1, 0)$ correspondingly, on the right side of the diagram the verteces' coordinates are $(0.5, 0.5)$, $(0.5, -0.5)$, $(-0.5, -0.5)$ and $(-0.5, 0.5)$, velocities take the following values: $(0, -0.25)$, $(-0.25, 0)$, $(0, 0.25)$ and $(0.25, 0)$.

3. The collision between the Milky Way and Andromeda

Besides the illustrative examples we can apply our approach to some real mass systems. One of the most convenient and informative system of gravitating sources we can observe and analyze is the Local Group containing out galaxy, the Milky Way, Andromeda galaxy and some dwarf galaxies. Building the system of Lagrange equations for the system of two bodies, particularly, for M31 and M33 galaxies, we can describe the dynamics of the Milky Way and Andromeda collision and obtain the numerical estimation of the time before their collision. In the centre-of-mass system we can get the equation of motion in the following form:

$$\ddot{L} = -G_N \frac{m_A + m_B}{L^2} + \frac{M^2}{\mu^2 L^3} + \frac{\ddot{a}}{a} L$$

where L is the absolute value of the distance between the galaxies' centres.

The following plot illustrates the dynamics of the galaxies' approach:

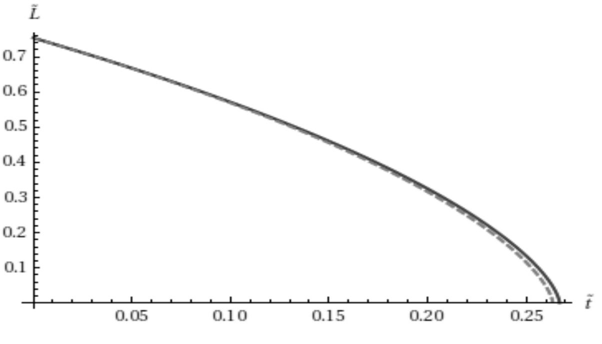

Figure 4: Dynamics of The Milky Way and Andromeda galaxies approach.

The collision of the Milky Way (of the mass $10^{12}\, m_\odot$) and Andromeda (of the mass $1.6 \times 10^{12}\, m_\odot$), located on the "physical" distance of 0.78 Mpc at the present time and approaching with the "physical" velocity 120 km/s, will occure in 0.2670 of Hubble time, i.e. 3.68 billion years. Without the gravitational attraction this collision will occure in 0.48 of Hubble time, i.e. 6.6 billion years. On the contrary, without taking into account the cosmological expansion, the collision will occur in 0.2636 of Hubble time, i.e. 3.63 billion years. Relative deviation of this estimation from the previous one is about 1,5 percent.

4. Hubble flow anisotropy

Dwarf galaxies in the Local Group form Hubble flows around the massive giant galaxies, the Milky Way and Andromeda. But the distance between these galaxies is significant enough to cause the flows anisotropy. We can consider the system of these two gravitating masses and analyze the acceleration of the test bodies in the resulting gravitational field.

We have built the 3D plot of the acceleration (see Figure 5). At the fixed moment of time it illustrates the spatial distribution of the acceleration value. Gravitating masses, the Milky Way and Andromeda galaxies, are placed in the centres of the plot peaks.

Besides that, we can visualize the localization of the zero-acceleration points (see Figure 6). Analysis indicates that there are no surfaces of zero-acceleration, but only the finite number of points of zero-acceleration. The yellow line on the plot shows the lines of the zero x-component of acceleration, the green line shows the line of the zero y-component of acceleration. Points of their intersection define the points of zero acceleration. Black points on the plot indicate the positions of the gravitating masses.

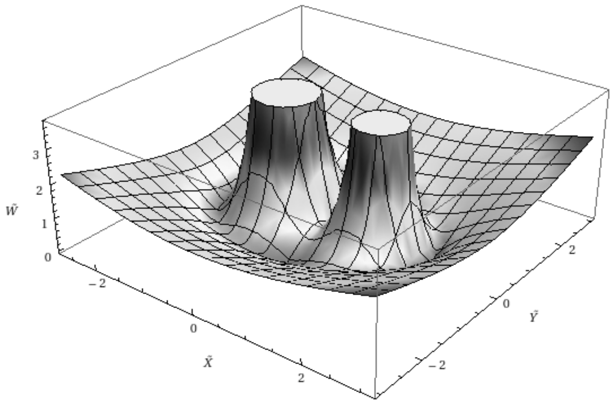

Figure 5: 3D-plot of the acceleration value in the Local Group.

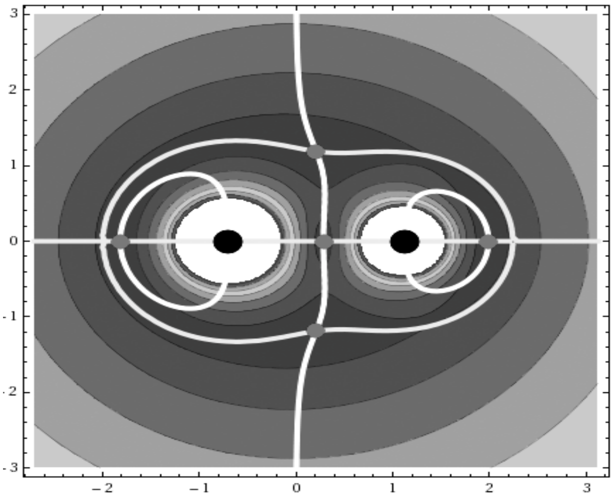

Figure 6: Points of the zero acceleration.

References

Eingorn M.V., Zhuk A.I.: 2012, *J. Cosmol. Astropart. Phys.*, **09**, 26.

Cox T.J., Loeb A.: 2008, *Astron.,* **07**, 28.

Roeland P. van der Marel, Gurtina Besla, T.J.Cox et al.: 2012, *ApJ,* **753-9.**

MOTIONS BY INERTIA AND THE COULOMB FIELD

Oleinik V.P.

Institute of High Technologies
Kiev National Taras Shevchenko University, Ukraine
valoleinik@gmail.com

ABSTRACT. It is proved that there exist accelerated motions by inertia which dropped out of the field of view of classical mechanics. The Coulomb law is not shown to be a universal and fundamental law of physics. Universal formula for the force of interaction between two particles does not exist.

Key words: Galileo's principle of inertia, accelerated motion by inertia, Coulomb's law.

According to Galileo's principle of inertia, there exists a frame of reference in which free body moves uniformly and rectilinearly. Newtonian mechanics is based on the assumption that this motion (called translational inertia) is the only kind of motion by inertia existing in nature. As the analysis of the motion problem shows [1, 2], a huge class of motions, which are natural extensions of translational inertia to curvilinear motions, drops out of sight of Newtonian mechanics. The case in point is the motions of particles with acceleration, which does not require any energy expenditure. We call them the accelerated (curvilinear) motions by inertia.

To reveal the physical nature of the phenomenon of curvilinear motion by inertia, let us turn to the equation of motion in classical mechanics $m\vec{a} = \vec{F}_{ext}$, where m and $\vec{a}$ are mass and acceleration of particle, $\vec{F}_{ext}$ is the force acting on the particle from its surroundings (the external force). This equation determines the forced motion of the particle under the action of external force, which is the cause of acceleration.

Consider now the motion of particle in terms of kinematics. According to the definition of the force accepted in mechanics, if a particle moves along a trajectory, there acts on the particle the force $\vec{F} = m\ddot{\vec{r}}$, where $\vec{r} = \vec{r}(t)$ is the radius vector of the particle at time t. Let us formulate the following problem: to find such a particle motion, in which the force acting on the particle does not do any work at any displacement of it along its trajectory. In this formulation, the force $\vec{F}$ is not the cause of accelerated motion, as in the equation of motion of mechanics, but its consequence. It does not force the particle to move, but only is an accompaniment of motion: the particle moves freely, without coercion and without any energy expenditure, i.e. by inertia. Solutions to the problem stated above describe a huge class of motions, which are accelerated motions of particles by inertia. So, there may exist both the motions, in which the force acts as an external force and is the cause of acceleration, and the motions, in which the force is generated by acceleration and is of purely kinematic origin. Arbitrary motion D of particle can be represented as a superposition of the accelerated motion by inertia D_{in} and the forced motion D_f: $D = c_1 D_{in} + c_2 D_f$ (c_1, c_2 are const). If the components of motion D are plotted on the axes of plane coordinate system, to Newtonian mechanics there corresponds only one point of the D_{in} axis: $c_1 = 0,\ c_2 = 1$. Thus, a continuum of motions is outside the field of view of the theory– such is the degree of incompleteness of Newtonian mechanics as a method of studying nature.

Accelerated motions by inertia are due to the inhomogeneity and anisotropy of space in which the particle moves [1,2]. In the inhomogeneous and anisotropic space, the particle tends to move without any energy expenditure. It is just this motion which represents the accelerated (curvilinear) motion by inertia and which may last infinitely long.

According to the conventional notions, the material body having charge (electric or gravitational) generates in surrounding space the Coulomb field, the physical nature of which is still not known [3]. Analysis of curvilinear motion by inertia of two-particle system [1] shows that the form of the law for the interaction force between the particles essentially depends upon relative motion of particles and upon the motion of the center of mass of the system. A wide variety of the force fields, connecting the moving particles in two-particle system, testifies that it is impossible in principle to specify a single, universal formula for the interaction force acting between the particles. The physical nature of the Coulomb field is not established so far for the reason that the Coulomb force as a single universal force of interaction between particles does not exist in nature. Obviously, because the character of the force interaction between particles is determined by a huge number of physical factors, any math tricks, such as the introduction of curvature or tortion of space, the involvement of the most fundamental physical principles, and many others, will not help us to find the universal force of interaction.

References

1. Oleinik V.P., Prokofjev V.P.: 2008, Physics of consciousness and life, cosmology and astrophysics, **8**, №2, 23-56;
2. Oleinik V.P.: 2009, ibid, **9**, №3, 24-56; 2010, ibid, **10**, №3, 24-55; 2012, ibid, **12**, №1, 17-54.
3. Feynman R. The character of physical law. Cox and Wyman LTD, London, 1965.

ISOLATED CLUSTERS OF PF CATALOGUE

E. Panko [1], S.Andrievsky [2]

[1] Nikolaev National University named after V.O. Sukhomlinsky,
Kalinenkov Astronomical Observatory, Nikolaev, Ukraine

[2] Department of Astronomy and Astronomical Observatory
Odessa National University, T.G. Shevchenko Park, Odessa 65014, Ukraine
[1]panko.elena@gmail.com, [2]scan-d@te.net.ua

ABSTRACT. The properties of isolated galaxy clusters are discussed. The clusters were found among 1746 PF clusters inclusive 50 and more galaxies in structure field. For 19 clusters with distances to the nearest neighbour larger than 68.5 h^{-1} Mpc we assigned the morphological types of these clusters according to Abell and Bauts & Morgan. The existence of preferential planes and angular momenta of isolated clusters was assumed. We connect evolution of isolated clusters with common large-scale characteristics.

Key words: large-scale structure: galaxy clusters

1. Introduction

The distribution of galaxy clusters, the largest virialized structures in the Universe, reflects the initial density perturbations. The characteristics of galaxy clusters both placed in rich regions and isolated ones can be used for better understanding of the formation of the large-scale structure.

Although considerable quantity of clusters belong to the larger-scale structures (Wray et al. 2006, Einasto et al. 2007, Panko 2011), there exist isolated clusters without neighbours. Lee (2012) investigated their relative abundance in connection with the dark energy equation of state. Godlowsky et al. (2012) compared the orientations of galaxies in clusters placed in and out of superclusters and found an influence on large scale structures formation both from nearest clusters and Supergalaxy.

The present study investigates the features of isolated galaxy clusters of PF catalogue (Panko & Flin 2006).

2. Observational data

The Catalogue of Galaxy Clusters and Groups (Panko & Flin 2006) was used as the input data for this investigation. The catalogue was created using data from the Muenster Red Sky Survey (Ungruhe et al. 2003), which is a large-scale homogeneous galaxy catalogue covering an area of about 5000 square degrees with galactic latitudes $b < -45°$. It is complete to a magnitude limit of $r_F = 18^{m}.3$. The same r_F magnitude limit defines the completeness limit for galaxies in the PF structures.

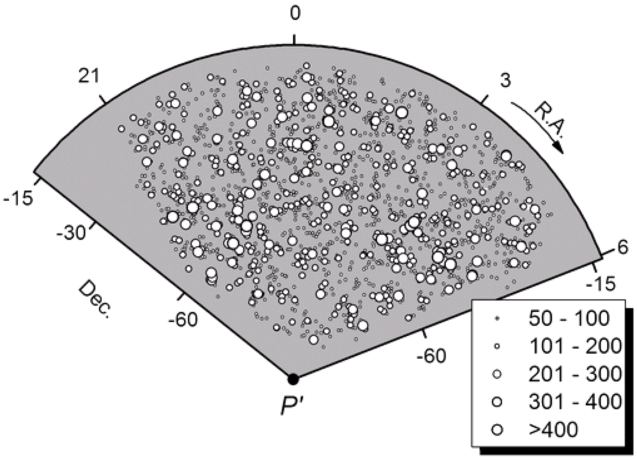

Figure 1: The distribution of PF clusters on the celestial sphere, symbol size correlates with the galaxy cluster richness.

For each of 6188 structures, were found the richness, area, major and minor semiaxes, and ellipticity parameter of the best ellipse.

Kolmogorov-Smirnov test applied to distribution of ellipticities in sets of PF objects with different richness indicates that structures containing more than 50 members in the structure field belong to some population, but others are members of another population (Biernacka et al. 2009*a*). First population was attributed as normal and rich galaxy clusters. Second population contains groups of galaxies and poor galaxy clusters. The distribution of

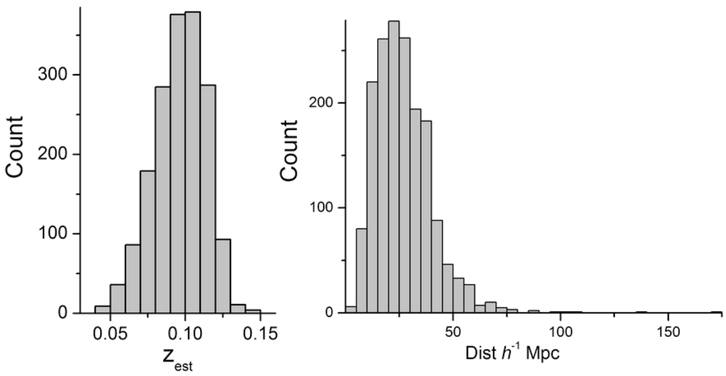

Figure 2: The distributions of redshifts (left panel) and distanced for nearest neighbours of PF clusters input list.

clusters from first population describes global large-scale features and second one detailed it (Panko 2008).

The positions on the celestial sphere of 1746 PF clusters input list is shown on Fig. 1 and rich and poor regions are clearly seen. The list of these PF clusters we shall name input list hereinafter. Galaxies of Muenster Red Sky Survey have no redshifts, so PF structures, have no redshifts too. In order to estimate distances for the PF structures, we calibrated the $\log z - m$ relation following Dalton et al. (1997), using the magnitude of the tenth brightness galaxy m_{10} as m in the calibration. We used dependence:

$$\log z_{\mathrm{est}} = -3.771+0.1660\, m_{10}\,, \quad (1)$$

based upon 455 data points from the ACO (Abell, Corwin & Olowin 1989) comparison and 374 from the APM (Dalton et al. 1997) comparison (Biernacka et al. 2009b). The distribution of estimated redshifts of PF clusters input list is shows in Fig. 2, so the detected isolated clusters are not remote objects.

For the search of superclusters, the *Friend-of-Friend* method (*FoF*) was applied (Panko 2009), and for each cluster from input list the distances to the nearest neighbours were calculated. They lie within 4.6 and 173.7 h^{-1} Mpc (Fig. 2, right panel). Although Lee (2012) in his analysis took into consideration as isolated all clusters placed out of the superclusters, we assigned minimal distance to the nearest neighbour for isolated clusters as 68.5 h^{-1} Mpc. This limit was formally obtained using mean value and standard deviation of all distances. It is rigid criterion, and we assumed that the formation of these clusters was defined by a global distribution of the matter.

This condition is met for only 20 clusters from input list.

3. The properties of isolated PF clusters

Taking into account the richness limit for the input data, we checked the positions of poor PF structures in environs of the 20 detected clusters. One cluster, PF 0540-5764, was excluded from further analysis. Its nearest neighbour distance – 173.7 h^{-1} Mpc – is the largest for all input PF clusters, but it places close by bound of the Muenster Red Sky Survey.

We compared the positions of 19 isolated clusters on the celestial sphere with the positions of the ACO clusters. Common information about isolated PF clusters is given in Appendix A. The estimated redshifts of isolated clusters are in the range from 0.041 to 0.144, and we found no correlation between parameters of clusters. Three clusters belong to the rich cluster population, while others contain from 50 to 88 galaxies in the cluster field with a mean value of 60. Only 8 PF isolated clusters correspond with those in the ACO, and only 4 of them have measured redshifts.

We assigned morphological types to isolated clusters using the Abell (1958), Bauts & Morgan (1970), and Rood & Sastry (1971) classifications (Appendix A, second column). Abell types were R – regular, I – irregular and intermediate types RI and IR. Bauts & Morgan (BM) types are defined by the positions of several brightest galaxies, and BM I is a cluster containing a c*D* galaxy. For all isolated clusters we plotted their maps, with positions of the brightest galaxies taken into account. Two such cluster maps are shown in Fig. 4.

Our morphological types agree with the types from the ACO catalogue for three clusters: PF 0381-1789 (ACO 464), PF 2380-3628 (ACO 4039), and PF 2380-3628 (ACO 2877); two of them are of BM type I. Two clusters clearly correspond to the Rood & Sastry L-type. The common distribution of isolated clusters by Abell and BM types is given in Table 1.

Table 1: Morphological type's distribution of isolated clusters.

Abell types		BM types	
R	5	I	4
RI	11	I-II	–
IR	3	II	5
I	–	II-III	3
		III	7

In a comparison of counts for BM types of all ACO clusters corresponding to PF clusters (Panko et al. 2009) with similar richness we note an excess of BM type III clusters. There is no dominant galaxy in clusters of this type. Along with an ellipticity range from 0.11 to 0.39, the excess is evidence of the influence of more distant

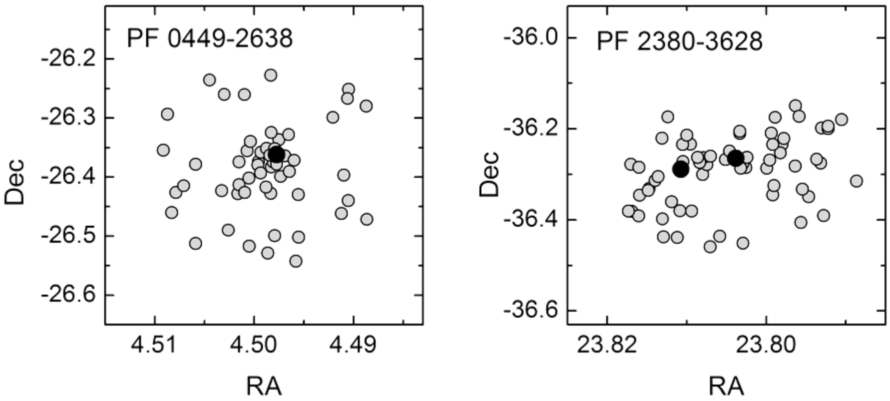

Figure 3: The BM I (left panel) and II clusters.

objects on the evolution of clusters, or a connection of cluster shape with common large-scale characteristics.

Values for the ellipticities argue for the existence of a preferential plane and angular momentum for clusters. The mean ellipticity of isolated clusters of E_{isol}=0.20 is equal to the mean ellipticity of PF structures containing 50 or more galaxies in the structure field. We assume the existence of a mean residual ellipticity for galaxy clusters independent of neighbours. Moreover, a preferential plane of clusters confirms Gamow's (1946) idea of a common Universe rotating (see, for example, Birch P. 1982, Flin et al. 2007).

4. Conclusion

We analyzed the nearest neighbour for 1746 PF clusters containing 50 or more galaxies in the structure field. The critical distance separating isolated clusters from others was formally defined using the mean value and standard deviation of all distances. We selected this sharp criterion with the result that it connects the properties of isolated clusters with those for global large-scale characteristics.

We found 19 isolated PF clusters and assigned morphological types to the clusters according to the Abell and Bauts & Morgan schemes. Features of the distribution of morphological types and mean value of ellipticities show the existence of preferential planes and angular momenta for isolated clusters.

Acknowledgements. The present research has made use of the NASA/IPAC Extragalactic Database (NED) and the NASA Astrophysics Data System. EP thanks the Jan Kochanowski University for partially support of this work.

References

Abell, G.O.: 1958, *ApJS,* **3**, *211.*

Abell G.O., Corwin H.G., Olowin R.P.: 1989, *ApJS*, **70**, 1.

Bautz L.P., Morgan W.W.: 1970, *ApJ*, **162**, L149.

Biernacka M., Flin P., Juszczyk T., Panko E.: 2009a, "The Properties of Nearby Galaxy Structures", in *Cosmology Across Cultures*, edited by J.A.Rubino-Martin, J.A.Belmonte, F.Prada, and A.Alberdi, *ASP Conference Series*, **409**, 29.

Biernacka M., Flin P., Panko E.: 2009b, *ApJ*, **696**, 1689.

Birch P.: 1982, *Nature*, **298**, 451.

Dalton G.B., Maddox S.J., Sutherland W.J., Efstathiou G.: 1997, *MNRAS*, **289**, 263.

Einasto J., Einasto M., E. Tago, E. Saar et al.: 2007, *A&A*, **462**, 811.

Flin P., Godłowski W., Szydłowski M.: 2007 "Is the Universe rotating?" in "Astrophysics and Cosmology After Gamow", eds. G. S. Bisnovaty-Kogan, S. Silich, E. Terlevich, R. Terlevich and A. Zhuk. – Cambridge Scientific Publishers, Cambridge, UK, 287.

Gamow G.: 1946, *Nature*, **158**, 549.

Lee J.: 2012, http://arxiv.org/abs/1108.1712v2.

Panko E.: 2008, *Odessa Astronomical Publications*, **21**, 88.

Panko E.: 2009, "A Catalogue of Galaxy Clusters and Groups as the Basis for a New Galaxy Supercluster Catalogue", in: "Astrophysics and Cosmology after Gamow". Proceedings of the 4th Gamow International Conference on Astrophysics and Cosmology after Gamow and The 9th Gamow Summer School, Odessa, Ukraine 17 – 23 August 2009, eds. S.K.Chakrabarti, G.S.Bisnovatyi-Kogan and A.I.Zhuk. – Melville, New York, 2009, *AIP Conference Proceedings*, **1206**, 417.

Panko E., Juszczyk T., Flin P.: 2009, *AJ*, **138**, 1709.

Panko E.: 2011, *Baltic Astronomy,* **20***,* 313.

Panko E., Flin P.: 2006, *J. Astron. Data*, **12**, 1.

Rood H. J., Sastry, G. N.: 1971, PASP. **83**, 313.

Wray J.J., Bahcall N.A., Bode P., Boettiger C., Hopkins P.F.: 2006, *ApJ*, **652**, 907.

Ungruhe R., Seitter W.C., Duerbeck H.W.J.: 2003, *J. Astron. Data*, **9**, 1.

NED: The NASA/IPAC Extragalactic Database: http://ned.ipac.caltech.edu/

Appendix A.

Parameters of PF isolated clusters.

The columns of the Table contain the following information:

Ident – structure identification, based on the first digits of R.A. and Dec.;
Classification – our classification according to Abel and Boutz & Morgan (as L marked clusters with clear L-type Rood & Sastry);
R.A., Dec. – Right Ascension and Declination for 2000.0;
N – the number of all galaxies in the cluster field;
a – semi-major axis of the fitted ellipse;
E – ellipticity of the cluster;
PA – the position angle of the semi-major axis of cluster,
z_{est} – estimated redshift according to relation 1;
$D_{nearest}$ – distance to the nearest neighbour in h^{-1}Mpc,
ACO – corresponding cluster in ACO Catalogue;
Klass A and BM – Abell and Boutz & Morgan types from ACO catalogue.

Ident	Classifications			R.A.	Dec.	N	*a*	*E*	PA	z_{est}	$D_{nearest}$	ACO	Klass A	BM
0016-5711		IR	II-III	0.167074	-57.107367	88	907	0.32	117.4	0.053	68.9	2731	I	III:
0024-2431		IR	III	0.247237	-24.300611	52	639	0.39	43.7	0.129	78.5			
0096-3921		RI	III	0.962162	-39.205838	52	655	0.11	69.8	0.142	136.9			
0115-4600	L	R	I	1.156725	-45.996573	260	1251	0.17	178.9	0.041	105.4	2877	R	I
0200-2252		RI	III	2.003679	-22.519040	52	690	0.12	105.5	0.133	73.0	S 213	R	I-II
0240-4218		R	II	2.402386	-42.175194	56	608	0.11	14.6	0.140	98.3	3014	I	III
0358-6952		RI	II	3.587338	-69.511811	53	1045	0.19	67.0	0.126	68.8			
0381-1789		R	I	3.817120	-17.885726	308	1688	0.24	38.9	0.069	73.5	464	R:	I
0397-6046		IR	III	3.973661	-60.450522	75	912	0.12	178.8	0.115	71.4			
0413-3091		RI	II	4.133604	-30.907580	271	1129	0.11	170.5	0.064	77.0	3223	RI	I
0444-3673	L	RI	II	4.446484	-36.724150	56	749	0.14	18.8	0.133	101.0			
0449-2638		R	I	4.498747	-26.377217	54	548	0.14	12.4	0.124	68.9	495	R	III
0450-6452		RI	III	4.501420	-64.516471	59	705	0.25	178.9	0.118	71.4			
0501-3610		R	II	5.017765	-36.090484	61	621	0.13	30.8	0.123	78.0			
2114-3750		RI	III	21.143841	-37.493762	55	748	0.25	45.7	0.127	69.0			
2175-1751		RI	III	21.750021	-17.503100	79	656	0.11	44.6	0.125	87.4			
2190-6118		RI	II-III	21.909741	-61.171245	58	681	0.28	34.3	0.119	73.1			
2195-7771		RI	I	21.956714	-77.709296	50	872	0.28	11.0	0.144	89.1			
2380-3628		RI	II	23.804412	-36.274714	65	734	0.35	61.3	0.126	69.7	4039	R:	II:

HIGHLY RELATIVISTIC CIRCULAR ORBITS OF SPINNING PARTICLE IN THE SCHWARZSCHILD AND KERR FIELDS

R.M. Plyatsko, M.T. Fenyk

Pidstryhach Institute for Applied Problems in Mechanics and Mathematics
of Ukrainian National Academy of Sciences,
Lviv, Ukraine, *plyatsko@lms.lviv.ua*

ABSTRACT. The solutions of the Mathisson-Papapetrou equations which describe highly relativistic circular orbits of a spinning particle in Schwarzschild's and Kerr's fields are considered. The domain of existence of those orbits and the necessary values of the particle's velocity for their realization are studied. These results can be applied while analyzing the synchrotron radiation in some astrophysical processes.

Key words: Mathisson-Papapetrou equations; highly relativistic spinning particle; gravitational field.

There are two possibilities to investigate the effects of interaction of the particle spin with the gravitational field on its motion in this field: (1) For a classical (nonquantum) particle the equations firstly derived by M.Mathisson [1] are effectively used; (2) For a quantum fermion particle one can use the general relativistic Dirac equation. It is important that in some quasiclassical limit the Mathisson equations follow from the Dirac equation. Just the Mathisson equations (also known as the Mathisson-Papapetrou equations) are in the focus of our consideration and now we continue the program of studying the specific properties of the highly relativistic motions of a spinning particle relative to the Schwarzschild and Kerr black holes. In this paper we present the results on highly relativistic essentially nongeodesic circular orbits of a spinning particle in the Schwarzschild and Kerr backgrounds. Note that practically any textbook on general relativity contains information concerning possible geodesic circular orbits of a spinless test particle in a Schwarzschild background as an important point of description of the black hole properties. On the contrary, the similar information on possible circular orbits of a spinning test particle in this background is not presented in the literature. Among other types of motions the circular highly relativistic orbits are of importance for investigations of possible synchrotron radiation, both electromagnetic and gravitational, of protons and electrons in the gravitational field of a black hole.

As in [2], we shall consider the Mathisson-Papapetrou equations under the Mathisson-Pirani supplementary condition in the Kerr metric using the Boyer-Lindquist coordinates $x^1 = r, \quad x^2 = \theta, \quad x^3 = \varphi, \quad x^4 = t$. However, in contrast to [2], where these equations were considered in some approximation, here we deal with the Mathisson-Papapetrou equations in their exact form. Our purpose is to investigate the equatorial circular orbits of a spinning particle in the plane $\theta = \pi/2$ of the Kerr source, when the spin is orthogonal to this plane. Then it follows from the MP equations that the space region of existence of the circular orbits and the dependence of the particle velocity for these orbits on their radius are determined by the solutions of set of the two algebraic equations. These equations can be written as

$$\begin{gathered}(\alpha^2 - y_1^3)y_7^2 - 2\alpha y_7 y_8 + y_8^2 - 3\alpha\varepsilon_0(y_1^2+\alpha^2)y_7^2 y_1^{-2} \\ +3\varepsilon_0(y_1^2+2\alpha^2)y_7 y_8 y_1^{-2} - 3\alpha\varepsilon_0 y_8^2 y_1^{-2} \\ +\alpha\varepsilon_0(3y_1^2+\alpha^2)(y_1^3-\alpha^2)y_7^4 y_1^{-3} - \alpha\varepsilon_0\left(1-\frac{2}{y_1}\right)y_8^4 y_1^{-3} \\ +\varepsilon_0(y_1^6 - 3y_1^5 - 3\alpha^2 y_1^3 + 9\alpha^2 y_1^2 + 4\alpha^4)y_7^3 y_8 y_1^{-3} \\ +\alpha\varepsilon_0(3y_1^3 - 11y_1^2 - 6\alpha^2 + 2\alpha^2 y_1^{-1})y_7^2 y_8^2 \\ +\varepsilon_0(4\alpha^2 - 4\alpha^2 y_1^{-1} - y_1^3 + 3y_1^2)y_7 y_8^3 y_1^{-3} = 0, \qquad (1)\end{gathered}$$

$$\begin{gathered}-\left(y_1^2+\alpha^2+\frac{2\alpha^2}{y_1}\right)y_7^2 + \frac{4\alpha y_7 y_8}{y_1} \\ +\left(1-\frac{2}{y_1}\right)y_8^2 = 1, \qquad (2)\end{gathered}$$

where y_i are the dimensionless quantities connected with the particle coordinate and 4-velocity by the definition

$$y_1 = \frac{r}{M}, \quad y_2 = \theta, \quad y_3 = \varphi, \quad y_4 = \frac{t}{M},$$

$$y_5 = u^1, \quad y_6 = Mu^2, \quad y_7 = Mu^3, \quad y_8 = u^4,$$

here M is Kerr's mass. The values ε_0 and α in Eqs. (1) and (2) are determined as

$$\varepsilon_0 \equiv \frac{S_0}{mM}, \quad \alpha \equiv \frac{a}{M},$$

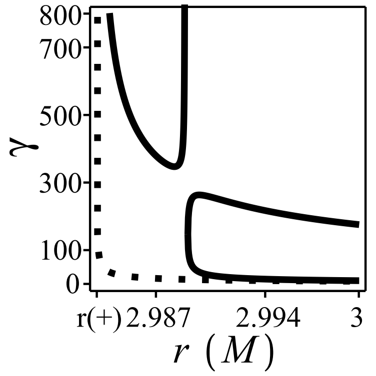

Figure 1: Dependence of the Lorentz factor on r for the highly relativistic circular orbits with $d\varphi/ds > 0$ of the spinning particle in Kerr's background at $a = 0.0145M$, $\varepsilon_0 = 0.01$ (solid lines). The dotted line corresponds to the geodesic circular orbits.

where $|S_0|$ is the absolute value of the particle spin and a is the Kerr angular momentum; according to the test condition for a spinning particle it is necessary $|\varepsilon_0| \ll 1$. Note that among eight values y_i only three of them, namely y_1, y_7 and y_8, are present in Eqs. (1) and (2), because for the circular motions we have $y_5 = 0$ and $y_6 = 0$. Therefore, for any fixed value of the radial coordinate, i.e. y_1, we have the two algebraic Eqs. (1) and (2) which let us find the necessary values of y_7 and y_8. By these values of y_1, y_7, y_8 one can calculate the relativistic Lorentz γ-factor of a moving particle as estimated by an observer which is at rest relative to the Kerr mass. The expression for this γ-factor for any circular motions in the equatorial plane is

$$\gamma = \left(1 - \frac{2}{y_1}\right)^{1/2} \left(y_8 + \frac{2\alpha y_7}{y_1 - 2}\right). \tag{3}$$

It is known that the geodesic equations in Kerr's background admit the highly relativistic circular orbits of a particle with the nonzero mass only in the small neighborhood of the values $r_{ph}^{(+)}$ and $r_{ph}^{(-)}$ that are the radial coordinates of the co-rotating and counter-rotating circular photon orbits.

Figures 1–4 illustrate both the domain of existence of the circular orbits and the dependence of the γ-factor on the radial coordinate for these orbits at some typical cases of different values of the Kerr parameter a, when $|\varepsilon_0| = 10^{-2}$. Figure 1 describe the case $a = 0.0145M$, when $r_{ph}^{(+)} \approx 2.983$ and $r_{ph}^{(-)} \approx 3.017$. Note that for $r \le r_{ph}^{(+)}$ there are not any circular orbits of the spinning particle, i.e. this situation is the same as for the spinless particle. In the narrow space region between $r = r_{ph}^{(+)}$ and $r \approx 3.006M$ there are the highly relativistic circular orbits with the much higher Lorentz factor than it is necessary for the spinless particle (for comparison the dotted line in Fig. 1 shows the curve for the

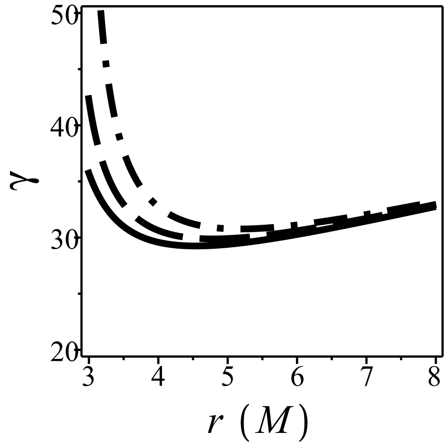

Figure 2: Lorentz factor vs. r for $\varepsilon_0 = 0.01$, $d\varphi/ds > 0$ at $a = 0.1M$ (dash-dotted line), $a = 0.5M$ (dashed line), and $a = M$ (solid line).

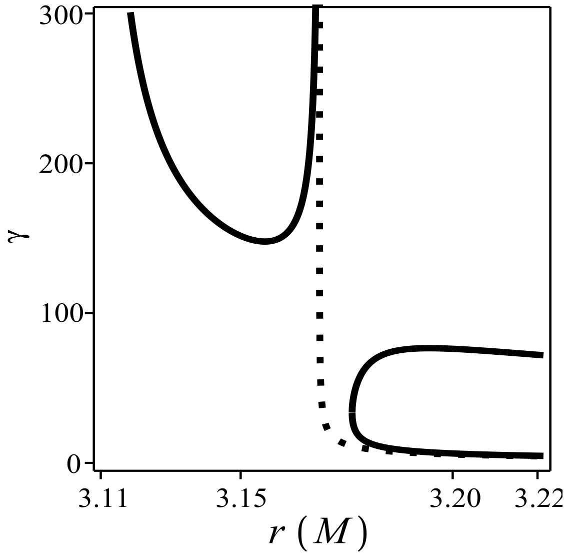

Figure 3: Lorentz factor vs. r for the highly relativistic circular orbits of the spinning particle in Kerr's background with $\varepsilon_0 = -0.01$, $d\varphi/ds < 0$ of the spinning particle in Kerr's background at $a = 0.15M$. The dotted line corresponds to the geodesic circular orbits with $r_{ph}^{(-)} \approx 3.17M$.

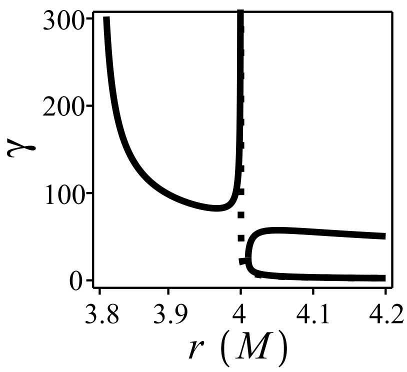

Figure 4: Lorentz factor vs. r for the highly relativistic circular orbits of the spinning particle in Kerr's background with $\varepsilon_0 = -0.01$, $d\varphi/ds < 0$ of the spinning particle in Kerr's background at $a = M$. The dotted line corresponds to the geodesic circular orbits with $r_{ph}^{(-)} = 4M$.

geodesic motion). We stress that the existence of those orbits is caused by the interaction of the particle's spin with the angular momentum of Kerr's source: in the Schwarzschild background the corresponding orbits are absent according to Fig. 1 from [3]. Also note that by the solutions of Eqs. (1) and (2) the necessary value γ tends to ∞ if a tends to 0. In the wide space region for r larger than $r \approx 3.006M$ Eqs. (1) and (2) admits for any fixed value r the two circular orbits and in this sense Fig. 1 below is similar to Fig. 1 from [3] for the Schwarzschild background.

Figure 2 shows the dependence γ on r for different values a in the space domain far from $r = r_{ph}^{(+)}$. For r grater than $r \approx 8M$ all the curves in Fig. 2 tend to the corresponding curve for Schwarzschild's case. We stress that all the curves $\gamma(r)$ for the spinning particle lay above the corresponding geodesic lines, i.e. here the spin-gravity interaction causes an additional significant attractive action as compare to the usual geodesic attraction.

In contrast to Figs. 1 and 2, Figs. 3 and 4 show the situations with another direction of the particle orbital motion, when $d\varphi/ds < 0$, and for the opposite orientation of the spin, when $\varepsilon_0 < 0$ (the last means that $S_\theta < 0$). The graphs in Figs. 3 and 4 which are located in the region with $r < r_{ph}^{(-)}$ describe the specific effects just in Kerr's field, in contrast to the graphs in the region $r > r_{ph}^{(-)}$ which are similar to the corresponding graphs for Schwarzschild's field. The existence of the orbits in the region $r < r_{ph}^{(-)}$ points out that in the case when $a > 0$, $\varepsilon_0 < 0$ and $d\varphi/ds < 0$ the spin-gravity interaction supplies the repulsive action on the spinning particle as compare to the motion of a spinless particle.

Since, according to Figs. 1–4 and others, which are not presented here for brevity, the highly relativistic circular orbits exist in Schwarzschild's and Kerr's fields in much wider space domain as compare to the case of a spinless particle.

Concerning the dependence of the Lorentz factor on the values of ε_0 we note that, as it is pointed out in [2], γ is proportional to $1/\sqrt{|\varepsilon_0|}$. The numerical estimates show that, for example, if M is equal to three of the Sun's mass (as for a black hole), then $|\varepsilon_0|$ for an electron is of order 4×10^{-17} and the sufficient value of γ-factor for the realization of some circular orbits is of order 2×10^8 [2]. For a neutrino with the mass $\approx 1eV$ we have $\varepsilon_0 = 2 \times 10^{-11}$ and $\gamma = 3 \times 10^5$. It is known that some particles from the cosmic rays posses these values.

References

1. Mathisson M.: 1937, *Acta Phys. Pol.,* **6**, 163.
2. Plyatsko R., Stefanyshyn O., Fenyk M.: 2010, *Phys. Rev. D*, **82**, 044015.
3. Plyatsko R., Fenyk M.: 2012, *Phys. Rev. D*, **85**, 104023.

RELATIVISTIC EFFECTS IN A SYSTEM OF GRAVITATIONALLY INTERACTING NON-DUST-LIKE PARTICLES

J.A. Shevchenko[1], M.V. Eingorn[2], A.I. Zhuk[3]

[1] Department of Thermal Physics and [2,3] Astronomical Observatory,
Odessa I.I.Mechnikov National University,
Odessa, Ukraine

[1]*london20092@yandex.ru*, [2]*maxim.eingorn@gmail.com*, [3]*ai_zhuk2@rambler.ru.*

ABSTRACT. The two-body problem in the Kaluza–Klein model with toroidal topology of additional spatial dimensions is investigated. The characteristic property of the considering gravitational field sources is the existence of tension into the compact subspace, which is necessary to achieve the agreement with experimental restrictions on the PPN-parameter γ. It is shown that the two-body problem does not possess the essential symmetry and is inconsistent in the above-mentioned model.

Key words: Kaluza–Klein models: latent solitons, two-body problem.

It is known that in the ($\mathcal{D} = D + 1$)-dimensional Kaluza–Klein (KK) models with toroidal compactification of extra spatial dimensions (ESDs) a dust-like matter source generates the metrics characterized by the PPN-parameter γ of the form $\gamma = 1/(D - 2)$. This result does not depend on size of ESDs. At the same time there exists a strict experimental restriction on the value of γ, following from the Shapiro time-delay experiment using the Cassini spacecraft: $\gamma = 1 + (2.1 \pm 2.3) \times 10^{-5}$. Obviously, the dust-like source can provide $\gamma = 1$ only when the total number of spatial dimensions $D = 3$, i.e. in general relativity. To satisfy that restriction in KK models with considering type of compactification, we can introduce a class of matter sources, which are characterized by tension in the compact space. The static spherically symmetric metric generated by the solitary source of that class is called a *latent soliton* (LS), hence such class of sources may be called *LS-sources*. In particular, black strings are LS-sources, corresponding LS are black branes. In the present work we intended to clarify how noncontradictory from physical point of view are the models with LS-sources. We investigate a system of two LS-sources with energy-momentum tensor (EMT) of the form:

$$T^{M\tilde{N}} = \tilde{\rho} c^2 u^M u^{\tilde{N}},\; T^{\bar{\mu}\bar{\nu}} = -\omega_{(\bar{\mu}-3)} \tilde{\rho} c^2 g^{\bar{\mu}\bar{\nu}} \qquad (1a)$$

$$\tilde{\rho} \equiv \sum_{p=1}^{2} \left[(-1)^D g\right]^{-1/2} \delta(\mathbf{x} - \mathbf{x}_p) m_p \frac{ds}{dx^0}, \qquad (1b)$$

where $M = 0, \ldots, 4$; $\tilde{N} = 0, \ldots, D$; $\bar{\mu}, \bar{\nu} = 4, \ldots, D$. $\omega_{(\bar{\mu}-3)}$ plays a role of the parameter of state into the compact subspace (e.g. $\omega_{(\bar{\mu}-3)} = -1/2$, $\forall \bar{\mu}$ for black strings). Using multidimensional Einstein equations we can find approximate (up to the $1/c^3$ and $1/c^4$ terms) expressions for the components of metric tensor, corresponding to the system. From these expressions it follows, that in the investigating model the PPN-parameter γ is given by the expression $\gamma = (1 - \Sigma)/(D - 2 + \Sigma)$, where $\Sigma \equiv \sum_{\forall \bar{\mu}} \omega_{(\bar{\mu}-3)}$. From experimental restrictions on γ it follows, that:

$$\gamma = 1 \quad \Rightarrow \quad \Sigma = (3 - D)/2. \qquad (3)$$

Also we construct the approximate expression for the Lagrangian of the system up to the $1/c^2$ terms. Using the relation between the one-particle and the two-particle Lagrangians: $\partial L_i^{(1)}/\partial \mathbf{r} = \partial \mathcal{L}^{(2)}/\partial \mathbf{r}_i$, $i = 1, 2$, where $L_i^{(1)} = -m_i c\, ds_i/dt$, we obtain two different two-particle Lagrangians $\mathcal{L}_i^{(2)}$. The symmetry of the two-body problem requires that $\mathcal{L}_1^{(2)} = \mathcal{L}_2^{(2)} = \mathcal{L}^{(2)}$. This equality involves the following one:

$$\Sigma = 0. \qquad (4)$$

It's obvious, that (3) and (4) are consistent only in case $D = 3$. Hence, the two-body problem could not be formulated noncontradictory in KK models with toroidal topology of ESDs.

References

Eingorn M., Zhuk A.: 2010, *Class. Quant. Grav.,* **27**, 205014.

Eingorn M., Zhuk A.: 2011, *Phys. Rev. D*, **83**, 044005.

Eingorn M., de Medeiros O.R., Crispino L.C.B. et. al.: 2011, *Phys. Rev. D*, **84**, 024031.

SIGNATURES OF LARGE-SCALE STRUCTURE OF UNIVERSE IN X-RAYS

A.V. Tugay

Taras Shevchenko National University of Kyiv,
Kyiv, Ukraine, *tugay.anatoliy@gmail.com*

ABSTRACT. A new sample of 4299 galaxies with X-ray emission was obtained in this work by cross-correlating 2XMM catalog of X-ray sources with HyperLeda database of galaxies. We analyzed distributions of optical and X-ray fluxes, redshifts and X-ray luminosities for this sample. Virgo and Coma galaxy clusters can be easily detected at redshift-space distribution of X-ray galaxies. X-ray luminosity function of our galaxies shows the evidences of cosmological evolution, even at low redshifts.

Key words: Galaxies: catalogues: X-rays; databases: XMM-Newton, HyperLeda.

1. Introduction

Modern space observatories such as Chandra and XMM-Newton can detect a large number of extragalactic X-ray sources. It is possible now to perform statistical analysis of such sources and study large-scale structure of Universe in X-ray band. One of the main characteristics of large-scale structure is two-point correlation function for spatial or angular distribution of extragalactic objects. This function was estimated for X-ray active galactic nuclei (AGN) within XMM-LSS project (Elyiv et al., 2012). XMM observations were also used for studying of cosmological evolution of AGN's luminosity function by Ebrero et al. (2009). X-ray galaxy luminosity functions based on Chandra data were obtained by Yencho et al. (2009) and Aird et al. (2010).

The largest current catalog of X-ray sources is XMM-Newton Serendipitous Source Catalog which is based on the whole XMM-Newton observations archive. Recent version of this catalog, Data Release 3 of 2XMM is available since 2010 (2XMMi-DR3, 2010). This data release contains 262902 automatically detected X-ray sources. XMM-SSC was previously used for estimating X-ray galaxy luminosity function by Georgakakis & Nandra (2011). In this work X-ray sources were identified as galaxies by cross-correlation with SDSS sources (Aihara et al., 2011) and checking SDSS spectra. The sample of X-ray galaxies found by this way in redshift interval from 0.1 to 0.8 consist of 209 objects.

In all previous works samples of X-ray galaxies don't exceed 500 objects. Here we present a new large sample obtained with the largest available now databases of X-ray sources and galaxies: 2XMM and HyperLeda. Now HyperLeda database has 1144990 entries marked as galaxies. Some of them, of course, are misidentifications or false data, the same may be said about some part of 2XMM catalog. Nevertheless, X-ray galaxy sample obtained by cross-correlation of these two large databases may be useful as a pool for statistical studies and for selection of certain interesting objects. In this paper we discuss distribution of initial parameters of our sample and X-ray luminosity - redshift dependence for extragalactic sources.

2. New large sample of X-ray galaxies

Since the angular resolution of XMM-Newton is equal to 7 arcsec, we decided to identify each HyperLeda galaxy as X-ray source when there was 2XMM source at distance no more than 7 arcsec from it. This gives us 4299 identifications which we will call "X-ray galaxies". To find the upper limit of the number of X-ray galaxies we enlarged correlation radius to the value of optical radius of HyperLeda galaxy. This procedure increases the number of cross-correlations to 5021. In this work we will consider only the first sample, because the latter should have a lot of misidentifications such as indefinite X-ray source close to center of thin edge-on galaxy that doesn't lie in the disc. All 4299 galaxies from the first sample has the main X-ray source in the center. In our paper (Tugay&Vasilenko, 2011) we show that X-ray emission of galactic disc without nuclei is very faint and rarely can be detected. So we can suppose that our new sample consist of AGN's of different types. Sky distribution of galaxies from our sample in equatorial coordinates is presented at Fig 1. The main density excesses at such sky map are Virgo and Coma galaxy clusters and XMM-LSS region in Cetus (the last is a selection effect caused by intesive XMM-LSS observational program). These regions are marked by circles. Except them and Milky Way zone of avoidance, angular distribution of X-ray galaxies is uniform.

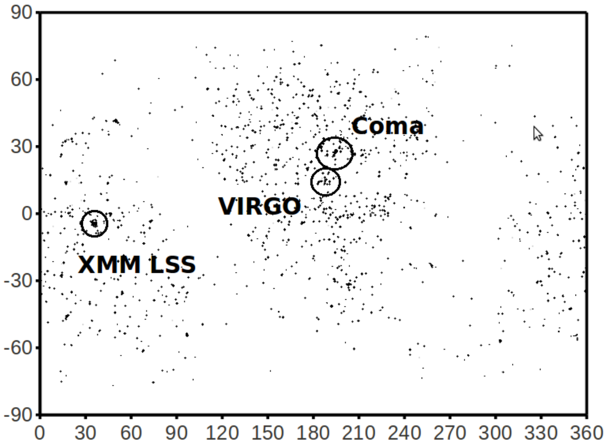

Figure 1: Sky distribution of X-ray galaxies.

Let's consider spatial redshift-space distribution of our galaxies in Local Supercluster plane. This region was observed intensively in Sloan Digital Sky Survey and include the most bright and nearby galaxies, so we should find here the largest density of observed objects. We selected region with $12h < RA < 14h$ and $DEC > 0$. 242748 galaxies from HyperLeda allows this coordinate constraints. Distribution of these galaxies is shown on Fig. 2.

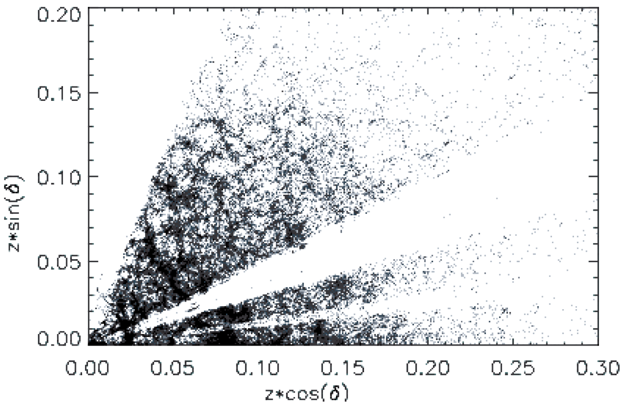

Figure 2: Redshift-space distribution of optical galaxies in Local Supercluster plane.

The region of supergalactic plane include 778 X-ray galaxies from new sample. At Fig. 3 we can see that only Virgo and Coma clusters can be detected in X-rays in Supergalactic plane. These clusters are the only elements from all large-scale structure that appear in X-rays with modern observational data.

Since the details of spatial large-scale structure can not be resolved with our sample, let's pass to luminosity distribution of X-ray galaxies. Fig. 4 presents the distribution of optical and X-ray brightness. u-band magnitudes (most data from SDSS) and X-ray fluxes in whole XMM energy range - 0.2-12 keV are plotted here. According to this distribution our sample seems to be homogeneous.

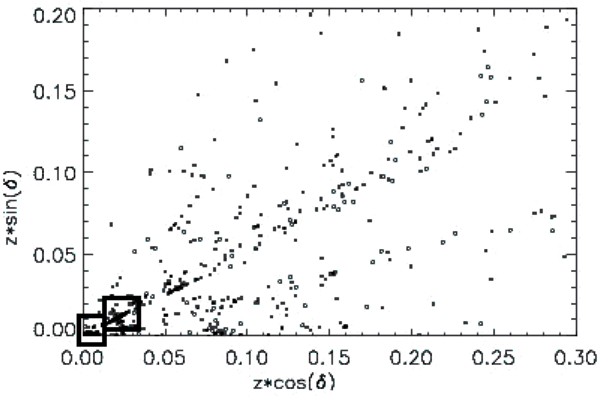

Figure 3: Redshift-space distribution of X-ray galaxies in Local Supercluster plane. Virgo and Coma Clusters are marked with squares.

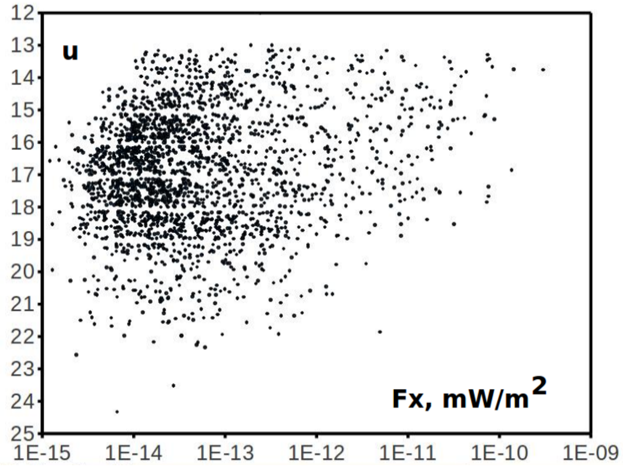

Figure 4: u-band magnitude against 0.2-12 keV flux for the 2XMM X-ray sources with optical galaxy counterparts.

Distribution of X-ray versus optical ratios and X-ray luminosities is plotted on Fig. 5. We see that the most galaxies has X-ray luminosity at 0.1% of optical. Larger ratios and luminosities corresponds to transition from Seyfert galaxies to QSO's and BL Lacs. Note that transition is continuous. Finally, the dependence of X-ray luminosity from redshift is shown in Fig. 6. Lower bound corresponds to the limit of XMM-Newton sensitivity.

To estimate X-ray luminosity function for our sample we calculated the numbers of galaxies in selected intervals of luminosity and redshift distribution. The results are presented in Table 1. Luminosity and redshift intervals corresponds to that from (Ebrero et al, 2009). Note that mean luminosity increases with

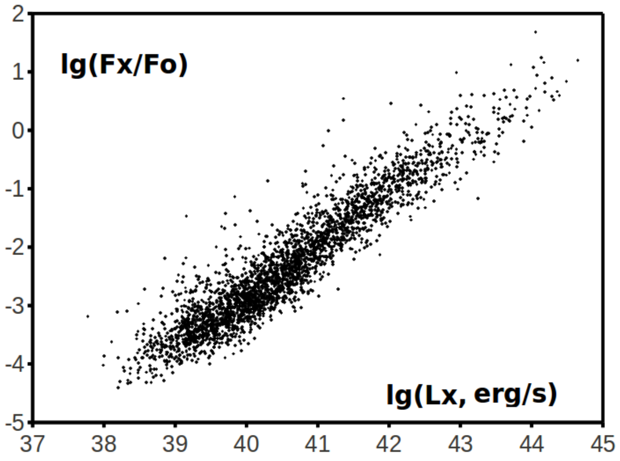

Figure 5: X-ray to optical flux ratio against X-ray luminosity.

redshift, that agrees with Ebrero et al. (2009) and other works. This effect is commonly interpreted as cosmological evolution of X-ray AGNs. New sample contain large number of galaxies at lower redshifts, so the evolution effect can be found at Fig. 6 for $z < 0.5$.

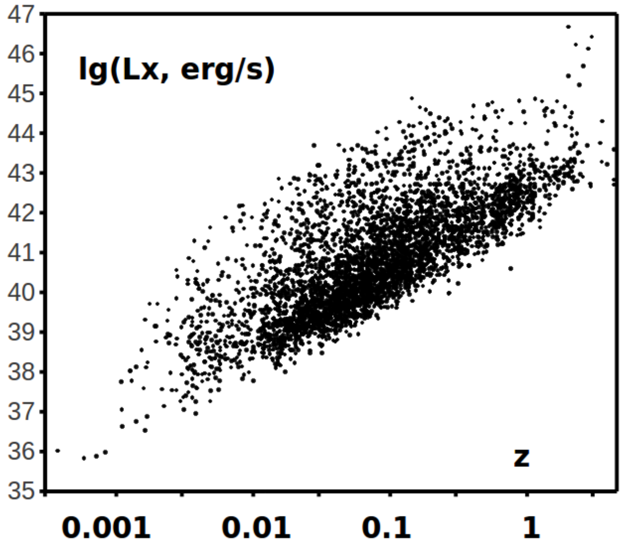

Figure 6: Redshift versus luminosity plot of our sample. Lower bound of distribution indicates the limit of XMM sensitivity.

Table 1: Luminosity distribution of X-ray galaxies for different redshift ranges.

$lg(L_x, erg/s)$	0.01-0.5	0.5-1.0	1.0-2.0	2.0-3.0
41-42	770	116	15	0
42-43	365	177	84	16
43-44	128	34	36	25
44-45	27	11	12	5
Whole luminosity range	3480	340	147	51

3. Conclusion

Although new sample of X-ray galaxies was made using non-homogeneous 2XMM and HyperLeda databases, its object shows uniform distribution both in space and luminocities. XMM-Newton observations can not reveal cell-like large-scale structure of Universe but are useful for investigation X-ray luminosity functions and individual X-ray sources.

References

Aihara H., Allende Prieto C., An D. et al.: 2011, *Ap. J. S.*, **193**, 29.

Aird J., Nandra K., Laird E.S.: 2010, *MNRAS*, **401**, 2531.

Ebrero J., Carrera F.J., Page M.J. et al.: 2009, *A& A.*, **493**, 55.

Elyiv A., Clerc N., Plionis M. et al.: 2012, *A& A.*, **537**, 131.

Georgakakis A., Nandra K.: 2011, *MNRAS*, **414**, 992.

Tugay A.V., Vasilenko A.A.: 2011, *Odessa Astron. Publ.*, **24**, 72.

Yencho B., Barger A.J., Trouille L. et al.: 2009,*Ap.J.*, **698**, 380.

2XMMi-DR3 (XMM-SSC): 2010, *http://vizier.u-strasbg.fr/viz-bin/VizieR?-source=IX%2F41.*

HyperLeda, *http://leda.univ-lyon1.fr.*

SCALAR COSMOLOGICAL PERTURBATIONS OF PRESSURELESS MATTER IN THE BRANEWORLD MODEL

A. V. Viznyuk, Yu. V. Shtanov

Bogolyubov Institute for Theoretical Physics, Nat. Acad. Sci. of Ukraine,
Kiev, Ukraine, *viznyuk@bitp.kiev.ua, shtanov@bitp.kiev.ua*

ABSTRACT. We present a complete set of differential equations describing the evolution of scalar cosmological perturbations of pressureless matter on the brane in the general case where the action of the model contains the induced-curvature term as well as the cosmological constants in the bulk and on the brane.

Key words: Extra dimensions; braneworld model; cosmological perturbations.

1. Introduction

The idea that our observable universe can be a four-dimensional manifold (the "brane") embedded in higher dimensional spacetime (the "bulk") with Standard Model particles and fields trapped on the brane was thoroughly investigated during the last two decades. The activity in the field was triggered especially by the Randall–Sundrum (RS) braneworld model (Randall & Sundrum, 1999), in which Einstein's theory of general relativity is modified due to extra dimensional effects at relatively high energies. Apart from interesting cosmological applications, it was shown that a modified theory of gravity based on the RS braneworld model potentially can explain the observations of the galactic rotation curves and X-ray profiles of galactic clusters without invoking the notion of dark matter (see, for example, Mak & Harko, 2004). This theory, however, was unable to address the cosmological implications of dark matter. On the other hand, an alternative braneworld model of Dvali, Gabadadze and Porrati (DGP, Dvali et al., 2000), in which gravity is modified at low energies, gave rise to a cosmology with late-time acceleration without cosmological constants on the brane or in the bulk.

The main feature of the DGP braneworld model is the induced-gravity term in the action for the brane. But cosmological constants are absent in this theory, in contrast to the RS braneworld model. A more general braneworld model contains the induced-gravity term as well as cosmological constants in the bulk and on the brane (Shtanov, 2000). Models of such generic form can describe late-time cosmological acceleration and, in doing so, they exhibit some interesting specific features. At the same time, this kind of braneworld model can be used to address astrophysical observations of dark matter in galaxies (Viznyuk & Shtanov, 2007).

Developing the theory of cosmological perturbations is a long-standing problem of the braneworld model. Regardless the computational complexity of this problem, a considerable progress has been made during the last years. A complete system of cosmological equations allowing for numerical computation was obtained in the framework of the RS (Cardoso et al., 2007) and DGP (Sawicki et al., 2007) braneworld models. Important analytical results are presented in Koyama & Maartens, 2006. However, the problem of cosmological perturbations in the braneworld model still remains to be solved in full generality. For a modern review of this problem, see Maartens & Koyama, 2010.

The existence of extra dimension requires specification of the boundary conditions in the bulk space. In the usual case of a spatially flat brane, the extra dimension is noncompact, and one has to deal with the spatial infinity of the extra dimension. This is a difficult situation with no obvious and unique choice for the boundary conditions. In the present work, we consider the case of a spatially closed brane, an expanding three-sphere, which is bounding a four-ball in the bulk space. The boundary condition for such configuration can be specified uniquely just as a regularity condition of the metric inside the ball.

2. The theory

The braneworld action, to lowest order in the bulk and brane curvature, can be written in the form:

$$S = M^3 \left[\int_{\rm bulk} (\mathcal{R} - 2\Lambda) - 2 \int_{\rm brane} K \right] + \int_{\rm brane} \left(m^2 R - 2\lambda \right) + \int_{\rm brane} L \left(g_{\mu\nu}, \phi \right) , \qquad (1)$$

where $\mathcal{R}$ is the scalar curvature of the five-dimensional bulk metric g_{AB}, and R is the scalar curvature of the induced metric $g_{\mu\nu}$ on the brane. The quantity K denotes the trace of the symmetric tensor of extrinsic curvature of the brane, and the symbol $L(g_{\mu\nu}, \phi)$ denotes the Lagrangian density of the four-dimensional matter fields ϕ whose dynamics is restricted to the brane so that they interact only with the induced metric $g_{\mu\nu}$. The symbols M and m denote the five-dimensional and four-dimensional Planck masses, respectively, Λ is the bulk cosmological constant, and λ is referred to as brane tension.

Action (1) leads to the Einstein equation with cosmological constant in the bulk,

$$\mathcal{G}_{AB} + \Lambda g_{AB} = 0\,, \tag{2}$$

and the following equation on the brane:

$$G_{\mu\nu} + \frac{\Lambda_{\rm RS}}{b+1} g_{\mu\nu} = \left(\frac{b}{b+1}\right)\frac{1}{m^2}T_{\mu\nu} + \frac{1}{b+1}\left(\frac{1}{M^6}Q_{\mu\nu} - C_{\mu\nu}\right)\,, \tag{3}$$

where $b = k\ell$, $k = \lambda/3M^3$, $\ell = 2m^2/M^3$ are convenient parameters of the braneworld model, $\Lambda_{\rm RS} = \Lambda/2 + 3k^2$ is the value of the effective cosmological constant in the Randall–Sundrum model,

$$Q_{\mu\nu} = \frac{1}{3}EE_{\mu\nu} - E_{\mu\lambda}E^{\lambda}{}_{\nu} + \frac{1}{2}\left(E_{\rho\lambda}E^{\rho\lambda} - \frac{1}{3}E^2\right)g_{\mu\nu} \tag{4}$$

is a quadratic expression with respect to the 'bare' Einstein equation $E_{\mu\nu} \equiv m^2 G_{\mu\nu} - T_{\mu\nu}$ on the brane, and $E = g^{\rho\lambda}E_{\rho\lambda}$. The symmetric traceless tensor $C_{\mu\nu}$ is the projection of the bulk Weyl tensor $\mathcal{C}_{ABCD}$ which carries information about the gravitational field outside the brane.

The background cosmological evolution on the brane can be presented in the following form (Sahni & Shtanov, 2003):

$$H^2 + \frac{\kappa}{a^2} = \frac{\rho+\lambda}{3m^2} + \frac{2}{\ell^2}\left[1 \pm \sqrt{1 + \ell^2\left(\frac{\rho+\lambda}{3m^2} - \frac{\Lambda}{6}\right)}\right]. \tag{5}$$

Here, $\rho = \rho(t)$ is the matter energy density on the brane. The Hubble parameter $H \equiv \dot{a}/a$ describes the evolution of the Friedmann–Robertson–Walker (FRW) metric $ds^2 = -dt^2 + a^2(t)\gamma_{ij}dx^i dx^j$, $\kappa = 0, \pm 1$ is a spatial curvature of a purely spatial metric γ_{ij}. Here and hereafter, we neglect the influence of symmetryc tensor $C_{\mu\nu}$ for the background geometry.

3. Scalar cosmological perturbations on the brane

Scalar cosmological perturbations of the induced metric on the brane are most conveniently described by the relativistic potentials Φ and Ψ in the so-called longitudinal gauge. The perturbed metric in the conformal coordinates reads

$$ds^2 = a^2\left[-(1+2\Phi)d\eta^2 + (1-2\Psi)\gamma_{ij}dx^i dx^j\right]\,. \tag{6}$$

We introduce the components of the linearly perturbed stress–energy tensor of matter in these coordinates:

$$\delta T^{\mu}{}_{\nu} = \begin{pmatrix} -\delta\rho\,, & -\dfrac{\nabla_i v}{a} \\ \dfrac{\nabla^i v}{a}\,, & \delta p\,\delta^i{}_j + \dfrac{\zeta^i{}_j}{a^2} \end{pmatrix}\,, \tag{7}$$

where $\delta\rho$, δp, v, and $\zeta_{ij} = \left(\nabla_i\nabla_j - \frac{1}{3}\gamma_{ij}\nabla^2\right)\zeta$ are scalar perturbations. Similarly, we introduce the scalar perturbations $\delta\rho_{\mathcal{C}}$, $v_{\mathcal{C}}$, and $\delta\pi_{\mathcal{C}}$ of the tensor $C_{\mu\nu}$:

$$m^2\delta C^{\mu}{}_{\nu} = \begin{pmatrix} -\delta\rho_{\mathcal{C}}\,, & -\dfrac{\nabla_i v_{\mathcal{C}}}{a} \\ \dfrac{\nabla^i v_{\mathcal{C}}}{a}\,, & \dfrac{\delta\rho_{\mathcal{C}}}{3}\delta^i{}_j + \dfrac{\delta\pi^i{}_j}{a^2} \end{pmatrix}\,, \tag{8}$$

where $\delta\pi_{ij} = \left(\nabla_i\nabla_j - \frac{1}{3}\gamma_{ij}\nabla^2\right)\delta\pi_{\mathcal{C}}$.

We call v and $v_{\mathcal{C}}$ the momentum potentials for matter and dark radiation, respectively, $\delta\rho$ and $\delta\rho_{\mathcal{C}}$ are their energy density perturbations, and ζ and $\delta\pi_{\mathcal{C}}$ are the scalar potentials for their anisotropic stresses.

Using this notation and equation (3), one can derive a complete system for perturbations on the brane, which, however, is not closed. To illustrate this problem, we present the result for *pressureless*[1] matter ($p = 0$, $\zeta = 0$):

$$\ddot{\Delta} + 2H\dot{\Delta} = \left(1 + \frac{6\gamma}{\beta}\right)\frac{\rho\Delta}{2m^2} + (1+3\gamma)\frac{\delta\rho_{\mathcal{C}}}{m^2\beta}\,, \tag{9}$$

$$\delta\dot{\rho}_{\mathcal{C}} + 4H\delta\rho_{\mathcal{C}} = \frac{1}{a^2}\nabla^2 v_{\mathcal{C}}\,, \tag{10}$$

$$\dot{v}_{\mathcal{C}} + 4Hv_{\mathcal{C}} = \gamma\Delta_{\mathcal{C}} + \left(\gamma - \frac{1}{3}\right)\rho\Delta + \frac{4}{3(1+3\gamma)a^2}\left(\nabla^2 + 3\kappa\right)\delta\pi_{\mathcal{C}}\,, \tag{11}$$

where $\Delta \equiv (\delta\rho + 3Hv)/\rho$ is a conventional dimensionless variable describing the matter perturbations, and, similarly, $\Delta_{\mathcal{C}} \equiv \delta\rho_{\mathcal{C}} + 3Hv_{\mathcal{C}}$. The time-dependent dimensionless functions β and γ are given by

$$\beta \equiv \pm 2\ell\sqrt{\left(\frac{\rho+\lambda}{3m^2} + \frac{1}{\ell^2} - \frac{\Lambda}{6}\right)}\,, \tag{12}$$

$$\gamma \equiv \frac{1}{3}\left[1 - \frac{\dfrac{\rho}{2m^2}}{\left(\dfrac{\rho+\lambda}{3m^2} + \dfrac{1}{\ell^2} - \dfrac{\Lambda}{6}\right)}\right]. \tag{13}$$

The system of equations (9)–(11) is not closed because it does not contain an evolution equation for the anisotropic stress $\delta\pi_{\mathcal{C}}$. The evolution of the Weyl tensor should be derived from the perturbed

---

[1] The case of more general matter is considered in Viznyuk & Shtanov, 2012.

bulk equation (2) after setting some natural boundary conditions in the bulk (Mukohyama, 2001).

4. Scalar perturbation of the bulk metric

To find the perturbed Weyl tensor, we consider a spatially closed braneworld model ($\kappa = 1$) which bounds the interior of flat ($\Lambda = 0$) bulk space with the spatial topology of a ball and demand that the bulk metric be regular in the brane interior. In the natural static coordinates, the background bulk metric can be written in this case in the form

$$ds^2_{\text{bulk}} = -d\tau^2 + dr^2 + r^2\gamma_{ij}dx^i dx^j \,, \tag{14}$$

where γ_{ij} is the metric of a 3–dimensional maximally symmetric space with coordinates x^i. In these coordinates, the FRW brane moves radially along the trajectory $r = a(\tau)$, and the relevant part of the bulk is given by $r \le a(\tau)$.

The components of the perturbed bulk Weyl tensor $\delta\mathcal{C}_{ABCD}$ and it's projection to the brane $\delta C_{\mu\nu}$ can be expressed in terms of the Mukohyama master variable in the following way:

$$\frac{\delta\rho_{\mathcal{C}}}{m^2} = -\,\frac{n(n+2)(n^2+2n-3)}{3a^5}\,\Omega_{\text{b}} \,, \tag{15}$$

$$\begin{aligned}\frac{v_{\mathcal{C}}}{m^2} &= \frac{(n^2+2n-3)}{3a^3}\Big[aH\left(\partial_r\Omega\right)_{\text{b}} - H\Omega_{\text{b}} + \\ &+ \sqrt{1+a^2H^2}\left(\partial_\tau\Omega\right)_{\text{b}}\Big] \,,\end{aligned} \tag{16}$$

$$\begin{aligned}\frac{\delta\pi_{\mathcal{C}}}{m^2} &= -\,\frac{\left(1+2a^2H^2\right)}{2a}\left(\partial^2_\tau\Omega\right)_{\text{b}} - \\ &- H\sqrt{1+a^2H^2}\left(\partial^2_{\tau r}\Omega\right)_{\text{b}} - \frac{\left(1+3a^2H^2\right)}{2a^2}\left(\partial_r\Omega\right)_{\text{b}} - \\ &- \frac{(n^2+2n-3)\left(1+3a^2H^2\right)}{6a^3}\,\Omega_{\text{b}} \,,\end{aligned} \tag{17}$$

where, $a = a(t)$ is a scale factor of the background Friedmann–Robertson–Walker metric on the brane, $H = \dot{a}/a$ is the Hubble parameter on the brane, and the function $\tau = \tau(t)$ is defined by the differential equation $d\tau/dt = \sqrt{1+a^2H^2}$. The subscript $\{\}_{\text{b}}$ means that the value of the corresponding quantity is taken at the brane. For example, $\Omega_{\text{b}}(t) \equiv \Omega[\tau(t), a(t)]$. Integers n numerates the discrete Laplacian eigenvalues on the three-sphere: $k_n^2 = n(n+2)$, $n = 0, 1, 2\ldots$

Mukohyama master variable $\Omega(\tau, r)$ in our case can be determined as a solution of equation (Mukohyama, 2000):

$$-\partial^2_\tau\Omega + \partial^2_r\Omega - \frac{3}{r}\partial_r\Omega - \frac{(n^2+2n-3)}{r^2}\Omega = 0 \,, \tag{18}$$

which can be solved in terms of special functions once the regulatory conditions in the bulk are imposed.

5. Concluding remarks

The problem of finding closed system of equations, describing the evolution of cosmological perturbations in the general braneworld model with induced curvature and cosmological constants, appears to be solved. Basic equation in the bulk (18) complemented with the boundary conditions on the brane (9–11), together with (15–17), represent the desired result for pressureless matter.

Having this result in mind, one can act in two possible ways: to develop numerical method for computation similar to those employed in the analysis of perturbations in the RS (Cardoso et al., 2007) and DGP (Sawicki et al., 2007) braneworld models, or to develop analytic approximate methods similar to the quasi-static approximation (Koyama & Maartens, 2006). Both are the subject of further investigation.

Acknowledgements. This work was supported in part by the Cosmomicrophysics section of the Programme of the Space Research of the National Academy of Sciences of Ukraine and by the Joint Ukrainian-Russian SFFR-RFBR project F40.2/108.

References

Cardoso A., Hiramatsu T., Koyama K., Seahra S.S.: 2007, *J. Cosmol. Astropart. Phys.*, **07**, 008.

Dvali G., Gabadadze G., Porrati M.: 2000, *Phys. Lett. B*, **485**, 208.

Koyama K., Maartens R.: 2006, *J. Cosmol. Astropart. Phys.*, **01**, 016.

Maartens R., Koyama K.: 2010, *Living Rev. Rel.*, **13**, 5.

Mak M. K., Harko T.: 2004, *Phys. Rev. D*, **70**, 024010.

Mukohyama S.: 2000, *Phys. Rev. D*, **62**, 084015.

Mukohyama S.: 2001, *Phys. Rev. D*, **64**, 064006.

Randall L., Sundrum R.: 1999, *Phys. Rev. Lett.*, **83**, 4690.

Sahni V,. Shtanov Yu.: 2003, *J. Cosmol. Astropart. Phys.*, **11**, 014.

Sawicki I., Song Y. S., Hu W.: 2007, *Phys. Rev. D*, **75**, 064002.

Shtanov Yu.: 2000, *arXiv*: hep-th/0005193.

Viznyuk A., Shtanov Yu.: 2007, *Phys. Rev. D*, **76**, 064009.

Viznyuk A., Shtanov Yu.: 2012, *Ukr. Phys. J.* (in press).

ASTROPHYSICS

TWO-COMPONENT VARIABILITY OF THE SEMI-REGULAR PULSATING STAR U DELPHINI

I.L. Andronov[1], L.L.Chinarova[2]

[1] Department “High and Applied Mathematics”, Odessa National Maritime University,
Odessa, Ukraine, *tt_ari @ukr.net*
[2] Astronomical observatory, Odessa National University, Odessa, Ukraine, *chinarova @pochta.ru*

ABSTRACT. Photometric analysis of photometric variability of the semi-regular pulsating variable U Del is analyzed. From the international AFOEV database, 6231 brightness values in the time interval JD 2451602-55378 were chosen. For the periodogram analysis, we have used a trigonometric polynomial fit. Using the criterion of minimal variance of the approximation at arguments of observations, the optimal degree is *s*=1. Initial epoch for maximum is T_0=JD2453340±3, the period $P=1198\pm4^d$. Mean brightness at maximum is 6.624±0.005, at minimum 7.124±0.005, i.e. the amplitude is 0.499 ± 0.005^m. Besides this slow variability, there is a faster oscillation of a period of 119.45 ± 0.06^d, amplitude 0.303 ± 0.005^m and an initial epoch for maximum 2453215.1±0.5. These results are mean during the time interval after that analyzed in the catalogue of Chinarova and Andronov (2000). Also the method of “running sines” with a filter half-width $\Delta t=0.5P$. The local mean (averaged over a short period) brightness varies in a range $6.58\text{-}7.41^m$, the semi-amplitude exhibits very strong variations from 0.01 to 0.46^m. The phase is also variable – typically of a full amplitude of 0.5. Close to JD 2452589, occurred a phase jump by a complete period during a descending branch of a slow wave. This effect was not observed during other cycles. No significant correlation between mean brightness and amplitude of short-period oscillation was found. Despite significant variability of amplitude, the periodic contribution is not statistically significant. Also characteristics of individual brightness extrema were found.

The study was made in a course of the international project “Inter-Longitude Astronomy" (Andronov et al., 2010) and national project "Ukrainian Virtual Observatory (Vavilova et al., 2012).

Key words: Stars: variable, pulsating, semiregular, individual: U Del

Long-period variables (LPVs) are pulsating stars at late stages of evolution. According to the “General Catalogue of Variable Stars” (GCVS, Kholopov et al, 1985; Samus’ et al., 2012), the main types are L, M, SR, RV, which are further subdivided into subtype. A review on long-period variables was presented by Kudashkina (2003). A catalogue of characteristics of 173 variables was published by Andronov and Chinarova (2000). After that time, new intensive observations were carried out, allowing further study of these variables. Some of them (e.g. RU And) show drastic variations of an amplitude of pulsations, formally indicating switches between the types of high-amplitude Mira-type stars and low-amplitude semi-regular variables. Sometimes pulsations may practically disappear (cf. Chinarova 2010). Other similar stars (S Aql, S Tri, Y Per) were recently discussed by Marsakova and Andronov (2012).

An analysis of historical variability of U Del was presented by Thompson (1998), who argued for a main period of 1150^d-1210^d. In the GCVS, 110^d is mentioned as the main period, type SRb, and Sp M5 II or III. From the AFOEV database, we removed “bad” and “fainter than” data, so used 6231 points. The periodogram analysis was carried out using a trigonometric polynomial fit (Andronov, 1994; Andronov and Baklanov 2004). The statistically optimal degree *s*=1. Corresponding parameters are listed in the abstract. The periodogram is shown in Fig.1.

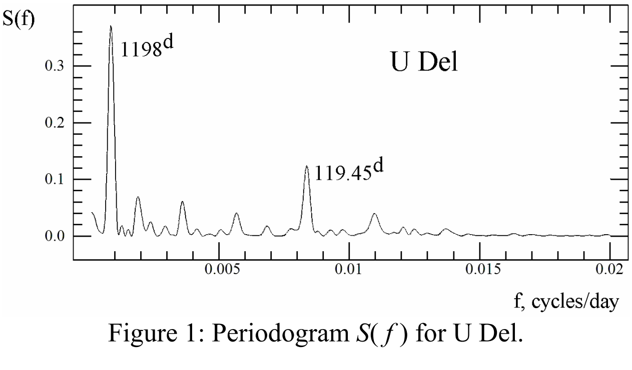

Figure 1: Periodogram $S(f)$ for U Del.

The highest peak corresponds to the “long” period P=1198±4^d. The second peak corresponds to the “short” period 119.45±0.06^d. Its relatively small height is due to a low coherence.

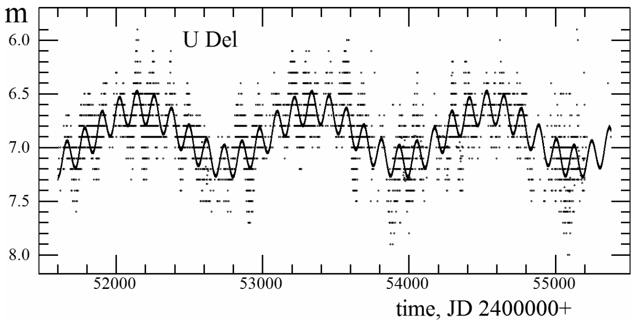

Figure 2: Individual observations and a bi-periodic fit using the periods P=1198^d and 119.45^d computed with the program MCV (Andronov and Baklanov, 2004).

For the analysis of variability of “approximately periodic” waves, we have applied the method of “running sines” (see Andronov (1997, 2003) for a detailed theory of running approximations using arbitrary basic and weight functions). In brief, the signal is approximated as

$$m_c(t) = C_0 - R\cos(2\pi((t-T_0)/P-\phi)) \tag{1}$$

where $C_0(t_0,\Delta t), R(t_0,\Delta t)$, and $\phi(t_0,\Delta t)$ are functions of the “shift” t_0 and “scale” Δt in the “wavelet terminology” (cf. Andronov, 1998). They may be interpreted as a “local mean” value (averaged over the period of “short” pulsation), semi-amplitude and phase, respectively. For our analysis, we have used a rectangular filter of a half-width $\Delta t = P/2$, so for a local approximation using the function (1), the observations from a trial interval $[t_0-\Delta t, t_0+\Delta t]$ are used. Also we computed envelope lines for maxima $(C_0 - R)$ and minima $(C_0 + R)$.

Contrary to a bi-periodic fit, where the amplitudes and phases are suggested to be constant, the running sine allows to check time variability of the parameters of individual cycles. Also one may see that “slow variations” (C_0) are not sinusoidal, one may even suggest more steep decline than incline. A noticeable phase jump at JD 2452700 by a complete period occurred at a decline, when the amplitude of pulsations drastically decreased. However, at other moments, the typical variation of phase reaches 0.5P, thus arguing for a better effectiveness of this method as compared with a model with stable periods and amplitudes.

The semi-amplitude varies from a practical zero (0.01^m) to 0.42^m. This is formally similar to RU And (Chinarova 2010), where the type of variability switched between Mira and SR (or even constant), and is listed in the GCVS as SRa. However, there were no long-period variations of the mean brightness in RU And, and in U Del the intervals of low amplitude are comparatively very short.

Thompson mentioned a drastic increase of the amplitude of variations in 1942-1949yrs, with a magnitude range of 5^m-8^m. Unfortunately, his compilation of data is not available as a table of observations, thus we can’t apply the same methods to provide an analysis of the all available interval of observations. This argues for a general necessity of publication of own data electronically to be available for the community.

Although the amplitude changes are significant, and some time intervals of drastic increase or decrease of amplitude were seen, the phase changes are typically smooth. There is no statistical dependence of characteristics of “fast” (120^d) variability with phase and/or brightness of the “slow” (1200^d) wave. These observational results may be used for probing models of pulsations.

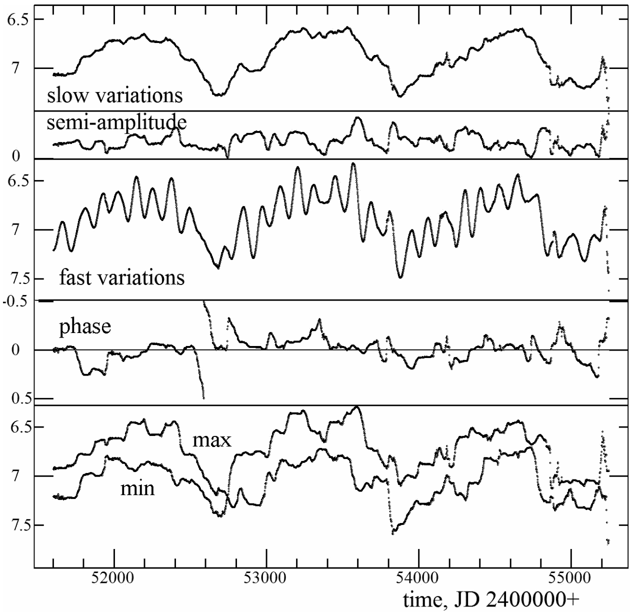

Figure 3: Characteristics of the “running sine” fit.

References

Andronov I.L.: 1994, *Odessa Astron. Publ.*, **7**, 49.
Andronov I.L.: 1997, *Astron. Astrophys. Suppl.*, **125**, 207.
Andronov I.L.: 1998, *Kinem. Phys. Celest.Bodies*, **14**, 490.
Andronov I.L.: 2003, *Astron.Soc.Pacif.Conf.,* **292**, 391.
Andronov I.L. et al.: 2010., *Odessa Astron. Publ.*, **23**, 8.
Andronov I.L., Baklanov A.V.: 2004, *Astronomy School Reports*, **5**, 264, *http://uavso.pochta.ru/mcv*
Andronov I.L., Chinarova L.L.: 2000, *Odessa Astron. Publ*, **13**, 113.
Chinarova L.L.: 2010, *Odessa Astron. Publ*, **23**, 25.
Chinarova L.L., Andronov I.L.: 2000, *Odessa Astron. Publ*, **13,** 116.
Kholopov P.N. et al: 1985, *General Catalogue of Variable Stars*, 4-th edition. Moscow: Nauka.
Kudashkina L.S.: 2003, *Kinem. Phys. Celest. Bodies*, **19**, 193
Marsakova V.I., Andronov I.L.: 2012, *Odessa Astron. Publ*, **25**, 60.
Samus N.N., Durlevich O.V., Kazarovets E V., Kireeva N.N., Pastukhova E.N., Zharova A.V., et al. General Catalog of Variable Stars (GCVS database, Version 2012Jan), http://www.sai.msu.su/gcvs/gcvs/
Thompson R.R.: 1998, *J.AAVSO*, **26**, 119.
Vavilova I.B. et al.: 2012, *Kinem.Phys.Cel.Bodies*, **28**, 85.

DETERMINATION OF CHARACTERISTICS OF NEWLY DISCOVERED ECLIPSING BINARY

2MASS J18024395 +4003309 = VSX J180243.9+400331

I.L. Andronov[1], V.V. Breus[1], S. Zoła[2,3]

[1] Department "High and Applied Mathematics", Odessa National Maritime University, Odessa, Ukraine, *tt_ari @ukr.net, bvv_2004@ua.fm*
[2] Astronomical Observatory, Jagiellonian University, Cracow, Poland
[3] Mt. Suhora Observatory, Pedagogical University, Cracow, Poland

ABSTRACT. During processing the observations of the intermediate polar 1RXS J180340.0+401214, obtained 26.05.2012 at the 60-cm telescope of the Mt. Suhora observatory (Krakow, Poland), variability of 2MASS J18024395 +4003309 was discovered. As this object was not listed in the "General Catalogue of Variale Stars" or "Variable Stars Index", we registered it as VSX J180243.9+400331. Additionally we used 189 separate observations from the Catalina Sky Survey spread over 7 years. The periodogram analysis yields the period of $0^d.3348837 \pm 0^d.0000002$.

The object was classified as the Algol-type eclipsing binary with a strong effect of ellipticity. The depths of the primary and secondary minima are nearly identical, which corresponds to a brightness (and maybe) mass ratio close to 1. The statistically optimal degree of the trigonometric polynomial *n*=4. The most recent minimum occurred at HJD 2456074.4904. The brightness range from our data is 16.56-17.52 (V), 16.18-17.08 (R).

The NAV ("New Algol Variable") algorithm was applied for statistically optimal phenomenological modeling and determination of corresponding parameters.

Key words: Stars: variable, binary, eclipsing, individual: VSX J180243.9+400331, USNO-B1.0 1300-00287487, 1RXS J180340.0+401214

During our monitoring of the intermediate polar 1RXS J180340.0+401214 (=RXJ1803), Breus (2012) discovered a new variable, which was absent in the "General Catalogue of Variable Stars" (Samus' et al. 2012) and "Variable Stars Index" (2012). The CCD images were taken by S.Zoła using V and R filters at the 60-cm telescope of the Mt.Suhora Observatory. Contrary to previous studies of the same field (cf. Andronov et al. 2011) with smaller field, these images contained this new variable. The variable was registered as VSX J180243.9+400331 (hereafter VSX1802). In this field, the brightness of some stars was calibrated by Henden (2005). The brightness of the "main" comparison star "1" is $V= 14.807^m$, $Rc=14.436^m$. For better accuracy, we have used the "multiple comparison stars" method (Andronov and Baklanov 2004, Kim et al., 2004). The color transformation equations are: $V_I-V_H=0.031-0.061(V-Rc)$, $R_I-R_H=-0.002-0.101(V-Rc)$, $(V-R)_I=0.035+0.855(V-Rc)$, $(V-Rc)=-0.028+1.144(V-R)_I$

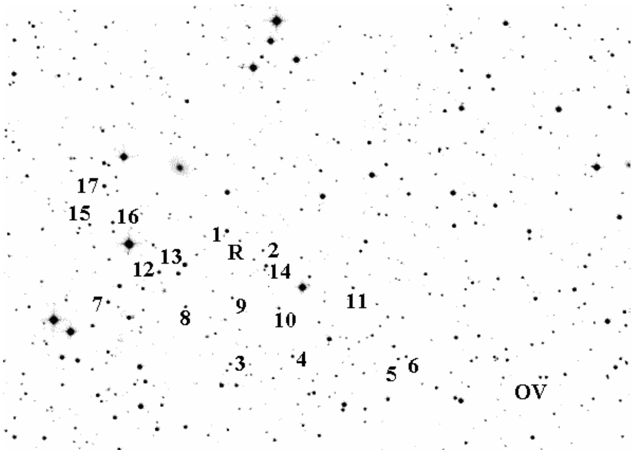

Fig. 1. Finding chart (20') with multiple comparison stars. The new variable is marked as "V" and RXJ1803 as "R", and OV Her as "OV". North is up and West is left. The numeration of comparison stars is as in Andronov et al. (2011), except the star "13".

with corresponding error estimates 0.013, 0.025, 0.020, 0.039, 0.018, 0.034, 0.021, 0.045. For the color index, the deviation of the coefficient from unity exceeds 4s and thus is to be taken into account. We recommend the same stars to be used at other telescopes for further joint analysis of the data.

Additionally we have found published data from the Catalina survey (Drake et al. 2009). Although they are noisy, the best accuracy for the period was obtained using the set "Catalina"+(scaled)"Suhora R". The parameters of the best trigonometric polynomial fit (Andronov, 1994, 2003) are listed in the abstract.

Although the star is not listed in the GCVS and VSX, it was independently found by Parimucha et al. (2011) and named "Kol5". They published brightness $\mathrm{Max_I}$=16.13, $\mathrm{Max_{II}}$=16.16, $\mathrm{min_I}$=16.89, $\mathrm{min_{II}}$=16.80 However, their period estimate was wrong, as one may see from the phase light curves. The minima are nearly of the same depth, and their "primary" minimum was in fact a secondary one leading to a 0.5 cycle miscount during a year. With a corrected ephemeris, all minima occur at proper positions.

A funny coincidence, but the cycle miscount during one year also was found for the "main" star RXJ1803, for which Breus et. al. (2012) published corrected elements

$$T_{\max}= 2454604.04449(14) +0.017596986(3)E$$

for the spin maxima.

The phase curve in VR is only partial, and only a primary minimum was covered. One should note an apparently larger amplitude of these recent observations as compared with that at the Catalina survey, thus we had to scale R data for further periodogram analysis.

To smooth the complete phase curve using the Catalina data only, we used the NAV algorithm (Andronov 2012). The best fit values are C_8=D/2=0.119 (filter half-width), $\beta_1=\beta_2=1$, mean brightness out of eclipse $C_1=16.236^{\mathrm{m}}(5)$, semi-amplitude of ellipsoidal variations $C_3=0.078^{\mathrm{m}}(7)$, unbiased depths of the primary ($C_6=0.568^{\mathrm{m}}(21)$) and secondary ($C_7=0.486^{\mathrm{m}}(23)$) minima. Coefficients C_2, C_4, C_5, which describe a reflection and O'Connell effect, are not statistically significant. The corresponding light curve is shown in Fig. 3.

The parameter Y (Andronov 2012), which is related to degree of eclipses (0 – "no eclipses", 1 – "both eclipses are full"), is equal to 0.768(18). This value is closer to "full eclipses" rather than "no eclipses". Another parameter corresponds to an effective ratio of the surface brightnesses i_1/i_2=1.130(53), i.e. exceeds unity by ~2σ only. However, the difference in brightness of minima is $\mathrm{min_I}$-$\mathrm{min_{II}}=0.083^{\mathrm{m}}(26)$ is more statistically significant.

Corresponding brightness from the fit $\mathrm{Max_I}$=16.155(6), $\mathrm{Max_{II}}$=16.160(6), $\mathrm{min_I}$=16.882(12), $\mathrm{min_{II}}$=16.813(11) are close to that determined by Parimucha et al. (2011), but the accuracy estimate is better by a factor of ~5.

Acknowlwdgements. We thank Dr. L.Hric for helpful discussions and hospitality during the stellar conference Bezovec-2012 and to the Queen Jadwiga Foundation for individual grants to I.L.A. and B.V.V. The study was made in a course of the projects "Inter-Longitude Astronomy" (Andronov et al., 2010) and "Ukrainian Virtual Observatory" (Vavilova et al., 2012).

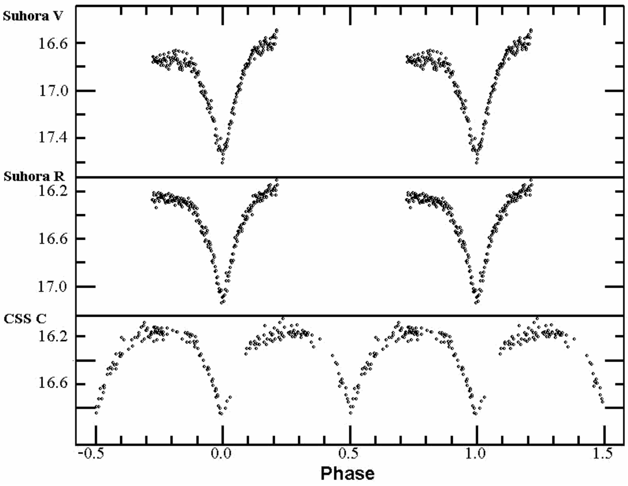

Fig. 2. Phase light curves of VSX1802

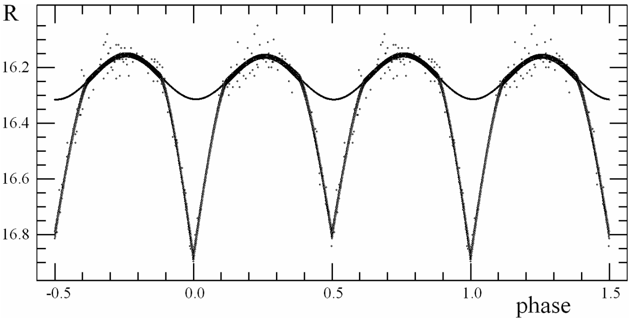

Fig. 3. The "NAV" fit for the phase curve and a corresponding "1σ" corridor. At the phases of eclipses, an additional curve corresponding to a continuation of "out of eclipse" parts is also shown.

References

Andronov I.L.: 1994, *Odessa Astron. Publ.*, **7**, 49.

Andronov I.L.: 2003, *Astron.Soc.Pacif.Conf.,* **292**, 391.

Andronov I.L.: 2012, *Ap* **55**, 536; *2012arXiv1208.3655A*.

Andronov I.L. et al.: 2010., *Odessa Astron. Publ.*, **23**, 8.

Andronov I.L., Baklanov A.V.: 2004, *Astronomy School Reports*, **5**, 264, *http://uavso.pochta.ru/mcv*.

Andronov I.L., Kim Yonggi, Yoon Joh-Na, Breus V.V., Smecker-Hane T.A., Chinarova L.L., Han Wonyong: 2011, *J. Korean Astron. Soc.*, **44**, 89.

Breus V.V.: 2012, *http://www.aavso.org/vsx/index.php ?view=detail.top&oid=282837*.

Breus V.V. et. al.: 2012, *Częstochowski Kalendarz Astronomiczny 2013*, *http://www.astronomianova.org/ publikacje.php*

Drake A.J., et al.: 2009, *Astrophys.J.*, **696**, 870.

Henden A.:2005, *ftp://ftp.aavso.org/public/calib/j1803.dat*

Kholopov P.N. et al: 1985, *General Catalogue of Variable Stars*, 4-th edition. Moscow: Nauka.

Kim Y., Andronov I.L., Jeon J.B.: 2004, *J.As.Sp.Sci.*, **21**, 191.

Parimucha Š., et al.: 2011, *New Astronomy*, **17**, 93.

Samus N.N., Durlevich O.V., Kazarovets E V., Kireeva N.N., Pastukhova E.N., Zharova A.V., et al. General Catalog of Variable Stars (GCVS database, Version 2012Jan), *http://www.sai.msu.su/gcvs/gcvs/*

"Variable Stars Index": 2012, *http://www.aavso.org/vsx*

Vavilova I.B. et al.: 2012, *Kinem.Phys.Cel.Bodies*, **28**, 8.

SPURS SYSTEM

Shatsova R.B., Anisimova G.B.

Southern Federal University, Rostov-on-Don, Russia
galina@iubip.ru

ABSTRACT. The system of nearby radioloops (spurs) is the screen to the remote objects and, perhaps, it distorts the real sky picture. But it is not due to the light absorption. Vise versa, the spurs system makes the objects brighter. Perhaps, it is the main reason for the fact that the majority of different scale objects, such as supernova, bright parts of Galactic spiral arms, main filaments of Local supergalaxy, etc are observed particularly through the spurs shells. Besides, the density of spiral structure' indicators, such as supergiants, Cepheids, and OB-associations, observed through the spurs, exceeds twice and more the same one in the neighbouring Milky Way regions. These facts can be explained either by making the objects brighter by spurs system, or by the existence of matter of higher density, contacting to spurs belts, or their combination.

Key words: Spurs, Radioloops, foreground, supernova, Local system, distribution

Radio Loops were discovered in the middle of 20th century. They are famous by strong radiation in radio continuum at different frequencies, in HI, in X-Rays, γ-radiation There is strong synchrotron radiation, strong magnetic field and polarization in spurs region (Page et al, [1]). Radio Loops are also interesting by their position: large angular dimensions and small distances (~>100 pc), spherical shape and large masses- 10^5 - 10^6 $M_\odot$ and other peculiarities.

More than a half of the sky is observed through these shells. The spurs region is considered transparent enough and they did not attract attention as the matter, rather distorting the real sky picture. We'll show, that Radio Loops take part in the formation of observed sky picture.

We have analyzed the influence of this foreground on the distribution of the different scale objects. And if the nearby and remote objects have the same peculiarities in their distribution, it means, that the observed picture is formed by the foreground.

We have analyzed a lot of objects of different scales:

- ✓ Stellar density –
  - the Supernova (SN Galactic extragalactic SNR)
  - the supergiants
  - the OB-associations
  - the Cepheids
- ✓ The supercluster of galaxies
- ✓ Local group of galaxies
- ✓ Light absorption

1. Supernova

1.1. Galactic Supernova

There were 12 very bright Supernova bursts from the beginning of our era. Their coordinates (l, b) and angular distances Δ from the nearest shell are given in Table 1. The angles Δ are obtained from

$$\Delta=\rho-\rho_s; \quad \cos\rho=\sin b \sin b_s + \cos b \cos b_s \cos(l-l_s) \qquad (1)$$

where ρ – the angular distance from the centre of s- spur, having coordinates (l_s, b_s) and ρ_s - the spur radius.

Table 1. Historical supernova, their coordinates (l, b) and angular distances Δ from the nearest shell

SN: year, name	l	b	Radioloop (s)	|Δ|(°)
1604 Kepler	4,5	6,8	I	
1408 CTB80	69	2,7	II, shell	0,3
1667 CasA	111,7	-2,1	(II, III)	3,0
902 CTA1	119,5	10,2	II, shell	1,1
1572 Tycho	120,1	1,4	(II, III)	2,7
369	129	-6	(II, III)	1,0
1181 3C58	130,7	3,1	II, shell	0,5
668 *	160	5,0	III, shell	4
	(156,2)	(5,7)		(0,5)
396	173	-22,0	V,VI;Eri,shell	
1054 Crab	184,6	-5,8	Ori-Eri	3
185 RCW86	315,4	-2,3	I	
1006	327,6	14,6	I,nucleus	3,2

The distance from the Loop I centre is $\Delta \equiv \Delta_c$ for SN1006. The Crab and SN396 are observed at the border of Orion-Eridan complex or at recently discovered loops V and VI [2].

The calculated Δ, Δ_p and Δ_c, between the share of degree and several degrees, are in the limits of the accuracy of parameters in table 2, or the shells thickness, having the same order.

It means that all 12 historical SN are observed through the spurs, through their shells, on the whole.

Table 2 shows the centre coordinates and the diameters of Radio loops over Berkhuijsen [3] and Heiles [4]. s is the number of spur in Roman numerals or the name. Number (II, III) in table 1 means, that the star is observed through the Lens, formed by the intersection of shells II and III, which have the mean plane along the Gould Belt (GB). The stars, having (II, III) $\Delta \equiv \Delta_p$ compared to p – the distance from GB, where

$$\sin p = \sin b \cos b^* - \cos b \sin b^* \sin (l-l^*) \qquad (2)$$

and parameters l* = 296°, b* = 21° over [5].

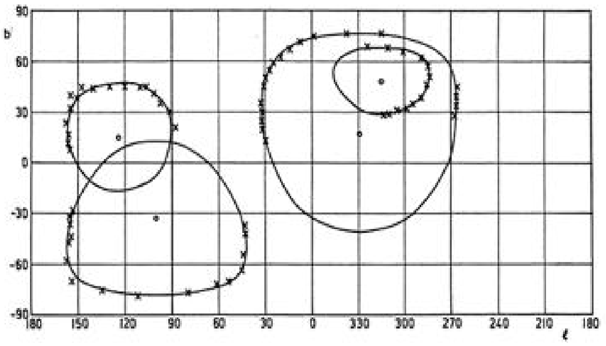

Fig. 1: The spurs, obtained theoretically from the equation (3)

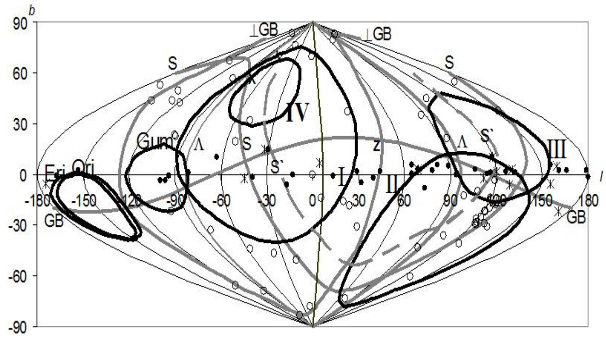

Fig. 2: Galactic SNR [7] and spurs, n=33(>1°)
l=207°-260° n=0

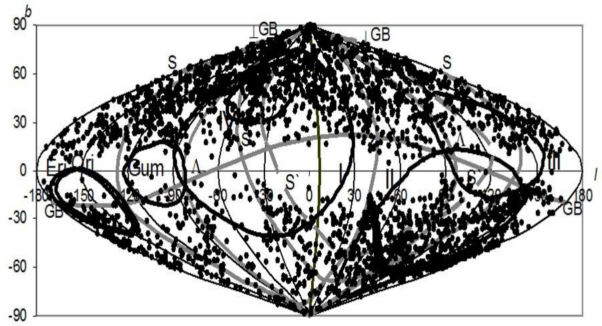

Fig. 3: SNR (out of Galaxy) [8] and spurs

Table 2. The centre coordinates and the diameters of Radio loops.

Spur	l_s	b_s	ρ_s
I	329°±1,5°	17,°5±3°	116°±4°
II	100°±2°	-32,°5±3°	91°±4°
III	124°±2°	15,°5±3°	65°±3°
IV	315°±3°	48,°5±1°	40°±2°
Ori-Eri	205°-209°	-19°	40°

The same results, presented in (Fig.1), we had obtained in [6] theoretically from the equation.

$$\rho_i = 2\pi/\kappa_i \quad \kappa_i\ –3, 4, 6, 9, 10;\ \text{multiple to 3} \qquad (3)$$

1.2. Supernova remnants

The list of these observed young SN can be enlarged by the old supernova remnants (SNR). The most large SNR (>1°, n=33) over Green catalogue [7] are presented at Fig.2. Only 3 of them are situated between the spurs, and 3 more are situated on Loops V and IV, recently discovered [2]. Hundreds of SNR over whole catalogue [7] give the same picture – the absence of SNR between *l*= 207° and 260°, that is between Eri-Ori and Gum Neb complexes. There are about 20 SNR between Loops I and II, that is over Loops V and VI [2].

1.3. Extragalactic Supernova

All SN and SNR are located on the small latitudes *b* and can't show the correlation with the spurs, stretched to b≈±78°. Thousands of extragalactic Supernovas from several catalogues can be used, for instance, from [8], to present the map in the galactic coordinates together with spurs (Fig.3). There is almost empty wide zone at |b|<10 – 15° (the known zone of avoidance of galaxies and SN in them). The densest zone passes along the celestial equator, which shows the selection: SNs were searched more often here, than in other regions.

The next on density is zone S, passing through the spur centres I – IV especially visible at Loop IV, the southern part of Loop I, the middle part of Loop II and between the Loops. The Loop IV is only one of all, located completely out of zone of avoidance, and it is well outlined by dense SN groups. Along the borders of other Loops one can also see a lot of dense SN groups. And there are many arcs, consisting of SN, and there are many candidates to the shell structures, over Hu [9] and Heiles [10] lists. These arcs may be used to check these candidates. But also here may be random arcs and selection.

So, the real and visible effects are interlaced in this map, and it is difficult to separate them. But many elements of the map can be attributed to the foreground, connected to the spur system, and in the predicted places.

2. The indicators of spiral arms

We also analyzed different indicators of spiral arms, among them there were 669 supergiants, 78 OB–associations over Humphreys [11, 12], and 270 Cepheids, over Melnic et al map [13]. The histograms of their distributions are given in Fig.4. The longitude intervals tangential to the Loops I, II, III are marked at x-axis.

All three groups of objects show large jump in density distribution at the border of loops, which show the correlation with spurs. It can be explained either by the higher density of these different objects, or by making objects brighter in the spurs regions, or by their combination.

If the contrast in density is attributed entirely to the process of making objects brighter, one can determine its value Δm. In conditions of homogeneous environment Δm means the exceeding of the process of making objects brighter Δm_l over the light absorption $A_v r$

$$\Delta m = \Delta m_l - A_v r \qquad (4)$$

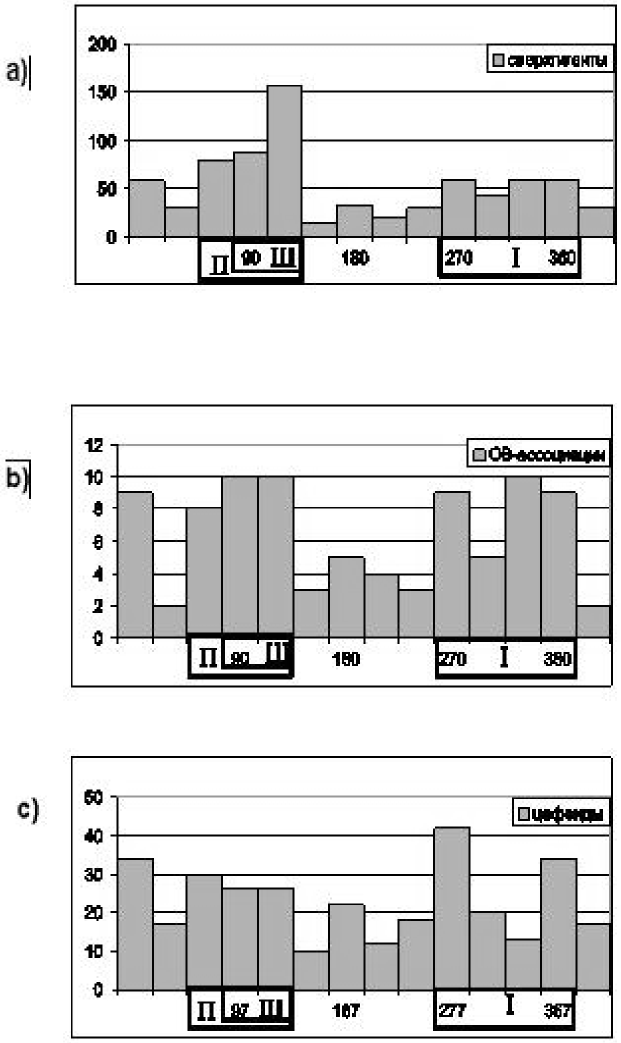

Fig. 4: The distribution of the objects number on longitude l

a) supergiants (669)
b) OB-associations (78) [11,12],
c) the Cepheids (270) [13]

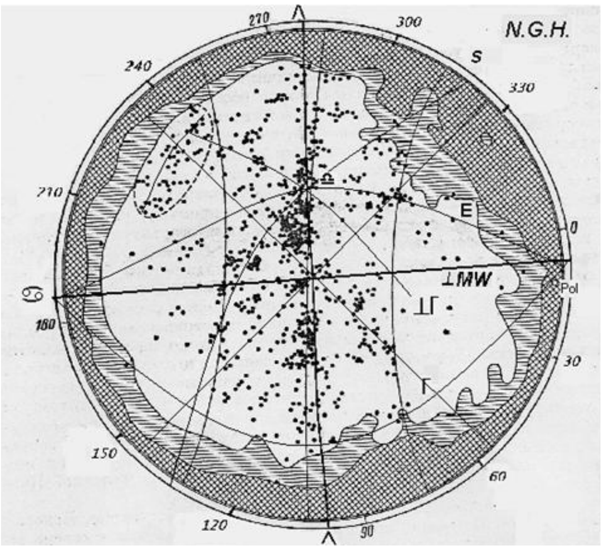

Fig. 5: Virgo supergalaxy [15] (NGH)

The more remote objects from the larger volume of radius r ($\sim r^3$) are as if displacing to the nearer volume of radius r_l ($\sim r_l^3$) due to the process of making objects brighter and become visually nearer. The observed density increases in comparison to the real density in the same nearby (out of spur) volume ($\sim r_l^3$). The object (stars) numbers $n(r)$ and $n_l(r_l)$ have the same sense.

On the one hand, for the identical absolute magnitudes

$\Delta m = 5 \lg (r/r_l)$ (5)

On another hand – $\lg (n_l/n) = 3 \lg (r/r_l)$ (6)

Excluding $\lg (r/r_l)$, we have

$\Delta m = 5/3 \lg (n_l/n)$ (7)

We determine $n_l/n \sim> 2$ for the spurs borders, using the histograms on fig.4. Only one case, for supergiants, gives the ratio about 11. There are shells of two loops (II and III) here at the same l, but having opposite sign of b, in projection to the Galactic plane. So, it can be attributed only a half to each loop (≈ 5). But it is also higher, than over the Cepheids, that can be the result of local peculiarities. We have $\Delta m \geq 0.^m5$, adopting $n_l/n \geq 2$. If the light absorption A_v at the same longitudes is in interval of $0.^m5$ to 2 m/kpc (over[14]), then the process of making objects brighter itself Δm_l may be several stellar magnitudes. Just the same magnitudes are needed to understand the visibility of bright SN.

The second alternative case is attributed to $\Delta m_l = 0$, when the contrast in number of stars is created by the belts of the higher density, passing near spurs border [5]. In reality we have the combination of these cases: the dense belts are combined with the process of making brighter the objects by spurs foreground.

3. The supercluster of galaxies (Vaucouleurs)

The Virgo supercluster of galaxies has the flattened filamentary shape. The whole Local group of the galaxies (and our Galaxy inside it) is surrounded by Virgo, but we are far from its centre. And the spurs system has also asymmetrical position over sky. One can see on Fig.5 over the Vaucouleurs map [15] (galaxies brighter 13^m) that a lot of filaments fit to the loops borders at $l_s \pm ½\rho_s$ or $b_s \pm ½\rho_s$ (table 2). The spurs system serves as a stencil to cut out in supercluster the regions of filament shape. And it means that this is not random, as we see this effect on all spurs. Hence, the real picture in supercluster rather differs from the visual one.

The individual galaxies from Local group over the lists [16,17], containing 65 nearby systems, were compared with the spurs. Their correlation is seen from Table 3 and Fig.2.

Table 3. Local group of galaxies (65), observed through spurs

Loop	Shell	SBelt	Loop Centre	Outside
I	11 (12)	4	2	
II	3 (4)	19		
III	9	-		
IV	1 ?	1 ?		
Gum Neb	2			
gap		5		
Outside				10

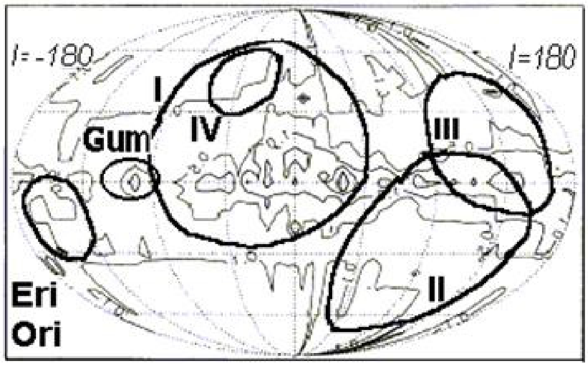

Fig. 6: Map of light absorption [14] and spurs

More than 80% of galaxies from Table 3 are projecting over the loops and s-belt ±20°wide, though their total area is smaller 40% of sky, except the part of Antlia group near the Galactic pole. The conditions of visibility differ for different loops and loops' parts.

4. The light absorption

The observed picture can't be explained by light absorption, as in the loops region the absorption is also larger than in the neighbouring region over [14] (Fig 6). So, taking into account the light absorption can only make the observed picture more contrast.

Conclusions

The spurs are screening more than a half of sky area from the distances of 100 – 200 pc and, perhaps, it distorts the real sky picture. The light absorption here rather slightly differs from its mean value at the same latitudes. Nevertheless, compact spurs are controlling the situation around. The spurs participate in the creation of visual sky picture, have the influence on the models of Galactic structure and even the large scale structures. The facts are:

The supernova and nearby galaxies projections coincide with spurs shells, spurs belt S and the spurs Lens

The indicators of spiral structure (the supergiants, the OB-associations, the Cepheids) have sharp density jumps at the longitudes of spurs borders

The coincidence of the spurs system map with the

- galactic distribution in the Local group
- filaments of Virgo supergalaxy
- CMB polarization, etc.

The large quantity of coincidences related to the objects of such different scales can't be random. Perhaps, being the foreground, the spurs create the conditions of visibility of such different structures, making them brighter for several stellar magnitudes.

We observe the objects brighter; and then what are they in reality?

And the Galactic spiral arm models were built over supergiants , OB-associations and the Cepheids. What will be the changes in the models, if we take into account the correlation of spiral indicators and the spurs (as foreground makes brighter the real objects)?

What will be the changes in the scale of distances?

What will be the changes in the luminosity function? The bright part becomes lower?

Resuming this theme, we can conclude, that many objects are rather more remote, than it is considered now.

References

1. Page L., Hinshaw G., Komatsu E. et al.: 2007, *Astrophys. J. Suppl. Ser.*, **170**, 335.
2. Borka V., Miloradov-Turin J., Uroševic D.: 2008, *Astron. Nachr.*, №1-6.
3. Berkhuijsen E.M.: 1971, *Astron. Astrophys.*, **14**, 359.
4. Heiles C.: 1998, *Astrophys. J.*, **498**, 689.
5. Shatsova R.B., Anisimova G.B.: 2003, *Astrophysica*, **46**, 319.
6. Shatsova R.B., Anisimova G.B.: 2008, *Odessa Astron. Publ.*, **21**, 106.
7. Green D.A.: 2006, *Galactic SNRs: Summary Data*, Cambridge CB3 The United Kingdom.
8. Barbon R., Buondi V., Cappellaro E., Turatto M.: 1999, The Asiago Supernova Catalogue (Dynamic Version) *A. Aph. Suppl. Ser.*, **139**, 531, *http://web.oapd.inaf.it/supern/cat/cat.txt*
9. Hu E.: 1981, *Astrophys. J.*, **248**, 119.
10. Heiles C.: 1984, *Astrophys. J. Suppl. Ser.*, **55**, 585.
11. Humphreys R.M.: 1970, *Astron. J.*, **75**, 602.
12. Humphreys R.M.: 1973, *Aph. J. Suppl. Ser.*, **38**, 309
13. Melnic A.M., Damdis A.K., Rastorguev A.C.: 2000, *«Variable stars»*, Arckhiz (Samus N.N.).
14. Hakkila J., Myers J.M., Stidham B.: 1991, *Astron. J.*, **114**, 2043.
15. de Vaucouleurs G.: 1959, *Astron. J.* (Ru), **36**, 977.
16. Drosdovsky I.: *http://www.astronet.ru/db/msg/1169715.*
17. *http://www.atlasoftheuniverse.com/galaxies.html.*

NEW STELLAR RADII, CALCULATION OF DIRECT METHODS

M.A.Babenko [1], V.A.Zakhozhay [2]

[1] Kherson State University, Kherson, Ukraine
[2] V.N.Karazin Kharkiv National University, Kharkiv, Ukraine
[1] babenkoma@gmail.com, [2] zkhvladimir@mail.ru

ABSTRACT. The results of radii calculation by direct methods of 469 stars within Gould Belt, including 35 stars in radius 10 pc from the Sun based on the data published in last 30 years are analyzed. Diagrams "radius-spectrum" for stars of different luminosity classes are constructed.

Key words: stellar radii, diagram "radius-spectrum".

Introduction

The radius is one of the basic physical properties of the stars, characterizing their models of an interior structure and evolution. Direct and indirect methods for definition of stellar radii are developed.

Direct methods of the linear radius determination of stars assume the measuring of their angular diameter and a parallax. It is possible to measure angular diameter of stars by following methods [1]:

- stellar interferometry;
- intensity interferometry;
- stellar occultations by celestial bodies;
- speckle interferometry;
- eclipsing variable stars.

Indirect methods can determine radii or angular diameters using statistical dependences between stellar parameters. These include [2]:

- photometric method;
- empirical methods.

By the beginning of 20th century with direct methods only 36 stellar radii has been measured and the distance to them doesn't exceed 25 pc [1]. However, in the last decade, the new interferometry measurements of the stellar angular diameters on the interferometer Mark III [14], CHARA [7], PTI [4], VLTI [16], etc. were obtained. In this article, we present the results of the stellar radii determination by measuring the angular diameters during the last 30 years.

1. Theoretical foundation

Knowing the angular diameter θ and parallax p, stellar radius R can be determined as follows. It is obvious the relation $\mathrm{tg}\theta/2 \approx R/r$, where r – is the distance to the star. Then, its linear radius equals $R \approx \frac{1}{2}\theta r$, where θ is expressed in radians. Expressing the stellar radius in solar radii, the formula for radius calculation is: $R \approx 107{,}4698 \cdot \theta / p$, where the angular diameter and parallax expressed in arc seconds. The absolute error of the radius is equal to: $\Delta R = R(\Delta\theta/\theta + \Delta p/p)$.

2. The calculation results

Data on the stellar angular diameter (measured on the assumption of a uniformly emitting stellar disk), were taken from the original papers published in the last 30 years [3-11, 13-16, 18]. Data on stellar parallaxes were taken from the new redaction of Hipparcos catalog of stars [12].

As result for analisis it was available 469 stellar radii (calculated by direct methods), in a distance of 500 pc from the Sun (that is, within the Gould Belt). Among them are the brightest star, Sirius A, α Centauri (A, B, C), Procyon, Deneb, Altair, Rigel, Vega, Betelgeuse, Fomalhaut, Antares, Dubhe, Spica and others. In the sample – 85% of the radii were calculated based on the measurements of the angular diameters with stellar interferometry, 6% – by the intensity interferometer and 9% – with the method of lunar occultations. All relative errors of radii measurements do not exceed 50%, 64% of the measured radius with an uncertainty of ≤10%. The measurements of the angular diameters with other direct methods give greater error than the above, so that data are not included in the sample .

Stellar distribution in the sample that was obtained based on the spectral types and luminosity classes are shown in Fig. 1 and 2. It is seen that most of the stars with the measured radius (85%) – the stars of spectral types G, K, M. Distribution of stars in the sample for the luminosity class is understandable: the ability to determine the radii of the Giants (64%) is connected with their size, and the possibility of determining the dwarfs (17%) – with a majority of the number of stars in the solar neighborhood.

The radii of only 35 stars closer than 10 pc from the Sun (Table 1) were determined. Only in this area at the end of 1990 it was 356 stars and substars [19], according to Simbad astronomical database[17] in this area there are 367 such objects. Thus, only 10% of the radius of the nearest stars can be calculated by direct methods. The radii of the other stars may be evaluated only indirectly.

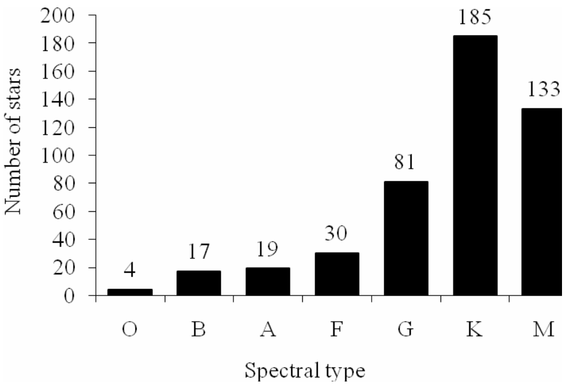

Fig. 1: Distribution of stars with the measured radius by the spectral types

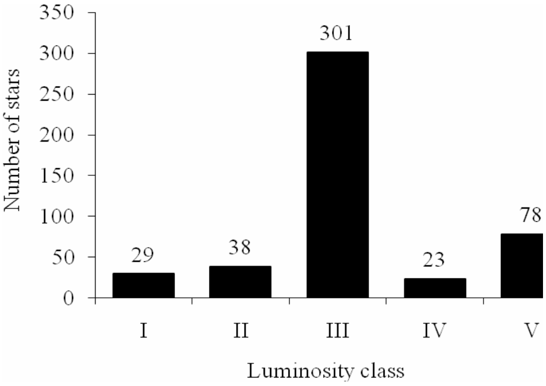

Fig. 2: Distribution of stars with the measured radius by the luminosity classes

Table 1: The radii of nearest stars, calculated by direct methods

HIP	$R/R_\odot$	$\Delta R/R_\odot$	HIP	$R/R_\odot$	$\Delta R/R_\odot$
1475	0,3794	0,0203	61317	1,0966	0,0291
3765	0,7299	0,0132	64394	1,0793	0,0125
3821	1,0094	0,0054	67155	0,4699	0,0092
5336	0,7687	0,0108	70890	0,1393	0,0701
8102	0,8120	0,0319	71681	0,8091	0,0937
8362	0,8049	0,0238	71681	0,8091	0,0937
12114	0,6328	0,0368	71683	1,2245	0,0138
15457	0,8978	0,0258	72659	0,8387	0,0128
16537	0,7431	0,0695	81300	0,8838	0,0308
22449	1,2903	0,0052	85295	0,5495	0,0329
27913	0,9562	0,0106	86974	1,6393	0,0574
32349	1,5933	0,1103	87937	0,1935	0,0084
37279	1,9924	0,0567	91262	2,5355	0,0717
37826	8,2289	0,2207	96100	0,7539	0,0076
49908	0,6641	0,0227	97649	1,8222	0,0490
54035	0,3878	0,0031	104214	0,5950	0,0171
56997	0,9162	0,0116	104217	0,6124	0,0136
57939	0,6634	0,0074	113368	1,7303	0,0145

Angular diameters of stars, calculated by direct methods are the basis for empirical methods for their linear radii determination. One of such methods is the determination of the radius with the dependence "radius-spectrum". Because spectral types and luminosity classes of our sample of stars are known, it is possible to plot the dependence "radius-spectrum" for different luminosity classes. To do this, it is advisable to introduce such a magnitude as the spectral code C_{Sp}, which numerically describes a spectral type of the object. We assume that the spectral code $C_{\mathrm{Sp}}=0$ corresponds to the spectral type Sp=O0, spectral code $C_{\mathrm{Sp}}=10$ – Sp=B0, etc.

The proposed introduction of a spectral code allows to plot the "radius-spectrum" dependence analytically and graphically. In Fig. 3–7 are shown the dependences of lg$R$ on the spectral code C_{Sp} for luminosity classes: I, II, III, IV and V, and Fig. 8 shows the general diagram of the "radius-spectrum."

Conclusions

For stars of different luminosity classes the statistical relation between the logarithm of the radius and the spectral code is observed, this allows to determine the radius of the indirect method, not only for dwarfs, but also for other stellar luminosity classes.

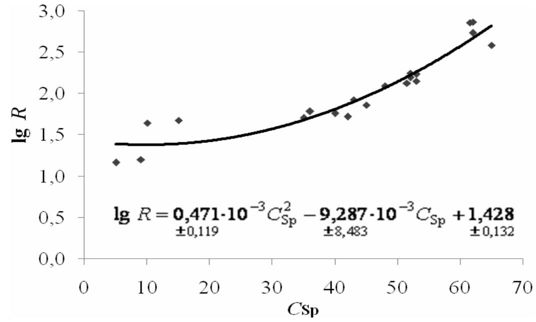

Fig. 3: Diagram "radius-spectral code" for supergiants (luminosity class I)

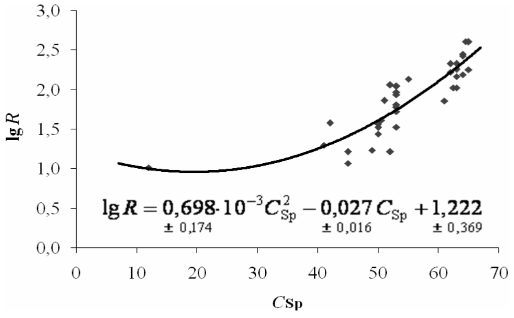

Fig. 4: Diagram "radius-spectral code" for bright giants (luminosity class II)

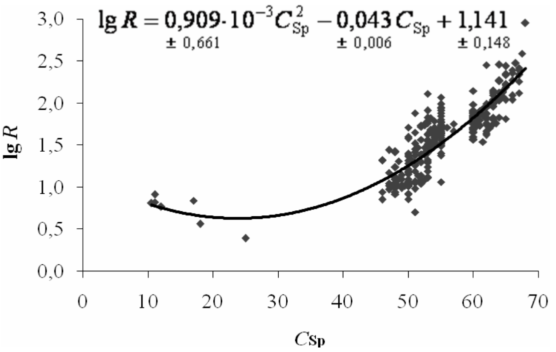

Fig. 5: Diagram "radius-spectral code" for giants (luminosity class III)

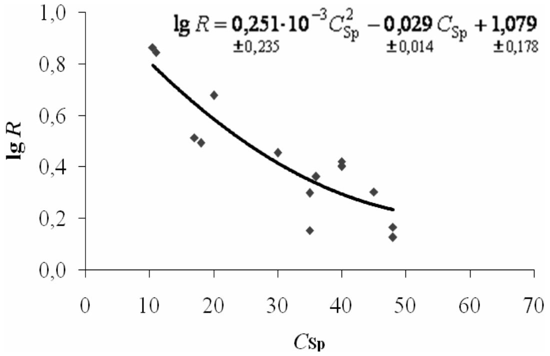

Fig. 6: Diagram "radius-spectral code" for subgiants (luminosity class IV)

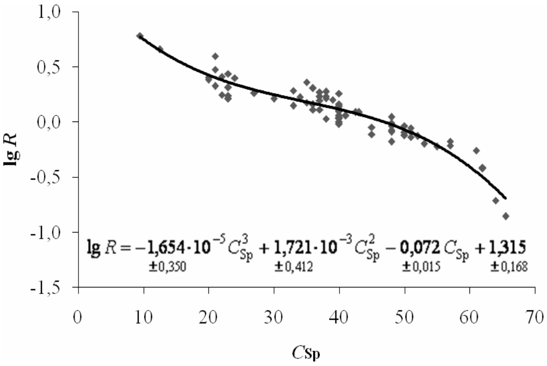

Fig. 7: Diagram "radius-spectral code" for dwarfs (luminosity class V)

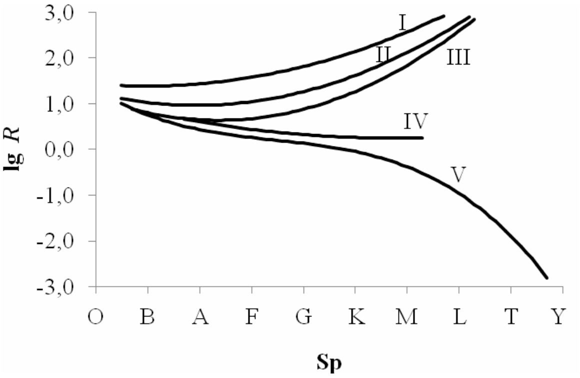

Fig. 8: Diagram "radius-spectrum" for stars of different luminosity classes

References

1. Захожай В.: 2002, *Кинем. физ. неб. тел*, **18**, 535.
2. Сахибулин Н.: 2003, Определение фундаментальных параметров звезд, 389.
3. Baines E.K., McAlister H.A., Brummelaar T.A. et al.: 2009, *Astrophys. J.*, **701**, 154.
4. Belle G.T., Braun K.: 2009, *Astrophys. J.*, **694**, 1085.
5. Belle G.T., Lane B.F., Thompson R.R., et al.: 1999, *Astron. J.*, **117**, 521.
6. Benson J.A.; Dyck H.M., Mason W.L. et al.: 1991, *Astron. J.*, **102**, 2091.
7. Boyajian T.S., McAlister H.A., Belle G.: 2012, *Astrophys. J.*, **746**, 101.
8. Crepp J.R., Mahadevan S., Ge J.: 2009, *Astrophys. J.*, **702**, 672.
9. Dyck H.M., Belle G.T.; Thompson R.R.: 1998, *Astron. J.*, **116**, 981.
10. Hanbury Brown R., Davis J., Allen L.R.: 1974, *Mon. Notic. Roy. Astron. Soc.*, **167**, 121
11. Lane B.F., Boden A.F., Kulkarni S.R.: 2001, *Astrophys. J.*, **551**, L81.
12. Leeuwen F.: 2007, *Astron. Astrophys.*, **474**, 653.
13. Mondal S., Chandrasekhar T.: 2005, *Astron. J.*, **130**, 842.
14. Mozurkewich D., Armstrong J. T., Hindsley R. B. et al.: 2003, *Astron. J.*, **126**, 2502.
15. Richichi A., Lisi F., Giacomo A.: 1992, *Astron. Astrophys.*, **254**,149.
16. Richichi A., Percheron I., Davis J.: 2009, *Mon. Notic. Roy. Astron. Soc.*, **399**, 399.
17. SIMBAD Astronomical Database, http://simbad.u-strasbg.fr/simbad.
18. White N.M., Feierman B.H.: 1987, *Astron. J.*, **94**, 751.
19. Zakhozhaj V.A.: 1996, *http://vizier.cfa.harvard.edu/viz-bin/VizieR?-source=V/101*.

LINES SELECTION TO DETERMINE THE CHEMICAL COMPOSITION OF STARS IN THE RANGE -3 ≤ [FE/H] ≤ -0.7

N.Yu.Basak, T.V.Mishenina

Astronomical Observatory, Odessa National University
T.G.Shevchenko Park, Odessa 65014 Ukraine
astro@paco.odessa.ua

ABSTRACT. Using the spectra obtained with echelle spectrograph SOPHIE (1.93 m telescope, OHP, France) and the data from about 20 papers of various authors, we have compiled a list for around four thousand lines of different chemical elements. Based on the spectra of the Sun and stars and also synthetic spectrum calculations in different ranges of metallicity, we selected 300 unblended lines of FeI, FeII and 200 lines of YII, ZrI, ZrII, LaII, CeII, PrII, NdII, SmII, GdII, that are recommended for the study of the chemical composition.

Key words: Stars: abundance – Stars: late-type

To study of the F, G, K-dwarfs and giants in a wide range of metallicity (-3 ≤ [Fe/H] ≤ -0.7) based on the spectra obtained with high resolution and signal to noise ratio (S/N) is need to create the list of unblended lines for the determination of chemical abundances.

The spectra for the thirty appropriate stars were selected from the archives of the spectrograph SOPHIE (Perruchot et al. 2008) at 1.93 m telescope (OHP, France). Processing of the spectra was performed using the new version of the DECH20 software by Galazutdinov (1992).

To create the list of the iron and s-and r-process - capture lines, we used some works (e.g. Boyarchuk et al. 1998; Grevesse N., et al. 1999; Sneden et al. 2009; Lawler et al. 2009; Takeda et al. 2005; Lai et al. 2008; Aoki W., et al. 2007; Ramirez I., et al. 2007; Pakhomov Yu.V., et al. 2011; Simmerer J., et al.: 2004; Coluzzi R. 1993; Den Hartog E.A., et al. 2006; Lawler J.E., et al. 2006 etc.) and we selected about four thousand lines of chemical elements. The atomic parameters of this line list were taken from the database VALD (Kupka et al. 1999). The elemental abundances were computed using the solar spectrum (S/N = 332) and the spectrum of the star HD6582 (S/N = 321) with this line list under the WIDTH program by Kurucz (1993). As a result 1600 unblended lines remained. Most of them there are the neutral iron lines (about 980 lines). The chemical composition of the Sun was calculated (by the model with parameters T_{eff} =5780 K, log =4.45, V_t = 0.8, [Fe/H] = 0) and compared with that given in Grevess et al (2010). Then for five stars using 820 lines of FeI, FeII, YII, ZrI, ZrII, LaII, CeII, PrII, NdII, SmII, GdII the chemical composition was computed and compared with the data from (Fulbright 2000; Gratton, et al., 2003 etc).

Finally, based on synthetic spectra calculation for stars with different metallicity we selected about 300 lines of FeI and FeII and about 200 lines of n-capture elements.

Results and conclusions

1. We selected about 500 unblended lines of FeI, FeII, YII, ZrI, ZrII, LaII, CeII, PrII, NdII, SmII, GdII.
2. This list of lines was tested for the five previously investigated stars.

Selected lines are recommended to study the elemental abundance both with the use of equivalent widths and for line profile computations.

Acknowledgments. This work was supported by the Swiss National Science Foundation (SCOPES project No.~IZ73Z0-128180/1).

References

Aoki W. et al.: 2007*, Astrophys. J.*, **655**, 492.
Boyarchuk A.A. et al.: 1998, *Astron. Zh.*, **75**, 586.
Coluzzi R.: 1993, *Bull. Inf. CDS* **43**, 7.
Fulbright J.P.: 2000, *Astron. J.* **120**, 1841.
Galazutdinov G.A.: 1992, *Prepr.SAO RAS*, **92**, 28.
Gratton, et al.: 2003, *Astron. Astrophys*. **404**, 187.
Grevesse N. et al.: 1999, *Astron. Astrophys*., **347**, 348.
Grevesse N. et al.: 2010, *Astrophys. Space Sci*, **328**, 179.
Den Hartog E.A. et al.: 2006, *Astrophys. J. Suppl. Ser.*, **167**, 292.
Kupka F. et al.: 1999, *Astron. and Astrophys. Suppl. Ser.*, **138,** 119.
Kurucz R.L.: 1993, CD ROM n13.
Lai D.K. et al.: 2008, *Astrophys. J.*, **681**, 1524.
Lawler J.E. et al.: 2006, *Astrophys. J. Suppl. Ser.*, **162**, 227.
Lawler J. E. et al.: 2009, *Astrophys. J. Suppl.*, **182**, 51.
Pakhomov Yu.V. et al.: 2011, *Astron. Zh.* **88**, 284.
Perruchot et al.: 2008, *"The SOPHIE spectrograph Proceedings of the SPIE,* 7014.
Ramirez I. et al.: 2007, *Astron. Astrophys*. **465**, 271.
Simmerer J. et al.: 2004, *Astrophys. J.*, **617**, 1091.
Sneden C. et al.: 2009, *Astrophys. J. Suppl. Ser*., **182**, 80.
Takeda Y. et al.: 2005, *Publ. Astron. Soc. Jap*. **57**, 27.

TOTAL AND GAS FLOW ACTIVITY OF THE SEYFERT GALAXY NGC3227 NUCLEUS FOR ITS DIFFERENT EVOLUTIONARY EPOCHS

I.F. Bikmaev [1], I.I. Pronik [2], L.M. Sharipova [2]

[1] Kazan (Volga) Federal University, Kazan, Russia, ibikmaev@yandex.ru
[2] Research Institute "Crimean Astrophysical Observatory", Nauchny, Ukraine,
pronik@crao.crimea.ua,, shali@crao.crimea.ua

ABSTRACT. A comparative analysis of time variations of spectral characteristics of the Seyfert galaxy NGC 3227 nucleus: equivalent widths (EW λ), relative intensities, the width of the Balmer line profiles was carried out. Spectral data obtained in April 2009 with the 1.5-m Russian-Turkish telescope (RTT-150) and data published in the literature were used. Results of the comparative analysis showed the weakening of total activity and, consequently, gas flow activity of the galaxy nucleus in the time interval of more than 30 years.

Key words: Galaxies: Seyfert – individual: NGC 3227.

1. Introduction

The galaxy NGC 3227 has an active Seyfert nucleus (AGN). The long-term studies of AGN, carried out across the electromagnetic spectrum, including optical, provide with rich material for understanding physical processes that take place in their nuclei. In particular, Rubin and Ford [1], Rosenblatt et al. [2,3], Wing, Peterson et al. [4] I.I. Pronik [5], I.F. Bikmaev, I.I. Pronik, L.M. Sharipova [6] studied these problems. I.I. Pronik, L.P. Metik [7,8] obtained the evidence of the 3-day flare in gas of the Broad line region in the period of maximum brightness of the Seyfert galaxy NGC 3227 nucleus in January 1977. A number of works were devoted to the study of variability of the Balmer line profiles in the spectrum of the galaxy NGC 3227 nucleus and its gas flow activity. Spectral data obtained with the 6-m telescope of the Special Astrophysical Observatory in January 1977, data obtained at the Crimean Astrophysical Observatory in March 1977, as well as data acquired with the Russian-Turkish Telescope (RTT-150) in April 2009 formed the basis of our investigations. Variations of spectral characteristics of the radiation from the galaxy NGC 3227 nucleus were analyzed. Results of our studies are presented below.

2. Comparative analysis of spectral characteristics

2.1 Variation of relative intensities of the Balmer lines with time

The investigations of variability of relative intensities of the Balmer emission lines in the spectrum of the galaxy NGC 3227 nucleus have been carried out at the Crimean Astrophysical Observatory over 40 years. In particular, I.I. Pronik [9] studied the nature of variability of relative intensities of the emission lines and obtained evidences of heterogeneity of physical conditions in the gaseous environment of the galaxy NGC 3227 nucleus. In this paper we have traced variations of relative intensities of the emission lines over the period 1977 to 2009. Relative intensities of the Balmer lines $IH\gamma / IH\beta$, $IH\alpha / IH\beta$ in 1977 were taken from [9]. Relative intensities of the same lines in 2009 were estimated on the spectral data obtained with the 1.5-m Russian-Turkish telescope (RTT-150). Results of the comparative analysis of variations of relative intensities of the Balmer and forbidden lines are given in Tables 1 and 2.

These two tables show a decrease of relative intensities of both Balmer and forbidden lines in the interval of time from 1977 to 2009. The decrease factor of relative intensities of the Balmer lines was 2 and 2.5, respectively. The decrease of relative intensities of the forbidden lines was rather significant (about 3 times), except the relative intensity of the [OIII] 5007Å line (roughly about 6%).

2.2. Comparison of equivalent widths of the Balmer lines

The equivalent widths (EWλ) of the Balmer lines were that spectral characteristics which may vary over the time. Investigations of these possible variations were carried out in our work. Table 3 shows EWλ values of the hydrogen lines Hδ, Hγ, Hβ, Hα for two epochs of the galaxy nucleus activity. Data presented in the table show a decrease of equivalent widths of the hydrogen lines by a factor of 2.6, 2.3, 1.7 and 1.5, respectively.

Table 1. Comparison of relative intensities of the hydrogen lines

Date	04. 2009	03. 1977	04. 2009	03. 1977
	IH γ/ IHβ		IH α/ IHβ	
	0.24	0.48	2.77	6.92
	0.22		2.84	
	0.22		2.84	

Table 2. Comparison of relative intensities of the forbidden lines

Date	04. 2009	03. 1977	04. 2009	03. 1977	04. 2009	03. 1977
	I[OIII]5007Å/ IHβ		I[OI]6300Å/ IHβ		I[SII]6716Å/ IHβ	
	3.11	2.98	0.26	0.7	0.36	1.1
	3.18		0.25		0.36	
	3.3		0.27		0.39	

Table 3. Variations of equivalent widths of the hydrogen lines Hδ, Hγ, Hβ, Hα

Date	01.1977	04.2009	01.1977	04.2009	01.1977	04.2009	01.1977	04.2009
	EWHδ		EWHγ		EWHβ		EWHα	
	29.3	11.2	47.3	20.7	97.9	57.1	412	301
	25.2	12.5	44.9	22.4	66.2	54.5	420	302
	27.1	12.6	45.0	20.9	67.9	53.9	446	296
	34.3		44.6			70.2	450	

2.3 Widths of the hydrogen line profiles

The width variations of the Hγ, Hβ, Hα hydrogen line profiles have been traced in the time interval of more than 30 years. Table 5 shows widths of the Balmer line profiles at the level 0.25 of peak brightness (0.25Imax).

Table 4. Widths of the hydrogen line profiles

Date	January 1977	April 2009
	0.25Imax, km / sec	0.25Imax, km / sec
Hγ	10404 ±449	4500 ±180
Hβ	6107 ±293	3816 ±107
Hα	4291±181	3367 ± 37

Table 4 shows that the width decreasing of the Hγ, Hβ, Hα line profiles at the level 0.25Imax in the time interval of more than 30 years was on the factor 2.3, 1.6, 1.3, respectively.

The comparative analysis showed a significant decrease of spectral characteristics over the time. This fact is the evidence of weakening the total activity of the galaxy nucleus. For this reason, it was of interest to follow the variation of hydrogen line profiles for determining the presence or absence of their components. Such components can be the pointers of gas flow activity of the galaxy nucleus.

3. Multi-component hydrogen line profiles and gas flow activity of the nucleus of NGC 3227

The multi-component structure of the Hβ line profile was first indicated by Rubin and Ford [1]. The authors studied the Hβ line profile in the epoch of deep minimum of brightness of the galaxy NGC 3227 nucleus. In our paper results of the comparative analysis of time variations of forms of the hydrogen line profiles are presented. The spectral data obtained with the 1.5-m Russian-Turkish telescope, as well as data published in the previous papers [5-8] were used in our investigations. The example of variable Hγ, Hβ line profiles for two epochs (1977 and 2009) is shown in Fig. 1 and Fig. 2. Components noted in [1] are labeled by numbers 1 - 5 in these figures. In the epoch of maximum brightness of the galaxy nucleus in January 1977 the blue wing of the Hγ, Hβ line profiles is seen to contain "blue" emission component (in our notation – component 6). In 2009 component 6 is absent in the Hγ, Hβ line profiles. Both figures show the scale rule of the estimation of the hydrogen lines gas velocity. It is 5000 km / sec.

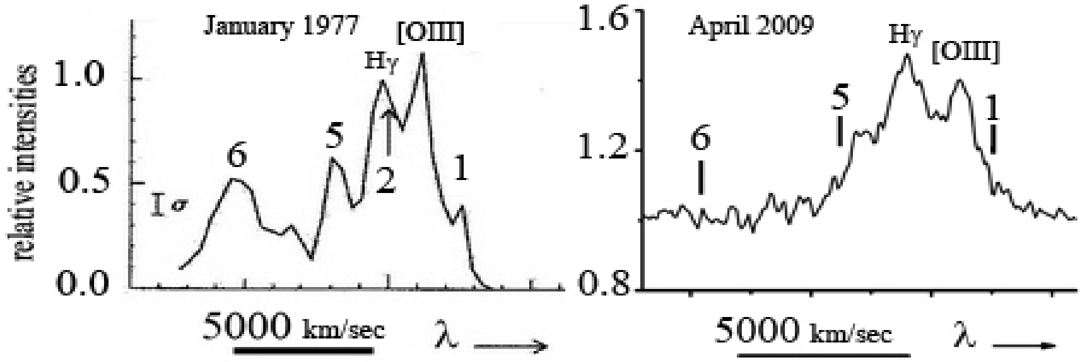

Fig. 1: Multi-component Hγ line profiles at different evolutionary epochs of the NGC 3227 nucleus

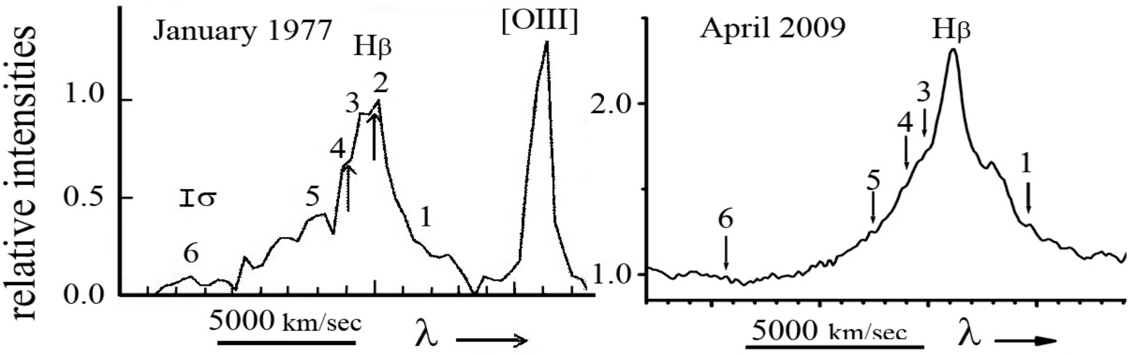

Fig. 2: Multi-component Hβ line profiles at different evolutionary epochs of the NGC 3227 nucleus

The intensities of emission components 1, 5, 6 in 1977 were 35%, 60%, 50% of the peak of Hγ line brightness, respectively. 30 years later the profile has changed: the intensities of the emission components 1 and 5 were 20%, 30% of the peak brightness of Hγ line, respectively. Components of the Hβ line profile show the similar variations over the time: the intensities of the emission components 1 and 5 of the Hβ line profile in January 1977 were 25%, 40% of the peak brightness of the Hβ line, respectively. In April 2009 the intensity of these components was only the 5th part of the Hβ line peak brightness.

Conclusions

The comparative analysis of spectral characteristics of the Seyfert galaxy NGC 3227 nucleus and the form of the Balmer line profiles showed their significant variations in the time interval of more than 30 years. These results may point at the fact that 32 years later after the flare in the gas of the Broad line region in January 1977, the physical conditions in the area of the hydrogen emission lines have changed. During this time there was a weakening of the total activity of the galaxy NGC 3227 nucleus and its gas flow activity as well.

References

1. Rubin V.C., Ford W.K.: 1968, *ApJ*, **154**, 431.
2. Rosenblatt E.I., Malkan M.A., Sargent W.L.W., Readhead A.C.S.: 1992, *ApJS*, **81**, 59.
3. Rosenblatt E.I., Malkan M.A., Sargent W.L.W., Readhead A.C.S.: 1994, *ApJS*, **93**, 73.
4. Winge C., Peterson B.M. et al.: 1995, *ApJ*, **445**, 680.
5. Pronik I.I.: 2009, *A&A*, **496**, 299.
6. Bikmaev I.F., Pronik I.I., Sharipova L.M.: 2011, *Odessa Astron. Publ.*, **24**, 59.
7. Pronik I.I., Metik L.P.: 2004, *Astron.Astrophys.Trans.*, **23**, 509.
8. Pronik I.I., Metik L.P.: 2005, *Ap.&SS*, **239**, 97.
9. Pronik I.I.: 1983, *Izv.Krimsk.Astrophys.Obs.*, **68**, 81.

CHEMICAL EVOLUTION IN ALGOLS

L.V. Glazunova[1,2]

[1]Odessa National Academy of Telecommunications, Kuznechnaya street 1, Odessa, Ukraine
[2]Astronomical Observatory, Odessa National University, Odessa, Ukraine
lvglazun@gmail.com

ABSTRACT. We discuss the chemical abundance in Algol-type systems produced by different authors. Till this time most evolutionary changes in the chemical abundance of the components of Algols were studied by carbon depletion. We obtained the following results: 1) detections of carbon abundance in the atmosphere of donor were reported in two articles, but them don't show dependence from the mass ratio and the mass donor, 2) the carbon abundance in the atmosphere accretor for the same system in research different authors is very different, also it isn't dependency from the ratio of the masses and the masses of accretor. Summary: while were observed evolutionary changes in the carbon abundance for Algol's component, but a precision was low and studied the small number of systems and can not linke to the carbon abundance and mass ratio and also the masses of the components – the basic parameters of the binary system evolution.

Key words: Stars: binary: abundances – binaries;close – stars; evolution – stars.

1. Introduction

The theory of evolution of close binary stars (CBS) predict significant changes of chemical composition of components as a result of nuclear processes inside stars couples and by exchange of matter, and, in contrast to the single stars, additional mechanisms of mixing in binary systems. De Greve & Packet (1990) have made calculations of the evolution of CBS with the analysis of the changes the chemical composition of the components in the case A (burning hydrogen in the core), and came to the conclusion that we can not explain the change in the chemical composition of the exchange only mixing in their atmospheres. In articles Sarna (1992) and Sarna & De Greve (1997) more fully present theoretical calculations of the change in the chemical composition of the components of CBS first phase of mass exchange for the evolutionary case AB and early B. Calculations of the evolution of CBS made using Pachinsky (1970) assumption: the total mass of M = 4,6,10 $M_\odot$, the mass ratio $q_0 = 10/9$ and 10/4, the relative abundance of hydrogen in the core for donor $X_C < 0.1$, nucleasynthesis calculate as Flower et.al 1975, in the case of non-conservative exchange accounted loss of angular momentum of the wind and the magnetic loss mass and angular momentum of the system of stellar winds. The change in the chemical composition of the atmospheres of the components are calculated according to the following mechanisms of mixing: 1) convective mixing in the donor, which can effectively change the CNO, only in the case of initial masses $< 3 \times M_\odot$ (mixing length $l > 0.1$) during a phase of slow exchange; 2) the accretion as a mechanism for mixing of the atmosphere accretor until the accretion rate is $\dot{M}_{accr} > 10^{-7} M_\odot$/year; 3) the thermohaline convection in the accretor, where the change of the molecular weight is positive $d\mu/dr > 0$ and the gradient transfer of radiative energy less gradient transfer of convective energy $\nabla_r < \nabla_{ad}$ is possible, when the time of accretion is much more time efficient diffuse mixing $\tau_{\dot{M}} >> \tau_{diff}$; 4) common envelope phase leads to equalization of the chemical composition of the components. The main conclusions of this work are as follows. 1) Were founded the real difference between the systems evolving from initial mass ratios of $q_0 = 10/4$ and $q_0 = 10/9$. The system with $q_0 = 10/9$ show twice the depletion of carbon of those with q0 = 10/4. It is concluded that the correlation between the carbon abundance and the mass ratio Algol, in a paper Cugier (1989), show only the bimodality of the initial mass ratio distribution for proto-Algol-type stars. 2) The conservative models have explained well the observed carbon abundance in accretor. 3) There is no significant differences in the chemical composition between case AB and early case B mass transfer. Determination of chemical composition of the components of Algol very difficult task for the following reasons: the high speed components, the total spectrum of the two components, the effect of gas envelopes on the spectral lines, the effect of gas envelopes at the level of the continuous spectrum of the system, the effects of reflection. Hence, in the spectra of these systems are observed mainly strong blended lines. So the definition of evolutionary change in the chemical composition of Algol-type systems on the same line as were done in Cugier, 1989; Ibanoglu et al., 2012 may not be accurate and may lead to incorrect conclusions. In last years were published works in which the chemical composition of Algol-type systems is determined for all the lines in a wide range of wavelengths. The purpose of this paper is to review all the published definitions of chemical elements in the spectra of components of Algol, calculating correlations of carbon content on the main parameters of the system and the comparison with theoretical studies.

2. Comparison values of carbon abundance for Algol-type systems

In Table 1 are collecected all available observational determinations for carbon and other chemical elements abundatce in Algol-type systems. There data are from Parthasarathy et al., 1983 (1), where the analysis of molecular lines CH 4310A, CN 4215 and 3883 for the donor systems U Cep and U Sge with accuracy 0.3 dex; Cugier 1989 (2) studied multiplets of CII 1324 and 1335 Å for accretors 6 systems with accuracy 0.2 dex; Yoon & Honeyocutt, 1992 (3) searched g-band of the CH molecule for 12 donors of Algol-type systems with precision 0.15 dex (standard lgN_C=8.43); Tomkin&Lambert 1989 for R CMa (5) and Tomkin et al., 1993 (5) studed carbon abandance using line CII 4267 for accretors 8 systems with precision 0.15 dex, (standard $lgNC = 8.28$), Tomkin & Lambert, 1994 (4) analysis CI,NI and OI lines of visual and near-ifrared regions in the donor of system V356 Sgr with accuracy 0.1 dex, Ibanogly et al., 2012 (6) studed the line CI 4267 Å in accretors for 15 systems with precision 0.2 dex (standard lgN_C=8.52). The first six columns of Table 1 are the names of the systems, the donor (II) or accretor (I), the orbital period, mass ratio and mass of accretor and donor. The next six columns are carbon abandance $[N_C/N_{tot}]$ and abandance other chemcal elements with references for these values. We took lgN_C = 8.52 for the solar abandance in Table 1 adopted from Grevesse and Sauval (1998). As we can see, that all attempts to study the chemical evolution of Algol were based on an analysis of mostly one element – carbon.In column 10 (4) of Table 1 shows the abandance of elements CNO cycle and iron for Algol-type systems, obtained by high-resolution spectra in the following work: R CMa – Glazunova et al., 2009, RZ Cas – Tkachenko et al., 2009, TW Dra – Tkachenko et al., 2008, TX UMa – Glazunova et al., 2011, V365 Sgr – Tomkin & Lambert, 1994. Model parameters for atmosphere accretors these components were refined over the observed and synthetic spetra in long wavelengths region, which allowed us to obtain a reliable estimate of the abandance of various elements.

We have calculated the coefficient of correlation between the carbon abandans and the basic parameters of the system – the mass ratio q and the component's masses of M_{don} and M_{accer}. Coefficient of correlation between the mass of the accretor and its carbon abandance is 0.25, and between the ratio of the mass and carbon abandance – 0.01. Coefficient of correlation between the ratio of the masses and the carbon abandance of the donor is also equal to 0.01, and between the carbon abandance in the atmosphere of the donor and his mass – 0.1 (excluding V356Sgr). As we can see, there is no relationship between the ratio of the masses and the chemical composition of the carbon, as the theory predicts, and were obtained in 1989 to 6 Cugier systems. Ibanogly et al.2012 for 15 Algol were obtained dependent deficit of carbon abandance in atmocphere of accretors of mass transfer rates in the systems, but this relation is uncertain, as virtually all of Algol their list are located in the phase of slow exchange with mass transfer rate $< \dot{M} = 10^{-9} M_{\odot}$/year.In this evolution phase the period of change mainly quasi-periodically or abruptly in consequence of the chromospheric activity of the donor, so the accuracy of the determination mass transfer rate out of the period of the change could not be better order.

3. Conclusions

1) Systems listed in Table 1 have a significant deficit of carbon. The mean values of the carbon abandance in the atmosphere of the donor (-0.65) and accretor (-0.57) were similar and significantly higher than the deficit of carbon for single giants (-0.24). 2) Lack of atmospheric carbon donor in 9 systems in Table 1 does not depend on its mass, and therefore there is no mechanism for the transfer of dependence – convection or radiant, although theoretical studies predict such a relationship. 3) Comparison of carbon in the atmosphere accretor obtained by different authors, such as system or δ Lib, RS Vul and others, show large differences exceeding the accuracy of its determination in these works. It is related to the accuracy of atmospheric parameters and with the methods of calculation of the chemical composition. For example, to determine the chemical composition of the accretor TX UMa used the following temperatures: Cugier, 1989 (2) – 12900 K, Glazunova et al., 2011 – 12900 K, Tomkin et al., 1992 (4) – 13300 K, Ibanogly et al., 2012 (6) – 13600 K. Hence the carbon abundance to differ for this system because has a strong dependence of the equivalent widths of carbon on temperature. Important to consider blending the lines of the secondary component, depending on the phase of the orbital period, so the equivalent width of the line carbon CI 4267 AA Systems for RZ Vul different authors is very different: 88mA – Ibanogly et al., 2012 (6) and 144mA – Tomkin et al., 1992 (4).

Table 1: Observed binary systems.

name	comp	P(day)	q	M_{accr}	M_{don}	(1)±.2	(2)±.15	(3)±.15	(4)±.15	(5)±.1	(6)±.2
RV Psc	II	0.6	0.6					CH(-1.22)			
X Tri	II	0.99	0.51		1.2			CH(-.41)			
R CMa	I	1.13	0.14	1.8			C(.0) N(.4) O(.3) Fe(.1)		C(.07) N(-.04) O(.01) Fe(.02)		
RZ Cas	I	1.17	0.34	2.0					C(.03) O(-.13) Fe(-.16)		
IM Aur	I	1.30	0.33	2.4							C(-.72)
V1898 Cyg	I	1.50	0.2	6.1							C(-1.26)
V548 Cyg	I	1.8									C(-.25)
RW Mon	II	1.9	0.39		0.99			CH(-1.08)			
HU Tau	I	2.1	0.27	4.5							C(-1.12)
U Her	I	2.1	0.36	7.8			C(-.1)			C(-.58)	
δLib	I	2.3	0.35	4.8			C(-.1)			C(.0)	C(.54)
U Cep	I	2.5	0.58	4.0							C(-1.24)
	II				2.3	C(-.45) N(.5) O(0)					
Z Vul	I	2.5	0.41	5.4							C(-.69)
TZ Eri	II	2.6	0.19		0.37			CH(-1.26)			
DM Per	I	2.7	0.28	7.3							C(-.78)
TW Dra	I	2.8	0.47	1.6					C(.08) O(-.14) Fe(.16)		C(-.34)
	II				0.74			CH(-.61)			
RR Dra	II	2.8						CH(-.18)			
RW Tau	II	2.8						CH(-.81)			
βPer	I	2.9	0.22	3.7			C(-.35)			C(-.46)	
TX UMa	I	3.1	0.3	4.5			C(-.32)		C(-.31) O(.05) Fe(.0)	C(-.59)	C(-.46)
WW Cyg	II	3.3	0.31					CH(-.55)			
U Sge	I	3.4	0.34	5.7			C(-.02)			C(-.42)	C(-.1)
	II				1.9	C(-.5) N(.55) O(.0)					
U CrB	I	3.5	0.29	4.8			C(-.41)			C(-.86)	C(-.80)
λ Tau	I	4.0	0.26	4.8			C(-.40)			C(-.72)	
TW And	II	4.1	0.19		0.3			CH(-.47)			
GU Her	II	4.3						CH(-.34)			
RS Vul	I	4.5	0.31				C(.0)			C(-.40)	C(-.99)
GT Cep	I	4.9	0.34								C(-1.91)
TU Mon	I	5.1	0.21	12.7							C(-1.41)
UX Mon	II	5.9	1.15		3.7			CH(-.68)			
V365 Sgr	II	6.8	0.39		4.7				C(-2.05) N(.8) O(-.33) Fe(-.32)		
RY Gem	I	9.3	0.18	2.8						C(.13)	
S Cnc	I	9.5	0.09	2.5						C(-.53)	
	II				0.23			CH(-.53)			
AU Mon	I	11.1	0.15	5.97						C(-1.88)	

For the determination of carbon in accretor system U Sge used parameters: Teff = 13,200 K, W (4267) = 58 mA – Tomkin et al., 1992 (4), and Teff = 13 900 K, W (4267) = 104 mA – Ibanogly et al., 2012 (6) and so long. Consequently, we must be very careful using the values of chemical elements from research, in which were defined the chemical abundance without taking into account the orbital phase and blending the lines of the secondary component, and without specifying the model parameters by comparing the observed and synthetic spectra over a wide wavelength range.

References

Cugier H.: 1989, *A&A*, **214**, 168.

De Greeve J.P.,Packet W.: 1990, *A&A,* **230**, 97.

Glazunova L.V., Yushchenko A.V., Mkrtichian D.E.: 2009, *Kinematika i Fizika nebesnyh tel,* **26**, 324.

Glazunova L.V., Mkrtichian D.E., Rostopchin S.I.: 2011, *MNRAS,***415**, 2238.

Flower W.A., Caughlan G.R., Zimmerman B.A.: 1975, *Ann.Rev.Astron.Astrophys.,* **13**, 69.

Ibanoglu C., Dervisoglu A., Cakirli O., Sipahi E., Yuce K.: 2012, *MNRAS,* **419**, 1479.

Lehmann H., Tkachenko A., Tsymbal V., Mkrtichian D.E.: 2008, *Commun.Asteroseismology,* **157**, 332.

Pachinsky B.: 1970, *Acta Astron.,* **23**, 47.

Sarna M.J.: 1992, *MNRAS,* **259**, 17.

Sarna M.J., De Greve J.P.: 1996, *Q.J.R. astr.Soc.,* **37**, 11.

Tkachenko A., Lehmann H., Mkrtichian D.E.: 2009, *A&A,* **504**, 991.

Tomkin J.,Lambert D.L.: 1989, *MNRAS,* **241**, 777.

Tomkin J., lambert D.L., Lemke M.: 1992, *MNRAS,* **265**, 581.

Tomkin J., Lambert D.L.: 1994, *PASP,* **106**, 365.

Yoon T.S., Honeycutt K.: 1992, *IAUS,* **151**, 355

ABOUT CHEMICAL COMPOSITION OF SUPERGIANT PMMR145 IN SMALL MAGELLANIC CLOUD. OSMIUM.

V.F. Gopka[1], A.V. Shavrina[2], S.V. Vasilyeva[1], S.M. Andrievsky[1]

[1] Astronomical observatory, Odessa National University
T.G.Shevchenko Park, Odessa, 65014, Ukraine, *gopka.vera@mail.ru*
[2] Main Astronomical Observatory of NAS of Ukraine,
Zabolotnogo str. 27, Kyiv, 03680, Ukraine

ABSTRACT. The abundance analysis of six K-supergiants of the Small Magellanic Cloud (Hill 1997) showed that the heavier elements (La, Ce, Nd, Eu) have the excess relative to iron [El/Fe]=+0.4 dex, on average, for the sample of five stars (PMMR23, PMMR27, PMMR48, PMMR102, PMMR145). We made the identification of spectral lines in the spectrum of PMMR145 based on the comparison of synthetic and observed spectra. The absorption lines of elements heavier than lanthanides including osmium were identified and abundance of osmium was found ([Os/Fe]=0.59 dex).

Key words: Small Magellanic Cloud, star, evolution, supergiants, PMMR145.

1. Introduction

Magellanic Clouds (MC) are the nearest galaxies to us. These are two irregular galaxies, namely the Large Magellanic Cloud (LMC) and Small Magellanic Cloud (SMC), which have smaller sizes and masses comparing to our Galaxy. The study of the objects outside our Galaxy give the possibility to verify the evolutionary theories, such as theories of chemical, stelar and galaxy evolution. That is why the MC objects are of great interest, and the corresponding researches are carried out in the wide range of wavelengths.

The observation of three galaxies (the Galaxy, SMC, and LMC) in X-rays by artificial satellites showed that the smallest galaxy SMC is a strong and stable source in this wavelength range. It proved to be a galaxy riched in such X-ray sources as HMXBs – high mass X-ray binary stars composed of either white dwarfs or neutron stars, or black holes and optical companion (Klus H. et al., 2012). Because the mass of SMC is 50 times lower than that of our Galaxy, and the SMC has almost the same number of HMXBs (Novara et al., 2012), we have the irrefutable proof that at some period of evolution the binary systems are characterized by the special conditions, resulting in unstable configurations for these stars which led to the explosive processes in this galaxy. Such conditions, according to several studies, could be the tidal forces caused by the closeness of the galaxies, and the smallest galaxy experienced the greatest damage, which is being observed. A large number of HMXBs indicates that in the result of explosion of Supernovas the SMC environment should be enriched first of all in r-process elements. Obviously, the neutron processing histories of stars in SMC have been different from our Galaxy. If our ideas are true, then the spectra of stars must exhibit the lines of heavy elements, which have been formed with major contribution of r-processes. Indeed, Hill's study of some SMC K-supergiants, based on spectra obtained at ESO 3.6-meter telescope, showed the excess of elements r- and s-prpcesses as La, Ce, Nd, and Eu (Hill, 1997).

2. About the chemical composition of SMC's K-supergiant PMMR145. R-process elements.

Let's consider shortly the results of investigation of chemical composition of the supergiant star PMMR145. As well as the other SMC supergiants, observed by Hill (1997), PMMR145 is a faint star and it has the photometric characteristics V=13.09, B-V=1.59. For our work we used the same spectra obtained and kindly given to us by Hill. The spectral resolution of used observation is R=30,000, the wavelength range is 5049-6357 A. The synthetic spectra were calculated with the code SYNTHV of V. Tsymbal (1996) and Kurucz' model atmospheres (1993). The atmosphere parameters found in previous papers have been tested and confirmed in this work, namely: the effective temperature T_{eff}=4300 K, the surface gravity logg=0.3, the microturbulent velocity V_{micro}=3km/s. Hill (1997) received the value [Fe/H] = -0.59. The average value of overabundances of the elements heavier than barium, is equal to [El/Fe]=0.4 dex, [Eu/Fe]= -0.39 dex (Hill, 1997).

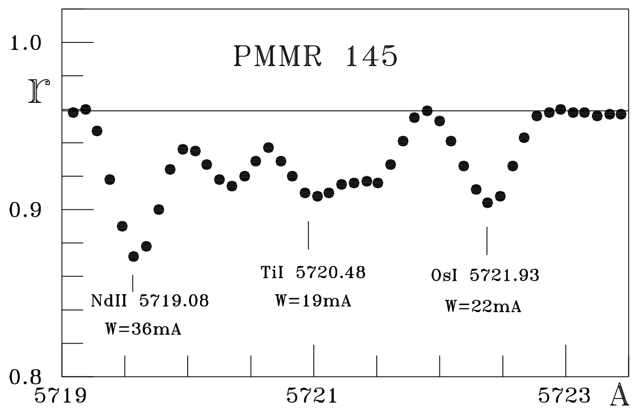

Figure 1: The spectrum of PMMR145 in the region of line OsI 5721.931 A

Based on comparing the observed spectra of SMC stars, obtained by Hill (1997), and the synthetic spectra of these stars, we have identified the lines of thorium in the visible part of the spectrum. According to work of Gopka et al. (2005, 2007) the mean values of thorium abundances in the atmospheres of PMMR23, PMMR39, PMRR144 and PMMR145 are equal to $\approx -0.10 \pm 0.13, -0.63 \pm 0.13, -0.69 \pm 0.09$, and +0.05 dex (in the scale logN(H)=12), using 6, 2, 4, and 1 thorium lines respectively. Thorium is an element which is formed exclusively by the r-process. Thorium lines in PMMR23 and PMMR144 spectra are clearly identified. The coincidence of the wavelengths and self-agreed result over different lines is the undeniable proof of the presence of r-process elements in the atmospheres of these stars. According to Wanajo et al. (2006), the discovery of thorium is a strong support of the contribution of r-process elements (which cannot be synthesized by s-process). Certainly, some difficulties exist in the abundance analysis of thorium, for example, due to blending by lines of other elements and we can not exclude the presence of lines of alternative elements near the third peak of r-process. The lines of Os, Ir, and Pt cannot be produced by s-process (Wanajo et al., 2006). We identified the osmium line at wave length 5721.931 A, equivalent width is equal E.Q=22mA, lg gf=-2.66 in the spectrum of PMMR145 (Fig. 1). The solar abundance log N(Os)=1.40 in the scale of log N(H)=12 (Asplund, 2009). The abundance of osmium in PMMR145 obtained from synthetic spectra near Os I line 5721.931 line is equal log N(Os)=1.40 also (Fig. 2), therefore, [Os/Fe]=0.59 dex. That value almost the same as [Th/Fe]=0.54 dex.

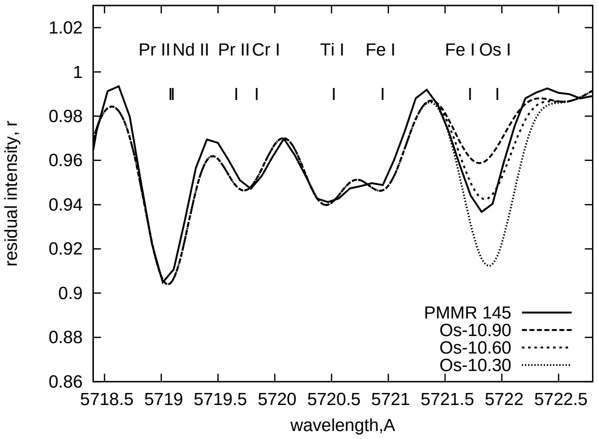

Figure 2: The spectrum of PMMR145 fitting by syntetic spectra for the line OsI

3. Conclusion

Although the place of r-process is not precisely determined, the most likely one is the outburst of type II Supernova. In this paper, such a scenario for the SMC galaxy, having a high number of detected HXMBs- massive binary stars with relativistic objects, which have enriched the environment in the heaviest elements in the past, is clearly evident. SMC supergiant PMMR145, as well as the other objects under study, showed the presence of lines of heavier elements in the spectra, namely of the elements with a predominant contribution of r-process and pure r-process.

References

Hill V.: 1997, *A&A,* **324**, 435.

Klus H., Bartlett E.S., Bird A.J. et al.: 2012, *MNRAS,* **324**, 435.

Novara G., La Palombara N., Megeghetti S. et al.: 2012, *A&A,* **532**, 8.

Gopka V.F., Yushchenko A.V., Andrievsky S.M. et al.: 2005, *IAUS,* **228**, 535.

Gopka V.F., Vasilieva S.V., Yushchenko A.V. et al.: 2007, *OAP,* **20**, 58.

Tsymbal V.: 1996, *Model Atmospheres and Spectrum Synthesis, ASP Conf.Ser.*, ed. Saul J.Adelman, Friedrich Kupka, Warner W. Weiss, **108**, 198.

Kurucz R.: 1993, *CD-ROMs 1-23.*

Wanajo S., Nomoto K., Iwamoto N. et al.: 2006, *ApJ,* **636**, 842.

Asplund M., Greveese M., Sauval A.J. et al.: 2009, *ARAA,* **47**, 481.

TIME DELAY BETWEEN IMAGES OF THE LENSED QUASAR UM673

E. Koptelova [1,2,3],W. P. Chen [2], T. Chiueh [1], B. P. Artamonov [3], V. L. Oknyanskij [3], S. N. Nuritdinov [4], O. Burkhonov [4], T. Akhunov [4,6], V.V.Bruevich [3], O.V. Ezhkova [3], A.S.Gusev [3], A.V.Sergeyev [5], Sh. A. Ehgamberdiev [4], M. A. Ibragimov [4]

[1] Department of Physics, National Taiwan University, Taipei, Taiwan
[ekaterina;chiuehth]@phys.ntu.edu.tw
[2] Graduate Institute of Astronomy, National Central University, Jhongli City, Taiwan
wchen@astro.ncu.edu.tw
[3] Sternberg Astronomical Institute (SAI), Moscow M.V. Lomonosov State University, Moscow, Russia [artamon;oknyan]@sai.msu.ru
[4] Ulugh Beg Astronomical Institute of the Uzbek Academy of Sciences, Tashkent, Uzbekistan

ABSTRACT. We study brightness variations in the double lensed quasar UM673 (Q0142-100) with the aim of measuring the time delay between its two images. Methods.. We analyzed the *V*, *R* and *I*-band light curves of the A and B images of UM673, which cover ten observational seasons from August 2001 to November 2010. We also analyzed the time evolution of the difference in magnitudes (flux ratio) between images A and B of UM673 over more than ten years. We find that the quasar exhibits both short-term (with an amplitude of ~ 0.1 mag in the *R* band) and long-term (with an amplitude of ~ 0.3 mag) variability on timescales of about several months and several years, respectively. These brightness variations are used to constrain the time delay between the images of UM673. From a cross-correlation analysis of the A and B quasar light curves and an error analysis we measure a mean time delay of 89 days with an rms error of 11 days.

Multiple images of lensed quasars show changes in their brightness over time. There are two main reasons for these brightness variations. One is that the quasar itself, as a variable source, changes in brightness with time. Brightness variations of the quasar are observed in the light curves of all quasar images, but they are not synchronized. Changes in brightness in one image follow or lead the brightness changes in others with certain time lags (time delays). The time delay between these brightness variations in any two images of the quasar is a combination of delays that arise from geometrical differences between the light paths (and thus light travel times) for each quasar image and the difference in the gravitational potential between quasar images. The geometrical term is related to the *Hubble* constant through the angular diameter distances (see Schneider et al. 1992). This relation gives us a method for estimating the *Hubble* constant independently of the distance ladder (Refsdal 1964). All references can see in Paper I and Paper II.

In this study we analyze brightness variations in images of the lensed system UM673 (Q0142-100) discovered by MacAlpine & Feldman (1982). The system consists of a distant quasar at redshift zq = 2.719 (Surdej et al. 1987, 1988) gravitationally lensed by an elliptical galaxy at redshift zl = 0.49 (Surdej et al. 1988; Smette et al. 1992; Eigenbrod et al. 2007) into A and B images with an image separation of 2.”2. We used monitoring observations of UM673 obtained during different observational seasons at two sites. The majority of the observational data were collected during the quasar monitoring program carried out by the Maidanak GLQ collaboration (see Dudinov et al. 2000). The data were obtained with the 1.5-m AZT-22 telescope of the Maidanak Observatory (Central Asia, Uzbekistan) during the 1998–2010 observational seasons in the Bessel *V*, *R* and *I* bands. A considerable part of these observations, the 2003–2005 data, have been presented in Koptelova et al.

(2008) and Paper I. The *V*, *R* and *I*-band observations of the lensed system were also made between July 28, 2008 and January 18, 2010 using the 1.3-m SMARTS telescope at CTIO, Chile. These observations were part of the ToO observations carried out by National Central University, Taiwan. UM673 was usually observed from August until December, or sometimes January, when it was well visible at both sites. The resulting Maidanak and CTIO *R*-band light curves of the A and B quasar images are shown in Fig. 1. More details of photometric processing and results in V, I –band light can see in Koptelova at al. (2012), Paper II.

The time delay was measured with the modified cross-correlation function (MCCF) method (see Oknyanskij 1993). The method, its application and the test performance for the analysis of time series containing large annual gaps have been described in Paper I. Here, we briefly outline the approach. In the MCCF method, each data point from the *B* light curve, *B*(*t*i), forms a pair with an interpolated point from the *A* light curve, *A*(*t*i + τ) at time *t*i + τ,where τ is the time lag. The pairs of data points for which τ− Δ*t* ≤ Δ*t*ij <τ+Δ*t* (where Δ*t*ij =| *t*j − *t*i |is the time shift between the *t*i point of the *A* light curve and the *t*j point of the *B* light curve) are then used to calculate the cross-correlation function. The interpolation interval Δ*t* is usually chosen as a compromise between the desire to decrease the interpolation errors and to find a sufficient number of data pairs to reliably calculate the correlation coefficient for a given time lag. For the analysis of the light curves presented in Paper I the value of Δ*t* was adopted to be 90 days. This was the lowest value of Δ*t* that one could choose because of the large annual gaps in the light curves of UM673. For this value of Δ*t* the MCCF method is insensitive to brightness variations shorter than 90 days. Therefore the short-term variations of the quasar that are comparable to, or sometimes shorter than, the interpolation interval of 90 days, are ignored by the method. In addition, interpolation errors produced for high values of Δ*t* can lead to an erroneous time delay estimate.

We used two interpolation intervals, Δ*t*max and Δ*t*min to account for the short-term variations in brightness and minimize the interpolation errors. The interpolation interval Δ*t*max = 90 days is the same interval as was adopted for calculations of the CCF in Paper I. The interpolation interval Δ*t*min was introduced to take into account the short-term brightness variations of UM673. It was used to calculate the cross-correlation function for those data pairs, for which both data points in the pair (the real point from the *B* light curve and the interpolated one from the *A* light curve) are within the same observational season. When the data points do not lie within the same season of observations, Δ*t*max was used instead of Δ*t*min. This approach was applied to calculate the cross-correlation function between the time-shifted interpolated A light curve and the discrete *B* light curve. The time lag τranges from −500 to 500 days with a step of 1 day. A value of 10 days chosen for Δ*t*min is comparable to average sampling of the light curves within one observational season. The origin of the high-amplitude rapid brightness variation observed in image B in January 2010 is unclear. It can be either intrinsic to the quasar, with the counterpart in image A that was missed, or unique for image B. To avoid the influence of the data points corresponding to this event on the correlation between the A and B light curves, these data were excluded from the time delay analysis. The resulting CCFs for the *R*, *V* and *I*-band data are shown in Figs. 4 and 5.(see Paper II). When observational data are regularly sampled and there is a good overlap between time-shifted light curves, interpolation can be avoided as in the method proposed by Pelt et al. (1994). In this method, the time delay is estimated by minimizing the dispersion spectrum of the combined A and time-delay-shifted *B* light curves. In the method, only pairs of data points within some interval, called the decorrelation length, contribute to the calculation of the dispersion spectrum. The dispersion spectra calculated for two values of the decorrelation length, 60 and 90 days, are shown in Fig. 6 by gray and black lines, respectively. We found only a tentative minimum in the global behavior of the dispersion spectra corresponding to a range of delays from 70 to 110 days. The shape of the minimum is not well constrained at longer delays, between 120 and 250 days. This region corresponds to the delays for which the A and B light curves do not overlap. Therefore, the method cannot be used to measure delays from this range. The minimum between 70 and 110 days consists of several secondary minima corresponding to different delays. We averaged the dispersion function in this range of time delays to estimate the location of its global minimum. The delay corresponding to the global minimum is 86 days in both cases, for values of the decorrelation timescale of 60 and 90 days. This estimate of the delay agrees with the time delay measured using the MCCF method. We found that in comparison with the dispersion function method, the MCCF method gives a more definite measurement of the delay. Uncertainties in time delay measurement due to photometric errors and systematic sampling effects were investigated with the Monte Carlo simulations. We performed simulations of 1000 artificial light curves using Timmer & Koenig's algorithm (1995) (these simulations are discussed in detail in Paper I). The distribution of the time delays recovered from cross-correlation analysis of the Monte Carlo simulated *R*-band light curves of images A and B, shifted by the input time delay of 88 days, is shown in Fig. 8 of Paper II For this distribution we found a mean time delay of 89 (marked by a dotted line in Fig. 8) and an rms error of 11 days. On the other hand, the most probable value of the delay that can be measured from light curves with similar statistical properties and variability pattern as the observed *R*-band light is curves is 95 (+5/+14 and -16/-29) days (68% and 95% confidence intervals).

The measured time delay can be used to estimate the *Hubble* parameter and constrain the mass model of the lensing galaxy. There have been several lens models that predict different time delays between the UM673 images. The predicted time delay for the lens with elliptical symmetry and *H*0 = 75 km s^{-1} Mpc^{-1} is about 7 weeks (Surdej et al. 1988). Leh´ar et al. (2000) fitted a set of four standard lens models (SIE, constant M/L models, and those with external shear). The SIE and constant M/L models predict time delays of *h*Δ*t* = 80 and *h*Δ*t* = 121 days, respectively. The SIE and constant M/L models with external shear predict time delays of $h\Delta t$ = 84 ÷ 87 and $h\Delta t$ = 115 days, respectively. Given that Δt = 89 days, the SIE and M/L models yield estimates of the *Hubble* constant H^{meas} of 90 and 136 km s^{-1} Mpc^{-1}, respectively. The SIE and M/L models with shear yield values of H^{meas} of 94 and 129 kms^{-1} Mpc^{-1}, respectively. These estimates of the *Hubble* constant are higher than the *Hubble* key project result of 72 ± 8kms^{-1} Mpc^{-1} (Freedman et al. 2001) or improved result of 74.2 ± 3.6km s^{-1} Mpc^{-1} (Riess et al. 2009). This might be due to an additional convergence to the lensing potential from nearby objects or objects on the line of sight to the quasar (see, e.g., Keeton et al. 2000). Leh´ar et al. (2000) estimated the total shear γT and convergence *k*T produced by nearby galaxies in the FOV of ten double lensed quasars observed with the *Hubble* Space Telescope (HST), including UM673. The total convergence from five galaxies within 20″ of UM673 was estimated to be 0.138 (see Table 4 of Leh´ar et al. 2000). In the calculations Leh´ar et al. assumed that each galaxy has an SIS mass distribution, and their M/L ratios and redshifts are the same as for the lensing galaxy. Because of the assumptions made, the derived value of *k(*T) can only be considered as approximate. For the SIS model, the *Hubble* parameter corrected for the field convergence of 0.138 as *H*0 = (1-k(T)), is 78±10 km s^{-1} Mpc^{-1}. This value roughly agrees within the errors with the *Hubble* key project value. The esult cran be improved even more when detail measurements of *k*T in the field of UM673 are available. An additional contribution to the total convergence produced by the objects on the line of sight to the quasar should also be investigated. Recently, Cooke et al. (2010) reported the discovery of a previously unrecognized DLA system at z = 1.63 in the spectrum of image A of UM673. They also found a weak Lyα emission line in the spectrum of image B at the same redshift as the DLA that indicates a star formation rate of 0.2 solar mass per year. The discovery provides evidence for an additional mass, a galaxy that gives rise to the DLA system toward the UM673 quasar. The accuracy of the *Hubble* constant from the time delay in UM673 can be improved in the future by analyzing the external convergence produced by the objects in the FOV of UM673 and reducing the error in the time delay measurement. The latter requires coordinated observations of UM673 at different sites over the time interval that can provide better overlap between time-delay-corrected light curves of the quasar images than the Maidanak-CTIO data do. UM673 might exhibit rapid brightness variations of more than 0.1 mag on timescales from one to several months. Observations of these rapid brightness variations during coordinated monitoring of the system can help to reduce the uncertainty in the time delay down to several per cent.

References

Dudinov V., Bliokh P., Paczynski B. et al.: 2000, *Kinematika i fizika nebesnyh tel*, **3**, 170.

Koptelova, E., Shimanovskaya E., Artamonov B.: 2005, *MNRAS*, **356**, 323.

Koptelova E. et al.: 2012, *A&A*, **544**, A51 (Paper II).

Koptelova E.A., Oknyanskij V.L., Shimanovskaya E.V.: 2006, *A&A*, **452**, 37.

Koptelova E.A., Artamonov B.P., Shimanovskaya E.V. et al.: 2007, *Astron. Rep.*, **51**, 797.

Koptelova E., Artamonov B.P., Bruevich V.V., Burkhonov O.A., Sergeev A.V.: 2008, *Astron. Rep.*, **52**, 270.

Koptelova E., Oknyanskij V.L., Artamonov B.P., Burkhonov O.: 2010, *MNRAS*, **401**, 2805 (Paper I).

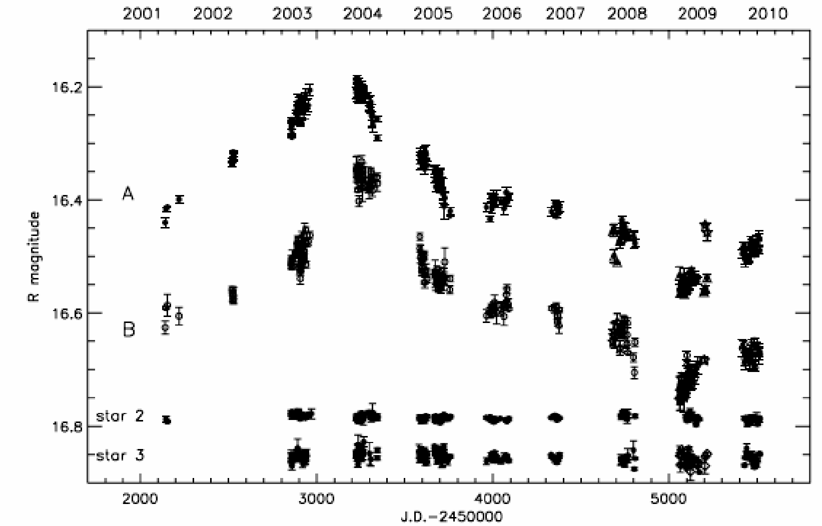

Figure 1: *R*-band light curves of the A and B images of UM673 from August 2001 to November 2010. For better representation, the light curve of image B is shifted by −1.87 mag. The light curves of reference stars 2 and 3 are shown at the bottom.

THE MAGNETIC FIELD IMPACT ON ACCRETION RATE IN A PROTOPLANETARY DISK

M.M. Kuksa

National Research Nuclear University “MEPHI”
Obninsk Institute of Nuclear Power Engineering
Obninsk, Russia, max@kuksa.ru

ABSTRACT. Recent observations are the evidence of a large-scale magnetic field in discs around classical T Tauri stars. A model of the axisymmetric thin protoplanetary disk in a global magnetic field is considered. A compressible magnetohydrodynamic set of equations is solved by using the explicit numerical method. The influence of a magnetic field and various turbulent kinematic and magnetic viscosity coefficients on the accretion rate in the disk is investigated.

Key words: magnetohydrodynamics; protoplanetary disk: accretion rate

1. Introduction

The origin of an angular momentum transport remains one of the central problems in the accretion disk theory, as molecular viscosity cannot provide the necessary accretion rate.

N.I.Shakura and R.A.Sunyaev (1973), D.Lynden-Bell and J.Pringle (1974) had noted that turbulence would cause enhanced viscosity. Several angular momentum transport mechanisms were offered such as convection, nonlinear hydrodynamic instability, gravitational instability and perturbations caused by external influences. However neither of them can transfer angular momentum for required time.

Progress has been made with the discovery of magnetorotational instability (MRI). MRI, originally studied by E.P.Velikhov (1959) and S.Chandrasekhar (1961), was applied to astrophysical disks by S.Balbus and J.Hawley (1991, 1992). MRI arises in a differentially rotating disk in the presence of a weak magnetic field. Numerical simulations (Hawley, Gammie, Balbus, 1995, 1996) have shown that MRI led to turbulence, transported the angular momentum outward and acted as a hydromagnetic dynamo, i.e. sustained magnetic field in the presence of dissipation.

It has been shown that in the so-called dead zone between active layers in protoplanetary disks, MRI cannot operate (Gammie, 1996). However the account of non-ideal effects such as Hall effect and ambipolar diffusion resulted in changing the stability and the saturation of MRI in weakly-ionized protoplanetary disks (Balbus, Terquem, 2001; Wardle, 1999, 2007).

In recent years direct measurements have shown a clear evidence of the magnetic field in protostellar disks. The existence of a significant azimuthal magnetic field of about 1 kG has been confirmed by observations around FU Orionis in the innermost regions of its accretion disk (Donati et al., 2005). Furthermore observations and analysis of a magnetic field on the surface of classical T Tauri stars suggest a strong octopolar field (~1.2 kG) and a smaller dipolar field (~0.35 kG) (Donati et al., 2007).

It should be noted that MRI is stable in a strong magnetic field and generation of a large-scale magnetic field by MRI is not observed (Brandenburg, Nordlund, Stein, 1995; Hawley, 2001).

Recently F.Ebrahimi and S.Prager (2011) have explored the possibility of an angular momentum transport in disks by tearing instabilities of plasma, which can exist in strongly magnetized regions, for instance, coronas. The effectiveness of it is equivalent to $\alpha \sim 0.01$ by the authors’ estimation.

Thus magnetic fields play an important role in accretion all across the disk. So it is reasonably to examine the influence of a magnetic field on the accretion rate in a global scale. This paper studies the 2D evolution model of a protoplanetary disk in a large-scale magnetic field.

2. Model

The thin gaseous disk evolution is described by the following set of equations

$$\begin{cases} \dfrac{\partial \Sigma}{\partial t} = -\boldsymbol{u}\cdot\nabla\Sigma - \Sigma\nabla\cdot\boldsymbol{u} \\ \dfrac{\partial \boldsymbol{u}}{\partial t} = -(\boldsymbol{u}\cdot\nabla)\cdot\boldsymbol{u} - c_s^2\nabla\ln\Sigma - \dfrac{GM_\odot}{r^2} + \\ \quad + \nu\left(\nabla^2\boldsymbol{u} + \dfrac{1}{3}\nabla\nabla\cdot\boldsymbol{u} + 2S\cdot\dfrac{\nabla\Sigma}{\Sigma}\right) + \dfrac{(\nabla\times\boldsymbol{B})\times\boldsymbol{B}}{4\pi\Sigma} \\ c_s^2 = c_{s0}^2\exp\left[(\gamma-1)\ln\dfrac{\Sigma}{\Sigma_0}\right] \\ \dfrac{\partial \boldsymbol{A}}{\partial t} = \boldsymbol{u}\times\boldsymbol{B} + \eta\Delta\boldsymbol{A} \\ \nabla\cdot\boldsymbol{B} = 0 \end{cases},$$

where t is the time, r is the radial distance, Σ and Σ_0 are the surface density and its initial value, respectively, $\boldsymbol{u}$ is the velocity vector, c_s and c_{s0} are the sound speed and its initial value, respectively, $\boldsymbol{A}$ is the vector potential, $\boldsymbol{B}$ is the magnetic induction vector, G is the gravitation constant, $M_\odot$ is the protosun mass, which equals to the modern solar mass, ν is the turbulent kinematic viscosity, η is the turbulent magnetic viscosity, $\gamma = 5/3$ is the adiabatic index and traceless strain rate tensor

$$S = \frac{1}{2}\left(\nabla \boldsymbol{u} + (\nabla \boldsymbol{u})^T\right) - \frac{1}{3}\nabla \cdot \boldsymbol{u} .$$

The pressure gradient acceleration in the equation of motion is expressed in terms of squared sound speed and logarithmic surface density gradient

$$\frac{\nabla p}{\Sigma} = \frac{\nabla(\Sigma c_s^2)}{\Sigma\gamma} = c_s^2 \nabla \ln \Sigma .$$

The turbulent kinematic viscosity is defined according to the standard prescription (Shakura, Sunyaev, 1973)

$$\nu = \alpha \frac{c_s^2}{\Omega} ,$$

where Ω is the angular velocity, α is the dimensionless parameter.

The turbulent magnetic viscosity according to (Campbell, 1997) may be specified similarly to the former one with the parameter β

$$\eta = \beta \frac{c_s^2}{\Omega} .$$

The resulting magnetic field is

$$\boldsymbol{B} = \boldsymbol{B}_d + \boldsymbol{B}_{ext},$$

where $\boldsymbol{B}_d = \nabla \times \boldsymbol{A}$ is the proper disk magnetic field, $\boldsymbol{B}_{ext} = (0,0,B_{ext,z})$ is the external magnetic field with a vertical component only.

The disk model is considered in polar coordinates (r, φ). The origin of coordinates is the center of the star and the coordinate plane coincides with the equatorial plane of a disk. The disk is suggested to be axisymmetric. The modeling region extends from 0.5 to 1.5 AU.

3. Numerical method

Numerical simulations are performed with the help of Pencil Code (Brandenburg, 2003). The modeling area is covered by a grid with $n = 1200$ points and constant spacing Δr. Spatial derivatives are approximated by the sixth order finite differences

$$f_i' = \frac{-f_{i-3} + 9f_{i-2} - 45f_{i-1} + 45f_{i+1} - 9f_{i+2} + f_{i+3}}{60\Delta r} ,$$

$$f_i'' = \frac{2(f_{i+3} + f_{i-3}) - 27(f_{i+2} + f_{i-2}) + 270(f_{i+1} + f_{i-1}) - 490 f_i}{180(\Delta r)^2} ,$$

where $i = 1,...,n$. Also the continuity equation is complemented by an upwinding term.

A time derivative is calculated by the third order explicit Runge-Kutta method. The time step Δt is derived from the Courant–Friedrichs–Lewy condition.

At the initial time moment the surface density is $\Sigma_0 = 2000$ g/cm^2, the sound speed $c_{s0} = 1.5 \cdot 10^5$ cm/s, the azimuthal velocity has Keplerian profile $u_{\varphi 0} = \sqrt{GM/r}$, the radial velocity and the vector potential in the disk are zero.

At the left edge (nearer to the star) and at the right edge (farther from the star) the grid is appended by three boundary points. Thus the general number of points is $N = n + 6$. At the each time step the boundary conditions are applied as in Table 1.

Table 1: Boundary conditions

Physical quantity	Boundary values	
	at the left in r_{-2}, r_{-1}, r_0	at the right in $r_{n+1}, r_{n+2}, r_{n+3}$
Surface density	Copy of $\Sigma(r_1)$	2000 g/cm^2
Radial velocity	Copy of $u_r(r_1)$	Copy of $u_r(r_n)$
Azimuthal velocity	Asymmetric extrapolation*	Keplerian $\sqrt{GM/r_i}$
Vector potential	Asymmetric extrapolation*	Asymmetric extrapolation**
* $V(r_{1-i}) = 2V(r_1) - V(r_{1+i})$ ** $V(r_{n+i}) = 2V(r_n) - V(r_{n-i})$, $i = 1, 2, 3$, V – extrapolated quantity		

4. Results

A series of numerical tests was performed with the model for various model parameters such as external magnetic field, turbulent kinematic and magnetic viscosity coefficients. Time-average values of surface density, radial velocity, proper disk magnetic field (vertical component) and the accretion rate <M′> are obtained at the distance of 0.5 AU from the star and presented in Table 2.

The characteristic property of model evolution is a mass transfer to the star side, i.e. accretion. There are neither artificial inflow nor outflow of mass in simulations, but there are only preconditions for it. The calculated accretion rate of about 10^{-7} $M_\odot$/year is the result of “free” (as far as boundary conditions allow) model evolution and agrees with observations of classical T Tauri stars.

Independently of mass source density (fixed density at the outer boundary) the turbulent kinematic viscosity provides only finite radial velocity of transfer. In addition the more viscosity the more is radial velocity magnitude (see models #1, #2 in Table 2).

In the presence of an external magnetic field and equal turbulent kinematic and magnetic viscosities the disk obtains a proper magnetic field. The initial unstable state excites oscillations of the proper magnetic field and

Table 2: Model parameters and evolution results

#	Parameters			Calculated values at 0.5 AU				Model behavior
	$B_{ext,z}$, G	α	β	<Σ>, g/cm^2	<u_r>, cm/s	<$B_{d,z}$>, G	<M′>, 10^{-7} $M_\odot$/ year	
1	–	0,01	–	1538	−394	0	4,4	Steady state
2	–	0,001	–	1453	−44	0	0,3	Steady state
3	1	0,01	0,01	1539	−394	−1	4,5	Decaying oscillations, steady state
4	1	0,001	0,01	1455	−43	−1	0,3	Decaying oscillations, steady state
5	−1	0,01	0,01	1539	−395	1	4,5	Decaying oscillations, steady state
6	0,001	0,01	0,001	–	–	–	–	Increasing oscillations, scheme instability
7	−1	0,01	0,001	–	–	–	–	Increasing oscillations, scheme instability
8	−1	0,01	0,05	1359↘	−360↗	−41↘	3,7↘	Increase of $\vert B_{d,z} \vert$, scheme instability
9	0,001	0,01	0,1	1070	−359	58	2,8	Increase of $\vert B_{d,z} \vert$, steady state

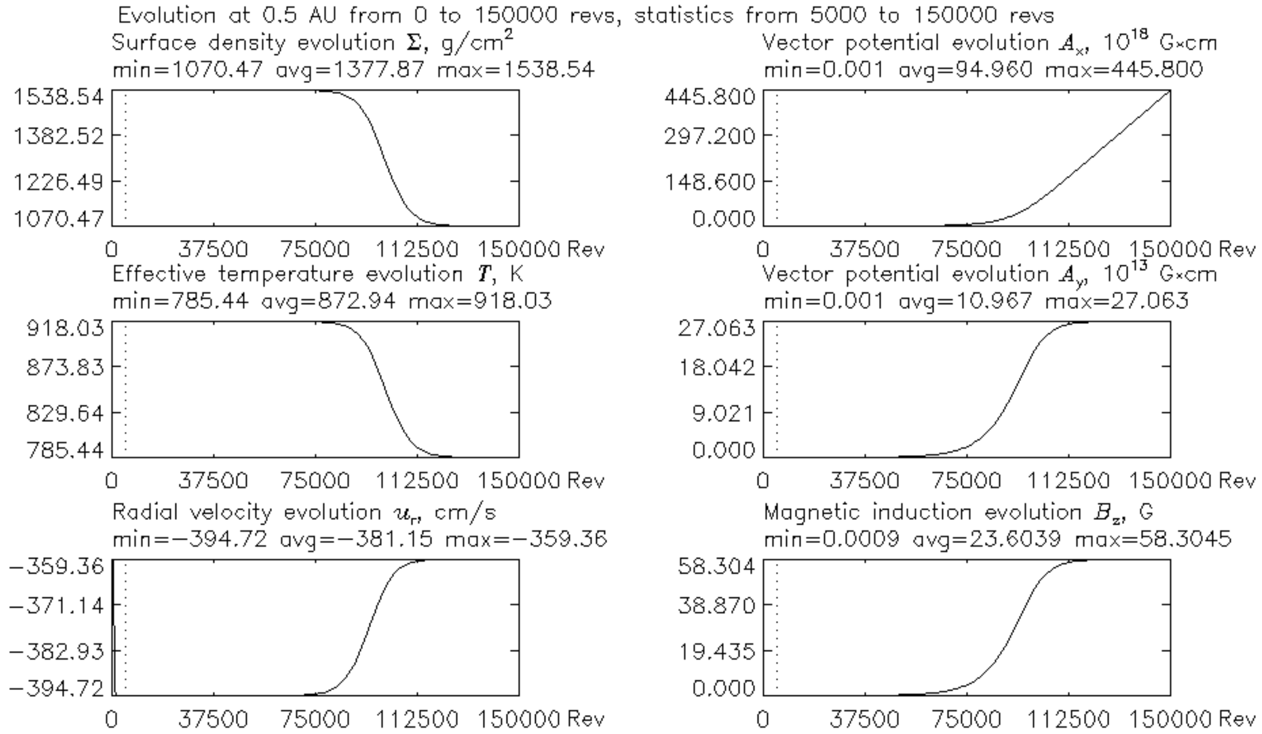

Figure 1: Evolution of the model #9. Revolutions about the star are marked at the abscissa.

velocities in the disk. However in the long run the model comes to steady state, when the proper magnetic field is equal in magnitude and opposite in sign to the external field. The proper disk magnetic field of the strength of 1 G doesn't influence the accretion rate (see #3, #5). The proper magnetic field is decaying when the external field is "turned off".

In the presence of an external magnetic field and different turbulent kinematic and magnetic viscosities there are several scenarios:

1) $\beta = 10\alpha$ and $\beta \le 0{,}01$ – decaying oscillations lead to the steady state, in which the magnetic field doesn't affect the accretion rate (see #4).

2) $\beta = 0{,}1\alpha$ and $\beta \le 0{,}001$ – increasing oscillations of a proper magnetic field and velocities in the disk lead to numerical instability, and independently of the magnetic field magnitude and orientation in a vertical direction (see #6, #7).

3) $\beta = 5\alpha$, $\alpha = 0{,}01$ and $|B_{\mathrm{ext},z}| = 1$ – increasing magnitude of the proper magnetic field is accompanied by the accretion rate reduction, then numerical instability occurs (see #8). So the model with the lower external field has been examined.

4) $\beta = 10\alpha$, $\alpha = 0{,}01$ and $|B_{\mathrm{ext},z}| = 0{,}001$ – increasing of the proper magnetic field as before is accompanied by the accretion rate reduction, but leads to the steady state (see #9 and Figure 1).

Thus in our simulations the growth of the proper magnetic field magnitude in a disk reduces the radial velocity in the absolute value and hence brings down the accretion rate (see #8, #9).

If new observational data evidence the existence of strong magnetic fields in protoplanetary disks it is reasonable to take the account of magnetohydrodynamic instabilities capable to operate under such conditions, for instance, tearing instabilities.

References

Balbus S.A., Hawley J. F.: 1991, *ApJ.*, **376**, 214.
Balbus S.A., Hawley J. F.: 1991, *ApJ.*, **376**, 223.
Balbus S.A., Hawley J. F.: 1992, *ApJ.*, **400**, 595.
Balbus S.A., Hawley J. F.: 1992, *ApJ.*, **400**, 610.
Balbus S.A., Terquem C.: 2001, *ApJ.*, **552**, 235.
Brandenburg A.: 2003, *The Fluid Mechanics of Astrophysics and Geophysics*, **9**, 269.
Brandenburg A., Nordlund A., Stein R. F., Torkelsson U.: 1995, *ApJ.*, **446**, 741.
Campbell C.G.: 1997, *Magnetohydrodynamics in binary stars*, 306 p.
Chandrasekhar S.: 1961, *Hydrodynamic and hydromagnetic stability*, 654 p.
Donati J.-F., Paletou F., Bouvier J. et al.: 2005, *Nature*, **438**, 466.
Donati J.-F., Jardine M.M., Gregory S.G. et al.: 2007, *Mon. Not. R. Astron.* Soc., **380**, 1297.
Ebrahimi F., Prager S.C.: 2011, *ApJ.*, **743**, 192.
Gammie C.F.: 1996, *ApJ.*, **457**, 355.
Hawley J.F., Gammie C.F., Balbus S.A.: 1995, *ApJ.*, **440**, 742.
Hawley J.F., Gammie C.F., Balbus S.A.: 1996, *ApJ.*, **464**, 690.
Hawley J.F.: 2001, *ApJ.*, **554**, 534.
Lynden-Bell D., Pringle J.E.: 1974, *Mon. Not. R. Astron. Soc.*, **168**, 603.
Shakura N.I., Sunyaev R.A.: 1973, *A&A.*, **24**, 337.
Velikhov E.P.: 1959, *Sov. Phys. JETP.*, **9**, 995.
Wardle M.: 1999, *Mon. Not. R. Astron. Soc.*, **307**, 849.
Wardle M.: 2007, *Astrophys. and Space Science*, **311**, 35.

THE MECHANISM OF ANGULAR MOMENTUM TRANSFER IN ACCRETION STELLAR DISKS BY LARGE VORTICAL STRUCTURES

A.Lugovskiy [1], V.Chechetkin [2], K.Sychugov [3]
Keldysh Institute of Applied Mathematics
Moscow, Russia
[1] alex_lugovsky@mail.ru, [2] chechetv@gmail.com, [3] c.kostik@gmail.com

ABSTRACT. Large-scale vortical flows arising in shear flows of stellar accretion disks with Keplerian azimuthal velocity distributions is investigated. The two reasons of the development of large-scale instability is shown: hydrodynamical instability and magnetorotational instability (MRI). The presence of large-scale structures leads to angular-momentum redistribution in the disk.

Key words: accretion disk, instability, magnetic field, angular momentum transfer, large-scale vortical flows

Introduction

The mechanism of removing of angular momentum from matter in an accretion disk is the most important factor determining the rate of disk accretion onto a compact object. Reasons of the removal of angular momentum in an accretion disk have long been of interest to researchers all over the world. There are a lot of mechanisms of angular momentum transfer (Shakura 1972, Shakura et al. 1973, Sawada et al. 1986, Fridman et al. 2003, Gribov et al. 1972, Bisnovatyi-Kogan et al. 1976, Balbus et al. 1991, Winters et al. 2003, Goodman 1993, Li et al. 2000) but all these mechanisms meet with some difficulties in attempts to explain the properties of accretion disks (Papaloizou et al. 1995, Balbus 2003). One widespread and well known means to transport momentum is the magnetorotational instability (MRI) (Velikhov 1959), but observations demonstrate that there exist systems which don't have magnetic field. It was first shown in (Velikhov et al. 2007, Lugovskii A.Yu. et al. 2008) that large vortical structures arising in shear flows of the accretion disk with a non-Keplerian velocity distribution, which develop and lead to a redistribution of angular momentum in the disk, could provide a mechanism for angular-momentum transport.

Here, we consider two options of the appearance and development of large-scale instability in an accretion disk with a Keplerian azimuthal-velocity distribution: hydrodynamical instability and MRI. In both cases we consider the redistribution of the angular momentum due to occurrence of large vortical structures in shear flows of the disk.

Case of hydrodynamical instability

In first case the problem is considered in a two-dimensional geometry in polar coordinates (r, □) in the domain $\Omega = (R1 \le r \le R2) \times (0 \le \square < 2\pi)$. The physical-mathematical model of the matter flows in a stellar accretion disk is given in (Velikhov et al. 2007), where a system of equations and techniques for their solution are presented. Here, we change the initial state, choosing an azimuthal-velocity distribution that is close to the observed one; i.e., we will assume an equilibrium state with a Keplerian velocity distribution. An analytical solution for the equilibrium configuration of a gas cloud near a gravitating center in the case of a Keplerian azimuthal-velocity distribution $V(r) = 1/\sqrt{r}$ was constructed in (Abakumov et al. 1996).

The behavior of the system with time in case of introducing small symmetric perturbation is considered. It was shown that at the initial time the vortical structures form in the region where the perturbations are specified; these structures, in turn, lead fairly quickly to the formation of spiral vortical structures in the entire disk (Fig. 1a). Thus, small perturbations specified in a narrow band develop into large-scale structures covering the whole disk and the flow pattern does not change qualitatively for a long time, retaining its symmetry. A considerable redistribution of the angular momentum has occurred with time, compared to the initial distribution.

These studies show that large vortical structures forming in the disk lead to a redistribution of angular momentum in the disk and a removal of matter and angular momentum through the outer boundary, but the accretion arising as a result of the angular momentum loss leads to

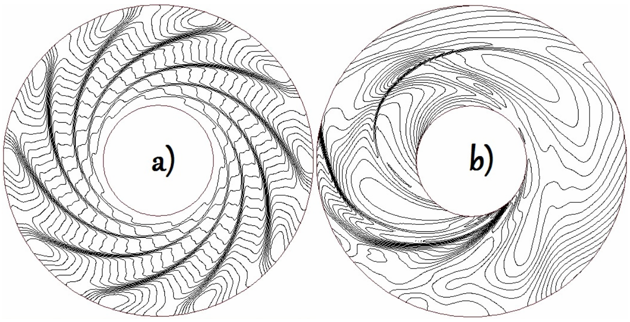

Figure 1: Flow pattern in the form of density contours for the disk with the Keplerian velocity distribution at time corresponding to t = 160 (five disk revolutions) (a) and t = 700 (twenty disk revolutions)

an inflow of the matter and,hence, an increase of the angular momentum. This quasi-stationary behavior of the system causes the observed pulsations of the parameters of the disk matter (Fig. 2).

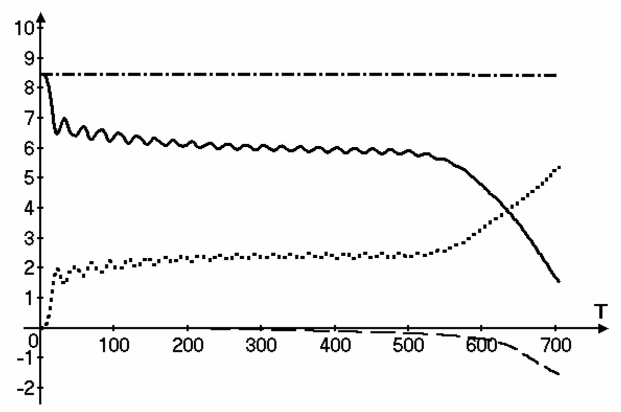

Figure 2: Time dependence of the mass in the computational domain (solid line), the total mass flux through the outer boundary (dotted line), the total mass flux through the inner boundary (dashed), and the sum of the masses in the computational domain and leaving the computational domain (dash–dotted line)

Further study of the system's evolution shows that, with time, the flow starts to lose its symmetry, leading to a qualitative change of the flow pattern — the joining and enlargement of the vortices (Fig. 1b). The flow has undergone considerable reconstruction and separate asymmetrical larger vortical structures have formed. Such two-spiral structures due to different physical processes occur fairly often in flow modeling in various stellar accretion disks.

The results obtained agree with those obtained earlier in (Belotserkovskii O.M. et al. 2000, Belotserkovskii O.M. et al. 2003), where the evolution of perturbations in various types of plane shear flows is considered and it is shown that perturbations develop, vortical structures are formed, the flow loses its symmetry, and several larger vortical structures are formed.

As was already noted above, the system is in a quasi-stationary state for a fairly long time. From the time of the symmetry loss by the flow ($t \approx 550$, 18 revolutions) and the onset of the growth of the vortical structures, the removal of angular momentum and disk matter through the outer boundary begins to occur. As a result, the rate of inward accretion increases strongly, and matter begins to flow out actively through the inner boundary (Fig. 2). Thus, large vortical structures provide a mechanism for the outward transport of the angular momentum of the disk matter, leading to matter accretion through the inner boundary of the computational domain towards the central gravitating body.

The results of our modeling of the flow in a Keplerian accretion stellar disk coincide qualitatively with the results for a non-Keplerian disk obtained in (Velikhov et al. 2007, Lugovskii A.Yu. et al. 2008).

Case of MRI

We investigate the role of the magnetic field in the collapse of a gas–dust cloud into a massive gravitating object. It is known that in the presence of a weak magnetic field, the shear flow may be subject to the development of strong instability, first discovered in (Velikhov 1959). This phenomenon, which has been called the magnetorotational instability (MRI), occurs for certain distributions of the rotational angular velocity of the matter and magnetic-field strengths. In (Balbus et al. 1991) first considered the appearance of local instability of shear flows in astrophysical disks in the presence of magnetic fields. They showed that a weak magnetic field can provide a means of angular-momentum transport in accretion disks by destabilizing the flow in the disk. The accretion of matter onto the star in the presence of a magnetic field has been considered in many studies and it was shown that the magnetic field can appreciably influence the structure of the accretion flow. We consider the development of large-scale vortical flows in a gas–dust disk in the presence of a magnetic field.

The physical-mathematical model of the matter flows in a stellar accretion disk with magnetic field is given in (Velikhov et al. 2012). All the computations were carried out in a two dimensional formulation and assuming azimuthal symmetry. Since the most "dangerous" perturbation modes in the development of MRI have azimuthal wave number $m = 0$ (Velikhov 1959), this assumption essentially does not impose any constraints on the linear stage of the development of the MRI. We used a spherical computational domain with its center cut out to model the collapse of a gas–dust cloud into a star. The protostar located inside the central region creates a spherically symmetrical gravitational potential. At the initial time, a uniform magnetic field oriented along the rotation axis is specified in the region. We adopt as the initial configuration an equilibrium distribution of the density and Keplerian rotational angular velocity of the matter.

A linear analysis of the perturbations carried out for local MRI in an accretion disk enabled us to establish the maximum increment and the characteristic size of small perturbations. The results obtained for the local model agree well with the initial growth stage of perturbations observed in numerical simulations. The critical magnetic field that stabilizes the flow was determined in (Velikhov 1959). In the problem considered here, the criterion for the strong magnetic field stabilizing the flow is the ratio of the gas and magnetic pressures. Figure 3 shows that MRI develops in regions where the matter density (gas pressure) appreciably exceeds the magnetic pressure. The characteristic size of the perturbations grows with increasing magnetic field.

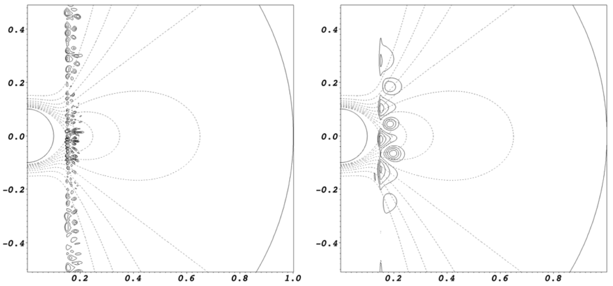

Figure 3: Perturbations of the rotational angular velocity of the matter for ratios of the gas and magnetic pressures near the equator of the inner region Pgas/Pmagn = 4000 (left) and Pgas/Pmagn = 40 (right).

Rotational shear flows can also be unstable in the absence of a magnetic field. In our current study, the initial state of the disk was chosen so that small perturbations do not appreciably disrupt the flow pattern in the absence of a magnetic field. The development of instability occurs in the presence of a fairly weak but non-zero vertical magnetic field.

At late stages in the development of the instability, the flow acquires a strongly non-linear character. As expected, the appearance of chaotic flows leads to the transport of angular momentum to the periphery of the computational domain. As it loses angular momentum, the matter near the central object begins to move into lower orbits, giving rise to accretion.

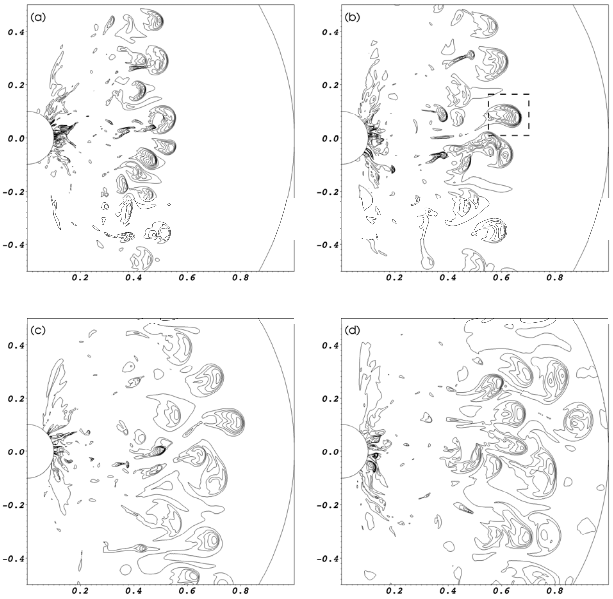

Figure 4: Positive perturbations of the angular momentum at times (from left to right, from top to bottom).

The angular momentum grows at large distances and decreases at small distances from the rotation axis with time. The magnetic field is amplified the chaotic motion of the fluid by several orders of magnitude relative to its initial magnitude. With the development of MRI, the characteristic scale for the chaotic flows becomes larger compared to the scale for the perturbations at the initial stage of development of the instability. Angular momentum is carried away by characteristic large-scale “bubbles”, whose sizes are comparable to the disk thickness. (Fig. 4).

Conclusions

Our computations have shown that the development of hydrodynamical or magnetorotational instability in an astrophysical accretion disk can lead to large-scale turbulence. Large vortical structures arising in the disk lead to a redistribution of the angular momentum of the disk matter; further, the enlargement of vortical structures leads to the more active removal of angular momentum from the disk matter, leading to considerable accretion. Thus, the larger the arising vortical structures, the more actively they remove angular momentum and the more intensively the disk matter begins to accrete.

The results indicate that large-scale turbulent flows that can lead to a considerable redistribution of the angular momentum of the disk matter and an increase in the inward accretion can arise in stellar accretion disks. In addition, quasi-periodic pulsations of the matter parameters giving rise to a non-stationary accretion rate are obtained for various accretion disks under various conditions. This accretion can explain the observed quasi-periodic pulsations of radiation during accretion onto the central body.

This work has been supported by the Russian Foundation for Basic Research (project code 12-01-31348), a Grant of the President of the Russian Federation for the State Support of Young Russian PhDScientists (grant MK-946.2012.2), and Governmental Contract №14.B37.21.0251.

References

Shakura N.I.: 1972, *Sov. Astron.*, **16**, 756.
Shakura N.I., Syunyaev R.A.: 1973, *Astron. Astrophys.*, **24**, 337.
Sawada K., Matsuda T., Hachisu I.: 1986, *Mon. Not. R. Astron. Soc.*, **219**, 75.
Fridman A.M., Boyarchuk A.A., Bisikalo D.V. et al.: 2003, *Phys. Lett. A*, **317**, 181.
Gribov V.N., Lipatov L.N.: 1972, *Sov. J. Nucl. Phys.*, **15**, 438.
Bisnovatyi-Kogan G.S., Blinnikov S.I.: 1976, *Sov. Astron. Lett.*, **2**, 191.
Balbus S., Hawley J.: 1991, *Astrophys. J.*, **376**, 214.
Winters W.F., Balbus S.A., Hawley J.F.: 2003, *Mon. Not. R. Astron. Soc.*, **340**, 519.
Goodman J.: 1993, *Astrophys. J.*, **406**, 596.
Li H., Finn J.M., Lovelace R.V.E., Colgate S.A.: 2000, *Astrophys. J.*, **533**, 1023.
Papaloizou J.C.B., Lin D.N.C.: 1995, *Ann. Rev. Astron. Astrophys.*, **33**, 505.
Balbus S.A.: 2003, *Ann. Rev. Astron. Astrophys.*, **41**, 555.
Velikhov E.P.: 1959, *Soviet Physics JETP*, **36**, 1398.
Velikhov E.P., Lugovskii A.Yu., Mukhin S.I. et al.: 2007, *Astron. Rep.*, **51**, 154.
Lugovskii A.Yu., Mukhin S.I., Popov Yu.P., Chechetkin V.M.: 2008, *Astron. Rep.*, **52**, 811.
Abakumov M.V., Mukhin S.I., Popov Yu.P., Chechetkin V.M.: 1996, *Astron. Rep.*, **40**, 366.
Belotserkovskii O.M., Oparin A.M.: 2000, *Numerical Simulations: From Order to Chaos* (Nauka, Moscow).
Belotserkovskii O.M., Oparin A.M., Chechetkin V.M.: 2003, *Turbulence: New Approaches* (Nauka, Moscow).
Balbus S.A., Hawley J.F.: 1991, *Astrophys. J.*, **376**, 214.
Velikhov E.P., Lugovskii A.Yu., Chechetkin V.M. et al.: 2012, *Astron. Rep.*, **56**, 84.

MULTI-STAGES OPTIMIZED PHOTOIONIZATION MODELLING OF PLANETARY NEBULA LMC SMP-21

B.Ya. Melekh, V.V. Holovatyy, N.V. Havrylova, M.M. Sokil, N.L. Tyshko, A.V. Demchyna

Department of Astrophysics of Ivan Franko National University,
Lviv, Ukraine, *bmelekh@gmail.com*

ABSTRACT. The new approximation expression for the representation of gas density distribution in planetary nebulae envelopes was proposed. The new multi-stages method for the caclulation of the chemical composition and physical parameters of planetary nebulae envelopes based on the optimized photoionization modelling was described. This method was used to the determination of physical characteristics and chemical composition in PN LMC SMP-21.

Key words: planetary nebulae; photoionization modelling.

The previous investigations on the gas distribution in the planetary nebulae (PNe) envelopes were based on analysis of the isophote maps for the sample of PNe with shape very close to the sphere at different evolution stages.

On the base of diagnostic methods results we obtained the relationships between electron density and the maximal value of hydrogen density as well as between above hydrogen density and radius of maximal density. In result, the method for the determination of the first approximation of the density distribution along sightline in PNe was developed. We propose accurate expression for the aproximation of the radial density distribution in real PNe envelopes: $\log n_H = (a0 + a1 * r)/(1 + b1 * r + b2 * r^2)$. Here r is the distance from the nebula center (in parsecs); the values of $a0$, $a1$, $b1$, $b2$ are obtained from the aproximation of the density distribution in galactic PNe.

The three stages method to the determination of the optimal photoionization model (OPhM) of PNe envelopes was proposed. At the first stage the ionization structure of PNe envelope is under determination, using mainly reproducing of the observed diagnostic ratios between line intensities. At the second stage the chemical elements abundances are under correction at the ionization structure obtained at previous stage. At the last third stage all free parameters are employed in optimization process to avoid the consequences due to the assumptions used for division of the optimization process into the two first stages.

The division into stages was made on the base of the modelling estimation results of the sensitivity of diagnostic ratios to the variation of heavy elements. It was concluded that chemical abundances He/H, O/H, and S/H must be included as free parameters at the first calculation stage. Also, the N/H abundance should be included too if it has high values.

The OPhM-method was used to the determination of physical characteristics and chemical abundances in PN SMP-21 in Large Magellanic Cloud (see Table 1). G. Ferland's code *Cloudy* (*http://www.nublado.org*) upgraded by us was used to the calculation of OPhM.

Table 1: The optimal values of free parameters obtained from stage III for PN LMC SMP-21.

Free parameters	Final optimal values of free parameters
$T^*_{eff}(Rauch^*)$, K	190546
$\log L_*$[erg/s]	36.75
$\log R_{in}$[cm]	15.54
log He/H	-0.99
log N/H	-3.65
log O/H	-3.70
log Ne/H	-4.40
log S/H	-5.18
log Ar/H	-5.69
Grain factor	0.0011
a0	3.57
a1	-33.73
b1	-24.22
b2	368.83
Filling factor	0.28

* - Rauch stellar atmospheres were used to the desription of energy distribution in ioizing spectrum of PN nucleous.

References

Melekh B.Ya.: 2009, *JPhS* **13, 3**, 3901.

Rauch T.: 2003, *A&A*, **403**, 709.

Holovatyy V.V., Mal'kov Yu.F.: 1992, *AZh* **69, 6**, 1166.

OPTICAL MONITORING OF NGC 4151: BEGINNING OF SECOND CENTURY

V. Oknyanskij, N. Metlova, B. Artamonov, O. Ezhkova, A. Lyuty, V. Lyuty

Sternberg Astronomical Institute, Moscow M.V.Lomonosov State University,
Moscow, Russian Federation
oknyan@sai.msu.ru

ABSTRACT. We present the historical light curve of NGC 4151 for 1906 – 2012. The light curve (Oknyanskij anf Lyuty, 2007) is primarily based on our published photoelectric data (1968 - 2007, about 1040 nightly mean measurements) and photographic estimates (mostly Odessa and Moscow plates taken in 1906–1982 (Oknyanskij, 1978, 1983), about 350 measurements). Additionally, we include all data obtained prior to 1968 (de Vaucouleurs and de Vaucouleurs, 1968; Sandage, 1967; Wisniewski and Kleinmann, 1968; Fitch et al., 1967) in total, 19 photoelectric observations from 1958–1967, reduced by us to the same diaphragm aperture as that used in our measurements) as well as photographic data (Pacholczyk et al., 1983) (Harvard and Steward observatories' patrol plates taken in 1910–1968, about 210 measurements).

The light curve includes our new photoelectrical and CCD data obtained during last 5 years. All these data were reduced to an uniform photometric system.

Key words: AGN, optical variability, historical light curve

NGC4151 is one of the most popular and well studied AGNs, it is most bright and high variable object, which is very often used as an example object: typical Sy1, typical Sy1.5, typical object changing classification type between Sy1 and Sy1.9. Now about the same cases of untypical variations were found for more then 10 AGNs. So it is more likely typical than untypical option for AGNs and it has to be explained in some unification model.

NGC 4151 – is one of the several Seyfert galaxies which were firstly discovered at 1967 as variable in optical region (Fitch et al., 1967). Shortly after that (at 1968) the photoelectric UBV monitoring of NGC 4151 object was started at Crimean Laboratory of Sternberg Astronomical Institute (Lyuty, 1977). Variability of the object before 1967 can be investigated only from the archive photographic observations and a few number of isolated photoelectrical observations. First long term optical variability investigations using photographic archive data (Harvard plates taken in the years 1932–1952 and Steward plates taken in the years 1956–1968) were published (in graphic form only) by Pacholczyk (1971). Our long term photometry of NGC 4151 using Odessa plates (1952–1975) was published in table and graphic forms Oknyanskij (1978). Then Pachalczyk et. al. (1983) published more complete photometrical data started from 1910 (in table form also). Finally, variability of NGC 4151 during 1906–1911 years was investigated using old Moscow plates (Oknyanskij, 1983). The longest uniform series of photometric observations was obtained of one us (Lyutyi, 1977), and so all other observations, as far as possible, were reduced to the system of the series (see details at Lyuty and Oknyanskij, 1987). Long-term historical light curve in filte B, including photographic and photoelectric data, was published by Lyuty and Oknynskij (1987), and then continued for the 100 years interval (Lyuty 2006, Oknyanskij and Lyuty, 2007). Our data were reproduced at historical light curves many times (for example by Czerny et al. (2003).

At the present work we continue the optical monitoring of NGC 4151. Our new data (118 nights) include the photoelectric UBV photometry (with the same telescope and equipments). Also we get CCD data, which were taken with the 4096x4096 SNUCAM camera mounted in 1.5-m reflector of Maidanak Observatory (Uzbekistan) and with the Apogee 47p camera mounted in the Cassegrane focus of the 0.6-m reflector at the Crimean Laboratory of the Sternberg Astronomical Institute.

The historical light curve of NGC 4151 in filter B for 1906-2012 years is presented at Fig. 1. The light curve with our new data (only filter B) for 2008-2012 years is shown at Fig. 2. At the light curves (Fig, 1 and 2) we can see different variable components: 1 – fast variations with time about tens of days, 2 – slow variations with time about several years, 3 – very slow component with time about tens of years. It is clear seen that after minimuma at 1984 the type of variability is not the same as it was before: the amplitude of the fast variations become smaller relative to the slow ones.

The work was partly supported by NSh-2374.2012.2.

References

Barnes T.G.: 1968, *Astrophys. Letters*, **1,** 171

Czerny B., Doroshenko V.T., Nikołajuk M. et al.: 2003, *MNRAS,* **342**, 1222C.

de Vaucouleurs G., de Vauculeurs, A.G.: 1968, *Publications University of Texas, Series II*, **7**, 1.

Fitch W.S., Pacholczyk A.G., Weymann R.J. : 1967, *Astrophys. J.*, **150**, L67.

Lyutyi V.M., Oknyanskij V.L.: 1987, *Soviet. Astronomy*, **31**, 245.

Lyuty V.M.: 2006, *ASP Conference Series*, **360**, 3.

Lyutyi V.M.: 1977, *Soviet. Astron*., **21**, 655.

Oknyanskij V.L., Lyuty V.M.: 2007, *Peremennye Zvezdy Prilozhenie*, **7**, 28.

Oknyanskij V.L.: 1978, *Peremenye Zvezdy*, **21**, 71.
Oknyanskij V.L.: 1983, *Astron. Tsirkulyar*, **1300**, 1.
Pacholczyk A.G.: 1971, *Astrophys. J.*, **163**, 149.
Pacholczyk A.G., Penning W.R.; Ferguson D.H. et al.: 1983. *Astrophys. Letters*, **23**, 225.
Sandage A.: 1967, *Astrophys. J.*, 1967, **150**, L177.

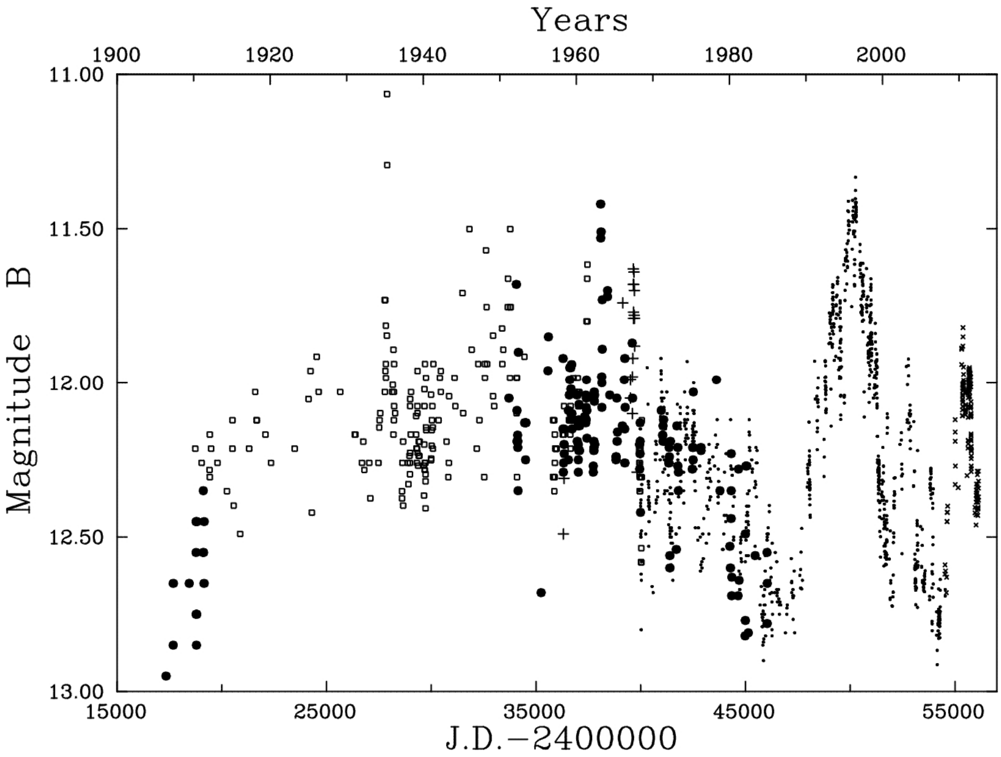

Figure 1: The historical light curve of NGC 4151. Filed circles – our photographic data, open circles – Pacholszyk et. al. (1983), pluses – photoelectric data obtained before 1968, dots – Crimean photoelectric monitoring, x – our new photoelectric and CCD data. The errors are of the order of 0.2 mag for Pachalcsyk's data, 0.1 mag or better for our photographic points, and ~ 0,02 mag for out photoelectric and CCD data.

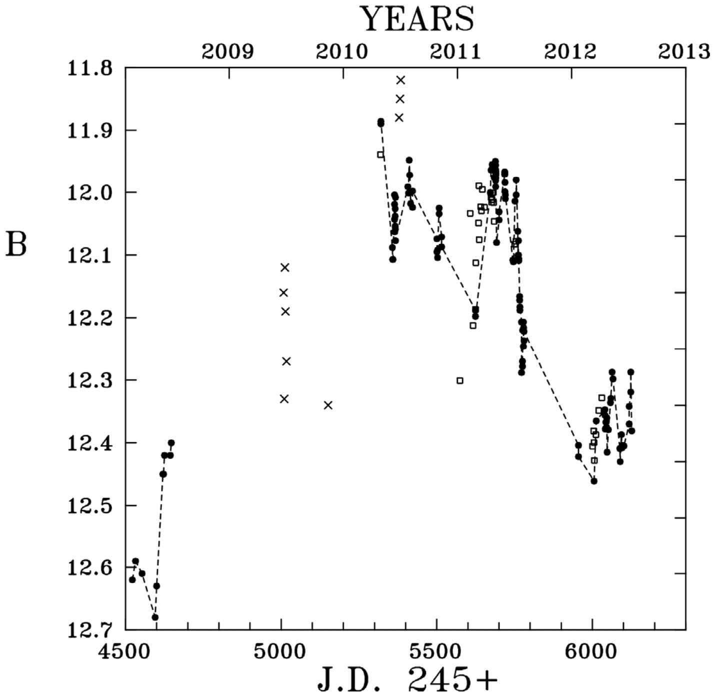

Figure 2: The light curve of NGC 4151 at 2008-2012. Our new, unpublished before data: filed circles – photoelectric data, x – Maidanak CCD observations, boxes – Crimean CCD data.

RADIO-ASTRONOMY

SEARCH FOR THE THIRD HARMONIC OF TYPE III BURSTS RADIO EMISSION AT DECAMETER WAVELENGTHS

Brazhenko A.I. [1], Melnik V.N. [2], Konovalenko A.A. [2], Pylaev O.S. [2], Frantsuzenko A.V. [1],
Dorovskyy V.V. [2], Vashchishin R.V. [1], Rucker H.O. [3]

[1] Poltava gravimetrical observatory of Institute of geophysics, National Academy of Sciences of Ukraine, Poltava, Ukraine
[2] Institute of Radio Astronomy, National Academy of Sciences of Ukraine, Kharkov, Ukraine
[3] Space Research Institute, Austrian Academy of Sciences, Graz, Austria

ABSTRACT. The results of observations of trio bursts consisting of type III bursts are presented in this paper. The instantaneous frequency ratio of trio components is near 1:2:3. We analyze flow, duration, frequency drift rate and polarization of trio components as well as dependencies of these characteristics on frequency.

Key words: type III bursts, drift rate, duration, polarization, second harmonic, third harmonic, decameter wavelength range…

The third harmonic is not usually observed in the solar type III (and associated with them) radio bursts. So new papers, reporting about registration of the third harmonic bursts, are very important for progress in theoretical aspects of researching solar corona. Detection of the third harmonic of type III bursts radio emission at decameter wavelengths can be useful for giving more precise definition to the plasma mechanism of emission and for accuracy of solar plasma parameters on relevant altitudes.

There are some records of the third harmonic in literature. Here we note a powerful U-burst recorded by Haddock and Takakura: their dynamic spectrum, presented in the monograph by Kundu (1965), shows a weak fundamental and intensive second and third harmonics. Another example is a type V burst observed by Benz (1973). Some features of dynamic spectrum of the burst are duplicated at 1.5 times higher frequencies. This indicates the presence of radio emission corresponding to the second and to the third harmonics. Also we point to numerous records of the J- and U-bursts made by Stewart (1962). Frequency ratio of that bursts lies in range 1.5-1.7. The radiation mechanism of the third harmonic was developed by Zheleznyakov & Zlotnik (1974). Afterwards this theory was improved by its authors and other scientists. For example there are papers by Takakura (1974) and Kliem (1992) based on the observations of J-bursts with frequency ratio 2:3 and the third harmonic of type II burst correspondingly. Also there are other observations of the third harmonic of type II bursts (Zlotnik 1998, Dorovskyy 2007). Only last paper refers to decameter wavelength range. Investigating the higher harmonics (Cairns 1988, Yoon 2003, Yi 2007, Rhee 2009), authors analyze similar radiation mechanisms.

Radiation mechanism

Type III radio bursts occur by so-called plasma emission. Their source is electron beam propagating along open magnetic field lines in upward direction. The propagation of electron beam through coronal plasma generates Langmuir waves (l) that can transform into escaping electromagnetic transverse waves (t) by number of processes. Fundamental plasma emission (first harmonic, t_I) results from scattering of Langmuir waves by thermal ions (i) near the local plasma frequency:

$$l + i \rightarrow t_I + i .$$

The second harmonic (t_{II}) of type III bursts occurs by coupling two Langmuir waves:

$$l + l \rightarrow t_{II} ,$$

or by coupling Langmuir wave with fundamental transverse wave:

$$l + t_I \rightarrow t_{II} .$$

It is evidently that the second harmonic radiates on double local plasma frequency.

So, the third harmonic radio emission is generated on the triple electron plasma frequency by interaction of three Langmuir waves:

$$l + l + l \rightarrow t_{III} ,$$

or by interaction of Langmuir wave and transverse wave of the second harmonic:

$$l + t_{II} \rightarrow t_{III} .$$

Observations

The bursts, we analyze in this paper, were registered during summer observations in 2011 and 2012 with the radio telescope URAN-2. It is one of the biggest radio telescopes of decameter wavelength range (effective square is 28000 m^2). URAN-2 can receive two linear (circular) polarizations. Spectrograph DSPz allows registering radiation with frequency resolution 4 kHz and time resolution 10 ms in a whole frequency band 8 – 32 MHz (or in a part of it).

We registered 12 trio composed of a combination of type III and type IIIb bursts. Observations were made in a frequency band 8 – 32 MHz with time and frequency resolution 100 ms and 4 kHz correspondingly. Example of trio consisting of IIIb-IIIb-III bursts is shown on Figure 1. We find such regularities in a structure of trio bursts: the first component was a type IIIb burst mostly, the second component was a type III burst as well as type IIIb burst, the third component was a type III burst in the most cases. Moreover, type III burst was the first component of trio only in a combination III-III-III, and type IIIb burst was the third component only in a combination IIIb-III-IIIb.

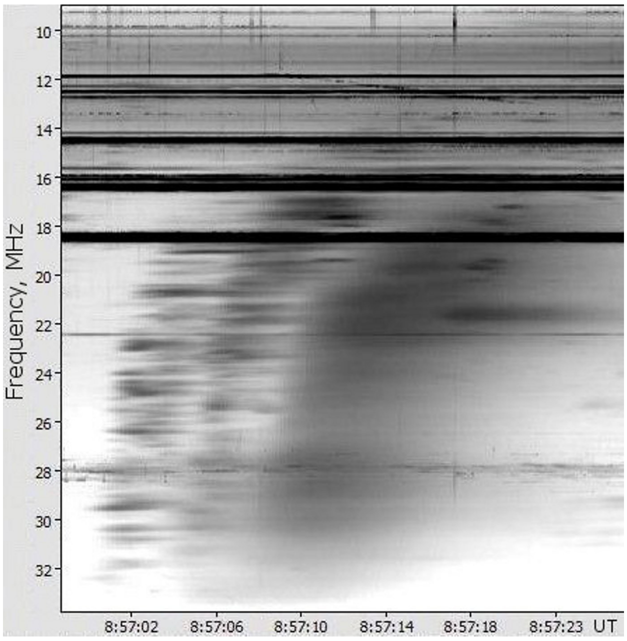

Figure 1: Example of trio.

We simulate an “average” trio for more clearly understanding the characteristic properties. The measurements of burst features, averaging in 4 MHz intervals, will be presented further.

Polarization

We find that components of each trio have the same sign of polarization. Polarization of type IIIb bursts is high, registered value is up to 60-70%. Type III bursts have smaller polarization, registered value is up to 10-20%. Polarization of the first component is always the highest in trio bursts. In addition there is a trend that the third component of trio has smaller polarization then second component (for the same type bursts).

Duration

We register duration at the level of 0.9-power, because measurements of duration were impossible at half-power level. We recalculate 0.9-power duration to half-power duration supposing that the form of burst is Gaussian. The values we derive for type III bursts vary from 2.3 s to 15 s. The most number of values concentrates in interval 5 – 10 s. The type IIIb bursts have always smaller duration at the same frequencies: from 0.5 s to 7 s. The majority of values lies in range 1.3 – 5 s.

Moreover we obtain that duration of bursts increases with decreasing of frequency. Figure 2 shows this dependency for “average” trio.

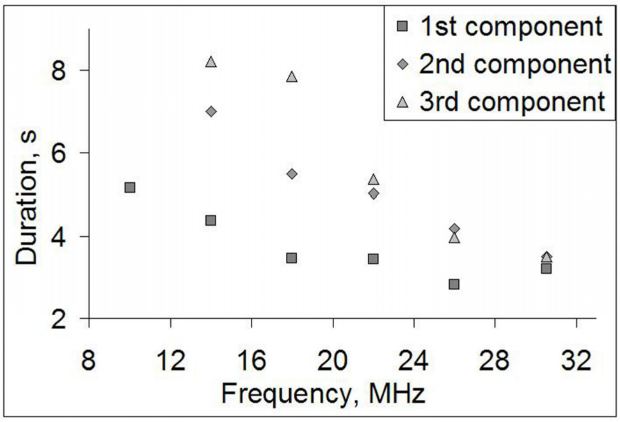

Figure 2: Average duration of trio components dependencies on frequency. Grey marks are results of measurements, that were averaging over all trio in proper frequency band

Frequency drift rate

The emission of all bursts in all registered trio drifts rapidly from high to low frequencies. The frequency drift rate decreases with decreasing frequency, its values vary from 1.1 MHz/s to 4.4 MHz/s. We find the drift rate dependence on frequency is linear:

$$df \big/ dt = -bf \, .$$

The value of factor b lies in interval from 0.07 to 0.18. Such results are confirmed by some papers (Wild, 1950; Melnik & Boiko, 2011), whose authors independently obtain similar proportional coefficient. The factor b indicates the size of coronal inhomogeneity over the active region. The linear dependency of drift rate on frequency is evidence of exponential corona (Melnik & Boiko, 2010).

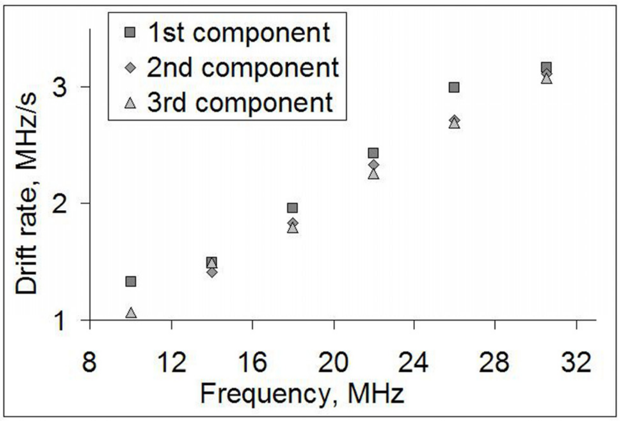

Figure 3: Average drift rate of trio components dependencies on frequency. Grey dots are results of measurements, that were averaging over all trio in proper frequency band.

Drift rate of different components of a trio differ a little in equal frequency intervals: average deviation is near 10%. Average drift rate of the first trio component is more than others. And the second trio component tends to drift faster than the third component. Figure 3 shows how drift rate of trio components depends on frequency.

Instantaneous frequency ratio

Many bursts were not visible at low frequencies through disturbances and influence of ionosphere. Therefore we have to simulate bursts to calculate the instantaneous frequency ratio.

To estimate a frequency ratio of trio components we approximate bursts (maximum flow of bursts) with different functional dependencies. The most correct model is described by the exponential function:

$$f = ae^{-bt},$$

where f – frequency, t – time of maximum flow from the beginning of the observation, a, b – coefficients calculating by the least-squares method. This conclusion is confirmed by the derived results about linear dependence of drift rate on frequency:

$$f = ae^{-bt},\ {}^{df}\!/_{dt} = -abe^{-bt} = -bf\ .$$

We obtain the instantaneous frequency ratio of trio components by averaging frequency ratio in points of time interval in which simulated trio arranges in frequency band 8 – 32 MHz (see Figure 4). Instantaneous frequency ratio of maximum flow of the first and the third "average" trio components is ${}^{f_3}\!/_{f_1} = 2.7$. The third trio component occurs at a 1.5 times higher frequency than second component: ${}^{f_3}\!/_{f_2} = 1.5$. The frequency ratio of the second and first trio components is ${}^{f_2}\!/_{f_1} = 1.8$, it is confirmed by the theoretical and observational papers about the second harmonic.

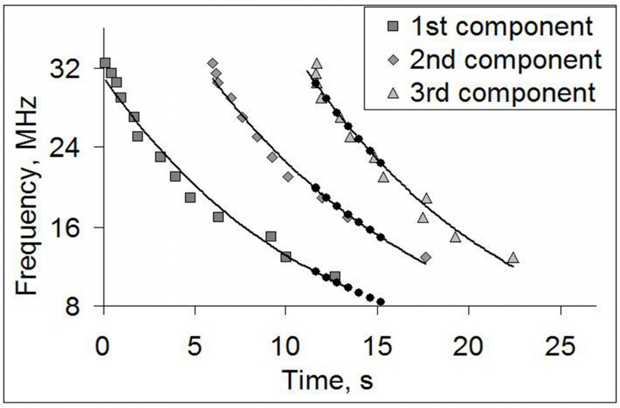

Figure 4: Approximation of trio. Grey points are average observed values of maximum flow. Curves present exponential model of bursts. The frequency ratio of trio components was calculated in black points.

So, there are a number of reasons that allow us to assert that registered trio components have harmonic relations:

1) polarization of the first component of trio is always higher than others; it is up to 60 – 70%, that corresponds to the generally accepted viewpoint about the first harmonic emission;

2) the second and the third components of trio have polarization (10 – 20%), that is typical for the second and the third harmonics according to the plasma radiation mechanism;

3) instantaneous frequency ratio is near to 1:2:3.

References

Kundu M.R.: 1965, *Solar Radio Astronomy*, Interscience Publ., New York.

Benz A. O.: 1973, *Nat. Phys. Sci.*, **242**, 39.

Stewart R.T.: 1962, *CSIRO Division of Radiophysics Report RPR*, **142**.

Zheleznyakov V.V., Zlotnik E.Ya.: 1974, *Solar Phys.*, **36**, 451.

Takakura T., Yousef S.: 1974, *Sol. Phys.*, **36**, 451.

Cairns I. H.: 1988, *J. Geophys. Res.*, **93**, 858.

Kliem B., Kruger A., Treumann R. A.: 1992, *Sol. Phys.*, **140**, 149.

Yoon P.H., Gaelzer R., Umeda T., Omura Y., Matsumoto H.: 2003, *Phys. Plasmas*, **10**, 364.

Yi S., Yoon P.H., Ryu C.-M.: 2007, *Phys. Plasmas*, **14**, 013301.

Tongnyeol Rhee, Chang-Mo Ryu, Minho Woo, Helen H. Kaang, Sumin Yi, and Peter H. Yoon: 2009, *Astrophys. J.*, 694:618 625.

Zlotnik E.Ya., Klassen A., Klein K.-L., Mann G.: 1998, *A&A*, **331**, 1087.

Dorovskyy V.V., Mel'Nik V.N., Konovalenko A.A., Rucker H.O., Abranin E.P., Stanislavsky A.A., Le-cacheux A.: 2007, *European Planetary Science Con-gress*, 688.

Wild J.P.: 1950, *Aust.J.Sci.Res.*, **3**, 541.

Melnik V.N., Konovalenko A.A., Rucker H.O., Boiko A.I., Dorovskyy V.V., Abranin E.P., Lecacheux A.: 2011, *Solar Phys.*, **269**, 2.

Boiko A.I., Mel'nik,V.N., Konovalenko A.A., Rucker H.O., Abranin E.P., Dorovskyy V.V., Lecacheux A.: 2010, *PRE VII*, 367.

THE RADIO CATALOGUES OF NSS102 SURVEY AT 102.5 MHZ (LSA OF LPI, RUSSIA) FOR ALL SKY ZONE OF OBSERVATION IN –16°≤ δ ≤+82°, AND COMPARATIVE ANALYSIS WITH OTHER RADIO CATALOGUES

R.A.Dagkesamanskii [1,3], V.A.Samodurov [1,2,4], D.R.Gadelshin [1], P.N. Semenyuk [1], E.V.Kravchenko [1]

[1] Pushchino Radio Astronomy Observatory of Lebedev Physical Institute,
Russian Academy of Sciences (Pushchino, Russia)
[2] National research university Higher school of economics (Moscow, Russia)
[3] rdd@prao.ru, [4] sam@prao.ru

ABSTRACT. In this paper we report the preliminary results of the total final processing of the entire radio survey observations. They made in 1991-93by LSA of LPI that is full aperture radio telescope in the program survey of the northern sky at a frequency of 102.5 MHz. As a result, the whole sky was covered in declinations and prodused radio sources catalog in –16°≤ δ ≤+82°.

Key words: radio survey, catalogues, radio sources

In this paper we present a beta version of the complete catalog of all the observational data - about 10 000 sources with fluxes exceeding 3 Jy for all declination zone –16°<δ<+82°. Only a part of the data (for declinations +14,1°…+33,5° and +60°…+82°) published and reported previously.

The survey produced by 8-beams diagram of LSA with characteristic sizes HPBW in R.A. and declination:

$$D_\alpha=47' \ , \ D_\delta= 24'\cdot\sec(Z)$$

In the paper observational methodic and processing algorithms and are described. Survey results are displayed in the form of the radio sources catalog, and the initial observation of the radio telescope scans with BSA, also as the isophotes of the observational data on the 102.5 MHz.

The preliminary version has 10187 sources with the fluxes more than 3 Jy. The numbers of radio sources with the fluxes:

≥ 4 Jy - 7597 sources,
≥ 5 Jy - 5738 sources,
≥ 10 Jy - 2629 sources

Extended sources represented by two-dimensional oriented Gaussians. Extended sources total number is 1992 sources. The number of radio sources with the scales:

≥ 10′ - 1314 sources
≥ 20′ - 1058 sources
≥ 30′ - 741 source
≥1° - 177 sources

The methods of processing of daily surveys in the mode of on-line, the first results of the identification with other radio catalogs, also as with catalogs of galaxies and quasars are discussed. According to the results of comparative analysis of cross-discussed data quality basic low-frequency catalogs: UTR (17-25 MHz), 8C (38 MHz), VLSS (74 MHz), 6C (151 MHz), Miyun survey (232 MHz) our catalogs has good flux scale as for pointed also as for extended sources.

Operating (not final) version of the catalog is available at PRAO ASC LPI:

http://astro.prao.ru/cgi/view_1.cgi?cat=nss102&mod=1

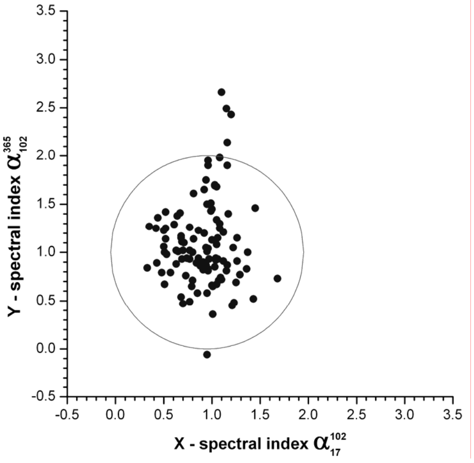

Figure 1: The example of radio sources identification in our data at 102 MHz, Txs data at 365 MHz and UTR data at 17 MHz. It represented by 2-dimentional spectral index diagram. The tail population points up are extended sources in Txs survey. NSS102 and UTR has good data agreement by small distribution spectral indexes on X.

NETWORK DEVELOPMENT OF THE PUSHCHINO RADIO ASTRONOMY OBSERVATORY OF ASC LPI

D.V. Dumsky[1], E.A. Isaev[1,2], V.D. Pugachev[1,2], V.A. Samodurov[1,2], S.F. Likhachev[3],
M.V. Shatskaya[3], M.A. Kitaeva[1]

[1] Pushchino Radio Astronomy Observatory ASC LPI,
Pushchino, Russia, *dumsky@prao.ru*
[2] National research university Higher school of economics,
Moscow, Russia, *is@itaec.ru*
[3] Astro Space Center LPI,
Moscow, Russia

ABSTRACT. All main changes in the network of the Pushchino Radio Astronomy Observatory has been related to introduction of the buffer data center in the recent years, upgrading internal and external communication channels and the exploitation of ip-telephony.

Key words: Networks: voip.

The main challenges of the buffer data center is to maintain the channels for scientific and telemetry data transfer and backup of the data in the storage as part of the space radio telescope project known as ”Radioastron. The channel connects the tracking station RT-22, buffered data center, located in the territory of the observatory and data center ASC LPI, Moscow. This channel with bandwidth of 1 Gbit/s is provided by Stack Group companies and stretched using technology MPLS (Multiprotocol Label Switching) to the M9, where is connected to the ASC LPI. Currently obtained from a space telescope experimental records are passed through this channel in Moscow, and at the same time are stored in the data center buffer storage with a capacity of 20 terabytes.

However, the work buffer data center is not limited to these tasks, it is also used to host the servers that serve the local network of the observatory. Here the servers for the storage of observational data obtained from three radio astronomy systems, database servers, mail and web-server, DNS, and server of network time synchronization. Through the further development of the data center, we have increased capacity networked storage (Open-E DSS v6) from 24 to 48 terabytes, and install additional UPS for servers and switches.

A new server with two processors Intel Xeon 22.53-2.80 GHz and 12GB of RAM designed for database storage and processing of astronomical catalogs is purchased. We installed virtualization platform based on a system of native container lxc instead used on another server system Openvz to the new server. This system does not require additional manipulation with operating system kernel and further more meets the safety requirements as distributive kernel is updated more frequently than the core OpenVz. Web-servers and database server Observatory were transferred to the new system virtualization.

Additional Gigabit Ethernet managed switches to provide backup links and connect servers purchased. In order to improve ip-telephony in the Observatory, as well as voice channels with ASC LPI we replaced old Voip equipment with more reliable solution from the company addPack.

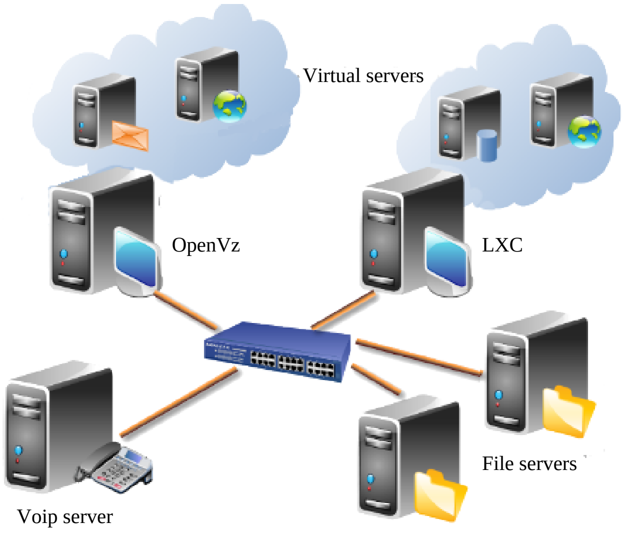

Figure 1: PRAO Data center servers

FOCUSING OF 3C144 SOURCE RADIATION BY THE SOLAR CORONA

Galanin V.V[1], Derevjagin V.G[2], Kravetz R.O[3]

Institute of Radio Astronomy of National Academy of Science of Ukraine,
Odessa, Ukraine
[1]gvv@breezein.net, [2]dvg@gmail.com, [3]krro@ukr.net

ABSTRACT. The research of solar corona by the compact cosmic source radiation was made on URAN-4 radio telescope. In the period from June 6 to June 20 2012 the flow of Crab nebula was measured on the 20 MHz and 25 MHz frequencies. During the eclipse we observe the great increase of 3C144 flow, which is compare with the flow of 3C461 source. Data and results of measurement analysis is presented.

Key words: radio source, solar corona.

Radio telescope URAN-4 is work in frequency range 10 to 30 MHz. Its antenna is representing the phased array with two polarizations. Its effective square is 5360 m^2 (Galanin et al., 1989). In 2010 there was perform the modernization of equipment and digital radiometer was created. In the period from June 6 to June 20 2012 on the radio telescope there was made an experiment of solar corona study by means of compact cosmic source. The observations were made in the period of solar activity maximum. We has study the transition region of solar corona with 2 to 15 solar radii, in which the solar wind is speedup.

In these days the Crab nebula 3C144 flow was measured on two frequencies 20 and 25 MHz. As a supporting source we take the CasA 3C461. Figure 1 show 3C461 to 3C144 flow ratio plots for two frequencies and two polarizations.

It's seen from this data that 3C144 flow is change from minimum, diffused, in the period from June7 to June 9, up to maximum from June 12 to June 18. In the period of maximum eclipse phase on June 15 the flow of 3C144 exceed near 4 times the flow of supporting source.

Figure 2 show records of sources 3C144, 3C274, 3C405 and 3C461 which were made from June 14 to June 15 2012.

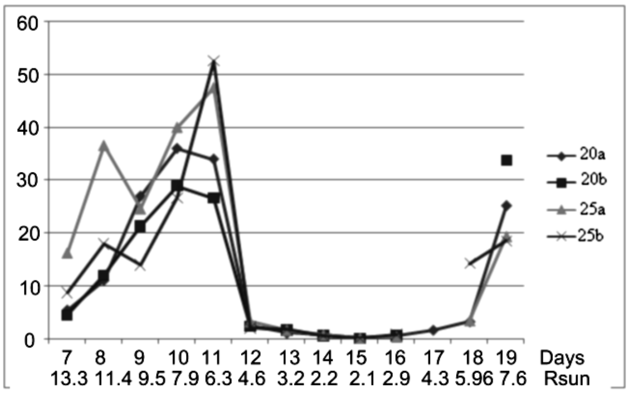

Figure 1: Ratio of 3C461 to 3C144 flow for two frequencies and two polarizations.

References

Galanin V.V. et al.: 1989, *Kinematika i fizika nebesnyh tel*, **5**, 5, 87.

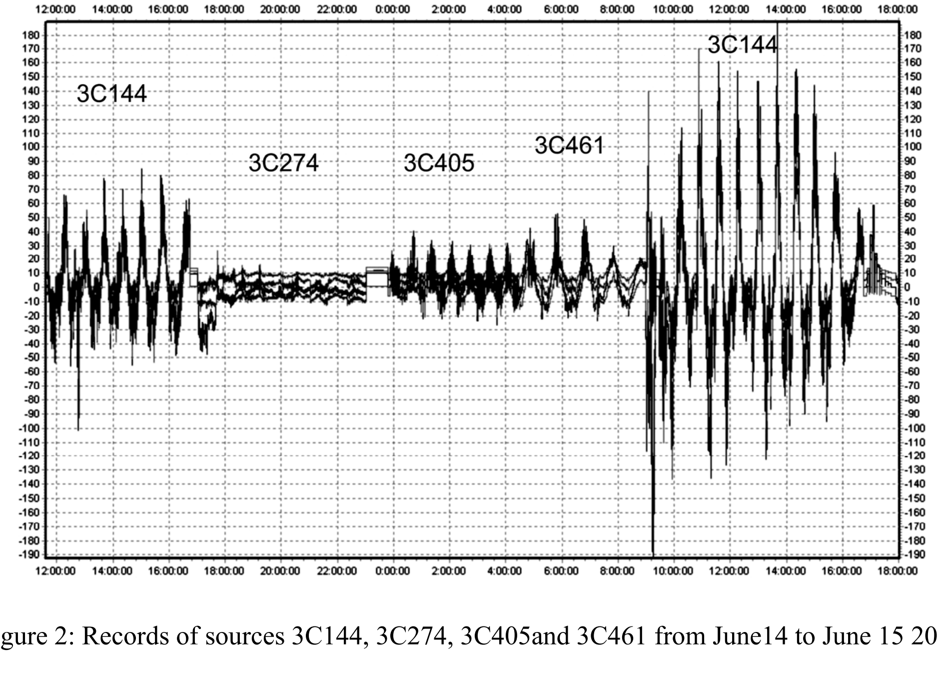

Figure 2: Records of sources 3C144, 3C274, 3C405and 3C461 from June14 to June 15 2012.

DATA CENTERS IN THE SCIENTIFIC INFORMATION INFRASTRUCTURE

E.A. Isaev[1,2,4,5], M.B. Amzarkov[2,3], V.D. Pugachev[1,2,5], V.A. Samodurov[1,2], R.R. Sukhov[2,3], N.A. Kobylka[2,4], Yu.A. Tarasova[2], E.Yu. Assur[5]

[1] Pushchino Radio Astronomy Observatory ASC LPI, Pushchino, Russia, *is@itaec.ru*
[2] National research university Higher school of economics, Moscow, Russia
[3] Uptime Technology INO, Moscow, Russia
[4] Stack Group, Moscow, Russia
[5] Itaec, Pushchino, Russia

ABSTRACT. There is a multiple increase of the volume of scientific data obtained in the course of research each year. Due to this there is a need for continuous improvement, such as data transmission channels and systems for handling and storage of scientific data. For example, data centers show current centers and storage of scientific data and advanced technology in this area, in particular the "cloud" technology. Particular attention is paid to the information infrastructure for data centers storing scientific information.

Key words: Data center.

Due to the multiple increase every year volumes of scientific data collected during the research, there is need for continuous improvement of channels for the transmission of such data as centers of scientific data.

The structure of a typical data center consists of:

1. Information infrastructure that includes server hardware and provides the core functionality of the data center - data processing and storage.
2. Telecommunications infrastructure for the interconnection of elements of the data center, as well as transfer of data between the data center and users.
3. Engineering infrastructure for the proper functioning of the main systems of the data center.

Classification of data centers:

a) in size;

b) the reliability;

c) for other purposes.

In more detail a typical example of a scientific-buffered data center data center space project "Radioastron" on PRAO ASC LPI (www.prao.ru). Data center is located in the building of an international test site project space radio telescope "Radioastron." For the placement of the data center has been allocated a special room where the server onto your mounted, uninterruptible power supply and cooling system. Data center PRAM has two storage servers with a capacity of 24 and 48 terabytes.

The next example of a modern data center is a parallel computing system (cluster) Pushchino Research Center (PSC), RAS, which was established in 2000 by the Institute of Mathematical Problems. The necessity of his appearance dictated by the demand solutions to many demanding computing tasks assigned research and educational groups PSC RAS.

Then move on to a modern network of commercial data centers Stack Data Network (SDN), which is Russia's first fault-tolerant network of data centers, in the design and development of which international best practice and experience of DC-outsourcing in Russia are reflected. Network uptime data centers SDN ensure geographical remoteness of its nodes and highly redundant core engineering systems (according to a N +1). One of the five data centers is located in the city of science SDN Pushchino. Pushchino and institutions have Sciences Centre's start to use these computing resources.

As an overseas data center is a typical example of the Harvard-MIT Data Center (HMDC, www.hmdc.harvard.edu), who is a member of the Institute IQSS. It was created in the early 1960s as a data center for Political and Social Sciences at Harvard University. Over the years into a HMDC information service and technology provider for social research and education for many departments, centers and research projects at the Faculty of Arts and Sciences and other schools at Harvard.

METHODS CONTROL RADIOASTRONOMY OBSERVATIONS AND PROCESSING OF COSMIC RADIO SOURCES

E.A. Isaev[1,2]

[1] Pushchino Radio Astronomy Observatory ASC LPI, Pushchino, Russia, *is@itaec.ru*
[2] National research university Higher school of economics, Moscow, Russia

ABSTRACT. In this paper the following methods represented: control of the radio astronomical observations using the estimation results, making decisions on the detection of cosmic sources, taking into account noise and interference, and recognizers classes of cosmic radio sources to the maximum of a posteriori probability (Bayesian approach). The problem researched is about storing and transferring large amounts of scientific information from cosmic radio sources to consumers.

Key words: information systems, computational biology, parallel processing system.

The method control of radio astronomical observations using the estimation results, which will significantly increase the efficiency of radio astronomical observations is considered in this work. There is a wide variety of assessment systems that require management procedures. On the other hand, there is not a smaller variety of control systems that require the estimation procedure. Schemes of these systems are provided.

In theory of detection and estimation of the parameters of radio signals some models are used. The model should, on the one hand, meet demand of its proximity to the real signal, and on the other hand allow you to carry out a theoretical analysis, which can be extended to more general cases. The method of decision making of detection of cosmic radio sources considering the noise and interference with the detection of the optimality criterion according to which you can choose the best one (likelihood ratio).

We use Bayesian approach for the method of recognition for classes of cosmic radio sources to the maximum of posteriori probabilities. The Bayesian approach is based on the theorem, which states that if the frequency function of each class is known, the required algorithm can be written in explicit analytic form. Moreover, this algorithm is optimal, ie, it has a minimal error rate.

Breakthrough in electronics, computing and information technology over the past 50 years have led to the fact that one of the dominant trends in modern science is the significant increase in the recorded and received data and the associated problems of storage and processing of this information. Synthesis of science and IT leads to the realization of the fact that a significant breakthrough in the knowledge of the world is possible only in case of possibility of processing of extra-large amounts of information and that the role of information and its processing in research is crucial. In particular, astronomers have faced with the fact that they need to handle the flow of information to several terabytes per day (more on the sites http://www.astrogrid.org/ and http://www.euro-vo.org/). Approximately everywhere, especially in research, there is a rapid replacement of the analog digital technologies. Examples of these trends in radio can be projects of unique and ambitious generation of radio telescopes: Atacama Large Millimeter Array (ALMA), Square Kilometer Array (SKA), Low Frequency Array (LOFAR) and others. This paper investigated on modern radiotelescopes task processing, storage and transmission of radio astronomical data.

THE CROSS-IDENTIFICATION, VISUALIZATION AND COMPARATIVE ANALYSIS OF ASTRONOMICAL CATALOGS IN A COMMON DATABASE RADC

M.A.Kitaeva [1,3], V.A.Samodurov [1,2,4], D.V.Dumsky [1], E.A.Isaev [1,2], V.D.Pugachev [1,2]
[1] Pushchino Radio Astronomy Observatory of Lebedev Physical Institute,
Russian Academy of Sciences (Pushchino, Russia)
[2] National research university Higher school of economics (Moscow, Russia)
[3] marina@prao.ru, [4] sam@prao.ru

ABSTRACT. The Pushchino Observatory of ASC LPI have been developing in some last years database of some astronomical catalogs (Radio Astronomy Data Center – RADC, look on http://astro.prao.ru/db/ and http://observations.prao.ru/). In the database have the most commonly used by radio astronomers data: survey catalogs of radio sources at different radio frequencies (as well as in other spectral bands), catalogs of the major sky objects studied in astronomy etc.

Key words: radio survey, astronomy catalogues, database

The Pushchino Observatory of ASC LPI has database of some astronomical catalogs and observatory observations (Radio Astronomy Data Center – RADC, look on http://astro.prao.ru/db/ and http://observations.prao.ru/).

Since 2011 the database of astronomical catalogs actively equipped visualization of data and compare catalogs between them. These funds will provide the basis for statistical analysis and cross-sectional analysis of various astronomical catalogs.

For this task we have developed the Graphical data representing from several catalogs within the chosen area on the sky, the map data and the statistical analysis of the main parameters as for each catalog as a whole, also as statistics cross-identifications of the user's favorite catalogs. At the moment the database will is improved by advanced visualization of individual radio sources as a result of identification in the elected by user catalogs (flux distribution over the frequencies, the distribution of spectral indexes, etc.).

Work was supported by the program of the Presidium of RAS "The origin, evolution and structure of objects in the universe," and program of the Department of Physical Sciences "Active processes and stochastic structures in the universe."

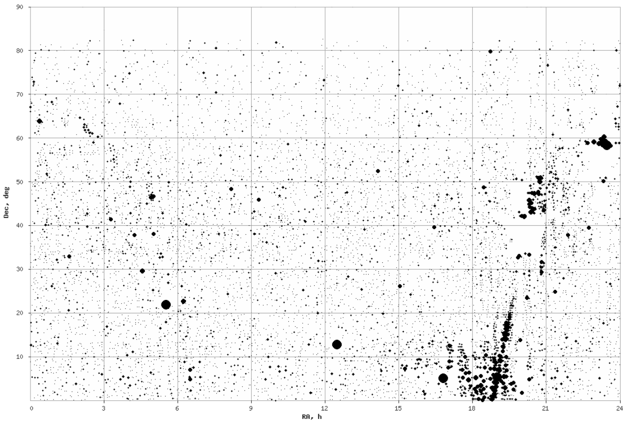

Figure 1: The example NSS102 radio catalog map. It is represented all sources of Pushchino catalog at 102 MHz with declination more than 0 degrees.

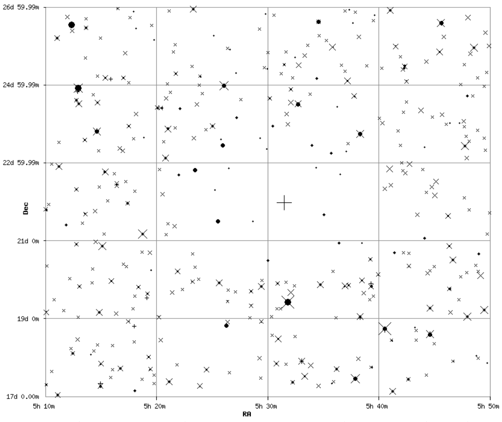

Figure 2: The example of a comparing of the data sky fields for three catalogues: 4C (178 MHz, by direct cross) 1400 MHz (circles) and GB6 (4850 MHz, oblique crosses). There are zone of avoidance near strong source that showed only in 4C catalog.

MODERN INFORMATION SYSTEMS FOR RESEARCH WORKS OF THE PUSHCHINO RESEARCH CENTER OF RAS

V.V. Kornilov[1,2,4], E.A. Isaev[1,3,4]

[1] Institute of Mathematical Problems of Biology RAS, Pushchino, Russia, *basil@psn.ru*
[2] Pushchino State Institute of Natural Science, Pushchino, Russia
[3] Pushchino Radio Astronomy Observatory ASC LPI, Pushchino, Russia, *is@itaec.ru*
[4] National research university Higher school of economics, Moscow, Russia

ABSTRACT. The current state of information systems of the Pushchino Research Center of the Russian Academy of Sciences allows us to successfully solve the problems of computational biology.

Key words: information systems, computational biology, parallel processing system.

The Pushchino Research Center (PRC) of the Russian Academy of Sciences (RAS) includes 9 institutes of RAS focusing on microbiology, molecular biology and biophysics and the Radioastronomical Station of the Astrocosmic Center of the Physics Institute. On the basis of the institutes of the PRC two universities: Pushchino State Institute of Natural Science and a branch of Moscow State University are working. PRC is a unique formation of global significance and has around about half of Russia's potential in the field of Physical and Chemical Biology.

At present the solution of problems in biology, especially in computational biology: bioinformatics, structural and computational genomics, molecular modeling, is needed for the use of powerful computing and communications resources. To successfully conduct the research on a global level the modern biologist needs a high-speed access to information contained in the world databases via Internet, high-speed processing of large volumes of data, using supercomputers with the goal of computer modelling of biological systems and so on.

In recent years, a great amount of work to meet these requirements has been done. Now all the institutes of PRC as well as educational foundations, data storage and data processing systems are combined into a single local area network built on fiber optical channels. It has high-speed access to Internet via optical communication channel with data rate 10 Gbit/s. It allows not only to find necessary information in the world wide web but to work with supercomputing centers such as Joint Supercomputer Center of RAS, supercomputer Lomonosov of Moscow State University, other Russian and foreign supercomputer centers.

The powerful parallel processing system (cluster) are working in PRC RAS on the basis of the Institute of Mathematical Problems of Biology to meet the acute need of PRC researchers for highly efficient computational resources so that they might solve numerous computational problems requiring mass computer memory and high speed of operation. At the present time the overall cluster performance is about 900 Gflops. In the further plans of improvement of the performance of the cluster is considered to increase the number of computing nodes and upgrade the internal cluster network.

Due to the organization of GRID-infrastructure developing within the framework of funded by EU project EGEE, enormous computational capacities and huge information volumes will be reachable for all scientific community.

In Pushchino State Institute of Natural Science successfully conducted training and graduate students with advanced multimedia teaching computer classes.

A number of other projects for creation and development of modern information systems are made and continued.

The direct optical channel from tracking station RT-22 in Pushchino to Moscow processing center has been created and put into operation to transfer large amounts of data at the final stage of the establishment of ground infrastructure for the international space project "Radioastron". A separate backup system for processing and storing data is organized in Pushchino Radio Astronomy Observatory to eliminate data loss during communication sessions with the Space Telescope.

IONOSPHERE DISTURBANCES OBSERVATIONS DURING THE PERIOD OF SOLAR ACTIVITY MAXIMUM

Kravetz R.O.[1], Galanin V.V.[2]

Institute of Radio Astronomy of National Academy of Science of Ukraine,
Odessa, Ukraine
[1]krro@ukr.net, [2]gvv@mail.ru

ABSTRACT. Strong ionosphere disturbances dates in the first half of 2012 year are defined on the data of ionosonds network. Sporadic E_s layer appearance and strong radio wave absorption phenomena, when the reflections from ionosphere are completely absence, are studied. We show, that frequency and duration of ionosphere disturbances are increased in summer months compare to winter ones.

Key words: ionosphere, ionogram

Ionosphere observations are provided for a long time and are an actual problem. It take place mostly because of ionosphere have a significant effect on radio communications in various frequency ranges. For the radio astronomy the ionosphere has also great importance, because it can significantly distort signals from cosmic radio sources, which is received by the earth based radio telescopes. The most serious distortions are appeared during the disturbances in ionosphere. So the problem of observation and registration of ionosphere disturbances are very important.

The base instrument for ionosphere observation is the ionosphere stations (ionosonds) network, which give all ionosphere parameters in real time. Results of ionosond measures are fixed on the ionograms, which represents the dependence of signals, reflected from ionosphere from the transmitted frequency

Most ionosondes in Europe are uniting in the common system named DIAS (European Digital Upper Atmosphere Server) [1, 2]. The data, provided by this system allow to estimate enough good ionosphere conditions, and particularly, to define presence of disturbances. In this work we use data mostly from Warsaw ionosond.

Ionosphere disturbances observations are in particular interest during the solar activity maximum, because in this period the number and the intensity of ionosphere disturbances are increased as a rule. In this work we study ionosphere disturbances, which occurred in the first half of 2012 year, i.e. in the period of solar activity maximum or the period that is closely precede to it.

The ionospheres disturbances are often connect with the varying of F2 layer critical frequency over it mean value. Such disturbances can be positive (when the critical frequency increase) or negative (when the critical frequency decrease). Ionosphere disturbances caused in most times by the solar flares and their consequences [3]. After the strong solar flare the X-ray stream is appear, then it reaches Earth and caused higher ionization of ionosphere (mostly of D layer). Such disturbances named sudden ionosphere disturbances. Something later the stream of particles, mainly protons, are reaches the Earth, and they also cause higher ionization and respectively ionosphere disturbances. But such disturbances are take place only on the high latitudes.

Other type of ionosphere disturbances is caused by magnetic storms [3], which lead to electron concentration changes and so to increase of radio waves absorption.

Along with the above mentioned types of ionosphere disturbances we may consider such phenomena as an E_s sporadic layer. This layer is not regular and it can appear in any time of the day and in any time of the year. Duration of it existence is not big and can be from some minutes to some hours. However, because of high electron concentration in this layer, it can significantly influence on the radio waves spreading. Particularly, when sounding ionosphere from the Earth, it can black out higher layers. On the other side, when the radio waves come from the space, as it take place during the radio astronomy observations, they may not reach the Earth. So, sporadic layer E_s appearance can significantly influence on the radio astronomy observations, and it study is very important.

The typical example of sporadic layer E_s appearance is showed on the figure 1, where some consequent ionorams are presented. Ionograms interval is 15 minutes. Sporadic layer E_s appeared as a horizontal strait trace and reflections from higher layers are absent because of black out effect. Within near half an hour, sporadic layer E_s is disappear and ionograms becomes to its original form.

From ionograms of the first half of year 2012 there was defined all dates of sporadic layer E_s appearance and it's approximately times of appearance and durations. This data is presented in table 1.

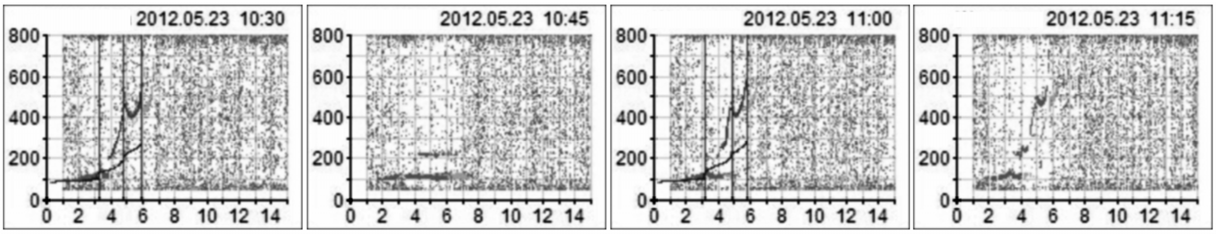

Figure 1: Ionograms 23.05.2012. Sporadic layer E_s appearance.

Table 1: Dates, time of appearance and durations of sporadic layer E_s in the first half of year 2012.

DATE	TIME	Duration	DATE	TIME	duration	DATE	TIME	duration
January 02	15:00	1	May 01	18:45	1	June 04	17:30	0.5
05	17:00	1	02	19:15	0.5	06	10:45	1
07	20:00	1	05	10:00	1.5	09	17:30	1
07	22:00	0.5	10	23:00	3	10	05:15	3
15	19:00	0.5	11	00:00	1	11	07:45	2
16	20:00	0.5	14	12:00	0.5	12	06:45	2
17	05:30	0.5	17	16:30	1	12	10:45	2
19	17:30	1.5	18	22:15	0.5	14	19:45	0.5
23	04:00	1	23	10:45	0.3	15	10:30	1
February 08	04:30	1	24	03:15	1.5	17	07:00	1
20	21:30	0.5	27	19:15	1	17	17:30	1
March 02	11:00	1	27	23:00	0.5	18	00:30	0.5
April 01	21:45	1	28	02:15	1	19	03:00	1
29	19:00	0.5	28	06:15	1	26	07:00	2
30	09:45	0.5	28	17:00	3	27	15:30	2.5
			28	17:00	3	28	17:00	1
			29	17:45	1	29	08:00	0.5
			29	23:15	1	29	14:30	3
			31	20:15	0.45	30	16:00	2

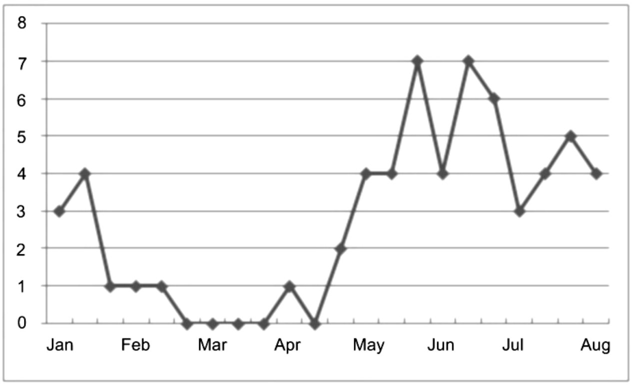

Figure 2: Sporadic layer E_s appearance frequency.

Also there was calculated approximately values of frequency of sporadic layer E_s appearance. Thees values were calculated as a ratio of number of days, when the sporadic layer E_s layer appears, to all days of observations in decade. This data is presented on figure 2. This plot shows that in summer months (beginning from May) the frequency of sporadic layer E_s appearance is significantly higher than in winter ones. Duration of sporadic layer E_s existence is also higher in summer month than in winter ones. The most notable days were July 2 and 17, when sporadic layer E_s was practically continuously exist for 10 and12 hours respectively.

When ionograms was analyzed, there was find some phenomena of strong radio wave absorption, when reflections from ionosphere are completely absent (so called black-outs). Example of such phenomena showed on figure 3. For the comparison, figure 4 show ionograms made in the same time of previous day, when the disturbance was absent. Such phenomena were observed several times during the given period.

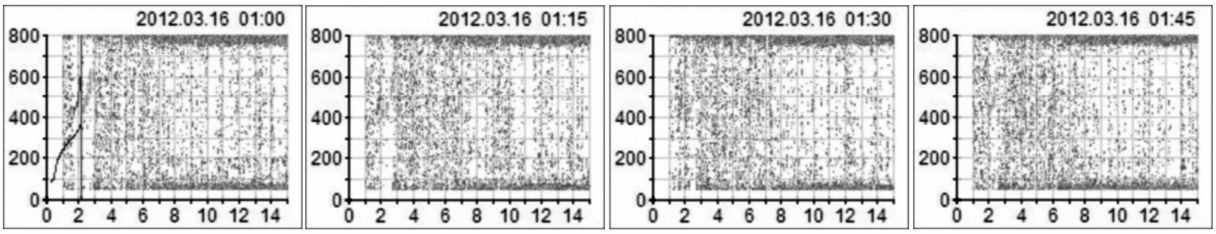

Figure 3. Ionograms 16.03.2012. Reflections from ionosphere are absent.

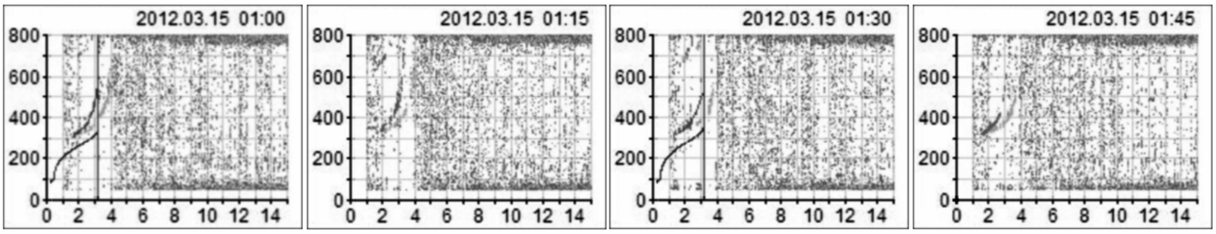

Fig.4. Ionograms 15.03.2012. Ordinary reflections from ionosphere.

The strongest effects of such type was observed on Mach 16, when reflections from ionosphere was absent for 2.5 hours, and on July 15, when reflections was absent for 2 hours. Similar phenomena were observed on January 24, April 24 and July 9, 11 and 19.

References

1. DIAS: European Digital Upper Atmosphere Server. *http://www.iono.noa.gr/dias*.
2. Belehaki A., Cander Lj. R., Zolesi B., Bremer J., Jurén C., Stanislawska I., Dialetis D., Hatzopoulos M.: 2005, *J. Atmos. Sol-Terr. Phys.*, **67(12)**, 1092.
3. Brjunelli B.E., Namgaladze A.A.: 1988, *Physics of Ionosphere*, M., Nauka.

GEMINGA: NEW OBSERVATIONS AT LOW RADIO FREQUENCIES

V.M .Malofeev [1], O.I. Malov, S.V. Logvinenko, D.A. Teplykh [2]
Pushchino Radio Astronomy Observatory, Lebedev Physical Institute,
142290, Pushchino, Moscow reg., RUSSIA
[1] *malofeev@prao.ru,* [2] *teplykh@prao.ru*

ABSTRACT. After nearly 10 years, we have succeeded to detect radio emission from Geminga more again. In this report we present new evidence for presence of radio emission from Geminga in the range 42-112 MHz. The observations were carried out on two sensitive transit radio telescopes We used three new digital receivers to detect the pulses and to obtain dynamic spectra.The examples of mean pulse profiles are presented. Exact value of the dispersion measure have been calculated using the simultaneous observations at three frequencies.

Keywords: pulsars, radio emission.

Introduction

Geminga was discovered in gamma-ray in 1975 (Fichtel et al., 1975). For a long time this source was remained unidentified until its detection as X-ray pulsar (Halpern & Holt, 1992) and slightly late as gamma-ray pulsar (Bertsch et al., 1992) with a period of 237 ms. All attempts to detect the radio source or pulsar have been unsuccessful till 1997, when three group from Pushchino Observatory (Astro Space Center, Lebedev Physical Institute, Russia) reported the detection of pulsed radio emission from Geminga at frequency 102.5 MHz (Malofeev & Malov 1997; Kuzmin & Losovsky 1997; Shitov & Pugachev 1998). In 1999 presence of radio emission were conformed at the same frequency 103 MHz (Vats et al., 1999). At now there is no evidence for detections of radio emission at more high frequency. But recently the weak continuum radio emission has been detected at the frequency 4.8 GHz (Pellizzoni et al., 2011).

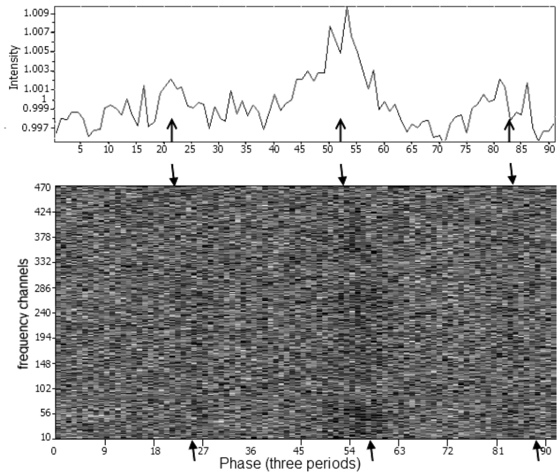

Figure 1: Example of a pulse profile (upper) and a dynamical spectrum (lower) of Geminga at 111 MHz, obtained by summing 36 selected groups (triple periods) on the 20.01.12. The horizontal axis is in samples of the triple period of the pulsar. The dispersion track is marked by arrows.

Observations and results

The observations were carried out on two sensitive transit radio telescopes in Pushchino in the range 42-112 MHz. First of them is Large Phase Array (LPA) antenna, with operating frequency 111.5±1.5 MHz and the effective area $3{\cdot}10^4\,m^2$. Second one is DKR-1000 (East - West arm), which operates at 30-110 MHz and has the effective area ~ 7000 m^2. New series of observations was obtained using a unique set of digital, multi-channel receivers designed for pulsar observations, which came into use in 2006-09. The spectrum of the signal is calculated using an instrumental realization of a 1024-point FFT processor. The time resolution that can be obtained is 0.2048 ms. The width of the operational frequency band is 2.5 MHz, which is separated by the FFT into 512 spectral channels with widths of 4.88 kHz each. The reduction programs implement several techniques for removing interference, using several criteria for distinguishing false pulses from real signals (see, for detail, (Malofeev et al. 2012)).

We continued the observations of Geminga at low radio frequencies and hoped to detect strong signal, but did not reported most of unsuccessful observations or the seldom week pulses. Suddenly in the beginning of this year new observations in Pushchino showed the evidence for the detection of Geminga at three low frequencies during two months (January-February of 2012) in a few sets of observations. Here, we present the results for three days 19 — 21 of January integrated profiles of selected groups at all three frequencies (Fig. 1-3). To check the presence the weak pulsar signal and to raise the reliability we determine the observing window or the group as three apparent pulsar period with the sampling interval 7.5776 ms. One observation set contained 280 or 841 groups (triple periods) at frequencies 111 MHz and 42/62 MHz accordingly. The direct integration of all groups showed weak signal with signal-to-noise ratio (S/N) about 5 in some observations. But if we used the method of visible pulses selection (Malofeev et al. 2012) for reduction of data in these observations, the value of S/N ratio can reach more than 10 in these days (Fig.1,3).

In this case we summed all group, where have been the pulses with S/N > 2 at selected phase. The mean profile of 36 selected groups is presented at Fig.1 (upper). Here the integration was carried out at phase sample 52 ± 3, but possible see two other more week pulses at the phases near samples 21 and 83. All three pulses are separated by one pulse period (31.29 samples). Next method was the summing of selected groups with pulses, which show S/N > 2 in folding profile for the observing window as one pulsar period, as shown in Fig.2b. This selection showed the presence of three pulses in the observing window (Fig. 2-3). Both types of selected groups of integration

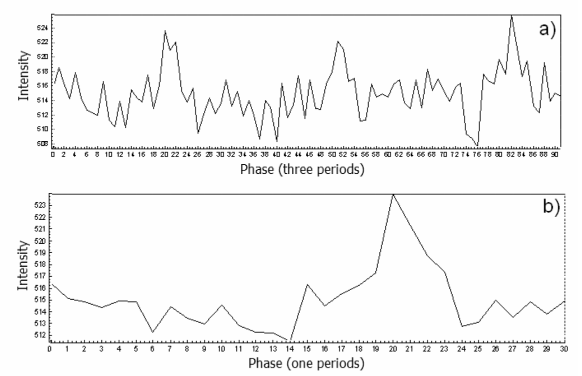

Figure 2: (a) Example of a pulse profile of Geminga at 62 MHz, obtained by summing 20 selected groups (triple periods) on the 20.01.12. (b) The mean profile for one period obtained by the folding of data. The horizontal axis is in samples of the triple period (a) and one period (b) of the pulsar.

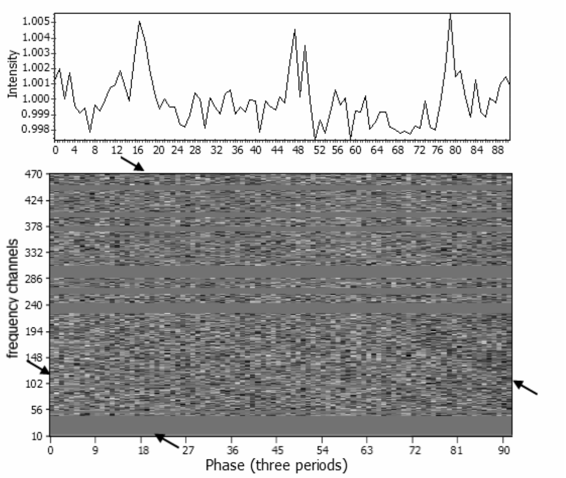

Figure 3: Example of a pulse profile (upper) and a dynamical spectrum (lower) of Geminga at 42 MHz, obtained by summing 23 selected groups (triple periods) on the 21.01.12. The dispersion tracks are marked by arrows.

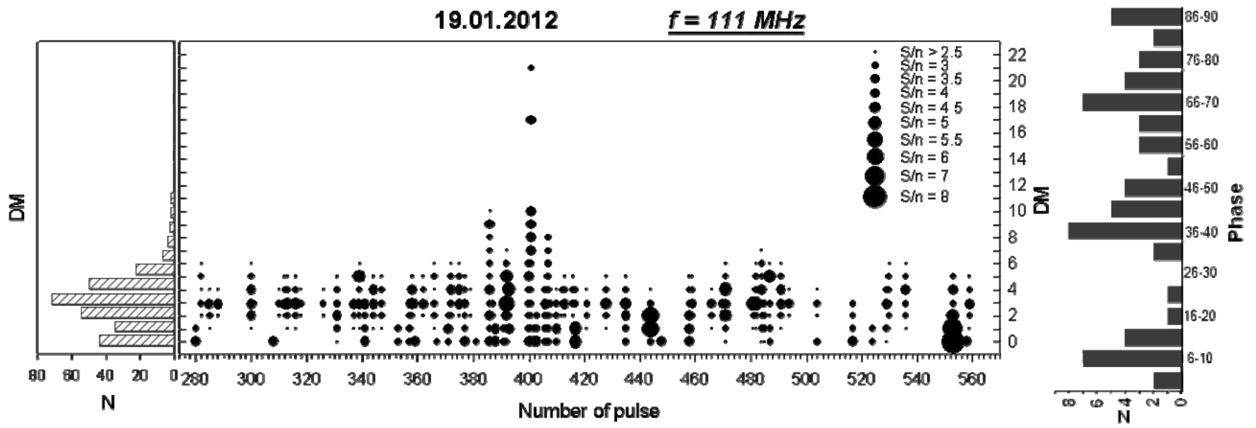

Figure 4: The central panel shows events with *S/N* > 2.5 at different DM versus number at pulse (time) (size of the circle indicates the value of the signal to noise ratio). The left panel shows the histogram of the number of events vs DM. The right panel shows histogram of the events with *S/N* > 2:5 versus of period phase for 19.01.2012 (triple period).

demonstrates the presence of periodical radio emission from Geminga at low frequencies. Next very important thing is the presence of the signal dispersion. We have been luck and first time new simultaneous observation at three frequencies on 20 of January give us possibility to measure more exactly the value of DM = 2.89 ± 0.02. The dispersion tracks are seen at dynamic spectra of Fig. 1,3 (bottom panels). Fig. 4 shows events with *S/N* > 2.5 in depend on number of pulse, DM and phase of period for 19.01.2012 at 111 MHz.

Conclusions

1. The presence of periodic radio emission has been confirmed at all three low frequencies.
2. We measured precise value of the dispersion measure (DM = 2.89 ± 0.02) using the simultaneous observations at three frequencies.
3. The long-term (a few years) intensity variation can be the cause of the absence of low frequency radio emission from Geminga during about 10 years.

Acknowledgments. This work was financially supported by the Russian Foundation for Basic Research (project code 12-02-00661) and Academy of Science (program nonstationary phenomenon in the objects of Universe 2012).

References

Bertsch D., et al.: 1992, *Nature*, **357**, 306.

Fichtel C.E., Hartman R.C., Kniffen D.A., et al.: 1975, *ApJ*, **198**, 163.

Halpern J., Holt S.: 1992, *Nature*, **357**, 222.

Kuzmin A., Losovsky B.: 1997, *Pis'ma AZh*, **23**, 323.

Malofeev V., Malov O.: 1997, *Nature*, **389**, 697.

Malofeev V., Teplykh D., Logvinenko S.: 2012, *Asron. Rep.*, **56**, 35.

Pellizzoni A., et al.: 2011, *MNRAS*, **416**, 45.

Shitov Y., Pugachev V.: 1998, *New Astronomy*, **3**, 101.

Vats H., Singal A., Deshpande M., et al.: 1999, *MNRAS*, **302**, 65.

OSCILLATIONS OF DECAMETER TYPE IV BURSTS OBSERVED ON APRIL 7, 2011

Melnik V.N.[1], Brazhenko A.I.[2], Konovalenko A.A.[1],
Panchenko M.[3], Frantsuzenko A.V.[2], Rucker H.O.[3]

[1] Institute of Radio Astronomy of NAS of Ukraine, Kharkov, Ukraine
[2] Poltava gravimetrical observatory of Institute of geophysics of NAS of Ukraine, Poltava, Ukraine
[3] Space Research Institute, Austrian Academy of Sciences, Graz, Austria

Introduction

The new branch of solar physics known as solar seismology (Nakariakov & Verwichte, 2005) reaches a huge progress last ten years. Since observations of oscillations and pulsations of different coronal structures (such as magnetic loops, prominences) become possible at the optical, x-ray and radio wavelength ranges with spacecrafts (TRACE, SOHO, SDO, etc). Analysis of obtained data gives an opportunity to estimate the plasma parameters of the source region using the theory of MHD oscillations. Periods of registered oscillations vary from several seconds to tens minutes. They are associated with fast magneto-acoustic, slow magneto-acoustic, Alfven and sound waves. There are some mentions (for example Mel'nik et al., 2008) about radio emission oscillations of the type IV bursts at the frequencies 10–30 MHz.

In this paper we consider oscillations of decameter radio emission of the type IV bursts registered on April 7, 2011 by the radio telescope URAN–2. Using Fourier and wavelet analyses we derive characteristic periods at different frequencies.

Observations and results

We registered decameter type IV bursts on the 7th of April, 2011 by radio telescope URAN–2 (Poltava, Ukraine) (Megn et al., 2003). In this day observations by URAN–2 were carried out from 06:12 to 14:02 UT.

There were two coronal mass ejections (CME) on April 7, 2011 according to SOHO. The first one propagated in southeast direction, and the second one moved in southwest direction. The first and the second type IV bursts were observed simultaneously with the first and the second CMEs.

In this paper we investigate oscillations with the largest periods. We used Fourier analysis and wavelet analysis. There are two main long-wave periods. The first one is near 75 minutes and associated with the first and the second bursts. The second long-wave period is near 40 minutes and related to the second event. We obtained that both periods decreased with time. Drift rate of the first period is 0.07. It changes from 88 minutes at the beginning of the first event to 77 minutes at the beginning of the second event and became stable till the end of the second burst. Drift rate of the second period is smaller. Its value is 0.06. This period changes from 47 minutes at the beginning to 38 minutes at the end.

Similar dependencies are obtained in the whole frequency band from 8 MHz to 32 MHz. These results are agreed by both Fourier and wavelet analyses.

Such long periods can be connected with oscillations of the CME core or very high magnetic arches. We show that more possible are oscillations of CME cores and they are associated with magneto-sound or Alfvenic waves. In the case of the first one the temperature of core plasma is $10^6-10^7 K$. If oscillations are connected with Alfvenic waves then for magnetic field surrounded the core we have 0.3–0.6 *G*. Both values and plasma density, and magnetic field are seen reasonable.

Conclusion

We discover radio emission oscillations of the decameter type IV bursts registered on April 7, 2011 by the radio telescope URAN–2. Fourier and wavelet analyses show the presence of oscillations with characteristic periods near 75 and 40 minutes. It seems that these are oscillations of CME cores.

References

Nakariakov V.M., Verwichte E.: 2005, *Living Rev. Sol. Phys.*, **2**, 3-65.

Mel'nik V.N., Rucker H.O., Konovalenko A.A., Dorovskyy V.V., Abranin E.P., Brazhenko A.I., Thide B., Stanislavskyy A.A. Solar Type IV bursts at frequencies 10-30 MHz // *Pingzhi Wang Solar Physics Research Trends*. – NewYork: Nova Science Publishers, 2008. – P. 287-325.

Megn A.V., Sharykin N.K., Zaharenko V.V., Bulatsen V.G., Brazhenko A.I., Vaschishin R.V.: 2003, *Radio Physics and Radio Astronomy*, **8**, 345–356.

SOURCES WITH LOW-FREQUENCY STEEPNESS SPECTRUM CONCERNING THE UNIFIED MODEL

A.P. Miroshnichenko
Institute of Radio Astronomy of the NAS of Ukraine
Kharkov, Ukraine
mir@ri.kharkov.ua

ABSTRACT. Based on data of the data of the Grakovo catalogue of the extragalactic sources, detected at the decametre band with the UTR-2 radio telescope , it was established, that properties of radio sources with low-frequency steepness of spectrum are in accordance with the long evolution. At that, quasars and galaxies with low-frequency steep spectra often are the sources of the infrared and the X-ray radiation. In the last case we use the possibility of alternative determination of the magnetic field strength in the sources necessary for the estimate of the ratio of the magnetic field energy and the energy of the relativistic particles. Also we obtained the relations of sources luminosities at the radio, infrared, optical, X-ray bands that revealed evolution effects. The analysis of considered relations for quasars and galaxies with low-frequency steepness of radio spectrum testifies for the unified model of sources.

Key words: radio spectrum, quasar, galaxy, magnetic field strength

Introduction

Radio sources with low-frequency steepness spectrum (type C+) correspond to conception of the long evolution of this class of sources, when the critical frequency of the synchrotron emission can displace to values less than 10 MHz. Before [1] we received estimates of the main physical parameters of quasars and galaxies with steepness spectrum over the sample of objects at the decametre band (at that the value of low- frequency spectral index exceeds 1). The examined sample of objects with spectrum C+ is compiled at the base of the Grakovo catalogue of extragalactic sources detected with the UTR-2 telescope at the declination ranges $\delta = -13^0 ... +20^0$ and $\delta = 30^0 ... 40^0$ with flux density more than 10 Jy at the frequency 25 MHz [1]. With given criteria 148 sources are selected, including 52 galaxies, 36 quasars and 60 optically non-identified objects. The optical and high-frequency data for sample sources have been get from the NED database (*http://nedwww.ipac.caltech.edu*). Note, that the redshift range of objects is enough vast and forms $z = 0.017....2.4$.

Calculations of the physical parameters of radio sources with spectrum C+ were carried out at the frame of ΛCDM -Universe model. These calculations showed, that galaxies and quasars of the sample have the great luminosity (by order of 10^{28} *W/Hz ster* at the frequency 25 MHz) and very extent radio structure with linear size by order of 1 Mpc and characteristic age by order of 100 million years [1].

Independent estimation of the magnetic field strength

Our further analysis of properties of considered sources with spectrum C+ reveals that 14 objects from 36 sample quasars are the infrared sources, and 15 objects from the sample are the X-ray sources. It is known that many extragalactic X-ray sources have the non-thermal X-ray spectrum. At the assumption that the X-ray emission of quasars and galaxies may be due to the inverse Compton scattering of radio photons of the microwave background by relativistic electrons, it is the independent estimation of the magnetic field strength of objects. To obtain the magnetic field strength B_{IC} (at the inverse Compton scattering) by the flux density of X-ray emission we transform the relation from [2]:

$$\begin{aligned} B_{IC} = ((5.05 \cdot 10^4)^{\alpha} \cdot 1.15 \cdot 10^{-16} \cdot (1+z)^{\alpha+3} \times \\ \times S_r \cdot \nu_r^{\alpha} \cdot S_X^{-1} \cdot \nu_X^{-\alpha})^{\frac{1}{\alpha+1}} (Gauss) \end{aligned} , \quad (1)$$

where all values are at the CGS system, α - is a spectral index of steep radio spectrum, z is a redshift of object, S_r is a flux density of radio emission at the frequency ν_r, S_X is a flux density of X-ray emission at the frequency ν_X. We accept $\nu_X = 2.42 \cdot 10^{17} Hz$ (at the energy of X-ray photons 1 keV), $\nu_r = 2.5 \cdot 10^7 Hz$ (decameter band). As a result of calculations from (1), we receive the estimates of the magnetic field strength for quasars (mean value) in the sample with spectrum C+: $\prec B_{IC} \succ = 1.03(\pm 0.45) \cdot 10^{-6} Gauss$, and for galaxies (mean value) in the sample with spectrum C+: $\prec B_{IC} = 0.67(\pm 0.25) \cdot 10^{-6} Gauss$. Let us compare these estimates with the values of the magnetic field strength *B,* derived by us for the same objects at the assumption about the equipartition of the magnetic field energy and the energy of relativistic particles in the sources [1]: $B = 6.15(\pm 0.30) \cdot 10^{-6} Gauss$ - for quasars in the sample with spectrum C+, $B = 8.14(\pm 0.58) \cdot 10^{-6} Gauss$ - for galaxies in the sample with spectrum C+. As one can see from the derived estimates, the value of magnetic field strength B_{IC} is, in average, by one order less than the value *B*, determined at the equipartition condition.

It is possible to estimate the energy of relativistic particles by the value B_{IC} and the value of radio luminosity L [3] in sources. So, in our case, the energy of relativistic electrons in sources with spectrum C+ is:

$$W_e = \frac{10^{12}\cdot L}{B_{IC}^{3/2}}\cdot\frac{\nu_2^{(1/2)-\alpha}-\nu_1^{(1/2)-\alpha}}{\nu_2^{1-\alpha}-\nu_1^{1-\alpha}}\cdot\frac{2-2\alpha}{1-2\alpha}(erg) \quad , \qquad (2)$$

where $\nu_1 = 10MHz$, $\nu_2 = 100MHz$. Note, that the energy of relativistic particles in sources, when take into account the relativistic protons, may be $W_p = 100\cdot W_e$. Then the mean values of the energy of relativistic particles with (2) are: $\prec W_p \succ = 3.32(\pm1.72)\cdot10^{63}\,erg$ (for quasars) and $\prec W_p \succ = 3.77(\pm1.55)\cdot10^{61}\,erg$ (for galaxies) in the examined sample. It is known that the magnetic field energy in sources is:

$$W_{IC} = \frac{B_{IC}^2}{8\pi}\cdot V(erg) \quad , \qquad (3)$$

where V is the volume of a source. The mean values of the magnetic field energy from (3) are: $\prec W_{B_{IC}} \succ = 1.19(\pm1.13)\cdot10^{62}\,erg$ (for quasars) and $\prec W_{B_{IC}} \succ = 9.35(\pm4.05)\cdot10^{58}\,erg$ (for galaxies) in the examined sample.

It turned out, that the mean values of the ratio of the magnetic field energy and the energy of relativistic particles for sources with spectrum C+ are: $\prec W_{B_{IC}}\,/\,W_p \succ = 0.13(\pm0.07)$ (for quasars) and $\prec W_{B_{IC}}\,/\,W_p \succ = 0.91(\pm0.81)$ (for galaxies) in this sample. So, we conclude from these ratios about the prevalence of the energy of relativistic particles over the energy of the magnetic field in the examined sources. The great extent of radio structure (~1Mpc) of quasars and galaxies with steepness spectrum at the decameter band may evidence in favor of such situation.

Ratios of emission at the different bands

Also, we examine the estimates of ratios of flux densities of emission in the different bands: decameter (frequency 25 MHz), centimeter (frequency 5000 MHz), infrared (IR), optical (opt), X-ray band for quasars and galaxies of the sample (at the logarithmic scale). These are identical to the ratios of the corresponding monochromatic luminosities (Table 1).

One can see, the mean values of corresponding ratios for quasars and galaxies in Table1 have enough close quantities. In that case, the obtained characteristics of radio sources with spectrum C+ are in concordance with the unified model of sources [4, 5]. Also, it follows from the presented ratios (Table 1), that galaxies contain more dust (which is responsible for the infrared emission) than quasars.

Let us examine relations for derived characteristics of quasars and galaxies with spectrum C+. In particular, the relation of the ratio of monochromatic luminosities at the decameter and infrared bands versus the redshift for the sample objects is presented in Figure 1.

Table 1. Mean values of the ratios of monochromatic luminosities at the different bands for quasars and galaxies with spectrum C+

Mean value of the ratio	Quasars	Galaxies
$\prec \lg(\frac{S_{25}}{S_{5000}}) \succ$	1.69(±0.08)	1.74(±0.05)
$\prec \lg(\frac{S_{25}}{S_{IR}}) \succ$	4.30(±0.11)	3.67(± 0.19)
$\prec \lg(\frac{S_{25}}{S_{opt}}) \succ$	5.00(± 0.10)	5.15(± 0.12)
$\prec \lg(\frac{S_{25}}{S_X}) \succ$	7.78(± 0.17)	7.89(± 0.33)
$\prec \lg(\frac{S_{IR}}{S_X}) \succ$	3.54(± 0.20)	4.68(± 0.47)

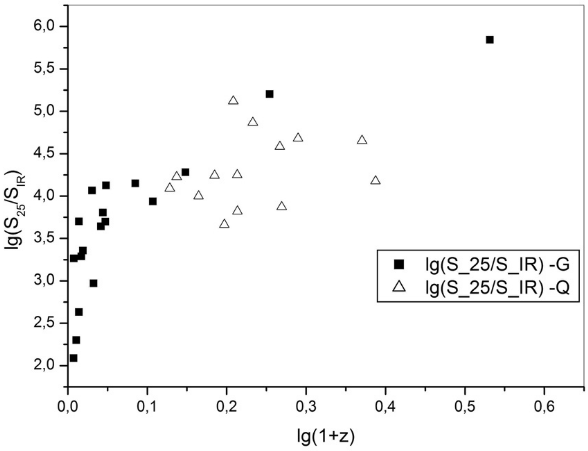

Figure 1: The ratio of monochromatic luminosities at the decameter and infrared bands versus the redshift

This relation evidences for the essential cosmological evolution of luminosities of sources with spectrum C+. The analogous picture is displayed in the relation of monochromatic luminosities of the sample objects at the decametre and optical bands versus the redshift (Figure 2).

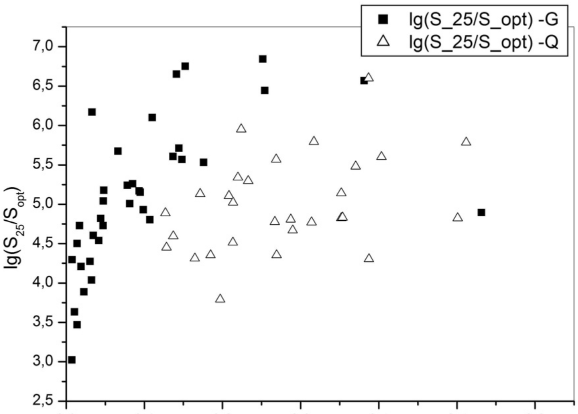

Figure 2: The ratio of monochromatic luminosities at the decameter and optical bands versus the redshift

The trend to increase of contribution of the decameter emission for more extent sources is noticeable in the relation of monochromatic luminosities versus the linear size of sources with spectrum C+ (Figure 3, Figure 4). The mutual relation of the monochromatic luminosities (Figure 5) for galaxies and quasars with spectrum C+ perhaps has maximum, indicating on the recurrence of the source's activity at the different bands.

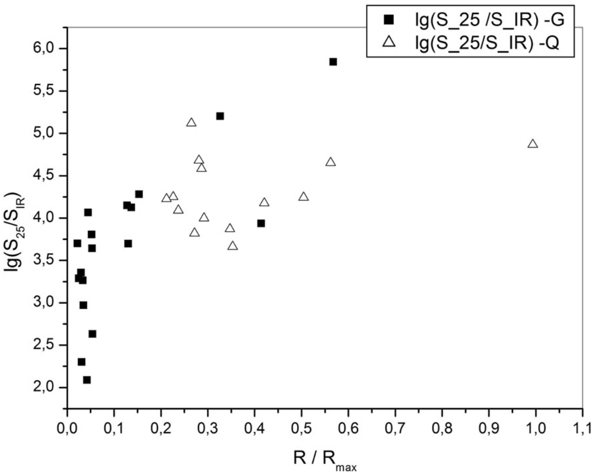

Figure 3: The ratio of monochromatic luminosities at the decameter and infrared bands versus the linear size

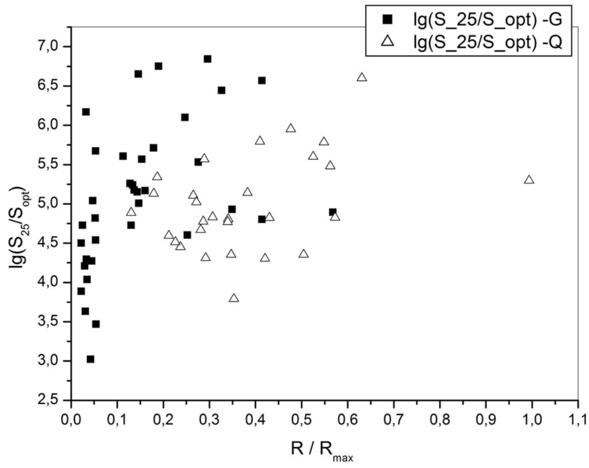

Figure 4: The ratio of monochromatic luminosities at the decameter and optical bands versus the linear size

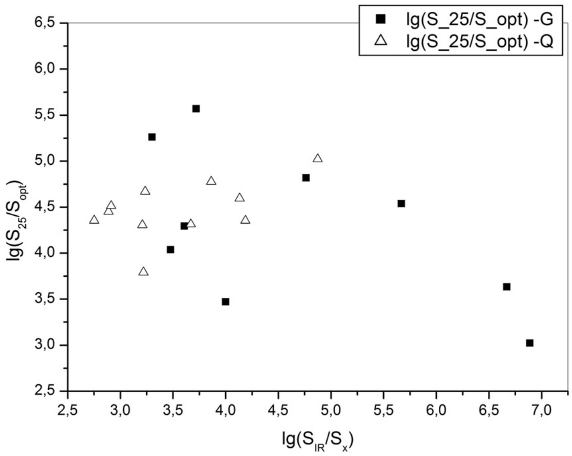

Figure 5: The mutual relation of monochromatic luminosities for the sample objects

Conclusion

The independent estimation of the magnetic field strength of the sources with spectrum C+ have been derived at the assumption about inverse Compton scattering for the X-ray emission of sources.

The contribution of the decameter emission increases for more extent sources with spectrum C+ and displays the evolution.

Similarity of the structure and the physical characteristics of galaxies and quasars with spectrum C+ testifies for the independence from the power of active nuclei and corresponds to the unified model of sources.

References

1. Miroshnichenko A.: 2012, *Radio Physics and Radio Astronomy*, **3**, 215.
2. Harris D., Grindley J.: 1979, *MNRAS*, **188**, 25.
3. Lang K.: 1974, *Astrophysical Formulae*, Berlin: Springer-Verlag.
4. Antonucci R.: 1993, *ARA&A*, **31**, 473.
5. Urry C., Padovani P.: 1995, *PASP*, **107**, 803.

VARIABILITY OF THE EXTRAGALACTIC RADIO SOURCES 3C120, CTA102, DA55 AND OJ287 ON CENTIMETER WAVES AND ITS CONNECTIONS WITH THE DATA OF VLBI OBSERVATIONS

M. Ryabov [1], A. Donskyh [2], A. Suharev [1], M. Aller [3]

[1] Odessa observatory "URAN-4" of the Radio-astronomical institute NAS Ukraine
[2] I.I.Mechnikov Odessa National University
[3] Radio observatory of Michigan University, Ann Arbor, USA

ABSTRACT. By data of the long-term monitoring (30-40 years) fluxes of extragalactic radio sources 3C120, CTA102, DA55 and OJ287 received on the RT-26, University of Michigan present results of data processing with use the wavelet analysis. Received analysis of trend and short-time components of the flux density changes in the studied frequencies 14.5, 8 and 4.8 GHz. For each time components on all frequencies found values of main periods and time of their existence, integrated power spectra for the phases activity for radio sources was built. From the results of VLBI observations in sources with long jets (3C120 and CTA102) detected quasi-periodic structures brighter components. Their appearance is linked to the dynamics of the interaction of shock waves in the jet emission from the cores. Quasi-periodic structures in the jet can be formed as a result of a return standing wave.

Introduction

Radio galaxy 3C120. Main characteristics: z ~ 0.033, the distance to the object ~142 Mpc. The observations were made at a frequency 14.5 GHz 33 years (1978–2011), 8 GHz 45 years (1966–2011) and 4.8 GHz 29 years (1980–2009). Diagram of the flux density at 3 frequencies for the common observation periods is presented in Fig. 1.

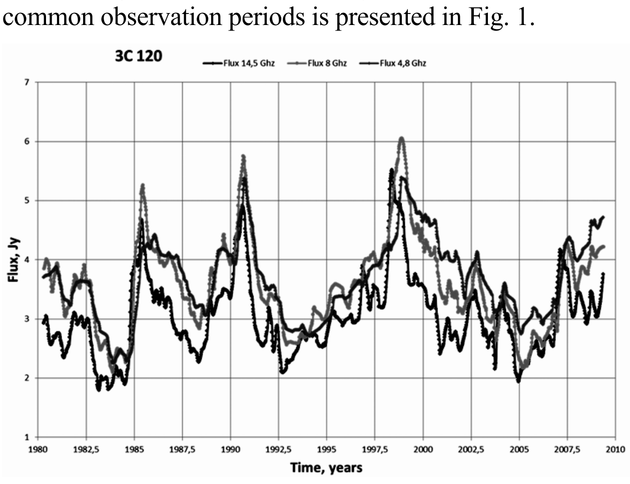

Figure 1: Graph of the fluxes at frequencies of 14.5, 8, 4.8 GHz, for the radio galaxy 3C120.

Quasar CTA102. Main characteristics: z ~ 1.037, the distance to the object ~6942 Mpc. For the source CTA102 data were obtained at frequencies of 4.8, 8 and 14.5 GHz for the 12-year period of observation (1999–2011).

Quasar DA55. Main characteristics: z ~ 0.859, the distance to the object ~5489 Mpc. For a source DA55 used data obtained at frequencies 4.8, 8 and 14.5 GHz for the 12-year period of observation (1999–2011).

Radio Source OJ287 refers to blazars, which are rapidly variability across the electromagnetic spectrum. Main characteristics: z ~ 0.306, the distance to the object ~1576 Mpc. We used the results of 30 years' observations (1979-2010) at frequencies 4.8, 8 and 14.5 GHz.

Observations

Investigation results monitored the 14.5, 8, 4.8 GHz fluxes of 3C 120, CTA 102, DA55, OJ 287 with the 26 m antenna of the University of Michigan Radio Astronomy Observatory. Details of the calibration and analysis techniques are described in Aller et al. (1985).

We used the average values of the fluxes of sources at regular intervals samples every 7 days.

With the use of a polynomial moving average (half-width of the interval 5 points), there was a decrease of noise and remove the casual bursts . Total flux densities of a radio source 3C120 are shown in Fig. 1. Allocation of short-component signals against the main period performed using Fourier filtering (O – C) (Gaydyshev, 2001). The change in the flux of sources at different frequencies has been observed mainly in time shift from the larger to the smaller frequency. The individual phases of activity sources can show the coincidence peaks at all frequencies.

FOURIER-analysis

In order to determine the periods Lomb-Scargle periodogram for data with an uneven readings on the time axis was built (Smolentsev, 2010). The spectral densities were calculated using the spectral Bartlet window. Examples of Fourier and wavelet spectra are shown in Fig. 2 and Fig. 3.

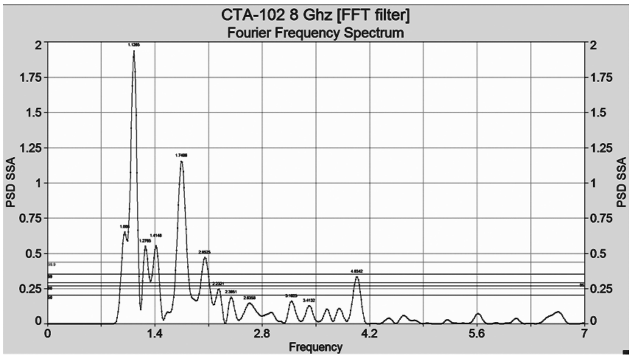

Figure 2: Periodogram for the source CTA102 at a frequency of 8 GHz.

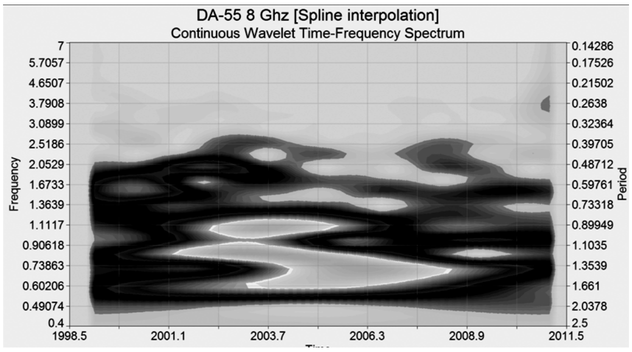

Figure 3: Continuous wavelet spectrum of the source of the «O – C» data for DA55, at 8 GHz.

WAVELET-analysis

Two-parameter analyzes function of one-dimensional wavelet transform is well localized in time and frequency. This distinguishes it from the ordinary Fourier analyzing function covers the entire time axis. Thus, it is possible to see the detailed structure of the process and the evolution of the harmonic components of the signal in time [4]. We used a continuous wavelet transform based on Morlet function. The example of the wavelet spectrum is shown in Fig. 4. On the wavelet spectra of the harmonic components of the signal are visible as bright spots, pulling in a strip along the time axis. The calculation of the integral wavelet spectra in the frequency range allows us to study the spectral variation of the signal power over time [3].

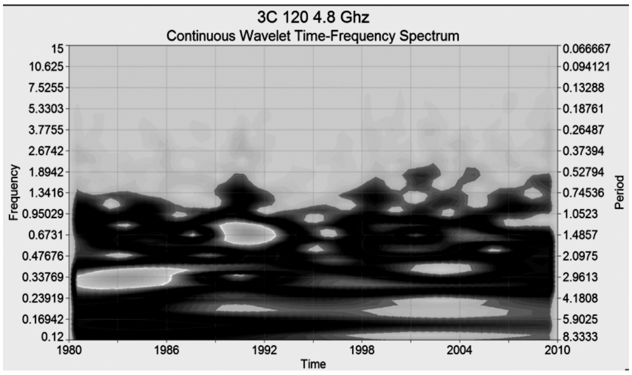

Figure 4: Continuous wavelet spectrum filtered series «O – C», for the source 3C120, at a frequency of 4.8 GHz.

Periods and phases of activity sources

3C120. The trend components.

The source 3C120 has a long-term 11 – 13-year-component at all frequencies. At 8 GHz found 24-year period. Phase of activity (bursts of spectral power) at the source 3C120 for the trend component observed at a frequency of 14.5 GHz – 1985, 1990 and 1998, at a frequency of 8 GHz – 1969 and 1974, at a frequency of 4.8 GHz -1990 and 1998 years.

Short periods (O – C). Periods about 2 and 5 years are also present at all frequencies. Similar values of periods 1.6 year (14.5 GHz), 1.3 year(8 GHz) and 1.6 year (4.8 GHz) may be a manifestation of the same process going on different frequencies. For the short-period component of this source activity phases were observed at a frequency of 14.5 GHz – 1990, 1992 and 1998, at a frequency of 8 GHz – 1990, 2004 and 2007, at a frequency of 4.8 GHz – 1990 year.

CTA102. The trend components.

The main period of the flux radio source is about 3 years. 2006 marked the largest phase of activity for the trend component at all frequencies.

Short periods (O – C). Source STA102 has components with periods 0.5 – 1 year. For the short-period component, activity phases were observed at a frequency of 14.5 GHz – in 2000, 2006 and 2009 years, at a frequency of 8 GHz – in 2009 and 2010 years , at a frequency of 4.8 GHz – in 2000.

DA55. The trend components.

There is long-period component of 6 – 8 years at all frequencies. For long-term component of the activity phases were of 14.5 GHz – in 2007 year, at a frequency of 8 GHz – 2004 and 2007 years, at a frequency of 4.8 GHz – in 2010.

Short periods (O – C). At all frequencies components 1 – 2 years and 3 years appear. Phase of activity for this components was observed at a frequency of 14.5 GHz – 1999, 2001, 2003 and 2010 years, at a frequency of 8 GHz – 2002, 2003 and 2005 years and at a frequency of 4.8 GHz – 2002 and 2010 years.

OJ287. The trend components.

At 8 and 14.5 GHz, the presence of 7 – to 8-year- long-period component. At frequencies of 4.8, 8 and 14.5 GHz 10 – 13-year component is shown. The peculiarity of this source in the presence of a trend at all frequencies. The period of this trend is likely to exceed 25 years.

Short periods (O – C). The source is the presence of 3-year component at frequencies 4.8, 8 and 22 GHz. At all frequencies the period of 1.6 to 1.1 years is changed. This change is the most evident in the frequency of 14.5 GHz. Phase of activity was at a frequency of 14.5 GHz – 1985 and 2010 years, at a frequency of 8 GHz – 1985 and 1989 years and at a frequency of 4.8 GHz – 1985 and 1989 years.

«Spectra periods»

For each year of observations graphics "spectra periods" were built to assess the contribution of individual periods in the activity of the radio source. In Fig. 5 shows an example of such a graph.

The use of a "spectrum of periods" allows comparisons with VLBI observations to determine the nature and dynamics of the processes in the jets.

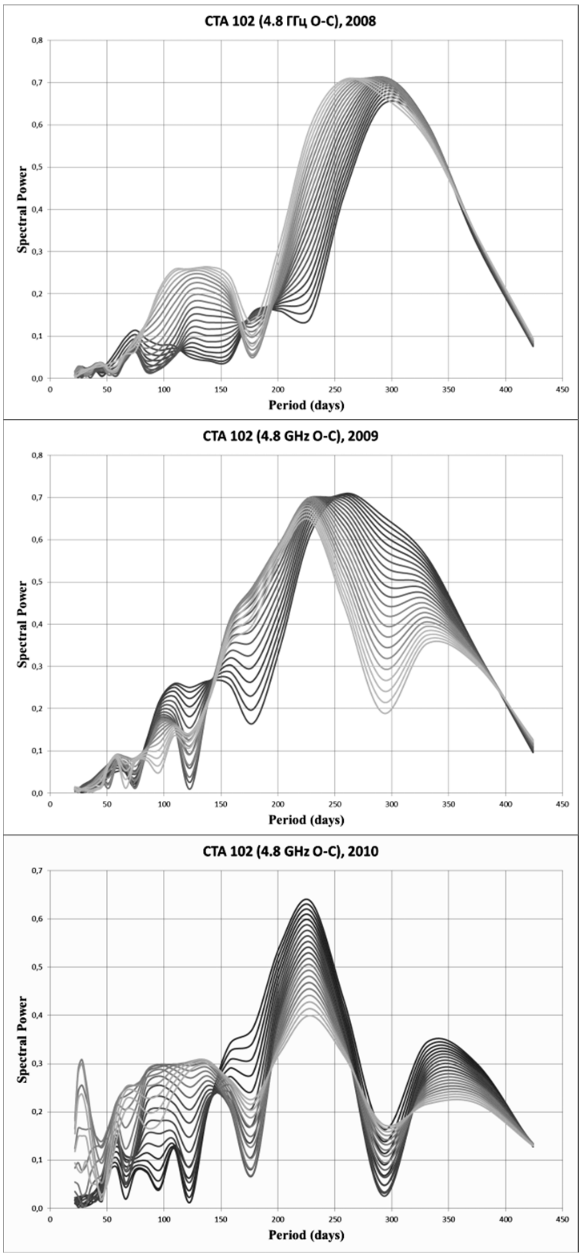

Figure 5: The graph shows the contributions of the individual periods in the activity of the radio source CTA 102 at a frequency of 4.8 GHz (O-C) for 2008–2010 years.

On the existence of quasi-stationary structures in the jets

In comparing the data on the availability of bright VLBI component in the jet being celebrated moving with time component and quasi-stationary structures bright knots occurring on the same distances from the cores. Such phenomena occur in sources with long jets 3C120 and CTA 102 (Fig. 6). Appearance of these nodes in the jets of brightness can be explained by a model of a standing backward wave.

Conclusions

Data processing based on wavelet analysis indicates the presence of a variable fluxes radio sources CTA102, 3C120, DA55 and OJ287 long-period and short components.

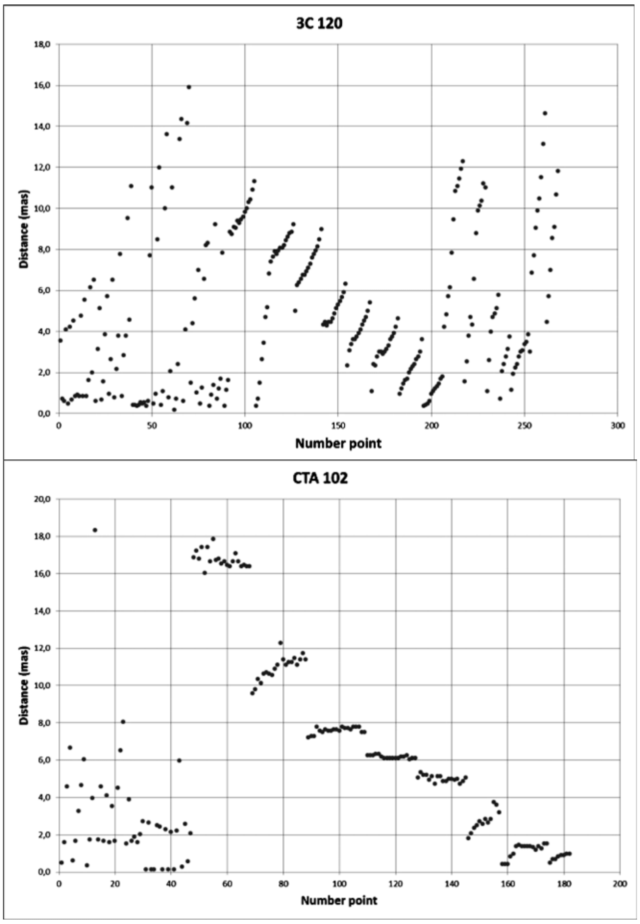

Figure 6: Quasi- stationary space structure of bright knots in the jet of 3C120 and CTA102.

Investigations the time of their existence, the main phases of activity and form the "spectra of periods." "The trend" component of the activity of radio fluxes formed by the long-term oscillations with a period in the range of 8 – 13 years or more. At the coincidence of the maxima of the trend component with maximum short-change flux with periods ranging from fractions to 3-year phase of the observed increased activity system «core- disk-jet». For each year of sources observations in all studied frequencies defined "spectra periods" determined by the contribution of the core and the jet activity. VLBI data show that the sources of 3C120 and STA102 with the activity of the cores are periodically increased flow from the jet. For sources DA55 and OJ287 core activity almost always prevails over the jet activity. In the VLBI data registration bright knots occur on the same distances from the core. This quasi-stationary structures found in jets from sources 3C120 and CTA 102.

References

Aller H.D., Aller M.F., Latimer G.E., Hodge P.E.: 1985, *ApJS*, **59**, 51.

Gaydyshev I.: 2001, Analysis and data processing (the special directory), St.Petersburg Publishing house.

Smolentsev N.: 2010, Veyvlet-analiz in MATLAB, DMK-Press.

RADIO VARIABILITY OF THE QUASAR 3C 273 ON THE CENTIMETRIC WAVES -WAVELET-ANALYSIS

Ryabov M. I. [1], SukharevA.L. [1], Sych R.A. [2]

[1] Odessa observatory "URAN-4" of the Radio-astronomical institute NAS Ukraine.
[2] Institute of solar and terrestrial physics, Siberian office Russian Academy of Sciences.
Aller M. F. Radio observatory of Michigan university, Ann Arbor, USA.

ABSTRACT. 3C 273– has been intensively investigated for many years, since opening of quasars in 1963. Since 1965 on radio telescope RT-26 of Michigan University on frequencies 14.5, 8 and 4.8 GHz long monitoring of this radio source have been carried out. Flux variability of a radio emission on studied frequencies consists a trend on which fast flux changes with characteristic time from 1 to 5 years are imposed. Fourier's methods and the wavelet-analysis that allowed investigating in details changes harmonious component of signals over time are applied. On a trend component the main period makes 8 years. With Fourier filtration have been received «O – C» data, for allocation high-frequency component in studied signals. By the results of calculations of wavelet-spectrums the periods of 3.5 and 2.3 years are revealed. On the basis of calculation of integrated wavelet-spectrums in a frequency range on «O – C» this «spectrum of the periods» characterizing main phases of activity of a source are defined. On the basis of the program written on IDL, supplementing the wavelet-analysis, delay change between fluxes on separate studied frequencies for each of periodic components has been defined eventually. The average delay for the 8 years periodic component in the range of frequencies of 4.8-8 GHz is about 1 year. In the range of frequencies 8 – to 14.5 GHz the average size of a delay was about 0.5 years. The average delay for all intervals of frequencies for the 3 years periodic components has appeared equal 0.3 years.

Introduction

3C273 – is the brightest quasar. It was opened in 1959. Main characteristics: red shift of Z ~ 0.16, visible magnitude V ~ 13, distance to object ~ 735 Mpc, mass of the central object of m ~ 886 million M_{SUN}, the linear extent of jet makes ~ 62 Kpc, the visible size – 23 ”. Luminosity of the object changes in all a wave band from radio waves to range scale within about several days or ten days. Observation on VLBI has revealed own movements of some component in jet of 3C273 [1].

Data processing

On the basis of the carried-out daily observations average values in 7 days with a non-uniform grid of counting are defined. According to the histogram of distribution of time intervals between counting the interpolation interval in 0.02 years (7,3 days) has been chosen. With using a polynomial moving average (half width an interval of 5 points) reduction of noise has been reached and random emissions have been removed [2]. By means of trigonometrical interpolation data have been provided to an even step on time. The initial schedule with the combined frequencies is presented on fig. 1. The allocation of short periodic components of signals, which were imperceptible against the main period, has been carried out by Fourier filtration «O – C» [3].

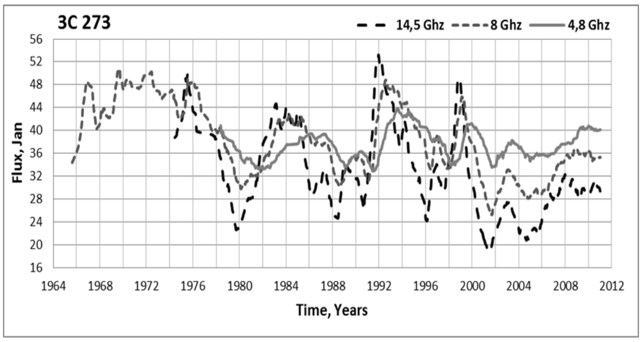

Figure 1: Monitoring of flux density quasar 3C 273 on 14.5, 8, 4.8 GHz.

FOURIER-analysis

For determination of values of the periods calculated Lomb-Scargle periodogram for data with non-uniformly located counting on time [4]. Frequencies with big spectral density, i.e. the frequency areas consisting of many close frequencies which make the greatest contribution to periodic behavior of all rows, were calculated with use of a Bartlett spectral window. Examples of Fourier and wavelet spectra are given on fig. 2 – 3. On all frequencies the most powerful period is close to 8 years. For «O – C» data the most appreciable periods with the values close by 2 and 3 years are found.

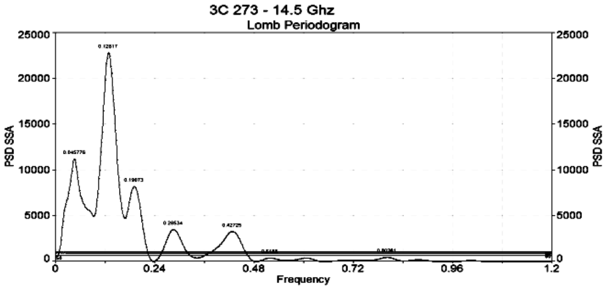

Figure 2: Periodogram for frequency of 14.5 GHz.

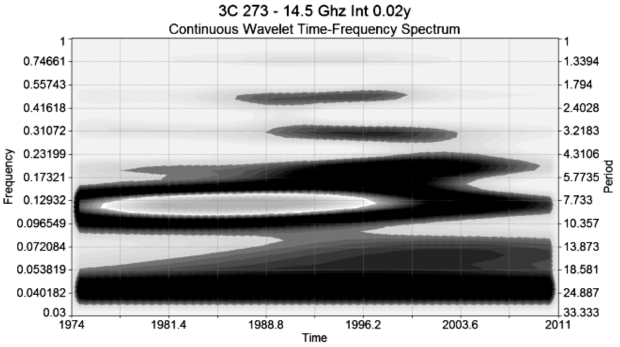

Figure 3: A continuous wavelet-spectrum of the initial smoothed data, frequency of 14.5 GHz.

WAVELET-analysis

Two-parametrical analyzing function of one-dimensional wavelet-transformation is well localized both in time and on frequency. That is distinguished from Fourier's usually applied transformation which analyzing function covers all time base. Thus it is possible to see detailed structure of process and evolution of a harmonious signal component in time [5]. Continuous wavelet-transformation on the basis of function Morlet was used. The example of a wavelet-spectrum is given on fig. 4. On wavelet-spectra harmonious components of a signal are visible in the form of the bright spots which are extending in strips along an axis of time.

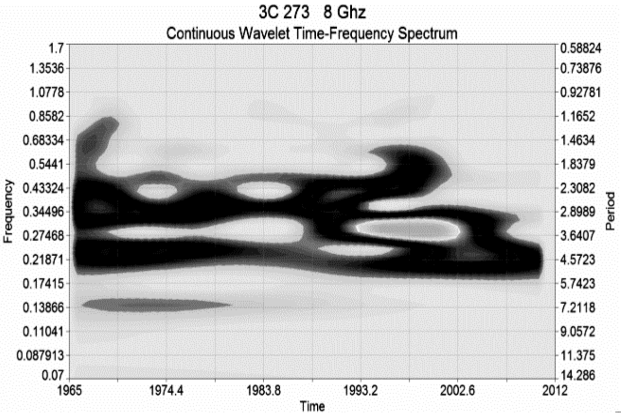

Figure 4: A continuous wavelet-spectrum for the filtered data «O – C», frequency of 8 GHz.

The analysis of ranges has shown existence in studied signals 8 years periods, and also the 3and 2 years periods, shorter periods with values are allocated about a year uncertainly and specification demand. Short time 2-3 years harmonicas are shown not on all length of a signal, and on its separate sites. Calculation of integrated wavelet-spectra in a frequency range for the filtered data has allowed studying change of spectral capacity of signals eventually. Activity phases (splashes in spectral power) were noted on frequency of 14.5 GHz – 1991.15, 1998.71 years; on frequency of 8 GHz – 1967.34, 1976.51, 1991.37, 1998.90; on frequency of 4.8 GHz – 1980.44, 1991.07, 1999.40. For each maximum on a global spectrum were constructed graphs of « spectrum of the periods», allowing to estimate a contribution of the separate periods to phases of activity of a radio source. On fig. 5 it is set an example such plot.

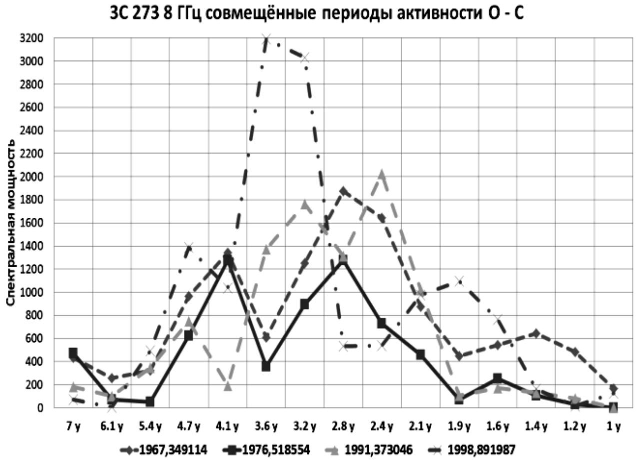

Fig. 5. On graphics contribution to of the separate periods to phases of activity of a radio source on frequency of 8 GHz are shown. For example, in a phase of activity of 1998.9 the most powerful period was of 3.6 years.

Use of «specter of the periods» allows to carry out comparison to data of VLBI observations and to define nature of dynamics of processes in jets. On the basis of the revealed regularities, it is possible to extend them to the entire period of the observation when sessions of VLBI of measurements were not.

Time delay between frequencies

For definition of delays between signals on different frequencies, calculation of direct and return wavelet-transformation was used [6]. This procedure is necessary for allocation of narrow-band signals of the found harmonicas and their comparison. Value of the strip wavelet-filter was fixed close ~ 3 and 8 years. The width of a window of the periods made 2 years. The capacity of fluctuations is non-uniformly distributed throughout the period of observation, there is their strengthening and the subsequent attenuation. For the period of 8 years this interval is in a range of 1979-2002, for the 3 years period

– in a range of 1986-2002. Then the time differences were found maximum and minimum of flux density for different spectral components. Values of positive half-cycles are designated by a dagger, negative are designated by a circle. On fig. 6 and 7 schedules of delays between frequencies for two allocated harmonicas are shown.

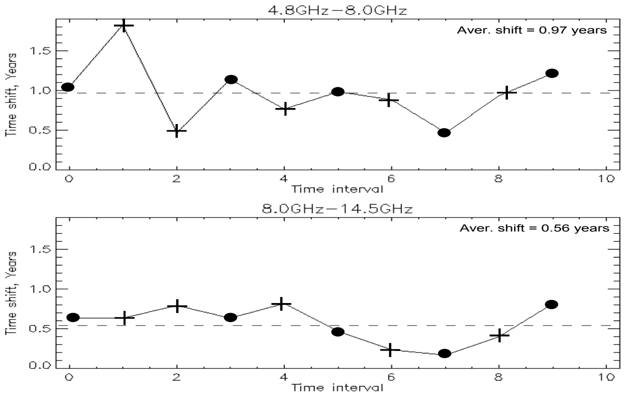

Figure 6: Delays between frequencies for a 8 years' period

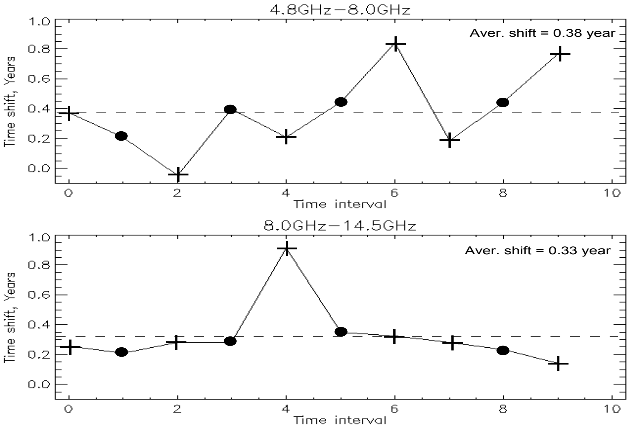

Figure 7: Delays between frequencies for a 3 years period

Conclusions

In this work, with using of a method of the wavelet-analysis existence of the 8 years' period on all studied frequencies that will be is consistent with results of other researches is defined. Fourier filtration method has allocated fast-variable components of signals with the periods of 3.5 and 2.3 years. Duration of the 3 years' period on frequency 14.5 GHz – 14.7 years, 8 GHz – 12.5 years, 4.8 GHz – 16.3 years. At a 8 years duration of manifestation on frequency 14.5 GHz – 14.3 years, 8 GHz – 15 years, 4.8 GHz – 13 years. On frequencies of 14.5 GHz and 8 GHz, probably, the period close to 5 years exist. Construct integrated wavelet-spectra in a frequency range for data «O – C». Activity phases of a source on frequency of 14.5 GHz are constructed – were shown in 1991.15, 1998.71 years. On frequency of 8 GHz in 1967.34, 1976.51, 1991.37, 1998.90 years. On frequency of 4.8 GHz – 1980.44, 1991.07, 1999.40 years. For each maximum on a global spectrum the schedules which allow to estimate a contribution of the separate periods to phases of activity of a radio source are constructed. The received results of delays between various frequencies of radio emission in a source 3C273 for the various periods allow to carry out further the detailed analysis of their physical reasons. For "trend" components with the period ~ time shift on frequencies in the range of 8 – 14.5 GHz twice are less than 8 years, than on lower frequencies (an interval of 4.8-8 GHz). Delays of high-frequency fluctuations do not show about 3 years change with frequency of generation. The average delay for the 8 year components in a range of 4.8-8 GHz is equal to 1 year, in a range 8 – 14.5 GHz a delay is about 0.5 years. An average delay for the 3 years components in all range of frequencies about 0.3 years. Long time changes of a radio flux 3C273 can be connected with quasiperiodic changes of rate of an accretion on a core [6]. 2 and the 3-year periods can be described by model of a shock wave in jet [7]. Variability models on the basis of a magnetic dynamo also well describe emergence of the short periods [8].

References

1. UchiyamaYa., Urry C.M., Cheung C.C., Jester S., Van Duyne J.: *Astrophys. J.*, **648** (2), 910.
2. Gaydyshev I. *Analysis and data processing* (the special directory), St. Petersburg Publishing house, 2001.
3. Davidov A.V. *Digital processing of signals: Thematic lectures*, Yekaterinburg: UGGU, IGIG, geoinformatics chair, 2007.
4. Vityazev V.V. *Analysis of non-uniform temporary ranks*, Publishing house of the St. Petersburg university, 2001.
5. Smolentsev N. *Veyvlet-analiz in MATLAB*, DMK-Press, 2010.
6. *Active kernels and star cosmogony* / Ed. Martynov. Publishing house of the Moscow university, 1987.
7. Marsher A.P.: 2006, in *confer. works: Astronomy 2006: traditions, present and future*, St.Petersburg State University.
8. Meyer F., Meyer-Hofmeister E. *The effect of disk magnetic fields on the truncation of geometrically thin disks in AGN.*

DATA PROCESSING CENTER FOR RADIOSTRON PROJECT

Shatskaya M.V.[1], Guirin I.A.[1], Isaev E.A.[2,3], Kostenko V.I.[1], Likhachev S.F.[1], Pimakov A.S.[1],
Seliverstov S.I.[1], Fedorov N.A.[1]

[1] Astro Space Center LPI, Moscow, Russia, mshatsk@asc.rssi.ru
[2] Pushchino Radio Astronomy Observatory ASC LPI, Pushchino, Russia, is@itaec.ru
[3] National research university Higher school of economics, Moscow, Russia,

ABSTRACT. Radioastron is the international project led by the Astro Space Center of Lebedev Phisical Institute. Moscow, Russian Federation. 10 m Space Radio Telescope is the main payload of Spektr-R spacecraft. It's designed by Lavochkin Association of Roscosmos Russia State Agency. The project goal is to create together with a ground based radio telescopes the huge Ground to Space interferometer with a baseline up to 350 km, to obtain images, positions and movements of various objects in the Universe with extremely high angular resolution (about 10e–6 arcsec). After successful launch on 18 July, 2012 the Radioastron missions starts systematic investigations of the Universe at broad radio frequencies range.

DATA PROCESSING CENTER is a fail safe complex centralized system of interconnected software and hardware components, and organizational procedures, which is designed for reliable data storage and processing, delivery of services and applications, and this system possessed a high degree of virtualization of its resources. The main tasks performed by SDPC: effective realization of data acquisition and storage in a specialized data repository for a preset time with given reliability; delivery of applied services to users; and data processing on high performance computer complex.

The complex includes: control unit, computer cluster, data repository with a capacity of 200 TB, backup system on magnetic tapes (200 TB), 24 TB redundant storage system in the Pushchino Radio Astronomy Observatory, Astro Space Center of Lebedev Physical Institute in Pushchino, Web and FTP servers, networks of management and data transmission.

Let us consider each component of the computer complex in more detail.

The cluster (the main component of the complex) is a group of computers connected with high speed communication channels. From the standpoint of users it is an integrated hardware resource. The computer cluster presented in this paper includes one control and ten computing servers assembled in a common rack. Processing power of created computer cluster according to Linpack was found to be equal to 1000 Gflop/s.

The storage system consists of primary storage systems on 200 TB HDD plus 200 TB backup system. The first step for ensuring high availability is to protect the most important part of the system, namely, the data. Storage reliability is achieved by using RAID6 similar to RAID5, but having a higher degree of reliability: 2 disk capacity is allocated for check sums, double sums are calculated using different algorithms. This method suggests the use of disk arrays available to users as a single logical disk. The disk array has additional capacity providing for the ability of restoring the data in case of sudden failures.

In the case of failure of any component of the computer complex or its disconnection, a 24_TB data storage system organized in Pushchino can make backup in order to prevent data losses.

For prompt data exchange with backup data storage unit an independent direct communications channel with 1 GB/s speed was created between the Pushchino Radio Astronomy Observatory of Lebedev Physical Institute and Moscow Astro Space Center.

The information into the Processing Center comes via the Internet. From places, where there are no high speed communication channels, delivery of data on hard disks is possible.

The structure and functions of ASC Data Processing Center are fully adequate to the data processing requirements of the Radioastron Mission and has been successfully confirmed during Fringe Search and Early Science Program in flight operations.

References

Esepkina N.A., Korol'kov D.V., Pariiskii Yu.N., Radioteleskopy i radiometry (Radio Telescopes and Radiometers), Moscow: Nauka, 1973.

Thompson A.R., Moran J.M., Svenson G.W., Interferometry and Synthesis in Radio Astronomy, New York: John Wiley & Sons, 1990. Translated under the title Interferometriya i sintez v radioastronomii, Moscow: Fizmatlit, 2003.

Morimoto R., Noel M., Droubi O., Mistri R., Amaris C., Microsoft Windows Server 2008 Unleashed. Translated by OOO I.D. Williams, Moscow, 2009.

SUN, SOLAR SYSTEM AND ASTROBIOLOGY

DYNAMIC CHARACTERISTICS OF THE MAIN INDEXES OF SPACE WEATHER AND THEIR APPLICATION TO THE ANALYSIS MONITORING OBSERVATIONS FLUX DENSITIES OF POWER RADIO SOURCES ON RT «URAN-4»

L.Guglya [1], M.Ryabov [2], S.Panishko[3], A.Suharev [4]

Radioastronomical Institute of National Academy of Sciences of Ukraine
Odessa, Ukraine
[1] guglya_lubov@mail.ru, [2] ryabov-uran@ukr.net, [4] magister_phys@yahoo.com

ABSTRACT. On radio telescope "URAN-4" of the Odessa observatory of Radio-astronomical Institute during twenty five years (since 1987 till present) monitoring of power galactic and extragalactic radio sources on frequencies 25 and 20MHz has been carried out. Data of the observation was spent in a current of the 22-23th cycles of solar activity and in the beginning of the 24th cycle. Long-term variations density fluxes of radio sources connection with change of a condition of ionosphere in a cycle of solar activity are considered. Means Fourier and Wavelet analysis determine dynamics of changes of the main indexes of space weather and the basic periods of activity are revealed. The obtained data will be used for interpretation of the observation changes flux of radio sources for during all investigated cycle of activity and periods of extreme developments of space weather.

Introduction

The program monitoring fluxes of power galactic and extragalactic sources on radio telescope «URAN-4» began in 1987.. The monitoring program includes investigation variation flux densities cosmic radio sources: Cas A (3C461), Virgo A (3C274), Taurus A (3C144) and Cygnus A (3C405). Observations of variation flux densities were conducted in directs ± 2 hours before and after the culmination of sources. In these directions the method is supplied at high values of the effective area the antenna of the radio telescope. The propagation time of radio sources 3C144, 3C274, 3C405 through the directional antenna beam made 40 minutes, for a radio source 3C461 – 60 minutes. As a whole the every day's general time of diurnal monitoring exceeded 13 hours. Processes in the upper atmosphere of the Earth it were investigated determined by a method «examine» radiation by a radio source. As a result of observations essential variations in level of radiation sources flow are marked. These changes are called by the phenomena and processes which characterize solar and geomagnetic activity. Thus, investigating data received as a result of monitoring of radio sources fluxes can be determined a degree and character of space weather influence on the upper atmosphere of the Earth.

Observational data

Results of data processing of observations cosmic of radio sources 3C144, 3C274, 3C405, 3C461 on frequency 25MGz, during the period from 1998 to 2005 are considered. In Figure 1 variations of level of a radiation source flux 3C461 in November, 2003, in the high level solar and geomagnetic activity are presented.

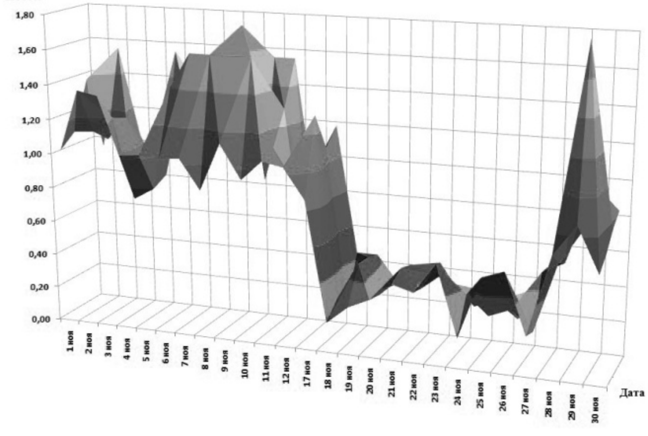

Figure 1: Variations flux densities of a radio source 3C461 on 25 MHz (November, 2003)

During the period of activity which began on November 17th. This day registration long time decrease level flux dencites of a radio source 3C461. In this period on the Sun there were 8 flares; the most high-power is M1.2 and M4.2 on X-ray scale classifications. On November 18th on the Sun disk there were 9 flares with the maximum M3.2, M3.9 and M4.5. The most geoeffective flare occurred on November, 18th which was accompanied by M3.2 and M3.9. The given flare created a large magnetic storm. Impulsive flare M1.7 was observed on November, 19th. On November, 20th the activity period has been continued by flares M9.6/2b and M5.8. From 21 to 23 November were marked flares B9.2, B8.8, C4.3 All these active events became the cause of long decrease flux densities radio sources in interval 17-27 November 2003.

Analyzing long-term variations of radio sources fluxes it is possible to track influence 11-th cycle of solar activity and the local periods by extreme developments of space weather (Fig. 2).

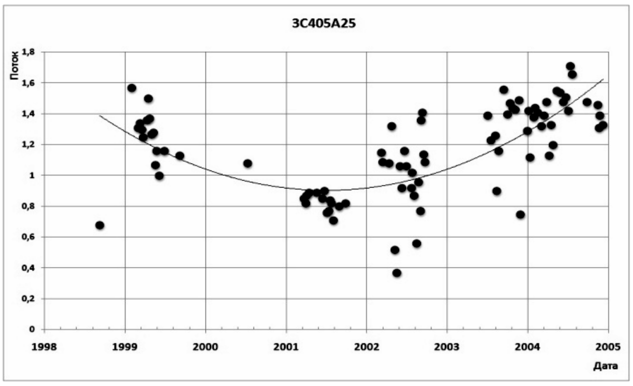

Figure 2: Variations of a radiation source flow 3C461 And 25MHz (November, 2003)

Fourier and Wavelet analysis

For definition of dynamics of changes of the basic indexes of space weather have been conducted them Fourier and Wavelet analysis. Were thus used Ap-index (Ap index characterizing a condition of geomagnetic activity) and F10.7 (Flux of a solar radio emission on a wavelength of 10.7 cm).

To calculation of the basic periods of indexes change of space weather the Fourier analysis has been applied. The analysis was conducted separately for each year of the 23rd cycle of Solar activity therefore 5 leading periods have been recorded in tables 1 and 2, for indexes F-10.6 and Ap, accordingly.

Table 1: The most significant periods of a solar radio emission on a wave of 10.7 sm (days)

1996	1997	1998	1999	2000	2001	2002	2003	2004	2005	2006	2007
183.0	13.5	8.9	182.0	366.0	182.0	364.0	21.4	13.6	8.9	6.7	26.0
30.5	15.2	19.2	28.0	16.6	8.9	182.0	91.0	26.1	9.1	28.0	9.1
26.1	9.3	364.0	6.5	13.1	5.8	121.3	13.5	61.0	60.7	9.1	30.3
13.1	12.6	24.3	8.5	8.9	14.0	91.0	19.5	18.3	121.	4.9	5.3
14.1	182.0	5.3	22.8	4.6	9.6	72.8	10.4	15.3	364.0	4.4	6.9

Table 2: The Most significant periods of Ap – index (days)

1996	1997	1998	1999	2000	2001	2002	2003	2004	2005	2006	2007
26.1	28.0	364.0	26.0	61.0	40.4	182.0	60.7	30.5	28.0	72.8	182.0
183.0	26.0	182.0	121.3	26.1	52.0	91.0	30.3	61.0	30.3	7.9	364.0
15.9	36.4	121.3	182.0	183.0	121.3	19.2	14.0	26.1	24.7	6.2	121.3
122.0	40.4	91.0	18.2	28.2	15.2	22.8	15.6	36.6	14.0	8.5	30.3
366.0	24.3	72.8	28.0	73.2	20.2	72.8	364.0	28.2	45.5	6.5	26.0

Thus as much as possible significant there were such periods variability of indexes :

F10.7 – 182 days, 28 days.

Ap – : 182 days, 26 days, 14 days, 8 days.

To data retrieval about spectral-space characteristics of a signal on all temporary number it was applied Wavelet the analysis. Wavelet the analysis supplies obtaining of data on presence of the basic periods and time of their existence.

As a result of such analysis time-and-frequency Wavelet a spectrum of energy density distribution has been constructed (Fig. 3).

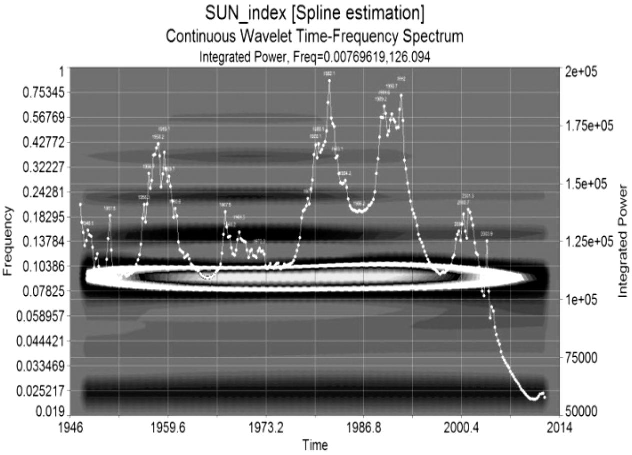

Figure 3: Time-and-frequency Wavelet spectrum of energy density distribution (f10.7)

On this spectrum the 11th year-old period which is the most intensive is essentially allocated. For a trend exception, has been calculated time-and-frequency Wavelet a spectrum for data with the filtered eleven-year period (figure 4). As a result of such analysis maxima of spectral activity. The following stage began to track, what basic periods make them. In figure 5 are shown 3 basic spectral maxima of the 23rd cycle of solar activity. The given maxima are formed by the long-period processes, corresponding to the periods: 575 days, 370 days.

The same procedure has been conducted for the Ap geomagnetic index. At the first stage the time-and-frequency spectrum for an initial number of data (figure 6) has been constructed, and then the basic period present on all time intervals about 5 years (figure 7) has been subtracted. Thus, long-period processes (the periods – 627 days and 374 days) and short-period processes (the periods – 53 days, 19 days and 13 days), shown on figure 8 have been determined.

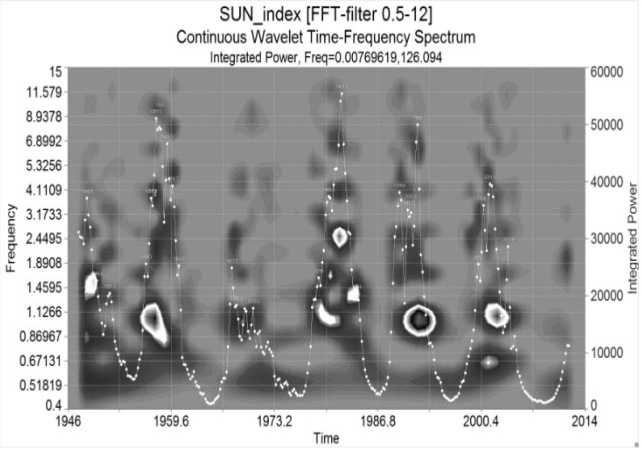

Figure 4: Time-and-frequency Wavelet spectrum of energy density distribution with a deduction of the 11th year period (F10.7)

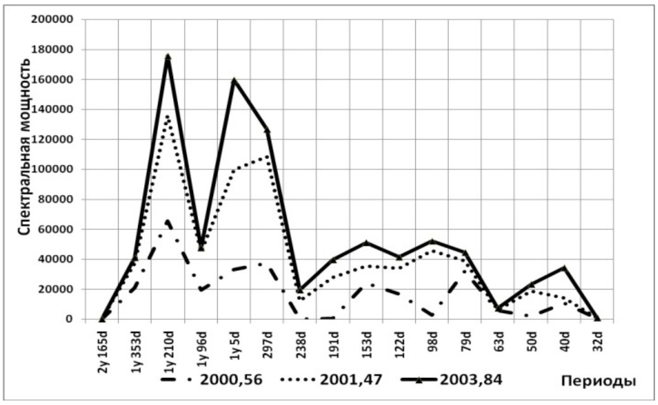

Figure 5: Spectrum of periods index F10.6

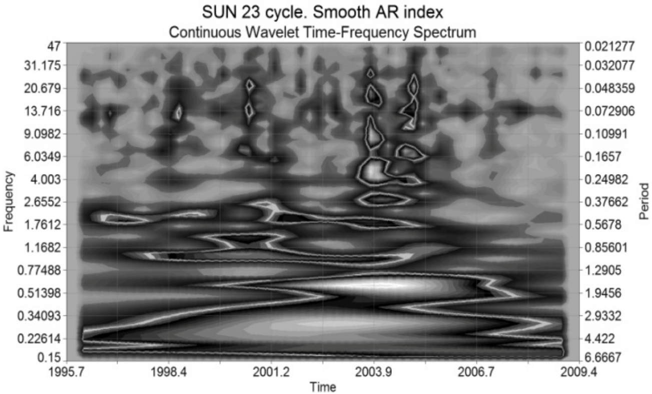

Figure 6: Time-and-frequency Wavelet spectrum of energy density distribution (Ap- index)

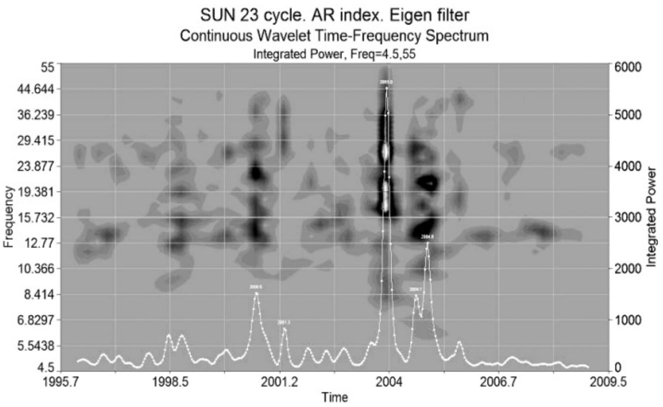

Figure 7: Time-and-frequency Wavelet spectrum of energy density distribution (Ap-index)

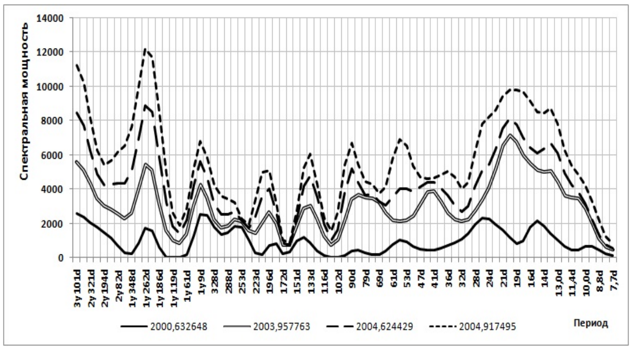

Figure 8: Basic spectral maxima of an Ap-index

Conclusions

1. While using the monitoring of flux densities power cosmic sources observations on radio telescope "URAN-4" allows to "examine" all upper atmosphere of the Earth and determines integrated effect of exhibiting solar and geomagnetic activity. The same results cannot be received by means of land radio physical and radar methods.

2. On results of construction Fourier of spectra the basic periods on each year the 23th cycles have been revealed.

For index F 10.7 the periods – 182 days and 28 days are received. For Ap-index – 182 days, 26 days, 14 days, 8 days.

3. By means of application of Wavelet analysis a detailed information on the periods, making the most intensive phases of activity have been received more.

For index F 10.6 the periods are found out: 575 days, 370 days. For Ap-index: 627 days, 374 days (long-period processes) and 53 days, 19 days, 13 days (short-period processes).

THE INVESTIGATION OF THE STRUCTURE OF THE SIGNAL OF GEOPHYSICAL AND ASTROPHYSICAL ORIGIN IN THE ELECTROMAGNETIC FIELD OF THE ATMOSPHERE BOUNDARY SURFACE LAYER

L. Grunskaya, V. Isakevich, V. Yefimov, A. Zakirov, D. Rubay, I. Leshchev

Vladimir State University
Vladimir, Russia
grunsk@vlsu.ru

ABSTRACT. There has been developed a program – analytical system for investigation the structure of the signal in the spectral and time ranges caused by geophysical processes. The main purpose of developing such system is – to investigate the structure of the signal in the spectral and time ranges, caused by geophysical and astrophysical magnetic field of the atmosphere boundary surface layer and to find under – noise periodical processes of geophysical nature. The analysis of the exposing efficiency in the time ranges of the components corresponding to the periods of the moon gravitational tides showed high efficiency of the eigen vectors, chosen according to the criterion MKK which provides very slight probably of the false alarm of omitting displayed signs at the level 10^{-4}.

Key words: an electrical field, a program – analytical system, moon tides.

Introduction

The main aim of the given investigation is connected with estimation of the mean value of the intensity amplitude of the electrical field vertical component of the atmosphere boundary surface layer at the frequencies of the moon tides. The task is done with methods of spectral estimation using great time series (years of continuous records) [1-6]. The main task of these investigations is a true discovering an effect of the moon tides on the electrical field of the atmosphere boundary surface layer.

The investigations are based on the experimental data of the ground of Vladimir State University and also of a number of stations which are provided with receiving and registration devices, developed in VSU. [7-8]

The results of the analysis of the possibilities of the spectral method of the investigations, including ones with an optimal recorder which allows to estimate the amplitude of the chosen spectral component, mean that the signal – to – noise ratio at the frequencies of moon tides is not enough for a true estimation of the influence of moon tides on the electrical field of the boundary surface layer.

To raise discovering of reliability of moon tides in the electrical field of the atmosphere boundary surface layer there has been developed a program analytical system of investigating the structure of signals in the spectral and time ranges caused by tide processes. The main purpose of such system is to investigate the structures of the signals in the spectral and time ranges, caused by tide processes in the electrical field of the atmosphere boundary surface layer. Using the method of eigen vectors can raise considerably the selectivity of any known analysis method (a spectral one as well) because the latter ones will be used not to the whole time series but to its independent components, time series but to its independent components, including those which have no power dominating (moon tides). It is shown an efficiency of using eigen vectors of the covariance matrix for exposing complex periodical components of the time series including the case when such components have no power dominating in the time series (moon tides).

Program – analytical system for investigating the structures of the signals caused by moon tides in spectral and time ranges

To investigate time series of natural phenomena both the method of spectral analysis and the methods, based on the appearance of the signals in the bases of eigen vectors of the covariance matrix, are widely used. [9-11] Eigen matrix are completely determined with the covariance matrix of the time series and the analysis interval chosen by an investigator. Eigen vectors forms an orthorated basis and each of basis vectors forms its own properties of the investigated nature object. The analysis of the situation defines the thing that if the nature has some distinctive properties, they must be shown by the definite group of the basis vectors. As the basis of the eigen vectors is determined by the time series itself during the investigation but not by an investigators “arbitrariness”, there is some hope for the thing that in the eigen vectors there will be expressed the properties of the investigated objects “by themselves”.

Each of eigen vectors brings its own power contribution into the analyzed time series, which is determinate by the ratio of the eigen value of this vector to the sum of all the eigen values. So analyzing the structures of eigen, having the information about typical nature phenomena allows to reveal features of these typical phenomena without any dependence on the power contribution of the specific eigen vector into the investigated time series.

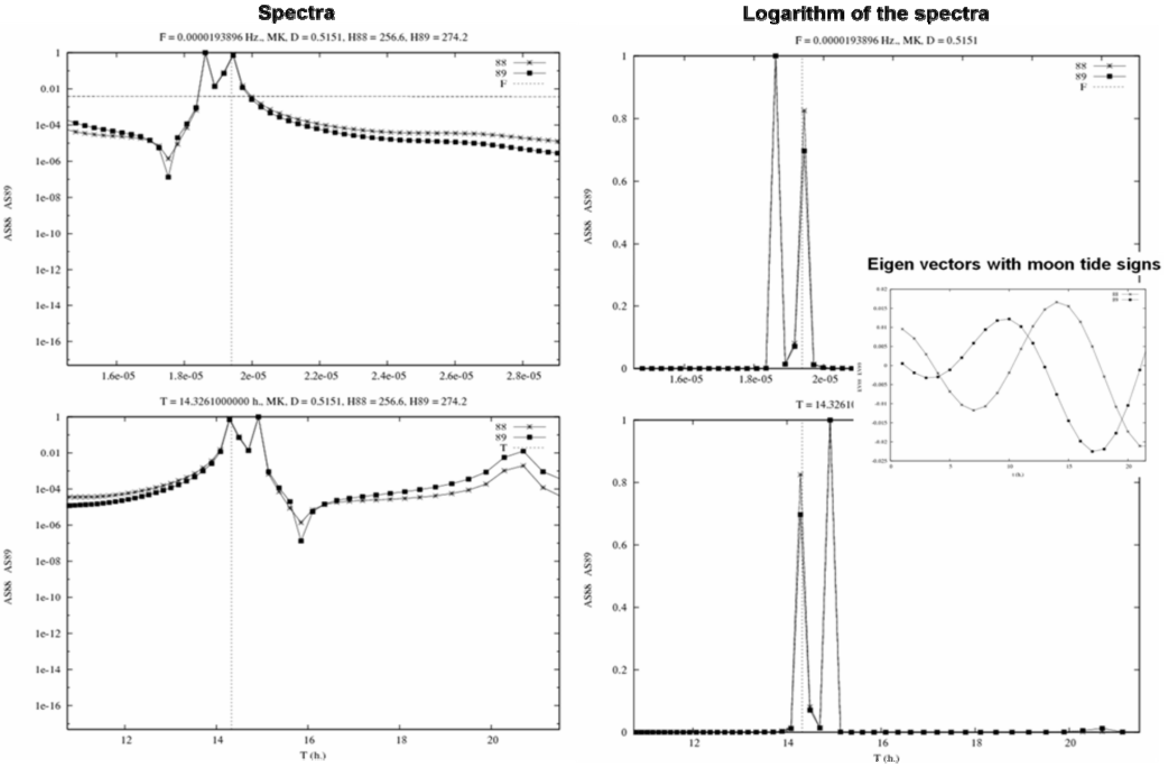

Figure 1: Amplitide spectra of eigen vectors, chosen according to the criteria of maximum correlation coefficient with a harmonic signal of tide frequency 2N2. Component Ez of the electrical field, VSU, 2003-2010

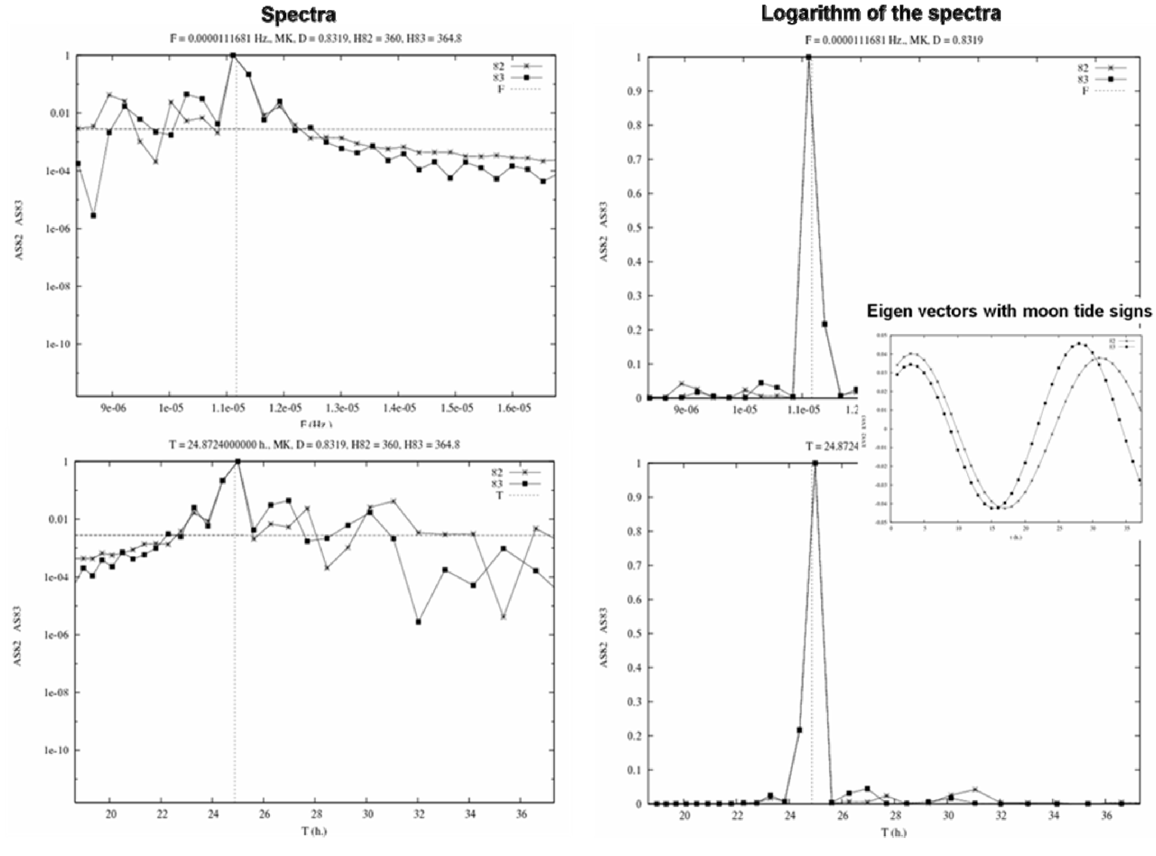

Figure 2: Amplitide spectra of eigen vectors, chosen according to the criteria of maximum correlation coefficient with a harmonic signal of tide frequency M1. Component Ez of the electrical field, Voeikovo, 1966-1995

The use of the method of eigen vectors doesn't eliminate using spectral analysis or some other methods, but they are used bearing no relation to the initial time series but in conformity with eigen vectors which are independent of each other each of them has its own conformation. Thus, using the method of eigen vectors can raise considerably the selectivity of any known method of analysis (including a spectral one) because the latter ones will be used not to the whole time series but to its independent components including to those ones which have no power dominating and they represent a "thin" structure of time

The example of the results received as result of the analysis of the time series with the purpose of discovering influence of moon tides on the electromagnetic field of the atmosphere boundary surface layer with PAK are shown at figures 1, 2.

The correlation coefficient (a median value) between the chosen CB and displaced sinusoid for component E2 for moon tides for the station with monitoring for dozens of years (Voyeikovo, Verhnyaya Dubrova, Dushety) is 0,78. For the stations with monitoring for a few years (VSU ground, Baikal, Obninsk) the median value of the correlation coefficient is 0,535. The signal - to - noise ratio (the ratio of the maximum value of the amplitude spectrum) at the closen eigen vectors to it's mean value for component E2 for the stations with long time monitoring (Voyeikovo, Verhnyaya Dubrova, Dushety) is mean 267 and for the stations of VSU ground, Baikal and Obninsk is mean 179.

Conclusion

There has been developed a program – analytical system to investigate the structures of the signal in the spectral and time series caused by geophysical processes. The main purpose of the development of such system is to investigate the structures of the signals in the spectral and time series caused by geophysical processes in the electrical field of the atmosphere boundary surface layer.

The novelty of the developed method consists in the thing that the initial time series itself is not subjected to spectral analysis but its eigen vectors are, to which the time series is distributed which allows to use spectral analysis to some non-correlated components of the time series connected with the definite physical processes.

When exposing frequencies coinciding with the frequencies of tides the final frequencies coinciding with the frequencies of tides the final frequency of the coincidences of the tides the final frequency of the coincidences of the amplitude spectrum maxima of the chosen eigen vectors of the electrical and geomagnetic fields with the frequencies of tides was 99 per cent.

The work was done with supporting by Programme RNPVCH №2.1.1/11281, FCP №16.740.11.0185, FCP №14.740.11.0407, Grant PFFI №09-05-99015-pofi.

References

Grunskaya L.V. Electromagnetism of boundary surface layer and its interconnection with geophysical and astrophysical processes: a monography / L.V.Grunskaya – Vladimir: Posad, 2003 – 103 p.

Grunskaya L.V. Experimental and theoretical investigations of variations of electric intensity, caused by solar and moon tides in the atmosphere boundary surface layer. / L.V.Grunskaya, V.N.Morozov // Proceedings of High Schools. Physics. – 2005-№8-p.33-39.

Grunskaya L.V., Morozov V.N. Moon and solar tides in the Earth atmosphere electrical field. The article in the magazine "Proceeding of High Schools" series of Physies, 2003, №12, p. 71-77.

Grunskaya L.V. Moon tides in the electrical field of the atmosphere boundary surface layer // L.V.Grunskaya, V.N.Morozov, V.A.Yefimov, A.A.Zakirov // Proceedings of High Schools. Physics. 2010. – v.53, №1, p. 22-27.

Grunskaya L.V. Spectral analysis of the vertical component of electrical intensity of the atmosphere boundary surface layer at the frequencies of the thermal and moon tides according to the spaced apart stations / L.V.Grunskaya, A.A.Zakirov, V.A.Yefimov, L.T.Sushkova // Biomedical radioelectronics – 2010 - №7, p. 18 – 23.

Grunskaya L.V. Estimation of the parameters of the electrical field of the atmosphere boundary surface layer on the basis of the correlative reception method. // A Monography Vladimir – Vladimir State University – ISBN 978-5-9984-0054-04-2010-123p.

Grunskaya L.V. Receiving and registrated equipment for investigation of interconnection of the electrical field of the atmosphere boundary surface layer with geophycical processes / L.V.Grunskaya, V.A.Yefimov // Projecting and technology of electronical devices / 2006 - №1, p. 63 – 68.

Grunskaya L.V. A mobile receiving and registrating system for monitoring electromagnetic field of the atmosphere boundary surface layer / L.V.Grunskaya // Projecting and Technology of electronical devices. – 2005 - №2, p.69-74.

Isakevich V.V. Functional models of purposeful searching of features of nature phenomena in the eigen vectors of covariance matrix of time series / V.V.Isakevich, L.V.Grunskaya, D.V.Isakevich, L.T.Sushkova, A.S.Batin / non-linear world. Issue Radio Engineering. 2010-№10-p.651-657.

Grunskaya L.V. The use of the basis of eigen vectors of covariance matrix for revealing complex periodical components of time series. / L.V.Grunskaya, V.V.Isakevich, L.T.Sushkova, A.A.Zakirov // Electromagnetical waves and electronic systems. Issue. Radio Engineering. 2010-№10-p.24-28.

Isakevich V.V. Investigation of the structure of signals in spectral and time ranges caused by moon and solar tides, with a program-analytical system. / V.V.Isakevich, L.V.Grunskaya, D.V.Isakevich, L.T.Sushkova // Biomedical radioelectronics – 2010 - №7, p. 38 – 44.

SUPERBOLIDES – DELIVERY TO THE EARTH THE SUBSTANCE OF SMALL BODIES OF SOLAR SYSTEM

N.A.Konovalova

Institute of Astrophysics Academy of Sciences of the Republic of Tajikistan
Dushanbe, Tajikistan
nakonovalova@mail.ru

ABSTRACT. The existence of the cometary meteoroid streams containing m-sized, high-strength meteorite-producing meteoroids that open a pathway to deliver primitive materials to the Earth are considered. The light curve, mechanism of ablation and physical properties (mass, bulk densities, structural strength and terminal height) of meteoroid are very important information specifying under what circumstances it is possible to expect a meteorite landing. The multi-instrumental aspect of the collected observed data of an extremely bright slow-moving fireball of July 23, 2008 (Tajikistan) that has enabled us to study in detail the passage of this a m-sized cometary meteoroid through the Earth's atmosphere are used. The heliocentric orbit of the meteoroid was found to be similar to the mean orbit of the June Bootid meteor shower, whose parental comet is 7P/Pons-Winnecke. The conclusion that the July 23, 2008 event occurred over Tajikistan is a good candidate to recover of cometary meteorites are made.

Key words: superbolide, meteorite, meteoroid.

Introduction

Many cometary meteoroid streams were formed the continuous sublimation of the ice-rich regions in cometary nuclei. Other important mechanism to form the meteoroid stream connected with the comet is the catastrophic disruption of cometary nuclei and formation of m-sized fragments. The formed large fragments are potential candidates to produce meteorite-dropping meteoroids which cross the Earth and can survive during interaction with the Earth's atmosphere. Reliable observed data about bright fireball allow to calculate their atmospheric trajectory, pre-atmospheric velocity, heliocentric orbit, and to reveal the connection with their parental bodies - asteroids and comets. Till now the observed data received by various systems of observation, including optical, seismic, infrasonic and from orbital satellite which have provided definition of exact heliocentric orbits of meteorites are still small.

Now in the many museums of the world are stored not less than 500 tons of meteorites. It is considered, that for days falls to the Earth about 10 tons of meteoric substance among which there can be meteorites both asteroidal and cometary origins. The terrestrial collection of meteorites includes 4 % of iron meteorites, 85 % of ordinary chondrite (OC) and 9 % of carbonaceous chondrites (CI, CII, CM) which possibly are insufficiently presented because of the fragility and low density (Grady 2000). In Table 1 lists 11 meteorites - ordinary chondrites type H4-H6 were produced by fireballs with asteroidal orbits. Other two meteorites Tagish Lake and Maribo are carbonaceous chondrites CM2 type. Tagish Lake meteorite is related to the known μ-Orionid fireball stream. Moreover, the 60-Orionid meteor stream and asteroid (4183) Cuno can be connected with the μ-Orionid fireball stream and the Tagish Lake meteorite. (Unusually fast fireball, formed meteorite Maribo, is connected with cometary source – the complex Taurid of comet Enke (Haack 2010).

Table 1: List of recovered meteorites with known orbits.

Meteorite name	Meteorite type	Year of fall
Pribram	H5	1959
Lost City	H5	1970
Innisfree	L5	1977
Peekskill	H6	1992
Tagish Lake	CM2	2000
Moravka	H5-6	2000
Neuschwanstein	EL 6	2000
Park Forest	L5	2003
Villalbeto de la Pena	L6	2004
Bunburra	Achondrite	2007
Almahata Sitta	Ureilite	2008
Maribo	CM2	2009
Mason Gully	H5	2010

The observed data and results

The flight and destruction in the Earth's atmosphere of the large, m-sized bodies is accompanied by the formation of light, as well as acoustic-gravitational and infrasonic disturbances. Such disturbances having reached a surface of the Earth cause occurrence of a seismic waves. Use the data of seismic registration of bolides and superbolides in a combination with the data of optical and infrasonic registration is now the established practice of scientific research. As a result it is possible to receive of importance information on the interaction of large meteoroids with the Earth's atmosphere, as well as the atmospheric trajectory, radiant, the heliocentric orbit of the bolide and the position of the place of possible falling of a meteorite.

We have presented here the results of the analysis of complex optical and seismic registration of atmospheric passage and explosion of extremely bright slow-moving fireball and its spectacular dust trail observed over Tajikistan on July, 23rd, 2008 at 14:45:25 UT. The fireball had a -20.7 maximum absolute magnitude. Some eyewitnesses who were from about 25 km from the epicenter of event, heard a whistling sound from the sky, drawn their attention. They have seen flying in the sky object as a small sphere with a tail and of white-blue colour. Soon the explosion which has frightened them has thundered, and there was a white dust trail, which was perceptible for about 20 minutes and was later on distorted by atmospheric winds. Several distinguishable strong knots in this persistent trail, probably produced by successive meteoroid fragmentations, are similar with dust trails of other fireballs observed in a similar manner.

A spectacular long-persistence dust trail was witnessed by numerous casual witnesses in a widespread region of Tajikistan and recorded by video and photo cameras. The fireball was also recorded by two infrasound (Popova et al. 2011) and five seismic stations too. Some observers reported intense rambling sound, such as “thunder” which was audible for several seconds. Sonic boom was heard as far as 100 km away from the burst location and was very strong in the area of about 30 km around the ground projection of the burst location. The fireball was bright enough to be recorded by a visible-light satellite system which provided the irradiated energy for the brightest part of the fireball light curve. The total radiated energy was 2.1 x 10^{11} J, which is equivalent to a total released energy of about 0.05 kT (Brown, 2008).

Statistical observed data about a large bolides testifies, that already at the realised energy equivalent to ≥0.02÷0.03 kilotons THT, at the explosion of a large bolide the shock wave forms acoustic and seismic waves. For the last 20 years among the 30 fireballs, registered by using the various systems of the observation only for 15 fireballs have been received besides optical, also infrasonic and seismic data. Such data were essential addition and have been used for more detailed and full analysis with the aim of definition of the fireball's atmospheric trajectory.

Among the numerous photos received by casual eyewitnesses fortunately two witnesses separated by a distance of 11.3 km were alert enough to capture with photo cameras the dust trail immediately after the flight of the fireball. These two records were an exceptional opportunity to carry out a detailed study of the event, much better opportunity than if only visual sightings were available as the primary sources for determining the fireball trajectory.

The image of fireball’s trail in these photos has been slightly distorted by atmospheric wind so that has given the chance for the measurement of coordinates of its axial line. The subsequent astrometric calibration on stars according to standard procedure of processing of meteor pictures (Babadzhanov, Kramer, 1963) was made. Measuring the rectangular coordinates of the positional stars and any feature point (beginning, terminal, and all flares and depressions) on the fireball trail, such measurements were converted to equatorial coordinates by using the astrometric method of the METEOR software package developed by the Meteor department (Institute of Astrophysics, Tajikistan). As a result of the astrometric measurements we were able to determine the atmospheric trajectory of fireball, coordinate of radiant, velocity, and heliocentric orbit (Table 1-3).

The exact duration of the fireball was known from the data of a visible-light satellite system (Brown 2008). The fireball was first recorded at a height, H_b of 38.2 ± 0.5 km when the velocity, v_b was 14.3 ± 0.5 km/s. The fireball traveled a 19-km observed luminous trajectory and terminated its light at a low altitude H_e of 19.6 ± 0.5 km when the fireball decelerated to 5.8 ± 0.5 km/s. The slope of the trajectory was extremely steep - the zenith distance of the radiant was only of about 10° and the difference between the beginning and the terminal height was 18.6 km.

Table 2: Atmospheric trajectory data

	Beginning	Maximum	Terminal
V (km/s)	14.3 ± 0.5	13.1 ± 0.5	5.8 ± 0.5
H (km)	38.2 ± 0.5	35.0 ± 0.5	19.6 ± 0.5
Abs. mag.	-	- 20.7	-

Table 3: Radiant data

Radiant (J2000.0)	Observed	Geocentric	Helio-Centric
α_R (deg)	221.83 ± 2.1	219.52 ± 2.1	-
δ_R (deg)	+32.40 ± 2.1	+30.95 ± 2.1	-
v_∞ (km/s)	16.0	11.6	38.5

Table 4: Obital data

Orbit (J2000.0)	
Semimajor axis (AU)	3.32
Eccentricity	0.694
Perihelion distance (AU)	1.015
Aphelion distance (AU)	5.624
Argument of perihelion (deg)	176.76.
Ascending node (deg)	119.709
Inclination (deg)	11.95°

The brightest flare was near the beginning of the trajectory at the height H_{max} = 35.0 ± 0.5 km when the first break-up must have occurred under an aerodynamic pressure P_{dyn} of about 1.5 MPa. At the heights of other two small flares the aerodynamic pressure was 2.9 MPa and 3.1 MPa respectively. The apparent radiant was in Bootes, which suggests that the bolide belongs to the J.Bootid meteor shower.

On the seismogram of the analogue seismic station «Hissar», located on the distance about 45 km from the epicentre of event, the weak signal which has arrived in a time interval corresponding to event of fireball has been registered. On July, 23rd, 2008 one five more digital stations «Chujangaron», «Gesan», «Igron», «Garm» and «Shaartus» was operated (Table 5). On the seismogramms of four digital seismic stations «Chujangaron», «Gesan», «Igron» and «Garm» the registration of the seismic signals which are corresponding to the moment of the flight of fireball has been found out

(Konovalova et al. 2011). As a result of the processing of seismic data some types of waves the most visible at the stations which are located more closely to the trajectory of the fireball have been identified.

Table 5: List of seismic stations.

Station	Latitude (°N)	Longitude (°E)	Altitude (m)
Garm	39.00	70.3160	1 305
Gesan	39.2833	67.7155	1 485
Igron	38.2203	69.3266	1 284
Chujangaron	38.6569	69.1582	1 049

For each station the arrival time of various types of the waves generated by the explosion of bolide and distance to the projection of the fireball's trajectory to a terrestrial surface where there was an explosion is defined (Table 6).

Table 6. Arrival time of various types of the waves

Station	Arrival time of seismic wave, u. m. s.	Arrival time of acoustic wave, u. m. s.
Garm	14:46:37.2796	14:50:01.1137
Gesan	14:44:31.5979	14:48:58.8562
Igron	14:45:26.0877	14:48:53.5208
Chujangaron	14:44:12.1039	14:48:14.8369

Using the amplitude of the registered seismic signal has been defined that the seismic energy generated by the explosion of fireball corresponds to the energy of earthquake with a power class 8.5, that is magnitude M = 2.5 (without filter application).

Conclusion

In order to obtain an accurate orbit, it is necessary for the fireball to be observed from multiple stations. In spite of the presence of only two records of the 23 July, 2008 fireball, the resulting data have a good accuracy. On the basis of this data we can conclude that the superbolide of July 23, 2008 was sufficience large and exhibiting high enough tensile strength to be a good candidate to produce meteorites. The break-up of comet 7P/Pons-Winnecke has probably produced high-strength meteoroids capable to produce meteorites under determinate geometric circumstances.

As a result we can conclude that both the fireball and the meteor streams of cometary origin can include large, m-sized meteorite-dropping bodies. The detailed study of physical and structural properties of this component of interplanetary bodies yields very important information about the sources of meteorites – comets and asteroids, from which they have occurred.

Acknowledgements. We are grateful to all the witnesses of the fireball of July 23, 2008 who volunteered their observations, and especially to those who offered photographs of the fireball.

References

Бабаджанов П.Б., Крамер Е.Н.: 1963, Методы и некоторые результаты фотографических исследований метеоров. МГГ, 1957-1959 гг. Изд-во АН СССР, Москва, **12,** 142 с.

Brown P.G.: 2008. *htpp:// astroalert.su/files/bolide.*

Grady M.M.: 2000, Catalogue of meteorites, 5th ed. Cambridge: *Cambridge Uneversity Press*. 670 p.

Haack H., Michelsen R., Stober G., Keuer D., and Singer W.: 2010, *73rd Annual Meteoritical Society Meeting*, abstract # **5085**.

Коновалова Н.А., Рислинг Л.И., Улубиева Т.Р.: 2011, *Докл. АН РТ,* **54**, 638.

Popova O.P. et al.: 2011, *Meteoritics and Planet Sci.*, **46**, 1525.

THE PHOTOMETRIC MODEL OF ARTIFICIAL SATELLITE AJISAI AND DETERMINATION OF ITS ROTATION PERIOD

E. Korobeynikova, N. Koshkin, S. Shakun, N. Burlak, S. Melikyants, S. Terpan, S. Strakhova

Astronomical Observatory, Odessa National University, Odessa, Ukraine
nikkoshkin@yahoo.com

ABSTRACT. Photometry is used to make remote diagnostics of an artificial satellite's motion around its centre of mass. Experimental satellite Ajisai was designed to explore the effects of the space factors, such as gravitation and magnetic fields, solar radiation and others, on its orbital motion and rotation. In the present study we consider the use of peculiar light curves of Ajisai, exhibiting a complex sequence of momentary flashes, for precise determination of the rotation period and velocity variations. For the first time, on the basis of the high-speed photometry, the model of placement of mirrors on the satellite's surface was designed to carry out further analysis of its kinematics.

Introduction

Geodesic artificial satellite Ajisai of mass 685 kg has a near-spherical shape (with radius 1.075 m). On its surface there are 120 laser corner reflectors and 318 quasi-flat mirrors (spherical in fact – the radius of curvature of the mirrors is 8.4÷8.7 m, and the size ≤ 0.25 m) (Sasaki & Hashimoto, 1987). Both types of reflectors are placed in 12 latitudinal rings and two polar caps on the satellite's surface. The mirrors are additionally inclined at different angles to the central latitude of their rings so that while the satellite is rotating around the axis of symmetry any three of them with the same inclination could always reflect the light towards the observer during one revolution. In the literature we have not found information on the actual placement of the whole set of mirrors. However, such data available can be used to estimate the precise rotation period and orientation of the artificial satellite according to the results of the photometric observations (Koshkin et al., 2009/2010).

Right after the launching the satellite rotated with the velocity of 40 revolutions per minute around the axis almost parallel to the Earth's axis of rotation. By the results of many years' laser ranging observations it is known that the rotational velocity slowly decreases with time. In so doing, the axis of rotation slowly oscillates in space, deviating from the celestial pole at the angle of ≈ 0÷3° (Kucharski et al., 2010). The current rotation period is about 2.2 sec, and, according to our estimates, the duration of satellite flashes does not exceed 0.006 sec.

There are two purposes that we pursue by using the photometric timing of moments of flashes when reflecting the sunlight from the mirrors of the fast-rotating satellite. At first, the interval between individual flashes along with the "fitted" rotation period allows us of developing the simulation model of Ajisai – the model of its mirrors' placement and orientation. And further that model is applied to compute the phase shift between far distant in time flashes from two (and more) mirrors that makes possible to considerably improve the accuracy of estimation of the current value of the sideric rotation period.

Model of Ajisai satellite

As is known, at least three flashes are observed during each revolution of Ajisai. That occurs on conditions that the declination of the phase angle bisector almost equals to the latitude of the normal of three mirrors (to simplify the description we use the concept of "normal" as for the flat mirror). In so doing, we neglect the deviation of the satellite's rotation axis from the celestial pole, as well as possible little deviation of the rotation axis from the Ajisai axis of symmetry. The central latitude of each ring with reflectors and the number of mirrors in the ring are known (Kucharski et al., 2010; Kucharski et al., 2009; Kucharski et al., 2010a; Kirchner et al., 2007). The techniques to proceed are as follows. Let us examine an individual light curve of Ajisai for its pass when the declination of the phase angle bisector varied rather widely. The flashes that follow each other with the time close to the current value of the rotation period stand out on the local section of the light curve. Usually, there can be three such sequences (the so-called "chains"), and it is necessary to determine the averaged time intervals between them as the portion of period. As the bisector declination changing (and the "plash of sunlight" shifting on the satellite's surface) the amplitude of certain chains is abruptly reduced; meanwhile, three other chains appear, and their amplitude is rapidly growing up to the optimum. Thereby passing from a certain chain of flashes to the next one, we restore the phase shift between them and the difference of longitudes between the respective mirrors. However, using inaccurate value of the rotation period leads to the error accumulation while shifting along the model's meridian. That is why that procedure demands successive accurate determination. The positions of the central "normal" of the mirrors in the most worked out in detail part of our model are shown in Figure 1.

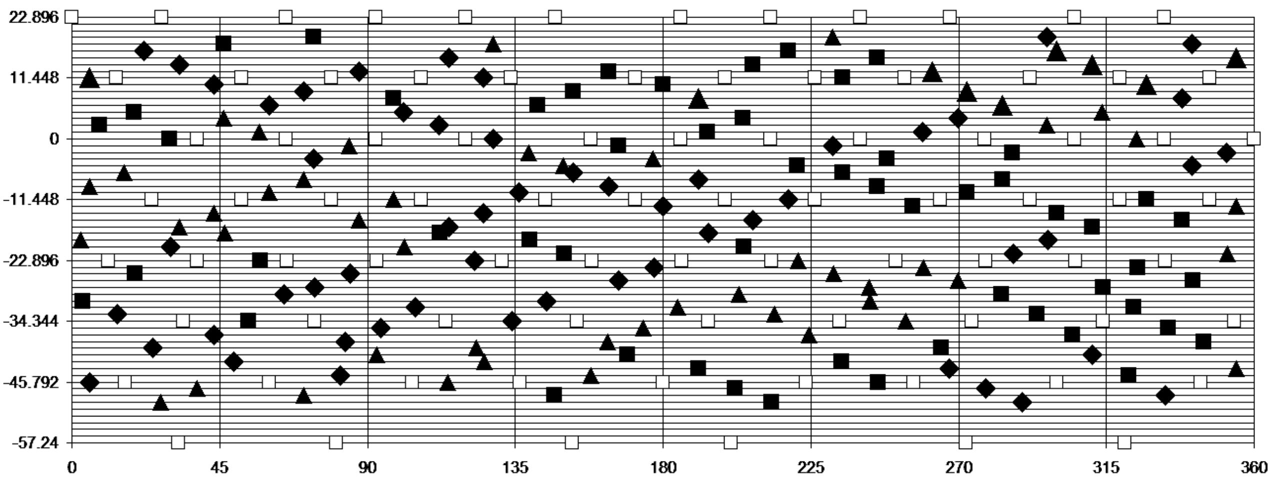

Figure 1. The model of artificial satellite Ajisai: the diagram of the mirrors' positions on its surface. The longitude is plotted on the X-axis, the latitude of the reflector is plotted on the Y-axis. The corner reflectors are marked as blank squares.

Rotation period determination

Neglecting little deviation of the rotation pole of Ajisai from the celestial pole, it is possible to calculate its sideric rotation period. Synodic period, determined by two flashes from the same mirror, equals to $P_{syn} = (t_2\text{-}t_1)/n$, where t_1 and t_2 – is moments of the flashes, n – the number of the satellite's complete revolutions around fixed coordinate frame. The sideric period P_{sid} can be determined by the formula: $P_{sid} = (t_2\text{-}t_1)/(n - \Delta\alpha'/2\pi)$, where $\Delta\alpha'$ – the change in the bisector's right ascension for the time $t_2\text{-}t_1$. When using flashes from different mirrors (not only from the same one), $t_2\text{-}t_1$ interval is to expand considerably, and the formula looks as follows: $P_{sid} = (t_2\text{-}t_1)/(n - \Delta\alpha'/2\pi + \Delta\lambda/2\pi)$, where $\Delta\lambda$ – the difference between longitudes of any two mirrors on the satellite. The averaging by many pairs of flashes allows us of appreciably improving the accuracy of estimation of the sideric period during one pass of the satellite over the observation point.

The change in the sideric rotation period of Ajisai for almost three years according to the photometric observations in Odessa using telescope KT-50 with TV CCD-camera is shown in Figure 2. For such an interval it is still possible to approximate the period change by the linear formula. The average daily increase of the period is 0.000088 sec.

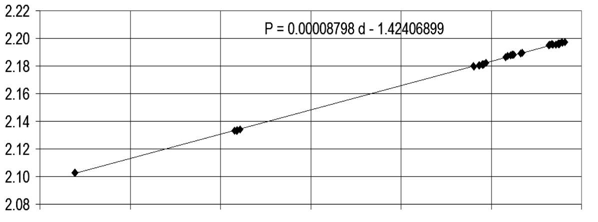

Figure 2. The change in the sideric rotation period of Ajisai according to the some photometric observations in Odessa in 2009-2012. The parameters of the linear approximation are presented.

When using the whole period of observations of Ajisai from the moment of its launching in 1986, the change in its sideric rotation period should be approximated by the exponent, whose parameters are determined by joint examination of the satellite laser ranging data (Kucharski et al., 2010) and our photometric observations:

$$P_{sid} = 1.485802 \cdot \mathrm{Exp}(0.0150114 \cdot T),$$

where T – the time interval in years from August 12, 1986 (since launching).

Deviations of the determined individual values of the rotation period from the approximation by the above indicated exponential formula are shown in Figure 3. It is obvious that those observations are not enough, and they cluster near the so-called "periods of observability" of the satellite from this site. However, those deviations are not random and they are within the same span ±8 msec, wherein their variations were found out by other researchers on the basis of the laser ranging data (Kucharski et al., 2010).

Results and discussion

The photometric timing is a useful instrument (Cusumano et al., 2012) to study variations of the rotation period of artificial satellite Ajisai. With actual time resolution (δt) of measurements equal 0.02 sec, on the observation interval of 7 minutes and more, the error of the period estimate is $\leq$ 0.0001 sec. And that makes possible to expand the analysed time span, for instance by two consecutive passes of the satellite, i.e. up to 120 minutes, thereby decreasing the total period error by one more order (Koshkin et al., 2009/2010). With such accuracies of period, begin to count the errors in the above indicated model of the Ajisai mirrors' placement, making about 3°and more in longitude. According to (Sasaki & Hashimoto, 1987) their structural accuracy in longitude does not exceed ±0.5-0.8°. To check the precision of the model when estimating the sideric period, several times

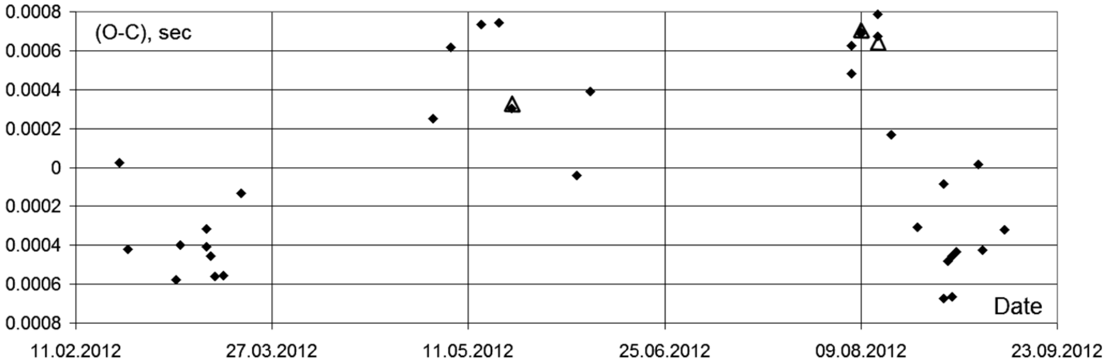

Figure 3. Deviations (O-C) of individual values of the rotation period in 2012 from the approximation by the exponential formula.

we used flashes from the same (!) mirrors in the beginning and in the end of the light curve. That is possible when the geometry of the satellite path relative to the observer is so that the bisector declination in the beginning and in the end of the pass assumes the same values (the patch of the reflected sunlight is shifting on the satellite's surface firstly down and then up the latitude). In that case the effects of the errors in the model on the period values are entirely eliminated (result is marked as blank triangles in the Fig. 3). Nevertheless, the rotation period values slightly differ from the values obtained with the model in that case too, and that is indicative of the model's adequacy.

There may be several components in the total error of the obtained values of the rotation period. First of all, those are local distortions of the model kind of "torsions" that arise due to inaccuracy of the period value, applied when developing the model; and also that can be the finite exposure time that considerably exceeds the flash duration. A small summand of the error is due to the disregard of the deviation of the satellite's axis of rotation from the celestial pole. And finally, it is not certain that the axis of rotation in the satellite's body coincides with the axis of symmetry. Quite the contrary, when observing the light reflection from the low-latitude mirrors additional chains of flashes appeared in very close longitudes; that is impossible for the mirrors of the same ring, but can be caused by some oscillating of the satellite and "engaging" of the mirrors of the adjacent ring.

However, the possibility to apply the developed model discovers new perspectives. At the new stage it is planned to improve and expand the model, as well use as to substantiate the hypotheses on the precession of the Ajisai axis of rotation. To do that thorough series of the photometric observations of the satellite from different sites, including the Southern hemisphere, are essential.

References

Sasaki M., Hashimoto H.: 1987, *IEEE Trans. Geosci. Remote Sens.*, **GE-25**, No. 5, 526.

Koshkin N.I., Korobeynikova E.A. et al.: 2009/2010, *Odessa Astron. Publ.*, **22**, 36.

Kucharski D., Otsubo T., Kirchner G., Koidl F.: 2010, *Adv. Space Res.*, **46 (3)**, 251.

Kucharski D., Kirchner G., Otsubo T. et al.: 2009, *Adv. Space Res.*, **44 (5)**, 621.

Kucharski D., Kirchner G., Otsubo T. et al.: 2010a, *IEEE Trans. Geosci. Remote Sens.*, **48 (3)**, 1629.

Kirchner G., Hausleitner W., Cristea E.: 2007, *IEEE Trans. Geosci. Remote Sens.*, **45 (1)**, 201.

Cusumano G., La Parola V., Capalbi M. et al.: 2012, *A&A*, **548**, A28; *DOI: 10.1051/0004-6361/201219968.*

DETERMINATION OF THE LIGHT CURVE OF THE ARTIFICIAL SATELLITE BY ITS ROTATION PATH AS PREPARATION TO THE INVERSE PROBLEM SOLUTION

Daniil Pavlenko

Research Institute Astronomical Observatory of the I. I. Mechnikov Odessa National University,
Odessa, Ukraine

rereclon@gmail.com

ABSTRACT. Developing the algorithm of estimation of the rotational parameters of the artificial satellite by its light curve, we face the necessity to compute test light curves for various initially given types of rotation and specific features of lighting of the satellite. In the present study the algorithm of creation of such light curves with the simulation method and the obtained result are described.

Introduction

In addition to the rotation that is consciously imparted to the artificial satellite and whose parameters are defined, the unplanned rotation can occur. And generally, the type of that rotation is not defined, and the attendant problems arisen in that case, such as impossibility to receive or to send signals and shortage of energy due to the satellite's inability to position itself by the Sun, do not allow of estimating the parameters of such rotation using the satellite's capabilities only. And that, in its turn, may lead to the loss of the expensive or unique satellite. But it is possible to support such abnormal satellite from the Earth by chasing changes in its light curve and interpreting them in the terms of the rotational parameters. It is possible to determine the rotational frequency by the periodicity of the brightness changes; and the orientation in space can be defined by the non-uniformity in reflection. Of course, it is not so easy, and there is great number of problems. For instance, before the launching, it is necessary to create the chart of specific features of the light reflection from the satellite, taking into account all possible positions of the satellite and the angle of the light reflection. And it is natural that those charts can turn out to be useless when the specific characteristics of the brightness change later in space, for example, due to the damages caused by micrometeorites or incomplete unfolding of the solar panels. Besides, one can not forget about errors both in the brightness charts and in the measuring of the satellite's brightness on orbit. Considering that, the determined rotational parameters will often look not as unique result, but as some range of solutions with different probability. Nevertheless, in most cases such investigation can provide useful and topical information on the rotational parameters of the satellite not using proper communication capabilities of the satellite.

Problem statement

When solving the problem of determination of the rotational motion of the artificial satellite by its brightness [1], one of the issues is the absence of real light curves for different types of rotation. Usually, the light curves are determined either for slowly rotating "active" satellites or for the satellites with undefined rotational parameters – the disabled satellites. Besides, real light curves do not allow of solving the problem "from easy to difficult", i.e. to conduct a gradual increase of the problem's complexity and similar gradual solving of the problems arisen during that process. In view of that, it is necessary to simulate the assumed light curves for the satellites with the given specific features of reflection, rotational velocity and path. In so doing, it is possible to progressively change the accuracy, duration and other characteristics of the obtained assumed light curves, as well as to find events important for the solution by continuous changing of the essential factors. By analogy with the "inverse problem", the task of which is to determine the body's rotation by its brightness, the simulation of the light curve itself based on different factors is to be hereinafter called the "direct problem".

Steps of the direct model problem solution

1. The construction of the brightness charts, i.e. correlation between the brightness of the satellite model and its orientation in space relative to the position of the light source and the observer. The data array is four-dimensional, but as the applied model of the body is axisymmetric [2] the obtained array of the brightness charts is three-dimensional. Its coordinates are the angles, defining the position of the

body's axis of symmetry relative to the Sun and the scattering plane, and the angle between the Sun and the observer – the phase angle. The step width for the chart angles is 1 degree. The example of the brightness chart of the applied model is shown in Figure 1.

2. The determination of the position of the satellite (whose orbit is a prototype for the model), observer and the Sun in the global coordinates in the given moments. The current position of the satellite is computed with algorithm SGP4 by its orbital data in the TLE format [3]. The coordinate system is geocentric equatorial.

3. Successive transfer of the position and orientation of the satellite in space, its direction by the Sun and the observer's location from the geocentric coordinate system (axis OZ – the Earth's axis of rotation) to the satellite-centric coordinate system (axis OZ – the axis of symmetry of the satellite) and then to the spherical coordinate system of the brightness charts using the translation and the rotation matrix.

4. The polar angle *"p"* and the longitude *"A"* of the longitudinal axis (the axis of symmetry) in the brightness charts' system, as well as the phase angle *"Φ"*, make possible to obtain the brightness of the model for the nearest by values nodal points in the brightness charts. The linear interpolation of data by points enables to determine the satellite's brightness for the specific values of those angles.

5. The construction of the light curve of the satellite's model.

Testing of the direct problem

Positions of the light source $\alpha=0°$, $\delta=90°$ ($p=0°$) and the observer $\alpha=0°$, $\delta=45°$; the axis of rotation in space: $\alpha=0°$, $\delta=60°$ ($p=30°$); the axis of rotation within the body: $\alpha=0°$, $\delta=45°$.

It means that the phase angle *Φ* is to be constant and equal to 45, and the angle between the axis of rotation and the axis of symmetry of the body is to be also always 45 degrees.

Figure 2 shows the change in the polar and azimuth angles *A* and *p*, defining the orientation of the longitudinal axis, from the angle of rotation of the model in degrees for the complete revolution.

The light curve is plotted in the same figure in certain relative values. The position of the axis of symmetry in space defines the value of brightness. As seen, the light curve is symmetrical, and it has two not significant peaks; angle *A* is gradually increasing from 0 to 360 degrees, the curve of changes *p* – a sinusoid with its maximum of 75 degrees in the initial point and the minimum of 15 degrees. The "selected" observations are marked with vertical lines.

As the whole light curve is obtained at the same constant phase angle (45°), then the trajectory of the longitudinal axis can be represented in single "brightness chart" in coordinates *A* and *p* (Figure 3).

As seen, the brightness chart is symmetrical in that section where the trajectory of the axis of symmetry of the body passes. The trajectory is also symmetrical, and that is the reason for the symmetry of the light curve. A narrow stripe of high brightness, which is twice intersected by the trajectory of the model's axis during its one revolution, can be seen in the brightness chart; that explains the positions and values of two peaks in the light curve. Within the range of change of *A* from 100 to 260° a significant fall of the brightness in the chart can be retraced (with angle *p* changing within 15÷25°), that corresponds to the minimum of the light curve.

On having compared the coordinates for the selected observation in the curve and in the chart, it is possible to make sure that the brightness in the curve corresponds to the brightness in the chart. For example, the coordinates of the first of the selected observations are A~25, p~75, and in the brightness scale it is somewhere between 140 and 160. That orientation corresponds to the point where the light curve value is 150.

In the context of the inverse problem solution, i.e. determination of the position of the axis of symmetry by the data on the brightness in that moment, let us consider how many points in the brightness chart correspond to one of the given brightness values, and how those points are located. The results for the second and the third selected points in the light curve are shown in Figure 4 below.

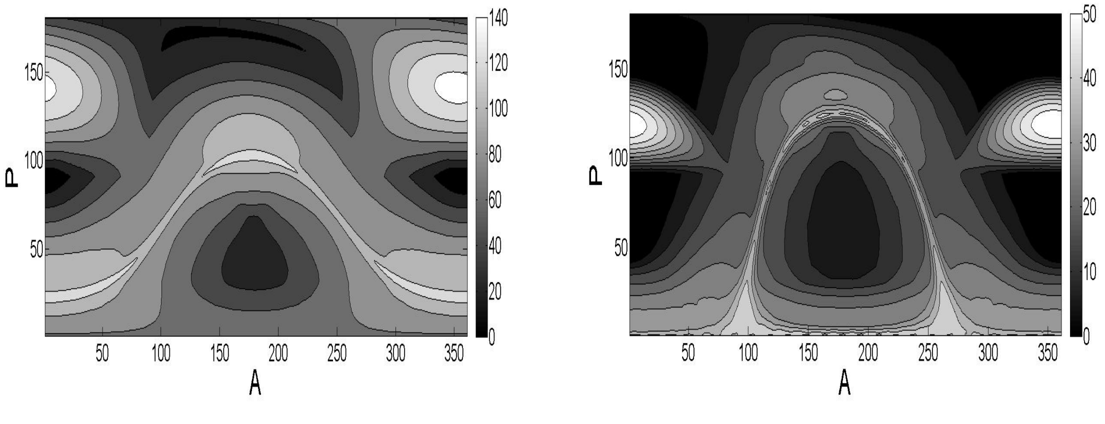

Figure 1. The brightness distribution of the model depending on the position of the longitudinal axis of the model for the phase angles 80 and 124 degrees. The axes show the longitude *A* and the polar angle *p* of the longitudinal axis.

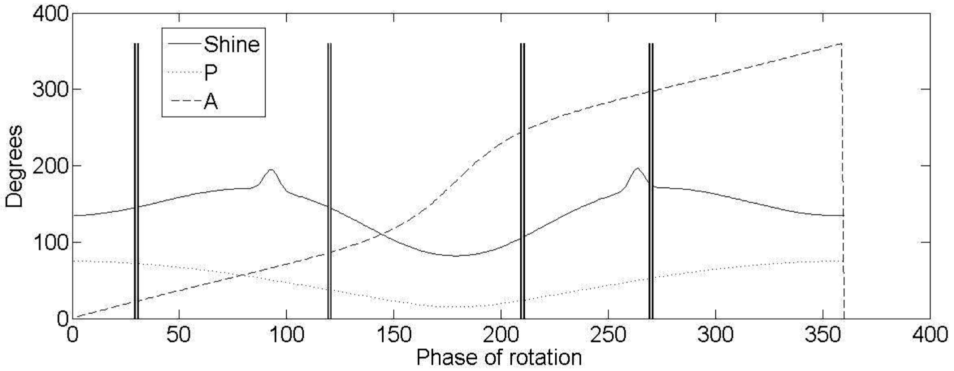

Figure 2. The change in the polar angles *p* (the dotted line) and longitude angles *A* (the dashed line) that define the orientation of the longitudinal axis and the corresponding light curve (the solid line).

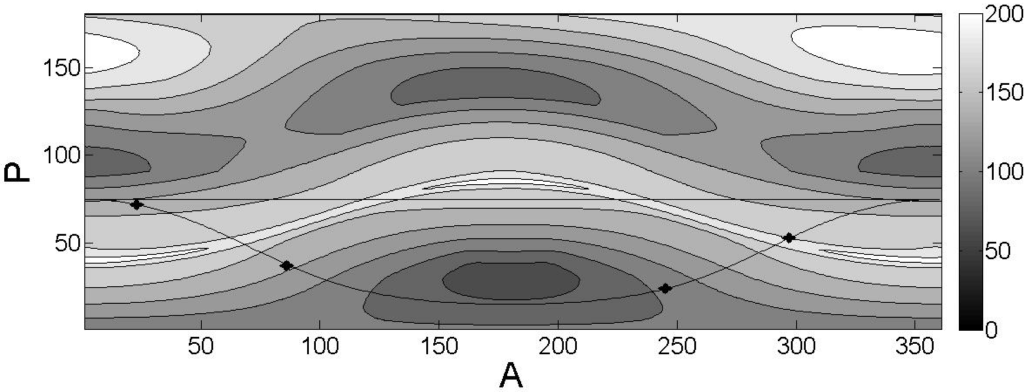

Figure 3. The brightness chart (renormalized) for $\Phi = 45°$ with the plotted motion path of the model's axis of symmetry (marked as the solid line); the selected observations are marked as crosses.

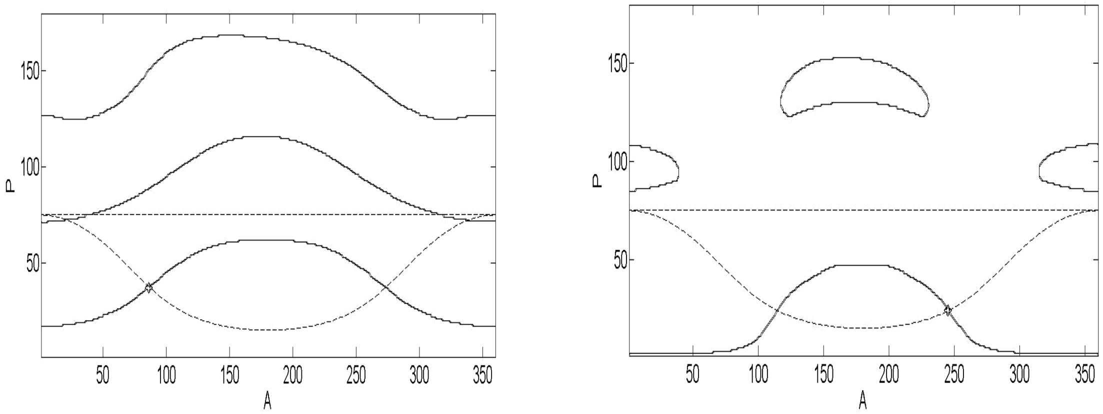

Figure 4. Isophots in the brightness chart ($\Phi = 45°$) for two values of the model brightness with the rotation phase 120° and 210°.

Conclusion and the study to conduct

The devised algorithms allow of estimating theoretical light curves of the satellite model by the given parameters of its motion and rotation for certain lighting and observation conditions. Thereby to solve the inverse problem, it is necessary to restore the kinematic parameters of the model on the basis of the "model" light curve data by available brightness charts.

References

1. The Rep. No. 365 "The investigation of the free motion of the artificial satellites and asteroids and ecological problems of the near-Earth space", Odessa, 2008, p. 111.
2. Меликянц С.М., Шакун Л.С., Кошкин Н.И., Драгомирецкий В.В. Страхова С.Л.: 2007, *Odessa Astron. Publ.*, **20, Part 2**, 72.
3. http://www.celestrak.com/NORAD/elements/

SPACE WEATHER PARAMETERS CAPABLE OF INFLUENCING HEALTH OF A HUMAN BEING

Samsonov S.N., Manykina V. I.

Yu.G.Shafer Institute of Cosmophysical Research and Aeronomy,
Siberian Branch of the Russian Academy of Sciences
Yakutsk, Russia
s_samsonov@ikfia.ysn.ru

ABSTRACT. Space weather is a state of Earth-orbital space. The Sun and cosmic rays of high energy affect this state. As the main contribution to a space weather state is made exactly by the Sun then changes of solar activity parameters, and also the changes of geophysical parameters caused by such influence have been considered in this study. A condition of cardiovascular system of a person of volunteer groups has been considered as a condition of health of a human being. An experiment has been carried out within the framework of Russian-Ukrainian project "Geliomed" (http://geliomed.immsp.kiev.ua) [Вишневский и др., 2009]. It has been found both the immediate influence of electromagnetic solar radiation and the influence of parameters of solar wind and interplanetary magnetic field on a condition of cardiovascular system of a human being mediated through geophysical parameters.

Key words: space weather, solar activity, solar wind, cardiovascular system of a human being, geophysical parameters, interplanetary magnetic field.

Introduction

It is known that the change of conditions in the environment influences a condition of health of a human being. The cardiovascular system, one of the first, joins in the process of adaptation to changing exterior conditions and, consequently, it is the indicator of such influence.

The term «space weather», put into practice for the last years, means a state of Earth-orbital space. The main influence on the state of Earth-orbital space is given by the Sun. One of the fundamental problems of contemporary science is revealing of relationship mechanisms of the solar activity to the functioning of various objects of the biosphere including a human being.

Biological objects on the Earth are under a constant action of environment factors. These are widely known meteorological factors and less known electromagnetic nature factors. Because of the topology peculiarity of magnetic shell of the Earth the changes of factors related to the Earth's magnetic field have the greatest value at high latitudes. Therefore, in this work the main attention will be given to studies in auroral and subauroral latitudes.

Experimental data and registration methods

The following solar activity parameters: the electromagnetic waves (X-rays and radio- ranges), charged high–energy particles, solar wind (speed, concentration and dynamic pressure), interplanetary magnetic field, and also geophysical activity (geomagnetic disturbance) have been considered as space weather factors. The daily meteorological data (pressure, temperature, humidity and wind speed) as parameters of usual ground weather have been used. The data on space and usual ground weather have been obtained from the Internet. An index of cardiovascular diseases is the number of calls around Yakutsk for the medical care by reason of the following diagnosis: HD - hypertensive disease; HC -hypertensive crisis; DR -patients registered in a dispensary. To define the functional state of cardiovascular system of a person the heart rhythm of volunteers has been measured in Yakutsk and Tixie with the express cardiograph "Fazagraf".

Results and discussion

In the earlier published paper [Самсонов и др., 2005] it has been shown that 2-4 days before a geomagnetic disturbance on the Earth the maximum number of calls for the medical care by reason of cardiovascular diseases is observed. The analysis of given fact has allowed to find out the fact that this maximum is related to the disturbance on the Sun. Then a question about what kind of solar activity parameters can provide a prompt (within 24 hours) influence on a human being on the Earth has appeared. For example, electromagnetic radiation (propagated up to the Earth in 8 minutes) and protons with the energy from 10^6 up to above10^9 eV (propagated to the

Earth from 15 minutes up to a few hours depending on energy) could be such parameters.

To reveal the definite physical parameters of solar activity responsible for the occurrence of maxima of calls for the medical care, the comparison of solar energy proton fluxes and also electromagnetic radiation of various periods (radio emission and X-rays) with medical indices has been carried out. All specified solar activity parameters have been treated using a superposed epoch technique. In this case, dates when the K-index of geomagnetic disturbances exceeded the value of 30 units (24 events for 1992) have been taken for a zero day.

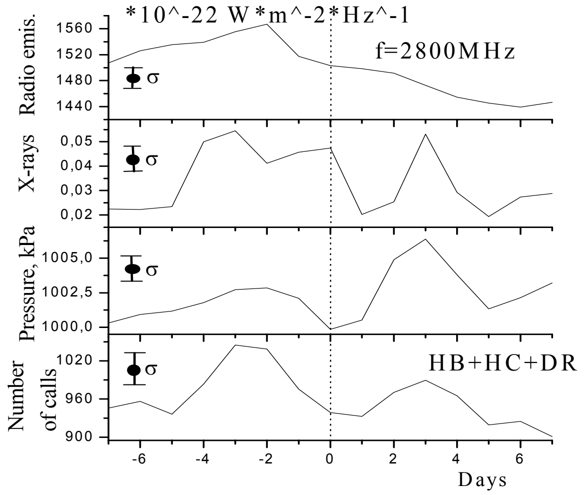

Figure 1: Dynamics of the change of radio emission and X-rays of the Sun, ground pressure and calls for the medical care for patients suffering from cardiovascular diseases relative to the geomagnetic disturbances

The treated data of solar electromagnetic radiation have been compared with the data of the number of calls for the medical care for patients suffering from the cardiovascular pathology. In the energy proton fluxes the presence of maximum at the moment of solar disturbance (2-4 days before the maximum in a geomagnetic disturbance) and maximum in 2-4 days after geomagnetic disturbance has not been revealed. At the same time in the solar electromagnetic radiation, i.e. in the intensity of radio emission with a wave of 10,7 cm length, and also in the X-rays with a wave of (0.5-8.0) nm length which are shown in Fig.1, the features coinciding with changes of the number of calls for the medical care for the patients suffering from a cardiovascular pathology have been found out. As is seen from Fig.1 both in the radio emission and in the X-rays there is a maximum coinciding with the first maximum in the medical indices. Besides, in the X-rays there is a maximum on the third day after the geomagnetic disturbance which coincides with the second maximum in the calls for the medical care. Besides, in the data of ground atmospheric pressure there are both maxima coinciding in time with maxima of calls for the medical care. The coincidence of maxima in the number of calls for the medical care with maxima in the electromagnetic solar radiation and maxima in the ground atmospheric pressure has demanded to clarify what kind of two factors: space or atmospheric (or both of them)one influences on a state of cardiovascular system of a human being.

Therefore, a special experiment on a group of volunteers numbering 45 persons in Yakutsk and Tixie was carried out. Every day instrument's indications of electrocardiogram of volunteers with the express - cardiograph "Fazagraf" were read. The symmetry coefficient of T-wave (SCT) of the electrocardiogram as an index of condition of cardiovascular system of a human being was used. The opportunity to use the SCT as an index of condition of cardiovascular system of a human being is shown in [Файнзильберг, 1998; Вишневский и др., 2003]. Thus, for each patient the individual series of the data for the October 5, 2009 to December 30, 2009 experiment period has been obtained.

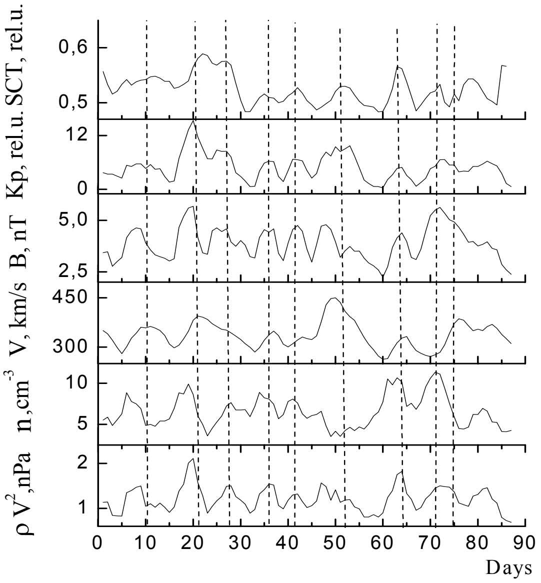

Figure 2: Changes of a condition of cardiovascular system of a half of volunteer group in Yakutsk and space weather parameters

Fig.2 presents SCT in Yakutsk, and also the following space weather parameters: Kp-index of geomagnetic disturbance, B – total intensity of the interplanetary magnetic field, V - solar wind speed, n – particle concentration of the solar wind, ρV^2 – solar wind dynamic pressure.

As is seen from this Figure almost all maxima and minima of the given parameters coincide in time of occurrence with the same maxima and minima in the group reaction of SCT of volunteers in Yakutsk. The experiment in Tixie has shown the same results (Figure is not shown because of limitation of paper space).

Such almost complete coincidence has been observed for a half group of volunteers in Yakutsk (12 persons) and Tixie (10 persons). Other halves of volunteers (11 persons in Yakutsk and 11 persons in Tixie) have shown a partial coincidence of SCT with space weather parameters, and 1 person did not have any coincidence with SCT. The best coincidence is observed for SCT with the total intensity of interplanetary magnetic field, solar wind dynamic pressure and the Kp-index of geomagnetic disturbance.

For example, the correlation coefficient between SCT in Yakutsk and the Kp-index is 0,55 and this fact is under the condition that SCT represents not the index of one person but the average value (group parameter) of a half of volunteers participating in the experiment.

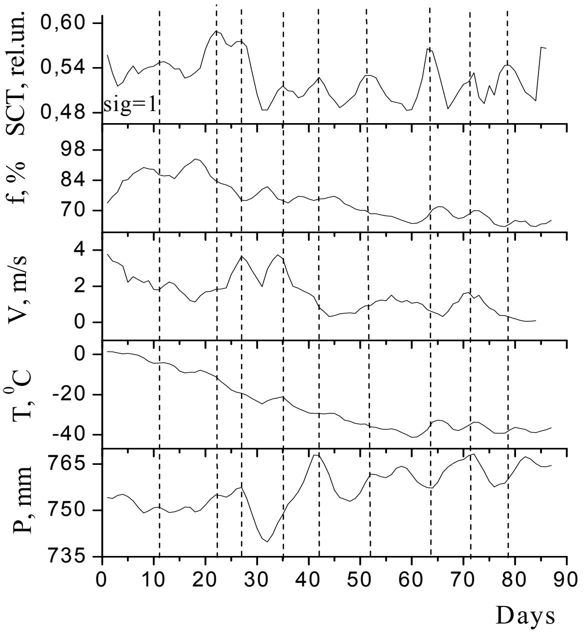

Figure 3: Change of the condition of cardiovascular system of a half of volunteer group in Yakutsk depending on meteoparameters

Then the change of condition of cardiovascular system of volunteers with meteoparameters has been compared. Fig.3 presents the changes of SCT of the group of volunteers in Yakutsk and meteoparameters: f % - humidity, V – wind speed, T - temperature and P - pressure of the ground atmosphere. As is seen from this Figure the coincidence of only separate changes of each of meteoparameters with SCT is observed. It means the presence of only partial influence of absolute values of meteoparameters on cardiovascular system of a person for the considered period at the best. The experiment in Tixie has shown the same results (Figure is not shown because of limitation of paper space).

Thus, it has been shown that the condition of cardiovascular system of a human being in the experiment carried out is connected, first of all, with the space weather parameter.

Conclusions

The study of connection of space weather parameters with a condition of cardiovascular system of a human being has allowed to find out that:

1. Dynamics of electromagnetic disturbances on the Sun (radio emission and X-rays) coincides with the dynamics of the number of calls for medical care by reason of cardiovascular diseases that indicates to the possible influence of electromagnetic solar emission on cardiovascular system diseases of a human being.
2. Coincidence of change of solar wind parameters, such as the density, speed and dynamic pressure of the solar wind, and also the total intensity of the interplanetary magnetic field and geomagnetic disturbance with a condition of cardiovascular system of a human being also indicates to the influence of space weather parameters on a condition of cardiovascular system of a human being.

The study has been carried out under the partial financial support of the Russian Fund for Basic Research (grants № 12-05-98522 and 12-02-98508).

References

Вишневский В.В., Файнзильберг Л.С., Рагульская М.В.: 2003, *Биомедицинские технологии и радиоэлектроника*, **3**, 3.

Вишневский В.В., Рагульская М.В., Самсонов С.Н.: 2009, *Вестник новых медицинских технологий*, **16**, 241.

Самсонов С.Н., Петрова П.Г., Соколов В.Д., Стрекаловская А.А., Макаров Г.А., Иванов К.И.: 2005, *Журнал неврологии и психиатрии им. С.С.Корсакова. Инсульт*, **14**, 18.

Файнзильберг Л.С.: 1998, *Управляющие системы и машины*, **4**, 40.

ON SIMILARITIES BETWEEN THE EARTH ROTATION AND TEMPERATURE CHANGES

L.V. Zotov

Sternberg Astronomical Institute of Moscow State University, Russia, *tempus@sai.msu.ru*

ABSTRACT. Earths rotation reflects processes in the atmosphere, ocean, Earths interior. The similarities between the global temperature oscillations and Earths rotation speed changes are well known, but still are not explained. We also have found similarities between $\sim$ 20-year temperature oscillations, Chandler excitation envelope and cycle of regression of the Moon orbital nodes. In this short article we want to attract attention to this fact.

Key words: Earth rotation: Chandler wobble: Climate Change.

1. Introduction

In recent decades huge amount of data upon the Earth was obtained by space and ground-based means of observations. Information retrieval requires developing of new processing techniques. Interpretation needs understanding of the Earth on a planetary scale.

Earth rotation variations can be considered as an index of activity of different processes in atmosphere, ocean, crust, and other parts of Earth system. Among the most discussed problem in Earth sciences today is the Climate Change. Its footprint is evident everywhere: the atmosphere temperature is rising, ocean level is increasing, ice sheets are melting all over the globe. Can this processes be reflected in the Earth rotation? It is known for decades, that correlations exists between the Earth rotation velocity and long-scale temperature changes. For this fact there is lack of explanations, or, better to say, there are many hypothesis, and none of them is preferable.

Below we present some comparisons and propose a new factor, whose influence could be underestimated. Particularly – the response of the Earth system to the Moon orbital precession cycle.

2. Chandler wobble excitation

Since S.C. Chandler discovered in 1981 one of the main component of polar motion, carrying his name, more then a century has passed, but the changes of the amplitude of this oscillation, which reaches 0.2 arcsec, remain enigmatic. The Earth is the viscous-elastic body and Chandler wobble should have been damped with the characteristic time of 50 years, but it does not happen. It is believed, that it is maintained by the hydro-atmospheric excitation (Yatskiv Y., 2000).

Have been studying polar motion, the author (Zotov, 2010c) developed several methods of reconstruction of the Chandler wobble causes – the excitation function. The Chandler excitation reconstruction from observations is tricky, because this excitation is very small in comparison with the nearby annual one and others. In (Zotov, Bizourad 2012) the Panteleev corrective filtering was proposed for solving this ill-posed problem (Zotov, Panteleev, 2012). The inverse operator is corrected in frequency domain to remove annual, low-frequency and other noise components.

In result the 18.6-year amplitude modulation of Chandler excitation, synchronous with the tidal variations caused by the lunar orbital nodes regression cycle was revealed. The excitation is shown on Fig. 3 together with the tidal harmonic, extracted from the IERS LOD zonal tide model and represented along the abscissa. We can trust the reconstruction only inside the 1870-1990 yrs interval because of the 20-yr border effects.

Study of atmospheric and oceanic angular momentum has shown the response of atmosphere and ocean to 18.6-year cycle of the tide (Zotov, Bizourad 2012). The amplitude increase is especially well seen in Ocean Angular Momentum changes, related to the mass redistribution. In this way the influence of the Moon on atmosphere and ocean can be transferred to the Chandler wobble excitation.

3. SSA of GMSTA

Singular Spectrum Analysis (SSA) is one of the useful techniques for signal study. This method is based on SVD decomposition of a trajectory matrix, what allows to decompose the time series into trend, oscillations of different periods and to remove noise. Initial time series splits into principal components (PC). The first one represents the most energetic part of the signal, the second – less intensive part and so on in decreasing order. Several first components together usually represent the most of signal variability. Here we will not describe the technique, which can be found in Golyandina, 2004; Zotov, 2010a, 2010b.

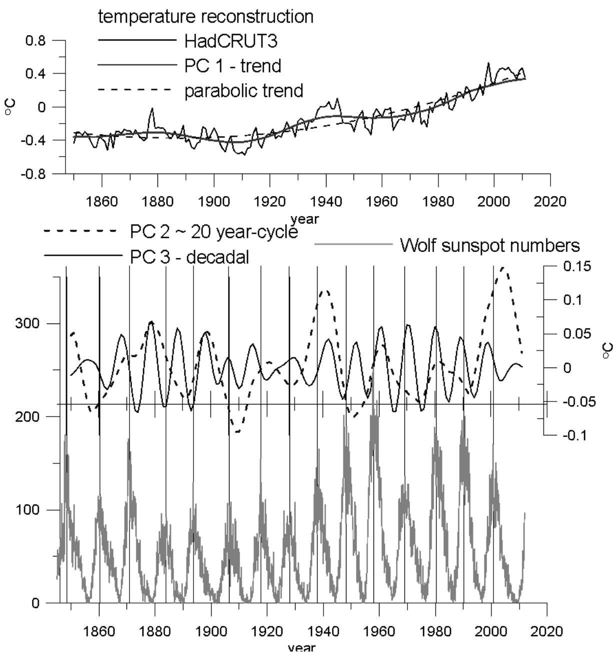

Figure 1: HadCRUT GMSTA and its SSA components compared with Wolf numbers.

By means of SSA we decomposed HadCRUT3 data upon the temperature anomaly on Earth – Global Mean Surface Temperature Anomaly (GMSTA). This time series starts in 1850 and is obtained by combining the sea surface and land surface air temperature records by meteorological and climate centres in UK. The original HadCRUT curve and its SSA-components are shown on Fig. 1. The first component PC 1 represents trend – the temperature rise, especially quick since the mid of XX cent. The total rise of $\sim 0.7^o$, it is believed, is caused by the anthropogenic global warming (IPCC Report, 2007; Zotov, 2010b). The second component PC 2 (Fig. 1 middle plot) has period of $\sim$ 20 years and the third PC 3 is decadal. The existence of this types of variability was also noted by Qian et al., 2010. So that some authors (Schrijver et al., 2011) speculate, that temperature changes are caused by the Sun variability, we show the main characteristic of it – Wolf sunspot numbers on Fig. 1, bottom. It can be seen, that decadal oscillation (PC 3) is not in phase with Wolf numbers curve. On one half of the interval – since 1920 $\sim$ 20-year oscillation (PC 2) can be found more or less in agreement with each second cycle of activity. Still, taking in account that the total solar irradiance changes in the solar cycle are less then 0.1% (IPCC report., 2007), we do not think Sun is responsible for Climate Change.

It was noted long time ago, that temperature anomalies and Earth rotation have similarities. It is mentioned already in Lambeck, 1980 monography, discussed in Sidorenkov, 2009, etc. In particular, it was found the inverse similarity between the length of day (LOD) and temperature. On Fig. 2 the GMSTA after the subtraction of parabolic trend (Fig. 1 top, dashed) is compared with the inverted LOD curve. The correlation coefficient is 0.43, for smoothed GMSTA – 0.55. Though the long-time LOD reconstruction since 1832 provided by JPL from LUNAR97 time series based on eclipses and occultation observations is not very exact for the XIX century, we believe, the similarity is real. When the temperature on Earth increases, the Earth accelerates. One of possible explanations is given in Sidorenkov, 2009, where it is supposed, that ice melting is responsible. The warming, which causes the ice melting in Greenland, Antarctica, etc. changes the Earth moment of inertia, what, together with postglacial rebound, can explain both LOD changes and trend in the Earth polar motion. From the other side, calculations of effect of sea level rise for the scenario of global warming made in (Landerer et al., 2007), give quite a small number: -0.12 ms in LOD for the next 200 years.

The correlation is not yet a proof of cause-effect relationship. Good physical model should be build and tested for this. It could be, that Climate Change does not influence Earth rotation directly, but some other factor exists, which influence them both and leaves similar footprints.

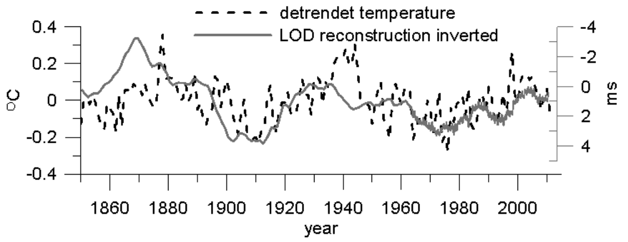

Figure 2: LOD and GMSTA without trend.

We found another interesting similarity. On Fig. 3 we represent Chandler excitation, reconstructed by Panteleev corrective filtering, together with the temperature PC 2 $\sim$ 20-yr component. The plot along abscissa shows 18.6 tidal wave in LOD. The similarity can be well seen everywhere, except the 20-year borders. Envelope of Chandler excitation agrees well with PC 2. The correlation coefficient[1] inside this interval (depicted by rectangle on Fig. 3) is 0.39.

We come to the conclusion, that temperature increases with the increase of Chandler excitation (at these moments Earth decelerates). The governing factor could be the influence of 18.6-yr Moon nodes regression cycle. Thus, the influence of the Moon on

---

[1] Linear correlation is not quite a good measure here because of different amplitude of oscillations.

atmosphere and ocean can be reflected in Chandler excitation and even in the temperature changes on the planet. The mechanism of this influence is yet to be explained.

4. Conclusion

The purpose of the presented research is to attract attention to similarities between Earth rotation and temperature changes on Earth. By means of SSA and correlation analysis we decomposed HadCRUT3 time series and detected different components of temperature changes – global warming trend, decadal and ~ 20-year oscillation. Comparison with Wolf sunspot numbers did not reveal similarities between the Sun activity cycle and any of the temperature components.

On the other side, our recent result upon the Chandler excitation attracted our attention to the 18.6 yr cycle of the Moon orbital nodes regression, which modulates Chandler excitation envelope. We compared ~ 20-year oscillation in temperature with this envelope and, surprisingly to ourself, found distinctive similarities. Thus we conclude, that the influence of such factor as the Moon orbital regression cycle can be underestimated. Its influence on ocean and atmosphere can be more important, then it was expected theoretically. The presence of Moon's signature in Chandler excitation and GMSTA makes it one of the governing factors of these and, may be, some other processes.

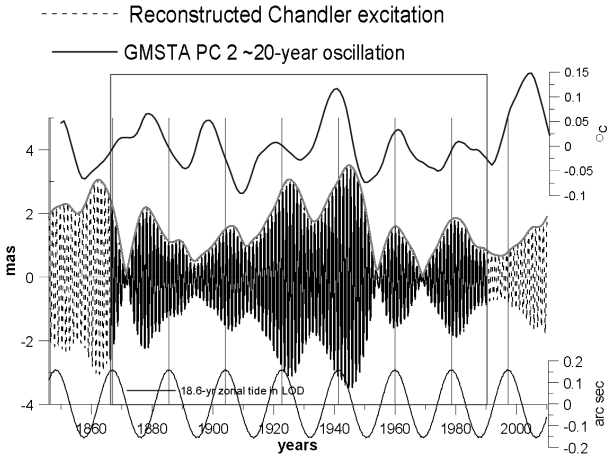

Figure 3: Chandler excitation and ~ 20-year temperature changes.

Acknowledgements. This work is supported by the Russian Foundation for Basic Research grants No 12-02-31184, No 10-05-00215 and Chinese Academy of Sciences grant for Young International Scientist.

References

Golyadina S.A.: 2004, Method "Caterpillar-SSA": analysis of the time series, Snt-Petersburg.

IPCC Fourth Assessment Report: Climate Change 2007 (AR4).

Qian W.H., Lu Bo, Zhu C.W.: 2010, *Chinese Science Bulletin.,* **55**, 19. 1963-1967.

Lambeck K.: 1980, The Earth's Variable Rotation; Geophysical Causes and Consequences, Cambridge University Press.

Landerer F.W., Jungclaus J.H., Marotzke J.: 2007, *GRL*, **34**, L06307, doi:10.1029/2006GL029106.

Schrijver C.J., Livingston W.C., Woods T.N., Mewaldt R.A.: 2011, *GRL*, **38**, L06701, doi:10.1029/2011GL046658.

Sidorenkov N.S.: 2009, The Interaction Between Earth's Rotation and Geophysical Processes, Wiley-VCH Verlag.

Yatskiv Y.: 2000, *ASP Conf. Ser.*, **208**, 383.

Zotov L., Bizourad C.: 2012, *Journal of Geodynamics, special issue "Earth rotation"*, doi: 10.1016/j.jog.2012.03.010.

Zotov L.V., Panteleev V.L.: 2012, *Computational Methods for Applied Inverse Problems* /Ed. by Y.F.Wang, A.G.Yagola and C.C.Yang, De Gruyter & Higher Education Press.

Zotov L.: 2010a, Theory of filtering and time series processing, course of lectures, Moscow State University.

Zotov L.V.: 2010b, *Proc. of the 10th Gamow Odessa Astron. Conf.*, 189.

Zotov L., 2010c, *Artificial satellites*, **45**, N 2, 95.

Participants of the XII Odessa International Astronomical Gamow's Conference-School "ASTRONOMY AND BEYOND: ASTROPHYSICS, COSMOLOGY AND GRAVITATION, COSMO-MICROPHYSICS, RADIO-ASTRONOMY AND ASTROBIOLOGY"